6. QUANTUM MECHANICAL REACTIVE SCATTERING FOR THREE

DIMENSIONAL ATOM PLUS DIATOM SYSTEMS: I. THEORY

Quantum mechanical reactive scattering for three dimensional atom plus diatom systems: I. Theory[*]

G. C. Schatz[†] and A. Kuppermann

A. A. Noyes Laboratory of Chemical Physics,[§]

California Institute of Technology, Pasadena, California 91125

A method is presented for accurately solving the Schrödinger equation for the reactive collision of an atom with a diatomic molecule in three dimensions.on a single Born-Oppenheimer potential energy surface. The Schrödinger equation is first expressed in body fixed coordinates. The wave function is expanded in a set of vibration-rotation functions, and the resulting coupled equations are integrated in each of the three arrangement channel regions to generate primitive solutions. These are then smoothly matched to each other on three matching surfaces which appropriately separate the arrangement channel regions. The resulting matched solutions are linearly combined to generate wave functions which satisfy the reactance and scattering matrix boundary conditions, from which the corresponding $\underset{\approx}{R}$ and $\underset{\approx}{S}$ matrices are obtained. The scattering amplitudes in the helicity representation are easily calculated from the body fixed $\underset{\approx}{S}$ matrices, and from these scattering amplitudes, several types of differential and integral cross sections are obtained. Simplifications arising from the use of parity symmetry to decouple the close coupled equations, the matching procedures and the asymptotic analysis are discussed

in detail. Relations between certain important angular momentum operators in body fixed coordinate systems are derived and the asymptotic solutions to the body fixed Schrödinger equation are analyzed extensively. Application of this formalism to the three-dimensional $H + H_2$ reaction is considered including the use of arrangement channel permutation symmetry, even-odd rotational decoupling and post-antisymmetrization. The range of applicability and limitations of the method are discussed.

1. INTRODUCTION

One of the most important goals of chemical dynamics is the
accurate calculation of cross sections for reactive bimolecular
collisions. Such calculations can be used to develop and test approxi-
mate reaction dynamic theories and statistical theories, to advance
our understanding of dynamical processes governing reactive collisions,
and to interpret, analyze and make predictions concerning the results
of experiments.

In recent years, a number of attempts have been made to solve
this problem accurately (i.e., quantum mechanically) for the simplest
possible such chemical reaction, the collision of an atom with a diatomic
molecule on a single electronically adiabatic potential energy surface.
One of the major difficulties in achieving this goal in the past has
been the absence of computationally efficient procedures for obtaining
accurate solutions to the Schrödinger equation for reactive collisions.
For the simple case in which the three atoms are confined to move
on a space-fixed straight line, adequately accurate and efficient
methods have been developed within the last several years and applied
to a variety of systems.[1-13] However, when the collinearity restric-
tion is eliminated, the problem becomes more difficult, especially
when the atom is permitted to react with either end of the diatom.
To tackle such noncollinear problems, several different techniques
have been proposed and to a certain extent tested. Baer and Kouri[14]
have developed an integral equation method and have applied it to a
simple three-dimensional model atom plus diatom system in which
reaction with only one end is permitted. Saxon and Light, and Alten-

berger-Siczek and Light[15] have investigated the coplanar $H + H_2$
reaction using a close coupling-matching procedure which ignored
closed vibrational channels, while Wyatt and coworkers[16] have devel-
oped a somewhat different close coupling procedure in which closed
channels are included, and for which the use of hindered rotor basis
functions leads to simple bifurcation properties. Quite recently,
Elkowitz and Wyatt[16a] have applied this procedure to the three-dimen-
sional $H + H_2$ reaction. Wolken and Karplus[17] have applied an integro-
differential equation method proposed by Miller[18] to 3D $H + H_2$ using
a one vibrational basis function approximation.

In a previous paper[19] (hereafter referred to as I) we described
a method for accurately solving the Schrödinger equation for reactions
of the type $A + BC \rightarrow AB + C \ (\rightarrow AC + B)$ on a single electronic potential
energy surface with the restriction that the motions of the three atoms
be constrained to lie in a single spaced fixed plane. An extensive
application of this method to the planar $H + H_2$ exchange reaction has
now been made.[20,21] The present paper describes an extension of
this method to three-dimensional atom-diatom collisions. It yields a
computationally practical procedure for accurately calculating reaction
cross sections for many atom-diatom chemical reactions. A number of
additional concepts not present in the planar problem are introduced,
and the simplifications occurring in an application to three-dimensional
$H + H_2$ are discussed. Preliminary results of an application of this
method to the $H + H_2$ reaction on a realistic potential surface have
recently been published[22] providing the first fully converged quantum
mechanical cross sections for a chemical reaction. The extension of

these calculations to energies above the threshold for vibrational excitation has lead to the discovery of a dynamical (Feshbach) resonance[23] for that reaction, a phenomena whose experimental detection may be an important tool in the characterization of reactive potential energy surfaces. A more complete description of these results for $H + H_2$ is forthcoming.[24]

The method utilizes a close coupling propagation technique to generate complete sets of solutions in each of the three arrangement channel regions of configuration space,followed by a "matching procedure" in which the solutions are smoothly matched to one another on a set of three appropriately chosen surfaces which separate these three regions. The scattering matrices, amplitudes and cross sections are then determined by analyzing the asymptotic behavior of these matched solutions. As thus formulated, the method is similar in spirit to the corresponding planar theory described in I and, for this reason, many of the concepts presented in that paper and which carry into the three-dimensional world without modification will only be summarized briefly. There are, however, several differences in application, most notably in the matching procedure, and these will be discussed in detail. In addition, the concepts of angular momentum coupling, of body and space fixed coordinate systems, and of parity symmetry decoupling will be developed thoroughly as their utilization is of great importance to the three-dimensional method.

In Section 2 we discuss the body fixed partial wave Schrödinger equation along with angular momentum coupling and the division of configuration space into arrangement channel regions. The fully

coupled Schrödinger equation for the four different internal configuration space regions of each arrangement channel region is discussed in Section 3 and the matching procedure is outlined in Section 4. In Section 5 the body fixed R and S matrices are defined and their relationships to the helicity representation scattering amplitudes and cross sections are derived. In Section 6 we discuss the limitations of the method and its possible generalizations. In each section, where appropriate, the simplifications pertinent   to the $H + H_2$ exchange reaction are indicated. Appendix A outlines the derivation of the body fixed Schrödinger equation and indicates relationships between several important angular momentum operators. Appendix B includes a discussion of parity symmetry and the simplifications in the method which may be gained by explicitly including it.

2. THE BODY FIXED ROTATIONALLY COUPLED SCHRÖDINGER EQUATION

2.1 Separation of Internal Configuration Space into Arrangement Channel Regions

We consider the three-dimensional collision of an atom A with a diatomic molecule BC and, in parallel, the B plus CA and C plus AB collisions. A convenient procedure for specifying the locations of A ($\equiv A_\alpha$), B ($\equiv A_\beta$) and C ($\equiv A_\gamma$) in the center of mass is depicted in figure 1. $\underset{\sim}{\bar{R}}_\alpha$ is the vector from the center of mass of BC to A and $\underset{\sim}{\bar{r}}_\alpha$ is the B to C internuclear vector. As $|\underset{\sim}{\bar{R}}_\alpha| \to \infty$, with $|\bar{r}_\alpha|$ remaining finite, we obtain the separated A + BC arrangement channel (denoted by the symbol α). The vectors $\underset{\sim}{\bar{R}}_\beta$, $\underset{\sim}{\bar{r}}_\beta$ and $\underset{\sim}{\bar{R}}_\gamma$, $\underset{\sim}{\bar{r}}_\gamma$ are

defined analogously for the arrangement channels β (B + AC) and

γ (C + AB), respectively. Note that the arrangement of the vectors

in Fig. 1 is cyclic in the indices $\alpha\beta\gamma$. We let $\lambda\nu\kappa$ represent any one

of the cyclic permutations $\alpha\beta\gamma$, $\beta\gamma\alpha$ and $\gamma\alpha\beta$, and define the vectors

$\underset{\sim}{\bar{R}}_\lambda$, $\underset{\sim}{\bar{r}}_\lambda$, $\underset{\sim}{\bar{R}}_\nu$, $\underset{\sim}{\bar{r}}_\nu$ and $\underset{\sim}{\bar{R}}_\kappa$, $\underset{\sim}{\bar{r}}_\kappa$ accordingly. We also introduce the scaled

variables $\underset{\sim}{R}_\lambda$, $\underset{\sim}{r}_\lambda$ which are related to $\underset{\sim}{\bar{R}}_\lambda$, $\underset{\sim}{\bar{r}}_\lambda$ by

$$\underset{\sim}{r}_\lambda = a_\lambda^{-1} \underset{\sim}{\bar{r}}_\lambda \tag{2.1a}$$

$$\underset{\sim}{R}_\lambda = a_\lambda \underset{\sim}{\bar{r}}_\lambda \tag{2.1b}$$

where

$$a_\lambda = (\mu_{\lambda,\nu\kappa}/\mu_{\nu\kappa})^{\frac{1}{4}} \tag{2.2a}$$

and $\mu_{\lambda,\nu\kappa}$ and $\mu_{\nu\kappa}$ are the reduced masses corresponding to $\bar{R}_\lambda$

and $\bar{r}_\lambda$ motion, respectively:

$$\mu_{\lambda,\nu\kappa} = m_\lambda (m_\nu + m_\kappa)/(m_\lambda + m_\nu + m_\kappa) \tag{2.2b}$$

$$\mu_{\nu\kappa} = m_\nu m_\kappa /(m_\nu + m_\kappa) \tag{2.2c}$$

This notation is identical to that used in I and is dictated by the con-

siderable mathematical convenience associated with using scaled

variables.[25-27]

We are interested in solving the six-dimensional Schrödinger

equation for the motions of the three nuclei, on a single electronically

adiabatic potential energy surface, obtained after the motion of the

center of mass of the system is removed. The surface (in the absence

of external fields) is a function of only three appropriately chosen

variables which specify the internal three atom configuration. A

convenient representation of this potential V is afforded by the use of

the variables R_λ, r_λ and γ_λ ($\lambda = \alpha, \beta$ or γ) where γ_λ is the angle between R_λ and r_λ defined by

$$\gamma_\lambda = \cos^{-1} \frac{\underset{\sim}{R_\lambda} \cdot \underset{\sim}{r_\lambda}}{|\underset{\sim}{R_\lambda}| \, |\underset{\sim}{r_\lambda}|} \quad ; \quad 0 \leq \gamma_\lambda \leq \pi \tag{2.3}$$

in terms of which $V = V^\lambda(r_\lambda, R_\lambda, \gamma_\lambda)$. As was discussed in I (Section 3.1), the variables $\underset{\sim}{R_\lambda}, \underset{\sim}{r_\lambda}$ are useful for describing the triatomic motions only for configurations in which R_λ is significantly larger than, say, R_ν or R_κ. This is most easily understood by representing V^λ in terms of variables $\zeta = (r_\lambda^2 + R_\lambda^2)^{\frac{1}{2}}$ (which, as shown in Section 4, is independent of λ), $\omega_\lambda = 2 \tan^{-1}(r_\lambda/R_\lambda)$ (in the 0 to π range) and γ_λ. The properties of such a representation have been discussed elsewhere[28], the most important one being that a change from polar coordinates ζ, $\omega_\lambda, \gamma_\lambda$ to ζ, ω_ν, γ_ν rotates the map of V without distorting it. For the Porter-Karplus H_3 surface, this representation of V is given in Fig. 2. From it, one can see that the three-dimensional internal configuration space is naturally divided into arrangement channel region subspaces, labelled by the indices $\lambda = \alpha, \beta, \gamma$. In region λ, for large ζ, R_λ is approximately equal to Z_λ and r_λ is approximately half of the distance of the point $P(\zeta, \omega_\lambda, \gamma_\lambda)$ to the Z_λ axis. Therefore, in that region, R_λ, r_λ, γ_λ are the "natural" variables for describing the translational, vibrational and rotational motions, respectively, of the three atoms, but these same variables are both awkward and inefficient for representing the corresponding motions in arrangement channels ν and κ. As a result, we will use R_λ, r_λ, γ_λ in region λ only. Associated to these, we will pick a set of three

additional external variables (which specify the orientation of the
instantaneous three atom plane with respect to a laboratory system)
which will also be different for different arrangement channel regions.
Accordingly, our procedure for solving the Schrödinger equation
involves first the generation of solutions in each of the three arrange-
ment channel regions $\lambda = \alpha, \beta, \gamma$ in separate calculations using variables
appropriate to each region. This is followed by a matching procedure
which yields a set of smooth and continuous solutions throughout all
of configuration space. To complete the problem, we need to
linearly combine these "primitive" solutions to generate ones which
satisfy the desired asymptotic boundary conditions.

The procedure thus outlined is general and can be applied to
any nondissociative reactive system but in any specific application,
we must specify the boundaries (in internal configuration space) of
the three arrangement channel regions. As was discussed in I, the
choice of bounding surfaces is primarily determined by the nature of
the potential surface, but for $H + H_2$ and many other reactive systems,
a very useful separation is obtained by the use of the three half-planes
$\pi_{\nu\lambda}$, $\pi_{\kappa\nu}$ and $\pi_{\lambda\kappa}$ of Fig. 2. They are limited by and intersect on the
Y_λ axis. $\pi_{\nu\lambda}$ makes an angle $\beta_{\nu\lambda}$ (in the 0 to $\pi/2$ range) with the Z_λ
axis given by

$$\cos \beta_{\nu\lambda} = \left[\frac{m_\nu m_\kappa}{(m_\lambda + m_\kappa)(m_\nu + m_\kappa)} \right]^{\frac{1}{2}} \tag{2.4a}$$

$$\sin \beta_{\nu\lambda} = \left[\frac{m_\kappa M}{(m_\lambda + m_\kappa)(m_\nu + m_\kappa)} \right]^{\frac{1}{2}} \tag{2.4b}$$

where

$$M = m_\lambda + m_\nu + m_\kappa \qquad\qquad (2.4c)$$

Analogous expressions are valid for the angles between $\pi_{\kappa\nu}$ and Z_ν, and between $\pi_{\lambda\kappa}$ and Z_κ. In terms of the internal variables $R_\lambda, r_\lambda, \gamma_\lambda$ the half planes π satisfy the equations

$$\pi_{\nu\lambda}: \quad r_\lambda = r_\nu \qquad 0 \leq \gamma_\lambda \leq \pi/2 \qquad\qquad (2.5a)$$

$$\pi_{\kappa\nu}: \quad r_\nu = r_\kappa \qquad 0 \leq \gamma_\nu \leq \pi/2 \qquad\qquad (2.5b)$$

$$\pi_{\lambda\kappa}: \quad r_\kappa = r_\lambda \qquad 0 \leq \gamma_\kappa \leq \pi/2 \qquad\qquad (2.5c)$$

These surfaces, called hereafter the matching surfaces, are analogous to those used in I and their properties are described in great detail in that paper (Appendix A). They are of great importance in the matching procedure of Section 4 and the method of solution of the Schrödinger equation in each arrangement channel region must include a procedure for determining the wave function on these surfaces. The remainder of this section will be concerned with the rotationally coupled Schrödinger equations for each arrangement channel region.

2.2 Partial Wave Analysis

In the system of coordinates specified by the index λ, the Schrödinger equation for the motions of the three nuclei is:

$$\left\{ -\frac{\hbar^2}{2\mu_{\lambda,\nu\kappa}} \nabla^2_{\underset{\sim}{R}_\lambda} - \frac{\hbar^2}{2\mu_{\nu\kappa}} \nabla^2_{\underset{\sim}{r}_\lambda} + V^\lambda(\underset{\sim}{r}_\lambda, \underset{\sim}{R}_\lambda, \gamma_\lambda) - E \right\} \Psi^\lambda(\underset{\sim}{r}_\lambda, \underset{\sim}{R}_\lambda) = 0 \qquad (2.6)$$

where $\nabla^2_{\underset{\sim}{R}_\lambda}$ and $\nabla^2_{\underset{\sim}{r}_\lambda}$ are the appropriate Laplacian operators and E is the total energy excluding that associated with the motion of the center of mass. Upon introduction of the scaled coordinates of Eq. 2.1,

Eq. 2.6 is converted to

$$\{-\frac{\hbar^2}{2\mu}(\nabla^2_{R_\lambda} + \nabla^2_{r_\lambda}) + V^\lambda(r_\lambda, R_\lambda, \gamma_\lambda) - E\} \Psi^\lambda(r_\lambda, R_\lambda) = 0 \qquad (2.7)$$

where the reduced mass μ is given by

$$\mu = (\mu_{\lambda, \nu\kappa}\mu_{\nu\kappa})^{\frac{1}{2}} = [m_\lambda m_\nu m_\kappa/(m_\lambda + m_\nu + m_\kappa)]^{\frac{1}{2}} \qquad (2.8)$$

We now introduce the space fixed coordinate system Oxyz (Fig. 3) centered on the center of mass O of the triatom system and whose axes are constantly parallel to the axes of a laboratory fixed system of coordinates. In Oxyz the polar and azimuthal angles of R_λ and r_λ are $\theta_\lambda, \phi_\lambda$ and $\theta_{r_\lambda}, \phi_{r_\lambda}$ respectively. By expressing the Laplacian operators in Eq. 2.7 in terms of R_λ, r_λ and these angles, the Schrödinger equation can be rewritten as:

$$\{-\frac{\hbar^2}{2\mu}(\frac{1}{R_\lambda}\frac{\partial^2}{\partial R_\lambda^2}R_\lambda + \frac{1}{r_\lambda}\frac{\partial^2}{\partial r_\lambda^2}r_\lambda) + \frac{j_\lambda^2}{2\mu r_\lambda^2} + \frac{l_\lambda^2}{2\mu R_\lambda^2} + V(r_\lambda, R_\lambda, \gamma_\lambda)$$

$$\qquad (2.9)$$

$$-E\}\Psi^\lambda(r_\lambda, R_\lambda) = 0$$

where l_λ and j_λ are the usual orbital and rotational angular momentum operators expressed in the spherical coordinates $\theta_\lambda, \phi_\lambda$ and $\theta_{r_\lambda}, \phi_{r_\lambda}$. The total angular momentum operator J is the vector sum of l_λ and j_λ

$$J = l_\lambda + j_\lambda \qquad (2.10)$$

and is independent of arrangement channel.

The operators J^2 and J_z (the z component of J) commute with each other and with the Hamiltonian H. In the partial wave analysis

procedure, we expand $\Psi^\lambda (r_\lambda, R_\lambda)$ in terms of simultaneous eigenfunctions $\Psi^\lambda_{JM} (r_\lambda, R_\lambda)$ of J^2, J_z and H with eigenvalues $\hbar^2 J(J+1)$, $\hbar M$ and E respectively:

$$\Psi^\lambda(r_\lambda, R_\lambda) = \sum_{J=0}^{\infty} \sum_{M=-J}^{J} C_{JM} \Psi^\lambda_{JM}(r_\lambda, R_\lambda) \qquad (2.11)$$

The Ψ^λ_{JM} still satisfy Eq. 2.9.

2.2 The Body-Fixed Schrödinger Equation

In the standard space fixed theory (as formulated, for example, by Arthurs and Dalgarno[29]), one now expands Ψ^λ_{JM} in terms of a set of simultaneous eigenfunctions of J^2, J_z, l^2_λ and j^2_λ thereby obtaining a set of coupled equations in the quantum numbers j_λ and l_λ. This derivation is summarized in Appendix A. A more convenient and computationally efficient procedure for our purposes is to transform to a system of body fixed coordinates. These coordinate systems were applied to quantum mechanical problems long ago by Hirschfelder and Wigner[30] and have been discussed extensively by Curtiss, Hirschfelder and Adler[31] and more recently by Pack[32] and much of the present development will follow that of Pack. In a fully converged calculation, both the body fixed and space fixed formalisms lead to the same number of coupled equations and, for fully converged nonreactive atom diatom calculations, they may be implemented with comparable ease. However, body fixed coordinate systems lead to an approximate decoupling of certain degrees of freedom which is not naturally present in the space fixed analysis and which is useful in the development of approximate theories. More important, the body fixed analysis leads

to both computational and conceptual simplifications in the matching procedure thus providing a considerable advantage in reactive scattering calculations over the corresponding space fixed theory.

We now introduce the two different body fixed coordinate systems $OX_\lambda Y_\lambda Z_\lambda$ and $Ox'_\lambda y'z'_\lambda$ (see Fig. 3) as follows: (1) $OX_\lambda Y_\lambda Z_\lambda$ (not to be confused with the internal configuration space coordinate system $OX_\lambda Y_\lambda Z_\lambda$ of Fig. 2) is obtained from $Oxyz$ by rotating through the Euler angles[33] $\alpha = \phi_\lambda$, $\beta = \theta_\lambda$, $\gamma = 0$ so that the resulting Z_λ axis points along the $\underset{\sim}{R}_\lambda$ direction and the Y_λ axis lies in the xy plane; (2) $Ox'_\lambda y'z'_\lambda$ is obtained from $OX_\lambda Y_\lambda Z_\lambda$ by rotating it counterclockwise about Z_λ ($\equiv z'_\lambda$) by an angle ψ_λ (in 0 to 2π range) so as to bring x'_λ into the $\underset{\sim}{R}_\lambda, \underset{\sim}{r}_\lambda$ plane and y'(which is independent of λ) perpendicular to it and oriented in the direction of $\underset{\sim}{R}_\lambda \times \underset{\sim}{r}_\lambda$:

$$y = \frac{\underset{\sim}{R}_\lambda \times \underset{\sim}{r}_\lambda}{|\underset{\sim}{R}_\lambda \times \underset{\sim}{r}_\lambda|} \qquad (2.12)$$

The Euler angles which rotate $Oxyz$ into $Ox'_\lambda y'z'_\lambda$ are therefore $\alpha = \phi_\lambda$, $\beta = \theta_\lambda$, $\gamma = \psi_\lambda$. In either of the body fixed coordinate systems $OX_\lambda Y_\lambda Z_\lambda$ or $Ox'_\lambda y'z'_\lambda$ the variables used to describe the system are r_λ, $R_\lambda, \phi_\lambda, \theta_\lambda, \psi_\lambda, \gamma_\lambda$. As seen from Fig. 2, ψ_λ is the clockwise angle from OY_λ to Oy'. Since OY_λ is perpendicular to the $OX_\lambda Z_\lambda$ plane and therefore the $\underset{\sim}{R}_\lambda, OZ$ plane, and Oy' is perpendicular to the $\underset{\sim}{R}_\lambda, \underset{\sim}{r}_\lambda$ plane, we conclude that ψ_λ is the angle between these last two planes. Therefore, a motion in which R_λ, ϕ_λ, θ_λ, r_λ and γ_λ are kept constant but ψ_λ varies is a "tumbling" (i.e., rigid rotation) of the triatomic system around the $\underset{\sim}{R}_\lambda$ vector. For this reason, the ψ_λ angle will be

called the tumbling angle. In what follows we will find it most convenient to use the coordinate system $OX_\lambda Y_\lambda Z_\lambda$ for deriving the coupled form of the Schrödinger equation and $Ox'_\lambda\ y'z'_\lambda$ in developing the matching procedure. The procedure for expressing the operators $\underset{\sim}{j}_\lambda^2$ and $\underset{\sim}{l}_\lambda^2$ of Eq. 2.9 in variables ϕ_λ, θ_λ, ψ_λ, γ_λ is described in Appendix A.

We now expand Ψ_{JM}^λ in terms of the elements of the Wigner rotation matrix $\underset{\approx}{D}_J(\alpha,\beta,\gamma)$ as follows:[32]

$$\Psi_{JM}^\lambda(\underset{\sim}{r}_\lambda,\underset{\sim}{R}_\lambda) = \sum_{\Omega_\lambda=-J}^{J} D_{M\Omega_\lambda}^{J}(\phi_\lambda,\theta_\lambda,0)\Psi_{J\Omega_\lambda}^\lambda(r_\lambda,R_\lambda,\gamma_\lambda,\psi_\lambda) \qquad (2.13)$$

The notation used for the matrix elements is that of Davydov.[33] $\Psi_{J\Omega_\lambda}^\lambda$ is called a body-fixed wave function. The quantum number Ω_λ in Eq. 2.13 specifies the component of the total angular momentum $\underset{\sim}{J}$ around $\underset{\sim}{R}_\lambda$ or, equivalently, OZ_λ. The component of $\underset{\sim}{l}_\lambda$ (the angular momentum conjugate to $\underset{\sim}{R}_\lambda$) around this axis vanishes and therefore Ω_λ also specifies the Z_λ component of the rotational angular momentum $\underset{\sim}{j}_\lambda$ in the body fixed frame. The equality of J_{Z_λ} and $j_{\lambda Z_\lambda}$ is verified independently in Table I (which is described in Appendix A). We will refer to either J_{Z_λ} or $j_{\lambda Z_\lambda}$ as the tumbling angular momentum (since it describes the tumbling of the triatom around $\underset{\sim}{R}_\lambda$) and Ω_λ as the tumbling quantum number in arrangement channel λ.

As outlined in Appendix A, substitution of Eq. 2.13 into Eq. 2.9, yields the following set of Ω_λ coupled equations for the $\Psi_{J\Omega_\lambda}^\lambda(r_\lambda,R_\lambda,\gamma_\lambda,\psi_\lambda)$:

$$H^{J\lambda}_{\Omega_\lambda,\Omega_\lambda} \Psi^{\lambda}_{J\Omega_\lambda} + H^{J\lambda}_{\Omega_\lambda,\Omega_\lambda+1} \Psi^{\lambda}_{J\Omega_\lambda+1} + H^{J\lambda}_{\Omega_\lambda,\Omega_\lambda-1} \Psi^{\lambda}_{J\Omega_\lambda-1}$$

$$= E\Psi^{\lambda}_{J\Omega_\lambda} \tag{2.14}$$

The $H^{J\lambda}_{\Omega_\lambda,\Omega'_\lambda}$ can be considered as the elements of a tridiagonal hamiltonian operator matrix $\underset{\sim}{H}^{J\lambda}(r_\lambda,R_\lambda,\gamma_\lambda,\psi_\lambda)$ whose diagonal and off diagonal elements are defined respectively by

$$H^{J\lambda}_{\Omega_\lambda,\Omega_\lambda} = -\frac{\hbar^2}{2\mu} \left(\frac{1}{r_\lambda} \frac{\partial^2}{\partial r_\lambda^2} r_\lambda + \frac{1}{R_\lambda} \frac{\partial^2}{\partial R_\lambda^2} R_\lambda \right) + \frac{j_\lambda^2}{2\mu r_\lambda^2}$$

$$+ \frac{1}{2\mu R_\lambda^2} \left[J(J+1)\hbar^2 - 2\Omega_\lambda \hbar j_{\lambda Z_\lambda} + j_\lambda^2 \right] + V^\lambda(r_\lambda,R_\lambda,\gamma_\lambda) \tag{2.15}$$

and

$$H^{J\lambda}_{\Omega_\lambda,\Omega_\lambda\pm1} = -\frac{\hbar}{2\mu R_\lambda^2} \sqrt{J(J+1) - \Omega_\lambda(\Omega_\lambda \pm 1)} \; j_\lambda^{\mp} \tag{2.16}$$

The $j_\lambda^{\mp}$ are the raising and lowering operators of the rotational angular momentum j_λ in the body fixed $OX_\lambda Y_\lambda Z_\lambda$ coordinate system. The $1/2\mu R_\lambda^2$ term in Eq. 2.15 results directly from the $l_\lambda^2/2\mu R_\lambda^2$ term in Eq. 2.9. Defining $\underset{\sim}{\Psi}^{\lambda}_J$ as the $2\Omega_\lambda + 1$ dimensional column vector whose elements are the $\Psi^{\lambda}_{J\Omega_\lambda}$, Eq. 2.14 can be put in the matrix form

$$\underset{\sim}{H}^{J\lambda} \underset{\sim}{\Psi}^{\lambda}_J = E\underset{\sim}{\Psi}^{\lambda}_J \tag{2.17}$$

Equations 2.14 or 2.17 are the body-fixed partial wave Schrödinger equation. Eq. 2.14 is identical to the corresponding result of Pack[32] and indicates that the kinetic energy operator is no longer diagonal

in the body fixed representation and is the sole mechanism which couples different tumbling quantum numbers Ω_λ. The potential coupling is diagonal in Ω_λ and is respondible for coupling between states of different vibration rotation quantum numbers $v_\lambda j_\lambda$. This separation of kinematic and potential coupling is of prime importance in the development of approximate decoupling procedures as will be discussed in the next section.

2.3 The Rotationally Coupled Schrödinger Equation; Tumbling-
Decoupling Approximations

We now expand the body fixed wave functions $\Psi^\lambda_{J\Omega_\lambda}$ in terms of the spherical harmonics $Y_{j_\lambda \Omega_\lambda}(\gamma_\lambda, \psi_\lambda)$ which, as discussed in Appendix A, are the simultaneous eigenfunctions of j_λ^2 and $j_{\lambda Z_\lambda}$:

$$\Psi^\lambda_{J\Omega_\lambda}(r_\lambda, R_\lambda, \gamma_\lambda, \psi_\lambda) = \sum_{j_\lambda = |\Omega_\lambda|}^{\infty} Y_{j_\lambda \Omega_\lambda}(\gamma_\lambda, \psi_\lambda) w^\lambda_{J j_\lambda \Omega_\lambda}(r_\lambda, R_\lambda) \qquad (2.18)$$

If we substitute this into Eq. 2.14, multiply throughout by $Y^*_{j'_\lambda \Omega'_\lambda}(\gamma_\lambda, \psi_\lambda)$ and integrate over γ_λ and ψ_λ (using the solid angle volume element $\sin \gamma_\lambda d\gamma_\lambda d\psi_\lambda$) and finally interchange the primed and unprimed quantum numbers it becomes a Schrödinger equation in the two distance variables r_λ, R_λ:

$$(t^{J\lambda j_\lambda}_{\Omega_\lambda, \Omega_\lambda} - E) w^\lambda_{J j_\lambda \Omega_\lambda}(r_\lambda R_\lambda) + \sum_{j'_\lambda = |\Omega_\lambda|}^{\infty} V^{\lambda \Omega_\lambda}_{j_\lambda j'_\lambda} w^\lambda_{J j'_\lambda \Omega_\lambda}(r_\lambda, R_\lambda)$$

$$+ t^{J\lambda j_\lambda}_{\Omega_\lambda, \Omega_\lambda+1} w^\lambda_{J j_\lambda \Omega_\lambda+1}(r_\lambda, R_\lambda) + t^{J\lambda j_\lambda}_{\Omega_\lambda, \Omega_\lambda-1} w^\lambda_{J j_\lambda \Omega_\lambda-1}(r_\lambda, R_\lambda) = 0$$

$$(2.19)$$

where

$$t^{J\lambda j_\lambda}_{\Omega_\lambda,\Omega_\lambda} = -\frac{\hbar^2}{2\mu}\left[\frac{1}{R_\lambda}\frac{\partial^2}{\partial R_\lambda^2}R_\lambda + \frac{1}{r_\lambda}\frac{\partial^2}{\partial r_\lambda^2}r_\lambda\right] + \frac{j_\lambda(j_\lambda+1)\hbar^2}{2\mu r_\lambda^2}$$

$$+ \frac{\hbar^2}{2\mu R_\lambda^2}[J(J+1) - 2\Omega_\lambda^2 + j_\lambda(j_\lambda+1)] \tag{2.20}$$

$$t^{J\lambda j_\lambda}_{\Omega_\lambda,\Omega_\lambda\pm1} = -\frac{\hbar^2}{2\mu R_\lambda^2}\xi_\pm(J,\Omega_\lambda)\xi_\pm(j_\lambda,\Omega_\lambda) \tag{2.21}$$

$$\xi_\pm(J,\Omega_\lambda) = [J(J+1) - \Omega_\lambda(\Omega_\lambda\pm1)]^{\frac{1}{2}} \qquad |\Omega_\lambda| \le J \tag{2.22}$$

and

$$V^{\lambda\Omega_\lambda}_{j_\lambda j'_\lambda}(r_\lambda,R_\lambda) = \langle j_\lambda\Omega_\lambda|V^\lambda(r_\lambda,R_\lambda,\gamma_\lambda)|j'_\lambda\Omega_\lambda\rangle \tag{2.23}$$

Eq. 2.19 is the three dimensional generalization of an analogous equation for collinear and coplanar[21] reactions. None of the four angular coordinates $\theta_\lambda, \phi_\lambda, \gamma_\lambda, \psi_\lambda$ appear in it, with only the two scaled distances r_λ, R_λ remaining. In the collinear case, none of the angular momentum quantum numbers J, Ω_λ or j_λ appear, and we have only one such equation. For systems confined to a space fixed plane, Ω_λ does not appear (or it can be considered to have the fixed value zero) since the system does not tumble, and there is therefore no Ω_λ coupling. In that case, j_λ assumes all integer values, including negative ones, and there is one set of j_λ coupled equations for each J. In the present three dimensional case, there is both j_λ and Ω_λ coupling, but still no J-coupling. Let us consider a kinetic energy matrix $\underset{\approx}{t}^{J\lambda}(r_\lambda,R_\lambda)$ and a potential energy matrix $\underset{\approx}{V}^\lambda(r_\lambda,R_\lambda)$ whose rows and

columns are scanned by the indices $j_\lambda, \Omega_\lambda$ and $j'_\lambda, \Omega'_\lambda$, respectively. They are defined by

$$(\underset{\approx}{t}^{J\lambda})_{j_\lambda \Omega_\lambda}^{j'_\lambda \Omega'_\lambda} = \delta_{j_\lambda j'_\lambda} \sum_{i=-1}^{1} \delta_{\Omega_\lambda, \Omega'_\lambda - i} \, t_{\Omega_\lambda, \Omega_\lambda + i}^{J\lambda j_\lambda} \qquad (2.24)$$

and

$$(\underset{\approx}{V}^\lambda)_{j_\lambda \Omega_\lambda}^{j'_\lambda \Omega'_\lambda} = \delta_{\Omega_\lambda \Omega'_\lambda} \, V_{j_\lambda j'_\lambda}^{\lambda \Omega} \qquad (2.25)$$

respectively where the several t and V were defined by Eqs. 2.20 through 2.23. It can be seen that $\underset{\approx}{t}^{J\lambda}$ is diagonal in j_λ (and tridiagonal in Ω_λ) whereas $\underset{\approx}{V}^\lambda$ is diagonal in Ω_λ. Defining $\underset{\sim}{w}_J^\lambda(r_\lambda, R_\lambda)$ as the column vector whose elements, scanned by Ω_λ, are the functions $w_{J j_\lambda \Omega_\lambda}^\lambda (r_\lambda, R_\lambda)$, Eq. 2.19 can be rewritten as

$$(\underset{\approx}{t}^{J\lambda} + \underset{\approx}{V}^\lambda) \, \underset{\sim}{w}_J^\lambda = E \, \underset{\sim}{w}_J^\lambda \qquad (2.26)$$

Eq. 2.26 shows clearly that the potential coupling is diagonal in Ω_λ. This, along with the weakness of the centrifugal coupling (due to the terms in $\underset{\approx}{t}^{J\lambda}$ of angular origin) for small J and j_λ has lead to the development of fairly accurate tumbling-decoupling approximations by several workers[32, 34, 35] in studies of nonreactive atom diatom scattering. In such procedures, the $t_{\Omega_\lambda, \Omega_\lambda \pm 1}^{J_\lambda}$ terms in Eqs. 2.19 and 2.24 are neglected thereby making Eq. 2.26 be diagonal in Ω_λ. In addition, the $\hbar^2/2\mu R_\lambda^2$ term in Eq. 2.20 (which arises from the $\underset{\sim}{l}_\lambda^2$ term in Eq. 2.9) is usually replaced by an approximate expression. Pack[32] replaces it by $\hbar^2 J(J + 1)/2\mu R_\lambda^2$, and McGuire and Kouri[34] by $\hbar^2 l_\lambda(l_\lambda + 1)/2\mu R_\lambda^2$ where l_λ is the orbital angular momentum

quantum number in the space-fixed system of coordinates.[36] Such additional approximations are unnecessary to produce Ω_λ decoupling and may furthermore introduce additional errors without significant computational simplification, and we suggest that they should be omitted. For the case of reactive scattering, an Ω_λ decoupling requires neglect of the $t_{\Omega_\lambda,\Omega_\lambda \pm 1}^{J\lambda j_\lambda}$ in Eq. 2.19 for each arrangement channel region $\lambda = \alpha, \beta, \gamma$. The exact matching procedure described in Section 3 may be retained, or be replaced by approximate ones which retain the spirit of Ω_λ decoupling. In a separate paper[24] we will present some results of an application of one of these possible procedures to 3D reactive scattering.

The elements of the potential coupling matrix of Eqs. 2.23 and 2.26 may be conveniently calculated by expanding the potential $V^\lambda(r_\lambda, R_\lambda, \gamma_\lambda)$ in a series of Legendre polynomials

$$V^\lambda(r_\lambda, R_\lambda, \gamma_\lambda) = \sum_{k=0}^{\infty} V_k^\lambda(r_\lambda, R_\lambda) P_k(\cos \gamma_\lambda) \tag{2.27}$$

which when substituted into Eq. 2.23 leads to[32]

$$V_{j_\lambda j'_\lambda}^{\lambda \Omega_\lambda}(r_\lambda, R_\lambda) = \sum_{k=0}^{\infty} \left(\frac{2j_\lambda + 1}{2j'_\lambda + 1}\right)^{\frac{1}{2}} C(j_\lambda k j'_\lambda; \Omega_\lambda 0 \Omega_\lambda)$$

$$C(j_\lambda k j'_\lambda; 000) V_k^\lambda(r_\lambda, R_\lambda) \tag{2.28}$$

where the Clebsch-Gordon coefficients C are expressed in the notation of Rose.[37] For collisions of an atom with a homonuclear diatomic molecule (as in $H + H_2$), the only nonzero terms in Eq. 2.27 occur for even k (since $V^\lambda(r_\lambda, R_\lambda, \gamma_\lambda)$ is symmetric about $\gamma_\lambda = \pi/2$). Since[38]

$$C(j_\lambda k j'_\lambda; 000) = 0 \quad \text{for } j_\lambda + k + j'_\lambda = \text{odd}, \tag{2.29}$$

we see that $\underset{\approx}{V}^\lambda$ does not couple even with odd rotational states. Use of this decoupling in reducing the necessary calculations for reactions like H + H_2 was discussed in I for the planar case and most of the simplifications described there are valid for 3D collisions as well. Note that Eq. 2.28 involves a single sum over products of Clebsch-Gordon coefficients, a substantial simplification over the corresponding space-fixed expansion which requires 6-j symbols.[32]

Let us now define a new function $F^\lambda_{Jj_\lambda \Omega_\lambda}(r_\lambda, R_\lambda)$ by

$$F^\lambda_{Jj_\lambda \Omega_\lambda}(r_\lambda, R_\lambda) = R_\lambda r_\lambda \, w^\lambda_{Jj_\lambda \Omega_\lambda}(r_\lambda, R_\lambda) \tag{2.30}$$

Substitution of this into Eq. 2.19 leads to

$$(t^{J \lambda j_\lambda}_{\Omega_\lambda, \Omega_\lambda} - E) F^\lambda_{Jj_\lambda \Omega_\lambda} + \sum_{j'_\lambda} V^{\lambda \Omega_\lambda}_{j_\lambda j'_\lambda} F^\lambda_{Jj'_\lambda \Omega_\lambda} + t^{J \lambda j_\lambda}_{\Omega_\lambda, \Omega_\lambda + 1} F^\lambda_{Jj_\lambda \Omega_\lambda + 1}$$

$$+ t^{J \lambda j_\lambda}_{\Omega_\lambda, \Omega_\lambda - 1} F^\lambda_{Jj_\lambda \Omega_\lambda - 1} = 0 \tag{2.31}$$

where

$$t^{J \lambda j_\lambda}_{\Omega_\lambda, \Omega_\lambda} = -\frac{\hbar^2}{2\mu} \left[\frac{\partial^2}{\partial R_\lambda^2} + \frac{\partial^2}{\partial r_\lambda^2} \right] + \frac{j_\lambda(j_\lambda + 1)}{2\mu r_\lambda^2}$$

$$+ \frac{\hbar^2}{2\mu R_\lambda^2} \left[J(J+1) - 2\Omega_\lambda^2 + j_\lambda(j_\lambda + 1) \right] \tag{2.32}$$

and the remaining quantities are defined by Eqs. 2.21 - 2.23. In matrix form, Eq. 2.31 can be written as

$$(\underset{\approx}{t}^{J\lambda} + \underset{\approx}{V}^\lambda) \underset{\sim}{F}^\lambda_J = E \underset{\sim}{F}^\lambda_J \tag{2.33}$$

where $\hat{\underline{t}}^{J\lambda}$ is defined similarly to $\underline{t}^{J\lambda}$ and $\underline{F}^{\lambda}_J$ similarly to $\underline{W}^{\lambda}_J$. Eqs. 2.31 and 2.33 are called the body-fixed rotationally coupled Schrödinger equation.

3. THE INTEGRATION IN ARRANGEMENT CHANNEL REGION λ

3.1 Division of r_λ, R_λ Configuration Space into Regions

To solve Eq. 2.31 or 2.33 we expand the wave function $F^{\lambda}_{Jj_\lambda \Omega_\lambda}(r_\lambda, R_\lambda)$ in terms of a set of one-variable pseudo-vibrational functions which locally span the r_λ, R_λ configuration space along cuts which are approximately perpendicular to a conveniently defined reaction coordinate. The resulting expansion coefficients satisfy coupled differential equations which must be numerically integrated through the arrangement channel region λ to generate a set of solutions to the Schrödinger equation in that region. In order to obtain an efficient representation of the pseudo-vibrational motion everywhere, we must change both coordinate systems and basis sets frequently during this propagation. This may be done in many different ways depending on the boundaries of the arrangement channel regions and the shape of the potential energy surface in these regions. For the $H + H_2$ reaction, and most others for which the choice of matching surfaces is given by Eq. 2.5, a convenient procedure consists of dividing the r_λ, R_λ configuration space into four areas called regions, as depicted in Fig. 4. For reference, contours of the potential matrix element $V_0(r_\lambda, R_\lambda)$ of Eq. 2.2 for the H_3 Porter-Karplus surface[39] are plotted on the same figure. The regions are denoted as: I - asymptotic region, II - weak interaction region, III - strong

interaction region, and IV - matching region. The boundary points P_0', P_0 and P_1 are required to lie in the high energy plateau region corresponding to dissociation of the triatomic system into A + B + C (i.e., large r_λ and R_λ), in positions which are primarily determined by certain geometrical criteria. These are described in detail in I and are unchanged in the present application. Within each region, we choose a set of orthogonal coordinates which efficiently describe the local vibrational and translational motion. For example, in the asymptotic region, r_λ is the natural expansion variable for describing vibrational motion and R_λ the appropriate propagation variable for describing translational motion. This is also true in the near interaction region, but in the strong interaction region, a more efficient representation is obtained in terms of the polar coordinates $\rho_\lambda, \eta_\lambda$ which are defined by (see Fig. 5):

$$r_\lambda = r_{\lambda_0} - \rho_\lambda \cos \varphi_\lambda \tag{3.1a}$$

$$R_\lambda = R_{\lambda_0} - \rho_\lambda \sin \varphi_\lambda \tag{3.1b}$$

where the origin of the corresponding coordinate system is located at $r_{\lambda_0}, R_{\lambda_0}$. Here, ρ_λ is the effective expansion (vibrational) coordinate and φ_λ is the corresponding propagation coordinate (for translational-like motion across region III). In the matching region, a different set of polar coordinates ζ, η_λ is used. These are defined by

$$r_\lambda = \zeta \sin \eta_\lambda \tag{3.2a}$$

$$R_\lambda = \zeta \cos \eta_\lambda \tag{3.2b}$$

and have as origin the point Q in Fig. 5. The quantity ζ was introduced after Eq. 2.3 and the angle η_λ is 1/2 of the angle ω_λ also introduced at that time and used in the representation of $V^\lambda(r_\lambda, R_\lambda, \gamma_\lambda)$ of Fig. 2. The variables ζ and η_λ constitute respectively convenient expansion (ζ) and propagation (η_λ) variables for region IV and also provide a convenient means for obtaining the wave function on the matching surface as will be summarized in Section 4.

3.2 The Coupled Schrödinger Equation in the Propagation Variable

We now consider the solution of Eq. 2.31 in each of the four regions in arrangement channel region λ. Much of this treatment is completely analogous to the corresponding coplanar theory (Section 3.4 of I) and that paper should be consulted for a more detailed explanation of the concepts involved.

3.2.1 The asymptotic region

The coordinates for this region are r_λ, R_λ. In terms of these, the potential function $V^\lambda(r_\lambda, R_\lambda, \gamma_\lambda)$ becomes the isolated diatomic potential $v^\lambda(r_\lambda)$ since the boundaries of the asymptotic region are chosen[19] so that the potential has assumed its asymptotic form. We now expand the wave function $F^\lambda_{Jj_\lambda\Omega_\lambda}(r_\lambda, R_\lambda)$ of Eq. 2.31 in terms of the eigenfunctions $\phi^\lambda_{v_\lambda j_\lambda}(r_\lambda)$ of the vibrational Hamiltonian:

$$F^\lambda_{Jj_\lambda\Omega_\lambda}(r_\lambda, R_\lambda) = \sum_{v_\lambda} g^{\lambda(a)}_{Jv_\lambda j_\lambda\Omega_\lambda}(R_\lambda)\phi^{\lambda(a)}_{v_\lambda j_\lambda}(r_\lambda) \tag{3.3}$$

where the (a) refers to asymptotic region and the $\phi_{v_\lambda j_\lambda}$ satisfy

$$\left[-\frac{\hbar^2}{2\mu}\frac{d^2}{dr_\lambda^2} + \frac{j_\lambda(j_\lambda + 1)\hbar^2}{2\mu r_\lambda^2} + v^\lambda(r_\lambda)\right]\phi_{v_\lambda j_\lambda}^{\lambda(a)}(r_\lambda)$$

$$= \epsilon_{v_\lambda j_\lambda}^{\lambda(a)}\phi_{v_\lambda j_\lambda}^{\lambda(a)} \tag{3.4}$$

with boundary conditions

$$\phi_{v_\lambda j_\lambda}^{\lambda(a)}(r_{\lambda_0}) = \phi_{v_\lambda j_\lambda}^{\lambda(a)}(0) = 0 \tag{3.5}$$

$\epsilon_{v_\lambda j_\lambda}^{\lambda(a)}$ is the asymptotic diatomic vibration rotation energy and

$r_\lambda^{-1}\phi_{v_\lambda j_\lambda}^{\lambda(a)}(r_\lambda)$, except for a normalization constant, is the radial part

of the corresponding diatomic eigenfunction. Substituting Eq. 3.3

into Eq. 2.31, using Eq. 3.4, multiplying by $\phi_{v'_\lambda j'_\lambda}^{\lambda(a)}(r_\lambda)$ and inte-

grating over r_λ, we obtain the Schrödinger equation for translational

R_λ motion in the asymptotic region:

$$\left\{\frac{d^2}{dR_\lambda^2} - \frac{1}{R_\lambda^2}\left[J(J+1) - 2\Omega_\lambda^2 + j_\lambda(j_\lambda + 1)\right] + k_{v_\lambda j_\lambda}^{\lambda(a)\,2}\right\}g_{Jv_\lambda j_\lambda \Omega_\lambda}^{\lambda(a)}(R_\lambda)$$

$$+ \frac{1}{R_\lambda^2}\left[\xi_+(J,\Omega_\lambda)\xi_+(j_\lambda,\Omega_\lambda)g_{Jv_\lambda j_\lambda \Omega_\lambda+1}^{\lambda(a)}(R_\lambda)\right. \tag{3.6}$$

$$\left. + \xi_-(J,\Omega_\lambda)\xi_-(j_\lambda,\Omega_\lambda)g_{Jv_\lambda j_\lambda \Omega_\lambda-1}^{\lambda(a)}\right] = 0$$

where

$$k_{v_\lambda j_\lambda}^{\lambda(a)\,2} = \frac{2\mu}{\hbar^2}(E - \epsilon_{v_\lambda j_\lambda}^{\lambda(a)}) \tag{3.7}$$

Note that while no vibrational or rotational coupling exists in Eq. 3.6,

the kinetic energy coupling between g's of different Ω_λ persists in

this asymptotic region, decreasing only as R_λ^{-2} (rather than exponen-

tially or as R_λ^{-6} as is often the case with potential coupling). Of course, as $R_\lambda \to \infty$ (the "far" asymptotic region), Eqs. 3.6 completely uncouple and the $g_{Jv_\lambda j_\lambda \Omega_\lambda}^{\lambda(a)}$ become solutions to:

$$\{ \frac{d^2}{dR_\lambda^2} + k_{v_\lambda j_\lambda}^{\lambda(a)\ 2} \} \, g_{Jv_\lambda j_\lambda \Omega_\lambda}^{\lambda(a)} (R_\lambda) = 0 \qquad (3.8)$$

which are simply linear combinations of $\exp(\pm i k_{v_\lambda j_\lambda}^{\lambda(a)} R_\lambda)$ for open channels $(E > \epsilon_{v_\lambda j_\lambda}^{\lambda(a)})$ and $\exp(\pm |k_{v_\lambda j_\lambda}^{\lambda(a)}| R_\lambda)$ for closed ones $(E < \epsilon_{v_\lambda j_\lambda}^{\lambda(a)})$. Eq. 3.6 may be solved analytically either by diagonalizing the Hamiltonian in that equation or by realizing that the corresponding space fixed Schrödinger equation is already diagonal[29], and thus its solutions may be linearly combined to satisfy Eq. 3.3.[35] The solutions of the space-fixed Schrödinger equation for open channels are related to spherical Bessel functions $j_{l_\lambda}(k_{v_\lambda j_\lambda}^{\lambda(a)} R_\lambda)$ and $y_{l_\lambda}(k_{v_\lambda j_\lambda}^{\lambda(a)} R_\lambda)$,[29] where l_λ is the orbital angular momentum quantum number. The corresponding body-fixed solutions are found by equating Eqs. A.5 and A.13 of Appendix A, and using Eq. A.14 to solve for the body fixed coefficients $w_{J_{j_\lambda} \Omega_\lambda}^\lambda$. Since Eqs. 2.30 and 3.3 apply equally to both space-fixed and body fixed solutions, we can immediately write the asymptotic body-fixed solutions for open channels as:

$$g_{Jv_\lambda j_\lambda \Omega_\lambda}^{\lambda(a)}(R_\lambda) = k_{v_\lambda j_\lambda}^{\lambda(a)} R_\lambda \left(\frac{2J+1}{4\pi}\right)^{\frac{1}{2}} (-1)^{j_\lambda - \Omega_\lambda}$$

$$\tag{3.9}$$

$$\times \sum_{l_\lambda} C(Jj_\lambda l_\lambda; \Omega_\lambda - \Omega_\lambda 0) \left\{ \begin{array}{c} j_{l_\lambda}(k_{v_\lambda j_\lambda}^{\lambda(a)} R_\lambda) \\[2ex] y_{l_\lambda}(k_{v_\lambda j_\lambda}^{\lambda(a)} R_\lambda) \end{array} \right\} \quad (E > \epsilon_{v_\lambda j_\lambda}^{\lambda(a)})$$

In the far asymptotic region, the Bessel functions become[38]

$$j_{l_\lambda}(k_{v_\lambda j_\lambda}^{\lambda(a)} R_\lambda) \sim \frac{\sin(k_{v_\lambda j_\lambda}^{\lambda(a)} R_\lambda - l_\lambda \pi/2)}{k_{v_\lambda j_\lambda}^{\lambda(a)} R_\lambda}$$

$$\tag{3.10a}$$

and

$$y_{l_\lambda}(k_{v_\lambda j_\lambda}^{\lambda(a)} R_\lambda) \sim - \frac{\cos(k_{v_\lambda j_\lambda}^{\lambda(a)} R_\lambda - l_\lambda \pi/2)}{k_{v_\lambda j_\lambda}^{\lambda(a)} R_\lambda}$$

$$\tag{3.10b}$$

and by expressing the sine and cosine in Eqs. 3.10 in terms of imaginary exponentials, one can immediately see that Eq. 3.9 satisfies Eq. 3.8 as desired. The use of Eq. 3.8 in formulating the asymptotic R and S matrix boundary conditions will be discussed in Section 5.1. For closed channels, the body fixed solution is still of the form in Eq. 3.9 but with the spherical Bessel functions j_{l_λ} and y_{l_λ} replaced by the modified spherical Bessel functions $i_{l_\lambda}(|k_{v_\lambda j_\lambda}^{\lambda(a)}|R_\lambda)$ and $k_{l_\lambda}(|k_{v_\lambda j_\lambda}^{\lambda(a)}|R_\lambda)$ [40] which behave asymptotically as

$$i_{l_\lambda}(|k_{v_\lambda j_\lambda}^{\lambda(a)}|R_\lambda) \sim \frac{1}{2} \frac{e^{|k_{v_\lambda j_\lambda}^{\lambda(a)}|R_\lambda}}{|k_{v_\lambda j_\lambda}^{\lambda(a)}|R_\lambda}$$

$$\tag{3.11a}$$

and

$$k_{1_\lambda}(|k_{v_\lambda j_\lambda}^{\lambda(a)}|R_\lambda) \sim \frac{e^{-|k_{v_\lambda j_\lambda}^{\lambda(a)}|R_\lambda}}{|k_{v_\lambda j_\lambda}^{\lambda(a)}|R_\lambda} \tag{3.11b}$$

Let us now introduce a matrix notation for the Schrödinger equation (Eq. 3.6). We consider the $g_{Jv_\lambda j_\lambda \Omega_\lambda}^{\lambda(a)}$ as elements of a column vector $g_{J}^{\lambda(a)}$ whose elements are labelled by the indices $v_\lambda j_\lambda \Omega_\lambda$, which are assumed to scan a total of N values (in a truncated close-coupling expansion). This vector represents one of $2N$ possible linearly independent solutions of Eq. 3.6. These $2N$ solutions which form $2N$ column vectors can be assembled into two matrices of dimension $N \times N$ which we label as $g_{J}^{\lambda(a)+}$ and $g_{J}^{\lambda(a)-}$ where a set of indices $v'_\lambda j'_\lambda \Omega'_\lambda$ analogous to the row indices explained above is associated with each column.[41] The labels $\pm$ are in general arbitrary, but may be chosen to distinguish the solutions generated in the propagation from region I to IV (labelled plus) and from IV to I (labelled minus). Both propagations are necessary to generate all $2N$ solutions (we get N from the propagation in each direction). In terms of this notation, Eq. 3.6 may be written as

$$\frac{d^2 g_{J}^{\lambda(a)\pm}}{dR_\lambda^2} = U_{J}^{\lambda(a)}(R_\lambda) g_{J}^{\lambda(a)\pm} \tag{3.12}$$

where

$$U_{J}^{\lambda(a)} = -K^{\lambda(a)2} + U_{J}^{c\lambda(a)} \tag{3.13}$$

$$(K^{\lambda(a)2})_{t_\lambda}^{t'_\lambda} = \delta_{t_\lambda}^{t'_\lambda} k_{v_\lambda j_\lambda}^{\lambda(a)2} \tag{3.14}$$

$$(U_{\approx J}^{c\lambda(a)})_{t_\lambda}^{t'_\lambda} = \frac{\delta_{v'_\lambda j'_\lambda, v_\lambda j_\lambda}}{R_\lambda^2} \{ \delta_{\Omega_\lambda, \Omega'_\lambda}[J(J+1) - 2\Omega_\lambda^2 + j_\lambda(j_\lambda+1)]$$

(3.15)

$$- \delta_{\Omega_\lambda+1, \Omega'_\lambda} \xi_+(J,\Omega_\lambda)\xi_+(j_\lambda,\Omega_\lambda) - \delta_{\Omega_\lambda-1, \Omega'_\lambda} \xi_-(J,\Omega_\lambda)\xi_-(j_\lambda,\Omega_\lambda)\}$$

where t_λ stands for the set of indices $v_\lambda j_\lambda \Omega_\lambda$ and the subscripts and superscripts on a matrix element designate its row and column respectively. The $U_{\approx J}^{c\lambda(a)}$ matrix arises from the $1/R_\lambda^2$ centrifugal terms. Eq. 3.12 is the full close-coupled propagation equation for the asymptotic region I.

3.2.2 The weak interaction region

In this region we still use the variables r_λ and R_λ to represent vibrational and translational motion but the potential $V^\lambda(r_\lambda, R_\lambda, \gamma_\lambda)$ is now dependent on R_λ and γ_λ as well as r_λ, so we no longer use the asymptotic vibrational eigenfunctions of Eqs. 3.3 and 3.4 to expand the wave function. Since it may be desirable to change vibrational basis functions several times within region II, we subdivide that region into n_{II}^λ subregions separated by lines of constant R_λ at $R_\lambda = (R'_{\lambda_0}, R'_\lambda, ..R'_{\lambda n_{II}^\lambda} = R_{\lambda_0})$. The range of R_λ for the ith subregion is $R'_{\lambda_{i-1}} \leq R_\lambda \leq R'_{\lambda_i}$ and we choose eigenfunctions for that subregion to be the eigenfunctions of a reference potential $V_{ref}^\lambda(r_\lambda; R_{\lambda_i}^o)$ where $R_{\lambda_i}^o$ is generally a point (such as the midpoint) within subregion i. The reference potential $V_{ref}^\lambda(r_\lambda; R_\lambda)$ is in general arbitrary provided that a complete vibration-rotation expansion can be used, but an efficient representation of the vibrational motions can greatly reduce the number of closed channels required for such completeness.

Examples of reference potentials are the $V_0^\lambda(r_\lambda, R_\lambda)$ of Eq. 2.27 and the exact potential $V^\lambda(r_\lambda, R_\lambda, \bar\gamma_\lambda)$ at fixed $\bar\gamma_\lambda$. Once a reference potential is chosen, the vibrational basis functions for subregion i may be determined by solving

$$\left\{ -\frac{\hbar^2}{2\mu}\frac{d^2}{dr_\lambda^2} + \frac{j_\lambda(j_\lambda + 1)\hbar^2}{2\mu r_\lambda^2} + V_{ref}(r_\lambda; R_{\lambda_i}^0) \right\} \phi_{v_\lambda j_\lambda}^{\lambda(w)}(r_\lambda; R_{\lambda_i}^0)$$

$$= \epsilon_{v_\lambda j_\lambda}^{\lambda(w)}(R_{\lambda_i}^0) \phi_{v_\lambda j_\lambda}^{\lambda(w)} \tag{3.16}$$

subject to boundary conditions analogous to Eq. 3.5 where the superscript (w) indicates weak interaction region. We now expand the wave function $F_{Jj_\lambda \Omega_\lambda}^\lambda$ in terms of these basis functions

$$F_{Jj_\lambda \Omega_\lambda}^\lambda(r_\lambda, R_\lambda) = \sum_{v_\lambda} g_{Jv_\lambda j_\lambda \Omega_\lambda}^{\lambda(w)}(R_\lambda; R_{\lambda_i}^0) \phi_{v_\lambda j_\lambda}^{\lambda(w)}(r_\lambda; R_{\lambda_i}^0) \tag{3.17}$$

Substituting this into Eq. 2.31, using Eq. 3.16 to simplify, then multiplying by $\phi_{v'_\lambda j'_\lambda}^{\lambda(w)}(r_\lambda; R_{\lambda_i}^0)$ and integrating over r_λ, we obtain the following coupled differential equations (in the matrix notation of Section 3.2.1):

$$\frac{d^2 \underset{\sim}{g}_J^{\lambda(w)\pm}}{dR_\lambda^2} = \underset{\approx}{U}_J^{\lambda(w)}(R_\lambda; R_{\lambda_i}^0) \underset{\sim}{g}_J^{\lambda(w)\pm} \tag{3.18}$$

where

$$\underset{\approx}{U}_J^{\lambda(w)} = -\underset{\approx}{K}^{\lambda(w)2} + \underset{\approx}{U}_J^{c\lambda(w)} + \underset{\approx}{U}_p^{\lambda(w)} \tag{3.19}$$

The matrices $\underset{\approx}{K}^{\lambda(w)2}$ and $\underset{\approx}{U}_J^{c\lambda(w)}$ are given by Eq. 3.14 and 3.15 with the superscript w substituted for a, while the J independent potential coupling matrix is given by

$$(\underset{\approx}{U}_p^{\lambda(w)})_{t_\lambda}^{t'_\lambda} = \frac{2\mu}{\hbar^2} \delta_{\Omega_\lambda \Omega'_\lambda} \int \phi_{v_\lambda j_\lambda}^{\lambda(w)} (r_\lambda; R_{\lambda_i}^0) [V_{j_\lambda j'_\lambda}^{\lambda \Omega_\lambda} (r_\lambda, R_\lambda)$$

$$-V_{ref}(r_\lambda; R_{\lambda_i}^0)] \phi_{v'_\lambda j'_\lambda}^{\lambda(w)} (r_\lambda; R_{\lambda_i}^0) dr_\lambda \qquad (3.20)$$

$$= \langle t_\lambda | V(r_\lambda, R_\lambda, \gamma_\lambda) - V_{ref}(r_\lambda; R_{\lambda_i}^0) | t'_\lambda \rangle$$

where t_λ was defined after Eq. 3.15 and the γ_λ integral is performed as indicated in Eq. 2.23. Eq. 3.18 must now be integrated (as described in Section 3.3) through each subregion i of Region II. At the boundary between two subregions (say i and i + 1), a vibrational basis set change is performed. If one makes both $\Psi_{J\Omega_\lambda}^\lambda$ and its derivative with respect to R_λ continuous at this boundary $R_\lambda = R'_{\lambda_i}$, the following relations between the "g" coefficients in two adjacent subregions are obtained:

$$\underset{\approx}{g}_J^{\lambda(w)\pm}(R'_{\lambda_i}; R_{\lambda_{i+1}}^0) = \underset{\approx}{S}_i^{\lambda(w)} \, \underset{\approx}{g}_J^{\lambda(w)\pm}(R'_{\lambda_i}; R_{\lambda_i}^0) \qquad (3.21a)$$

$$\frac{d\underset{\approx}{g}_J^{\lambda(w)\pm}(R'_{\lambda_i}; R_{\lambda_{i+1}}^0)}{dR_\lambda} = \underset{\approx}{S}_i^{\lambda(w)} \frac{d\underset{\approx}{g}_J^{\lambda(w)\pm}(R'_{\lambda_i}; R_{\lambda_i}^0)}{dR_\lambda} \qquad (3.21b)$$

where the overlap matrix $\underset{\approx}{S}_i^{\lambda(w)}$ is given by

$$[\underset{\approx}{S}_i^{\lambda(w)}]_{t_\lambda}^{t'_\lambda} = \delta_{j_\lambda \Omega_\lambda}^{j'_\lambda \Omega'_\lambda} \langle \phi_{v_\lambda j_\lambda}^{\lambda(w)} (r_\lambda; R_{\lambda_{i+1}}^0) | \phi_{v'_\lambda j'_\lambda}^{\lambda(w)} (r_\lambda; R_{\lambda_i}^0) \rangle$$

$$(3.22)$$

as discussed in I (Section 3.4.2), $\underset{\approx}{S}_i^{\lambda(w)}$ should be orthogonal for a for a complete vibrational expansion. For a truncated expansion, as required by practical considerations, $\underset{\approx}{S}_i^{\lambda(w)}$ must be nearly orthogonal

in order for us to obtain scattering matrices which satisfy conservation of flux (see Section 5) to an acceptable degree of accuracy. The transformation between regions I and II is accomplished by setting $i = 0$ in Eqs. 3.21 and interpreting $R_{\lambda_0}^0$ to mean R_{λ_0}' (Fig. 4) and $\phi_{v_\lambda j_\lambda}^{\lambda(w)}(r_\lambda; R_{\lambda_0}^0)$ to mean $\phi_{v_\lambda j_\lambda}^{\lambda(a)}(r_\lambda)$.

3.2.3 The strong interaction region

In this region we use the polar coordinates ρ_λ, φ_λ of Eq. 3.1 and regard φ_λ as the propagation variable. Before we can expand our wave function in terms of a set of pseudo-vibrational eigenfunctions in the variable ρ_λ, we must first transform Eq. 2.31 to these polar coordinates. The only important change in this transformation occurs in $\bar{t}_{\Omega_\lambda \Omega_\lambda}^{J \lambda j_\lambda}$ (of Eq. 2.32) which becomes:

$$\bar{t}_{\Omega_\lambda \Omega_\lambda}^{J \lambda j_\lambda} = -\frac{\hbar^2}{2\mu}\left[\frac{1}{\rho_\lambda}\frac{\partial}{\partial \rho_\lambda}\rho_\lambda\frac{\partial}{\partial \rho_\lambda} + \frac{1}{\rho_\lambda^2}\frac{\partial^2}{\partial \varphi_\lambda^2}\right]$$

$$+ \frac{j_\lambda(j_\lambda + 1)\hbar^2}{2\mu(r_{\lambda_0} - \rho_\lambda \cos\varphi_\lambda)^2} + \frac{\hbar^2[J(J+1) - 2\Omega_\lambda^2 + j_\lambda(j_\lambda+1)]}{2\mu(R_{\lambda_0} - \rho_\lambda \sin\varphi_\lambda)^2}$$

(3.23)

As for region II, we divide region III into n_{III}^λ subregions bounded by lines of constant φ_λ ($= \varphi_{\lambda_1}', \varphi_{\lambda_2}' \ldots \varphi_{\lambda n_{III}}' = \varphi_{\lambda_0}$). We choose our vibrational basis set to satisfy

$$\left\{-\frac{\hbar^2}{2\mu}\frac{d^2}{d\rho_\lambda^2} + V_{ref}^\lambda(\rho_\lambda; \varphi_{\lambda_i}^0)\right\}\phi_{v_\lambda}^{\lambda(s)}(\rho_\lambda; \varphi_{\lambda_i}^0)$$

$$= \epsilon_{v_\lambda}^{\lambda(s)}(\varphi_{\lambda_i}^0)\phi_{v_\lambda}^{\lambda(s)}$$

(3.24)

with boundary conditions analogous to Eq. 3.5. $\varphi_{\lambda_i}^0$ is generally a point within the ith subregion and the reference potential has been

re-expressed in the polar coordinates so that it has the shape of a diatomic potential as a function of ρ_λ for a given $\varphi_{\lambda_i}^0$ within region III (see Fig. 4). The superscript s in Eq. 3.24 refers to strong interaction region. Note that the centrifugal term appearing in Eqs. 3.4 and 3.16 has been omitted. (It has been transferred to Eq. 3.30 below.) This results in a vibrational function $\phi_{v_\lambda}^{\lambda(s)}$ independent of j_λ, which simplifies the matching procedure (Section 4) and should not seriously slow down the rate of convergence of the method. If we now expand $F_{Jj_\lambda\Omega_\lambda}^\lambda$ in terms of these $\phi_{v_\lambda}^{\lambda(s)}$,

$$F_{Jj_\lambda\Omega_\lambda}^\lambda(\rho_\lambda,\varphi_\lambda) = \rho_\lambda^{-\frac{1}{2}} \sum_{v_\lambda} g_{Jv_\lambda j_\lambda\Omega_\lambda}^{\lambda(s)}(\varphi_\lambda;\varphi_{\lambda_i}^0)\phi_{v_\lambda}^{\lambda(s)}(\rho_\lambda;\varphi_{\lambda_i}^0), \tag{3.25}$$

we obtain the following matrix equation:

$$\frac{d^2 \underset{\sim}{g}_{J}^{\lambda(s)\pm}}{d\varphi_\lambda^2} = \overline{\underset{\sim}{U}}_J^{\lambda(s)}(\varphi_\lambda;\varphi_{\lambda_i}^0)\underset{\sim}{g}_J^{\lambda(s)\pm} \tag{3.26}$$

where

$$\overline{\underset{\sim}{U}}_J^{\lambda(s)} = \underset{\sim}{\rho}_\lambda^2(\varphi_{\lambda_i}^0)\underset{\sim}{U}_J^{\lambda(s)}(\varphi_\lambda;\varphi_{\lambda_i}^0) \tag{3.27}$$

and

$$\underset{\sim}{U}_J^{\lambda(s)}(\varphi_\lambda;\varphi_{\lambda_i}^0) = -\underset{\sim}{K}^{\lambda(s)2} + \underset{\sim}{U}_J^{c\lambda(s)} + \underset{\sim}{U}_p^{\lambda(s)} \tag{3.28}$$

The matrix $\underset{\sim}{\rho}_\lambda^2$ (whose elements have the physical dimension of the square of a length) is given by:

$$[\rho_\lambda^2(\varphi_{\lambda_i}^0)]_{t_\lambda}^{t'_\lambda} = \delta_{j_\lambda\Omega_\lambda}^{j'_\lambda\Omega'_\lambda} \langle v_\lambda | \rho_\lambda^2 | v'_\lambda \rangle \tag{3.29}$$

while the centrifugal coupling matrix $\underset{\sim}{U}_J^{c\lambda(s)}$ is

$$[\underset{\widehat{\approx}}{U}{}^{c\,\lambda(s)}_J (\varphi_\lambda;\varphi_{\lambda_i}^{\,0})]^{t'_\lambda}_{t_\lambda} = \delta^{j'_\lambda\Omega'_\lambda}_{j_\lambda\Omega_\lambda} \{\langle v_\lambda | [-\frac{1}{4\rho_\lambda^2} + \frac{J(J+1) - 2\Omega_\lambda^2 + j_\lambda(j_\lambda+1)}{(R_{\lambda_0} - \rho_\lambda \sin\varphi_\lambda)^2}$$

$$+ \frac{j_\lambda(j_\lambda+1)}{(r_{\lambda_0} - \rho_\lambda \cos\varphi_\lambda)^2} \} |v'_\lambda\rangle - \delta_{j_\lambda j'_\lambda} \langle v_\lambda | \frac{1}{(R_{\lambda_0} - \rho_\lambda \sin\varphi_\lambda)^2} |v'_\lambda\rangle$$

$$[\delta_{\Omega_\lambda+1,\Omega'_\lambda} \xi_+(J,\Omega_\lambda)\xi_+(j_\lambda,\Omega_\lambda) + \delta_{\Omega_\lambda-1,\Omega'_\lambda} \xi_-(J,\Omega_\lambda)\xi_-(j_\lambda,\Omega_\lambda)]\}$$

$$(3.30)$$

The matrices $\underset{\widehat{\approx}}{K}{}^{\lambda(s)^2}$ and $\underset{\widetilde{\approx}p}{U}{}^{\lambda(s)}$ are given by equations analogous to Eqs. 3.14 and 3.20 with superscripts and coordinates appropriate to the strong interaction region substituted where necessary. Note that the centrifugal coupling (Eq. 3.30) is no longer diagonal in v_λ. The effective potential matrix $\overline{U}_J^{\lambda(s)}$ is not symmetric in this region but rather is equal to the product of two symmetric matrices (Eq. 3.27) one of which $(\underset{\approx}{\rho}_\lambda{}^2)$ is the matrix representation of a positive definite operator. Complications resulting from the use of a nonsymmetric $\underset{\widetilde{\approx}J}{\overline{U}}{}^{\lambda(s)}$ in integrating Eq. 3.26 were discussed in I (Section 3.5).

To solve the Schrödinger equation in region III we need to propagate the solution of Eq. 3.26 through each subregion of that region, relating solutions in adjacent subregions by an equation analogous to Eqs. 3.21 and 3.22. To relate the solutions at the boundary of regions II and III, we use the following formula (which is derived in a manner analogous to Eq. 3.21):

$$\underset{\approx}{g}{}^{\lambda(s)\pm}_J(\varphi_\lambda = 0;\varphi_{\lambda_i}^{\,0}) = \underset{\approx}{\rho}_\lambda^{\frac{1}{2}} \underset{\approx}{g}{}^{\lambda(w)\pm}_J(R_{\lambda_0};R_{\lambda n_{II}}^{\,0}) \qquad (3.31a)$$

$$\frac{dg_{\underset{\sim}{J}}^{\lambda(s)}(\varphi_\lambda = 0; \varphi_{\lambda_i}^{0})}{d\varphi_\lambda} = - \rho_{\underset{\sim}{\lambda}}^{3/2} \frac{dg_{\underset{\sim}{J}}^{\lambda(w)\pm}(R_{\lambda_0}; R_{\lambda n_{II}^\lambda}^{0})}{dR_\lambda} \tag{3.31b}$$

where

$$[\rho_{\underset{\sim}{\lambda}}^b]_{t_\lambda}^{t'_\lambda} = \delta_{j_\lambda \Omega_\lambda}^{j'_\lambda \Omega'_\lambda} \langle \phi_{v_\lambda}^{\lambda(s)}(\rho_\lambda; \varphi_{\lambda_1}^{0}) | \rho_\lambda^{b} | \phi_{v'_\lambda j'_\lambda}^{\lambda(w)}(r_{\lambda_0} - \rho_\lambda; R_{\lambda n_{II}^\lambda}^{0}) \rangle \tag{3.32}$$

$$b = 1/2, \, 3/2$$

3.2.4 The matching region

The polar coordinates ζ, η_λ of Eqs. 3.2 are used in region IV with η_λ acting as the propagation variable. Upon transformation of Eq. 2.31 to these coordinates, the operator $\bar{t}_{\Omega_\lambda, \Omega_\lambda}^{J\lambda j_\lambda}$ of Eq. 2.32 becomes

$$\bar{t}_{\Omega_\lambda, \Omega_\lambda}^{J\lambda j_\lambda} = - \frac{\hbar^2}{2\mu}[\frac{1}{\zeta}\frac{\partial}{\partial\zeta}\zeta\frac{\partial}{\partial\zeta} + \frac{1}{\zeta^2}\frac{\partial^2}{\partial\eta_\lambda^2}] + \frac{\hbar^2 j_\lambda(j_\lambda + 1)}{2\mu\zeta^2 \sin^2 \eta_\lambda}$$
$$+ \frac{\hbar^2[J(J + 1) - 2\Omega_\lambda^2 + j_\lambda(j_\lambda + 1)]}{2\mu\zeta^2 \cos^2 \eta_\lambda} \tag{3.33}$$

Similarly to region III, region IV is divided into n_{IV}^λ subregions by lines of constant η_λ, with the vibrational eigenfunctions of each subregion satisfying an equation analogous to 3.24:

$$[- \frac{\hbar^2}{2\mu}\frac{d^2}{d\zeta^2} + V_{ref}(\zeta; \eta_{\lambda_i}^{0})] \phi_{v_\lambda}^{\lambda(m)}(\zeta; \eta_{\lambda_i}^{0}) = \epsilon_{v_\lambda}^{\lambda(m)}(\eta_{\lambda_i}^{0}) \phi_{v_\lambda}^{\lambda(m)} \tag{3.34}$$

where the superscript m denotes matching region. Writing

$$F^{\lambda}_{Jj_{\lambda}\Omega_{\lambda}}(\zeta,\eta_{\lambda}) = \zeta^{-\frac{1}{2}} \sum_{v_{\lambda}} g^{\lambda(m)}_{Jv_{\lambda}j_{\lambda}\Omega_{\lambda}}(\eta_{\lambda};\eta^{0}_{\lambda_i})\phi^{\lambda(m)}_{v_{\lambda}}(\zeta;\eta^{0}_{\lambda_i}) \qquad (3.35)$$

the counterpart of Eq. 3.26 becomes:

$$\frac{d^2}{d\eta_{\lambda}^2} \underset{\approx}{g}^{\lambda(m)}_J = \underset{\approx}{\overline{U}}^{\lambda(m)}_J(\eta_{\lambda};\eta^{0}_{\lambda_i})\underset{\approx}{g}^{\lambda(m)\pm}_J \qquad (3.36)$$

where

$$\underset{\approx}{\overline{U}}^{\lambda(m)}_J = \underset{\approx}{\zeta}^2(\eta^{0}_{\lambda_i})\underset{\approx}{U}^{\lambda(m)}_J(\eta_{\lambda};\eta^{0}_{\lambda_i}) \qquad (3.37)$$

and

$$\underset{\approx}{U}^{\lambda(m)}_J(\eta_{\lambda};\eta^{0}_{\lambda_i}) = - \underset{\approx}{K}^{\lambda(m)2} + \underset{\approx}{U}^{c\,\lambda(m)}_J + \underset{\approx}{U}^{\lambda(m)}_p \qquad (3.38)$$

The matrix $\underset{\approx}{\zeta}^2(\eta^{0}_{\lambda_i})$ is defined analogously to $\underset{\approx}{\rho}^2_{\lambda}$ of Eq. 3.44 with ζ substituted for ρ_{λ}. The matrices $\underset{\approx}{K}^{\lambda(m)2}$ and $\underset{\approx}{U}^{\lambda(m)}_p$ are given by equations similar to Eqs. 3.14 and 3.20 respectively with the super-script m inserted and the appropriate coordinate changes made. The centrifugal coupling matrix $\underset{\approx}{U}^{c\lambda(m)}_J$ is given by:

$$[\underset{\approx}{U}^{c\lambda(m)}_J(\eta_{\lambda};\eta^{0}_{\lambda_i})]^{t'\lambda}_{t_{\lambda}} = \langle v_{\lambda}|\zeta^{-2}|v'_{\lambda}\rangle\{\delta^{j'_{\lambda}\Omega'_{\lambda}}_{j_{\lambda}\Omega_{\lambda}}[- \tfrac{1}{4} + (J(J+1)-2\Omega^2_{\lambda}$$

$$+ j_{\lambda}(j_{\lambda} + 1))/\cos^2\eta_{\lambda} + j_{\lambda}(j_{\lambda} + 1)/\sin^2\eta_{\lambda}] \qquad (3.39)$$

$$- \delta_{j_{\lambda},j'_{\lambda}}[\delta_{\Omega_{\lambda}+1,\Omega'_{\lambda}}\xi_+(J,\Omega_{\lambda})\xi_+(j_{\lambda},\Omega_{\lambda})$$

$$+ \delta_{\Omega_{\lambda}-1,\Omega'_{\lambda}}\xi_-(J,\Omega_{\lambda})\xi_-(j_{\lambda},\Omega_{\lambda})]/\cos^2\eta_{\lambda}\}$$

To solve the Schrödinger equation in region IV, one must integrate Eq. 3.37 through each subregion, relating solutions in adjacent sub-regions by equations analogous to Eqs. 3.21 and 3.22. The transforma-

tion between regions III and IV is accomplished by equations analogous to Eqs. 3.31a and 3.31b (with a plus rather than a minus sign in the right hand side of the latter) and the matrix $\underset{\approx}{\zeta}^b$ substituted for $\underset{\approx}{\rho}_\lambda{}^b$ where

$$[\underset{\approx}{\zeta}^b]_{t_\lambda}^{t'_\lambda} = \delta_{j_\lambda \Omega_\lambda}^{j'_\lambda \Omega'_\lambda} \langle \phi_{v_\lambda}^{\lambda(m)}(\zeta, \eta_\lambda \overset{o}{\underset{1}{}}) | (\frac{\zeta}{\rho_{\lambda_0} - \zeta})^b | \phi_{v_\lambda}^{\lambda(s)}(\rho_{\lambda_0} - \zeta; \varphi_{\lambda n}{}_{III}^{o}) \rangle \qquad (3.40)$$

$$b = 1/2, \ 3/2$$

with ρ_{λ_0} defined in Fig. 3.

3.3 Integration of the Schrödinger Equation

We generate the solution $\underset{\approx}{g}_J^{\lambda+}$ and its derivative with respect to the propagation variable by choosing at $R_\lambda = R'_{\lambda_0}$ (Fig. 3) arbitrary initial values for these two matrices and integrating numerically Eqs. 3.12, 3.26 and 3.36 from the beginning of region II to the end of region IV. The solution $\underset{\approx}{g}_J^{\lambda-}$ and its derivative are determined by integrating the same equations from the end of region IV to the beginning of region II. Any appropriate numerical procedure may be used to solve these coupled ordinary second order differential equations. A particular one which is well suited to such equations and which we used is the Gordon method[42]. More particulars of this procedure are described in I (Section 3.5).

For the H + H_2 reaction, the coupled equations need only be solved in one of the three equivalent arrangement channels. Reactions of the type A + B_2 involving two identical atoms will require two such integrations, and reactions with three different atoms will require

three. For arrangement channels for which the target is homonuclear,
Eq. 2.29 implies zero potential coupling between odd and even rota-
tional states. Since all kinetic energy coupling is diagonal in j_λ
in all four regions, our matrix differential equations may be decoupled
into separate ones for the even and odd rotational states with a subse-
quent savings in computation time. Both must be integrated before
the matching, which mixes these two sets of solutions, can be performed.

Any chemical reaction displays in addition parity (i.e., inver-
sion through the center of mass) symmetry, as shown for triatomic
systems in Appendix B. Although the body-fixed wave functions ob-
tained from Eqs. 2.13, 2.18, 2.30 and either 3.3, 3.17, 3.25 or
3.35 are not eigenfunctions of the parity operator, they may be
linearly combined to yield solutions which are, and this transformation
to the "parity representation" results in a partial decoupling of
Eqs. 3.18, 3.26 and 3.36 into two sets, one for even and one for odd
parity. A description of this transformation and other consequences
of the parity operation are given in Appendix B. By using parity
eigenfunctions, the integration in each arrangement channel is done
in two separate steps (four for homonuclear targets). Since the
transformation between arrangement channels preserves parity
(as shown in Appendix B), the matching procedure also can be done
separately for solutions of each parity, as can the calculation of the
reactance and scattering matrices. The final plane wave solution
is not, however, an eigenfunction of the parity operator, and as a
result the calculation of scattering amplitudes requires a transformation
back to the body fixed representation of the previous two sections.

The enormous reduction in computation time more than outweighs the additional work involved in this transformation. Appendix B describes this in more detail.

4. THE MATCHING

4.1 The λ to ν Transformation

At the completion of the integrations in each of the three arrangement channel regions, we have obtained solutions to the Schrödinger equation which span all of configuration space but which are neither smooth nor continuous at the internal configuration space boundaries of these regions. In this section we describe the procedure for linearly combining these solutions so as to produce a smooth matching at those boundaries. This procedure will also include the transformation from λ to ν coordinates (appropriate for arrangement channels λ and ν respectively), a transformation which is both conceptually and numerically facilitated by the use of body fixed coordinates. Our analysis will focus primarily on the behavior of the wave function in the vicinity of the half-plane matching surfaces defined by Eqs. 2.4 and the remarks preceding and following it.

Equations describing the λ to ν transformation have been derived for coplanar reactions in Appendix A of I, and most of these expressions are still valid in 3D. However, some angles which span a range of 2π in 2D become polar angles in 3D (with a range of π) so some care is required in making the analogy. The basic equations which govern the transformation are given by:[19]

$$\begin{pmatrix} R_{\sim\nu} \\ r_{\sim\nu} \end{pmatrix} = \begin{pmatrix} \cos\alpha_{\nu\lambda} & -\sin\alpha_{\nu\lambda} \\ \sin\alpha_{\nu\lambda} & \cos\alpha_{\nu\lambda} \end{pmatrix} \begin{pmatrix} R_{\sim\lambda} \\ r_{\sim\lambda} \end{pmatrix} \tag{4.1}$$

where $\alpha_{\nu\lambda}$ is the angle between $\pi/2$ and π defined by

$$\alpha_{\nu\lambda} = \pi - \beta_{\nu\lambda} \tag{4.2}$$

$\beta_{\nu\lambda}$ having been given by Eqs. 2.4. Eq. 4.1 may be easily derived from Fig. 1 and Eq. 2.1. By taking the scalar products $R_{\sim\nu} \cdot R_{\sim\nu}$, $r_{\sim\nu} \cdot r_{\sim\nu}$ and $R_{\sim\nu} \cdot r_{\sim\nu}$ in Eq. 4.1 and using Eq. 2.3, we find the following expressions for the $R_\lambda, r_\lambda, \gamma_\lambda \rightarrow R_\nu, r_\nu, \gamma_\nu$ transformation

$$R_\nu^2 = \cos^2\alpha_{\nu\lambda} R_\lambda^2 + \sin^2\alpha_{\nu\lambda} r_\lambda^2 - \sin 2\alpha_{\nu\lambda} \cos\gamma_\lambda r_\lambda R_\lambda \tag{4.3}$$

$$r_\nu^2 = \sin^2\alpha_{\nu\lambda} R_\lambda^2 + \cos^2\alpha_{\nu\lambda} r_\lambda^2 + \sin 2\alpha_{\nu\lambda} \cos\gamma_\lambda r_\lambda R_\lambda \tag{4.4}$$

$$\cos\gamma_\nu = (R_\nu r_\nu)^{-1}[\tfrac{1}{2}(R_\lambda^2 - r_\lambda^2)\sin 2\alpha_{\nu\lambda} + R_\lambda r_\lambda \cos 2\alpha_{\nu\lambda} \cos\gamma_\lambda] \tag{4.5}$$

Eqs. 4.3 and 4.4 may be combined to yield

$$R_\nu^2 + r_\nu^2 = R_\lambda^2 + r_\lambda^2 \tag{4.6}$$

which, together with Eqs. 3.2, proves the invariance of ζ to arrangement channel. Also of use in our analysis below is the polar angle $\Delta_{\nu\lambda}$ (in 0 to π range) between $R_{\sim\lambda}$ and $R_{\sim\nu}$ which is determined by

$$\cos\Delta_{\nu\lambda} = \frac{R_{\sim\nu} \cdot R_{\sim\lambda}}{R_\nu R_\lambda} = \cos\alpha_{\nu\lambda}\frac{R_\lambda}{R_\nu} - \sin\alpha_{\nu\lambda}\cos\gamma_\lambda\frac{r_\lambda}{R_\nu} \tag{4.7}$$

We now examine the consequences of Eqs. 4.3 - 4.7 on the matching surface $\pi_{\nu\lambda}$. Combining Eq. 2.5a with Eq. 4.6 gives

$$R_\lambda = R_\nu \tag{4.8}$$

385

and this equation together with Eqs. 2.5a and 4.3 leads to

$$\frac{R_\lambda}{r_\lambda} = -\cot \alpha_{\nu\lambda} \cos \gamma_\lambda + (1 + \cot^2 \alpha_{\nu\lambda} \cos^2 \gamma_\lambda)^{\frac{1}{2}}. \qquad (4.9)$$

which is the equation of the matching surface $\pi_{\nu\lambda}$ in $R_\lambda, r_\lambda, \gamma_\lambda$ coordinates. If Eqs. 2.5a, 4.8 and 4.9 are now substituted into Eq. 4.5, we find

$$\cos \gamma_\nu = -\cos \gamma_\lambda$$

and since $0 \leq \gamma_\lambda, \gamma_\nu \leq \pi$, we conclude that on $\pi_{\nu\lambda}$

$$\gamma_\nu = \pi - \gamma_\lambda \qquad (4.10)$$

Eqs. 2.5a, 4.8, 4.9 and 4.7 may be combined to yield

$$\cos \Delta_{\nu\lambda} = \cos \alpha_{\nu\lambda} - \sin \alpha_{\nu\lambda} \cos \gamma_\lambda [\cot \alpha_{\nu\lambda} \cos \gamma_\lambda$$
$$+ (1 + \cot^2 \alpha_{\nu\lambda} \cos^2 \gamma_\lambda)^{\frac{1}{2}}] \qquad (4.11)$$

which implies that $\Delta_{\nu\lambda}$ is a function only of γ_λ on $\pi_{\nu\lambda}$.

It will also be useful to convert R_λ, r_λ in Eqs. 4.7 - 4.11 to the polar coordinates ζ, η_λ (of Eqs. 3.2). First, from Eqs. 4.8 and 3.2, we have

$$\eta_\lambda = \eta_\nu \qquad (4.12)$$

and, after some manipulation, Eq. 4.9 becomes

$$\cot 2\eta_\lambda = -\cot \alpha_{\nu\lambda} \cos \gamma_\lambda \qquad (4.13)$$

which is the equation of $\pi_{\nu\lambda}$ in $\zeta, \eta_\lambda, \gamma_\lambda$ coordinates. Since $\eta_\lambda = \tan^{-1}(r_\lambda/R_\lambda)$ and is in the 0 to $\pi/2$ range, we conclude that

$$\eta_\lambda = \tfrac{1}{2}\omega_\lambda . \tag{4.14}$$

where ω_λ was defined after Eq. 2.3. Therefore, Eq. 4.13 is equivalent to

$$\cot \omega_\lambda = -\cot \alpha_{\nu\lambda} \cos \gamma_\lambda \tag{4.15}$$

which is the equation of the $\pi_{\nu\lambda}$ half-plane of Fig. 2 in the polar coordinates $\zeta, \omega_\lambda, \gamma_\lambda$. Finally, Eq. 4.11 may be reexpressed in $\eta_\lambda, \gamma_\lambda$ coordinates as

$$\cos \Delta_{\nu\lambda} = \cos \alpha_{\nu\lambda} - \sin \alpha_{\nu\lambda} \cos \gamma_\lambda \tan \eta_\lambda \tag{4.16}$$

We now consider the transformation from the body-fixed coordinate system $Ox'_\lambda y'z'_\lambda$ (Fig. 3) to $Ox'_\nu y'z'_\nu$. Both systems have the same y' axis (which is perpendicular to the three atom plane) and from Eq. 4.1 and Fig. 3 it can easily be shown that this coordinate transformation is a clockwise rotation about y by $\Delta_{\nu\lambda}$.

Let us determine the effect of the $\underset{\sim}{R}_\lambda, \underset{\sim}{r}_\lambda \to \underset{\sim}{R}_\nu, \underset{\sim}{r}_\nu$ transformation on the wave functions. The complete body fixed wave function, as obtained from Eqs. 2.13, 2.18 and 2.30 is

$$\Psi_{JM} = \sum_{j_\lambda \Omega_\lambda} D^J_{M\Omega_\lambda}(\phi_\lambda, \theta_\lambda, 0) Y_{j_\lambda \Omega_\lambda}(\gamma_\lambda, \psi_\lambda) \frac{F^\lambda_{Jj_\lambda \Omega_\lambda}(r_\lambda, R_\lambda)}{r_\lambda R_\lambda}$$

$$= \frac{1}{\sqrt{2\pi}} \sum_{\Omega_\lambda} D^J_{M\Omega_\lambda}(\phi_\lambda, \theta_\lambda, \psi_\lambda) \chi^\lambda_{J\Omega_\lambda}(r_\lambda, R_\lambda, \gamma_\lambda) \tag{4.17}$$

where, from Eq. A.2,

$$\chi^{\lambda}_{J\Omega_{\lambda}} = \sum_{j_{\lambda}=|\Omega_{\lambda}|}^{\infty} \frac{\mathcal{P}^{\Omega_{\lambda}}_{j_{\lambda}}(\cos \gamma_{\lambda}) \, F^{\lambda}_{Jj_{\lambda}\Omega_{\lambda}}(r_{\lambda}, R_{\lambda})}{r_{\lambda} R_{\lambda}} \quad (4.18)$$

In the second line of Eq. 4.17, the $\exp i\Omega_{\lambda}\psi_{\lambda}$ part of $Y_{j_{\lambda}\Omega_{\lambda}}(\gamma_{\lambda}, \psi_{\lambda})$ has been incorporated into the rotation matrix $D^{J}_{M\Omega_{\lambda}}$ which trivially converts Ψ_{JM} from the $OX_{\lambda}Y_{\lambda}Z_{\lambda}$ to the $Ox'_{\lambda}y'z'_{\lambda}$ coordinate system. If Ψ_{JM} is fully matched (i.e., a smoothly continuous solution of the Schrödinger equation), it may be expressed in the $Ox'_{\nu}y'z'_{\nu}$ coordinate system in an analogous way:

$$\Psi_{JM} = \frac{1}{\sqrt{2\pi}} \sum_{\Omega_{\nu}} D^{J}_{M\Omega_{\nu}}(\phi_{\nu}, \theta_{\nu}, \psi_{\nu}) \chi^{\nu}_{J\Omega_{\nu}}(r_{\nu}, R_{\nu}, \gamma_{\nu}) \quad (4.19)$$

Since the λ to ν transformation in the body fixed coordinates $Ox'_{\lambda}y'z'_{\lambda}$ is accomplished by a counterclockwise rotation by an angle $- \Delta_{\nu\lambda}$ about y, the corresponding body fixed wave functions may be related by:

$$\chi^{\lambda}_{J\Omega_{\lambda}} = \sum_{\Omega_{\nu}} d^{J}_{\Omega_{\nu}\Omega_{\lambda}}(\Delta_{\nu\lambda}) \chi^{\nu}_{J\Omega_{\nu}} \quad (4.20)$$

where

$$d^{J}_{\Omega_{\nu}\Omega_{\lambda}}(\Delta_{\nu\lambda}) = D^{J}_{\Omega_{\nu}\Omega_{\nu}}(0, \Delta_{\nu\lambda}, 0) \quad (4.21)$$

in the notation of Davydov.[33] Eq. 4.20 relates the matched solutions χ^{λ} and χ^{ν} for any values of the internal variables.

4.2 Projection of the Wave Function onto the Matching Surface Basis Functions

In this section we consider the evaluation of the unmatched wave functions and normal derivatives obtained from the integrations in both channels λ and ν on the matching surface $\pi_{\nu\lambda}$, and their expansion in a set of functions $T^{\nu\lambda}_{v_\lambda j_\lambda \Omega_\lambda}(\zeta,\gamma_\lambda)$ which span that surface. The complete, unmatched wave function in the $Ox'_\lambda y'z'_\lambda$ coordinate system, in region IV of internal configuration space (subregion i) is (from Eqs. 4.17, 4.18, 3.35 and 4.14):

$$\Psi^{\lambda t'_\lambda \pm}_{JM} = \frac{1}{\sqrt{2\pi}} \sum_{\Omega_\lambda} D^J_{M\Omega_\lambda}(\phi_\lambda,\theta_\lambda,\psi_\lambda)\overline{\chi}^{\lambda t'_\lambda \pm}_{J\Omega_\lambda}(\zeta,\eta_\lambda,\gamma_\lambda) \tag{4.22}$$

where

$$\overline{\chi}^{\lambda t'_\lambda +}_{J\Omega_\lambda} = \sum_{v_\lambda j_\lambda} \frac{\mathscr{P}_{j_\lambda \Omega_\lambda}(\cos\gamma_\lambda)\phi_{v_\lambda}(\zeta,\eta_\lambda^{\,o})g^{\lambda t'_\lambda \pm}_{Jv_\lambda j_\lambda \Omega_\lambda}(\eta_\lambda;\eta_{\lambda_1}^{\,o})}{\zeta^{5/2}(\frac{1}{2}\sin 2\eta_\lambda)} \tag{4.23}$$

Here we have dropped the superscript (m) as it will be implicit throughout this section, but we have included the labels $t'_\lambda \pm \equiv (v'_\lambda j'_\lambda \Omega'_\lambda \pm)$ to denote the 2N linearly independent solutions obtained (from an N coupled-channel calculation). Eq. 4.23 may be evaluated on $\pi_{\nu\lambda}$ by using Eq. 4.13 to relate η_λ and γ_λ. Since $0 \le \gamma_\lambda \le \pi/2$ on $\pi_{\nu\lambda}$, we find that η_λ must lie between $\eta_{\lambda_0} = (\pi - \alpha_{\nu\lambda})/2$ and $\eta_{\lambda_1} = \pi/4$ to satisfy Eq. 4.13. In order to evaluate Eq. 4.23 over this range of η_λ, it is convenient to change to a common set of vibrational basis functions $\phi_{v_\lambda}(\zeta)$ for all subregions i. This is accomplished by transformations analogous to Eq. 3.21 and 3.22 with the result that

$$\overline{\chi}_{J\Omega_\lambda}^{\lambda t'_\lambda \pm} = 2\zeta^{-5/2} (\sin 2\eta_\lambda)^{-1} \Phi_{J\Omega_\lambda}^{\lambda t'_\lambda \pm} \tag{4.24}$$

where

$$\Phi_{J\Omega_\lambda}^{\lambda t'_\lambda \pm} = \sum_{v_\lambda j_\lambda} \mathcal{P}_{j_\lambda}^{\Omega_\lambda} (\cos \gamma_\lambda) \phi_{v_\lambda}(\zeta) g_{Jv_\lambda j_\lambda \Omega_\lambda}^{\lambda t'_\lambda \pm} (\eta_\lambda) \tag{4.25}$$

To insure a smooth matching, we must also consider the derivative

of $\overline{\chi}_{J\Omega_\lambda}$ normal to $\pi_{\nu\lambda}$ (other derivatives are possible). Expressions

for this normal derivative operator were derived in I (Appendix A)

where we found

$$\frac{\partial}{\partial n_{\nu\lambda}} = \frac{1}{\zeta} \frac{\sin \alpha_{\nu\lambda}}{\sin \omega_\lambda} \left[\frac{\partial}{\partial \omega_\lambda} + \cot \alpha_{\nu\lambda} \sin \gamma_\lambda \frac{\partial}{\partial \gamma_\lambda} \right]$$

$$= \frac{1}{\zeta} \frac{\sin \alpha_{\nu\lambda}}{\sin 2\eta_\lambda} \left[\tfrac{1}{2} \frac{\partial}{\partial \eta_\lambda} + \cot \alpha_{\nu\lambda} \sin \gamma_\lambda \frac{\partial}{\partial \gamma_\lambda} \right] \tag{4.26}$$

$$= -\frac{1}{\zeta} \frac{\sin \alpha_{\nu\lambda}}{\sin 2\eta_\lambda} \left[\tfrac{1}{2} \frac{\partial}{\partial \eta_\nu} - \cot \alpha_{\nu\lambda} \sin \gamma_\lambda \frac{\partial}{\partial \gamma_\nu} \right]$$

Applying this operator to Eq. 4.21, and evaluating the result on $\pi_{\nu\lambda}$,

we find

$$\frac{\partial \overline{\chi}_{J\Omega_\lambda}^{\lambda t'_\lambda \pm}}{\partial n_{\nu\lambda}} = \frac{2\sin \alpha_{\nu\lambda}}{\zeta^{7/2} \sin 2\eta_\lambda} \Phi'^{\lambda t'_\lambda \pm}_{J\Omega_\lambda} \tag{4.27}$$

where

$$\Phi'^{\lambda t'_\lambda \pm}_{J\Omega_\lambda} = \sum_{v_\lambda j_\lambda} \phi_{v_\lambda}(\zeta) G'^{\lambda t'_\lambda \pm}_{Jv_\lambda j_\lambda \Omega_\lambda} \tag{4.28}$$

and

$$G'^{\lambda t'_\lambda \pm}_{Jv_\lambda j_\lambda \Omega_\lambda} = [\tfrac{1}{2} \mathcal{P}^{\Omega_\lambda}_{j_\lambda}(\cos \gamma_\lambda) \frac{d g^{\lambda t'_\lambda \pm}_{Jv_\lambda j_\lambda \Omega_\lambda}(\eta_\lambda(\gamma_\lambda))}{d\eta_\lambda} - \cot \alpha_{\nu\lambda}$$

$$\times g^{\lambda t'_\lambda \pm}_{Jv_\lambda j_\lambda \Omega_\lambda}(\eta_\lambda(\gamma_\lambda))\{j_\lambda \cos \gamma_\lambda \mathcal{P}^{\Omega_\lambda}_{j_\lambda}(\cos \gamma_\lambda) - (\frac{2j_\lambda + 1}{2j_\lambda + 3})^{\tfrac{1}{2}} \qquad (4.29)$$

$$\times [(j_\lambda + 1)^2 - \Omega_\lambda^2]^{\tfrac{1}{2}} \mathcal{P}^{\Omega_\lambda}_{j_\lambda+1}(\cos \gamma_\lambda)\}]$$

In deriving Eq. 4.29, the use has been made of Eq. A.3 and certain recursion relations between the associated Legendre polynomials.[38]

We now wish to expand Eqs. 4.25 and 4.28 on the matching surface in terms of a set of functions $T^{\nu\lambda}_{v_\lambda j_\lambda \Omega_\lambda}(\zeta, \gamma_\lambda)$ which are ortho-normal and complete on it. (We choose ζ and γ_λ to be the independent variables which scan $\pi_{\nu\lambda}$.) The $T^{\nu\lambda}_{v_\lambda j_\lambda \Omega_\lambda}$ are given by

$$T^{\nu\lambda}_{v_\lambda j_\lambda \Omega_\lambda}(\zeta, \gamma_\lambda) = \phi^{\lambda}_{v_\lambda}(\zeta) D^{\nu\lambda}_{j_\lambda \Omega_\lambda}(\gamma_\lambda) \qquad (4.30)$$

where the $\phi^{\lambda}_{v_\lambda}$'s are identical to those of Eq. 4.25 and the $D^{\nu\lambda}_{j_\lambda \Omega_\lambda}$ are a set of rotational functions which must be orthonormal (with weight function $\sin \gamma_\lambda$) and complete on the domain $0 \le \gamma_\lambda \le \pi/2$. The reason for this choice of the domain of γ_λ is analogous to that used for the coplanar matching in I (Section 5.1). An important consequence of this procedure is that the number of functions $T^{\nu\lambda}_{v_\lambda j_\lambda \Omega_\lambda}$ used to expand the wave function of Eq. 4.25 for each $v_\lambda, \Omega_\lambda$ must be less than the number of vibration rotation basis functions $\phi_{v_\lambda}(\zeta)\mathcal{P}^{\Omega_\lambda}_{j_\lambda}(\cos \gamma_\lambda)$ in that equation. For many reactions, including $H + H_2$, the number of $T^{\nu\lambda}_{v_\lambda j_\lambda \Omega_\lambda}$'s should be half the number of vibration-rotation basis functions and we shall use this number in the discussion below. This

would imply that the number of j_λ's for each $v_\lambda, \Omega_\lambda$ used in the close

coupling expansion must be even. An example of how this might be

done would be to use a complete set of Ω_λ's for each j_λ within a given

vibrational manifold, except for the case $j_\lambda = j_{\lambda_{max}}$. For this case

(as long as $J \geq j_{\lambda_{max}}$) one uses $\Omega_\lambda = j_{\lambda_{max}} - 1, j_{\lambda_{max}} - 3 \ldots -j_{\lambda_{max}} +1$

For $J < j_{\lambda_{max}}$, we use the same procedure and then eliminate

those Ω_λ for which $|\Omega_\lambda| > J$. Other choices are possible but this

particular set of quantum numbers is useful because it leads to an

asymptotic uncoupling of those terms in Eq. 2.31 which are not

diagonal in Ω_λ for $j_\lambda = j_{\lambda_{max}}$ and this allows us to solve for the asymp-

totic behavior of these partially truncated solutions in a simple way.[43]

Whatever the choice, this restriction on the method is seldom a

serious limitation because it only affects the highest rotational state

j_λ for each $v_\lambda, \Omega_\lambda$, and this channel is usually closed in a converged

treatment. An example of a choice which is orthonormal over the

0 to $\pi/2$ range (weighted by $\sin \gamma_\lambda$) is:

$$D_{j_\lambda \Omega_\lambda}^{\nu\lambda}(\gamma_\lambda) = \begin{cases} \sqrt{2}\, \mathcal{P}_{j_\lambda}^{\Omega_\lambda}(\cos \gamma_\lambda) \text{ for } j_\lambda + \Omega_\lambda = \text{odd} \\ \\ 0 \text{ for } j_\lambda + \Omega_\lambda = \text{even} \end{cases} \tag{4.31}$$

This choice is very appropriate for expanding the γ_λ dependent part

of Eq. 4.25 for a collinearly dominated reaction such as $H + H_2$

because these $D_{j_\lambda \Omega_\lambda}^{\nu\lambda}$ vanish at $\gamma_\lambda = \pi/2$ (where the interaction potential

on the matching surface is high and the wave function very small)

and are most effective in representing the wave function near $\gamma_\lambda = 0$.

(where the potential is low). Other choices for the $D_{j_\lambda \Omega_\lambda}^{\nu\lambda}$ may be made in analogy with those discussed for the planar problem in I.

We now expand Eqs. 4.25 and 4.28 in terms of the $T_{v_\lambda j_\lambda \Omega_\lambda}^{\nu\lambda}$, obtaining

$$\Phi_{J\Omega_\lambda}^{\lambda t'_\lambda \pm} = \sum_{v_\lambda j_\lambda} h_{J v_\lambda j_\lambda \Omega_\lambda}^{\lambda t'_\lambda \pm} \, T_{v_\lambda j_\lambda \Omega_\lambda}^{\nu\lambda} (\zeta, \gamma_\lambda) \tag{4.32}$$

$$\Phi'^{\lambda t'_\lambda \pm}_{J\Omega_\lambda} = \sum_{v_\lambda j_\lambda} h'^{\lambda t'_\lambda \pm}_{J v_\lambda j_\lambda \Omega_\lambda} \, T_{v_\lambda j_\lambda \Omega_\lambda}^{\nu\lambda} (\zeta, \gamma_\lambda) \tag{4.33}$$

$$h_{J v_\lambda j_\lambda \Omega_\lambda}^{\lambda t'_\lambda} = \sum_{j''_\lambda} \int_0^{\pi/2} D_{j_\lambda \Omega_\lambda}^{\nu\lambda} (\gamma_\lambda) \mathscr{P}_{j''_\lambda}^{\Omega_\lambda} (\cos \gamma_\lambda) g_{J v_\lambda j''_\lambda \Omega_\lambda}^{\lambda t'_\lambda \pm} (\eta_\lambda(\gamma_\lambda)) \sin \gamma_\lambda \, d\gamma_\lambda \tag{4.34}$$

and

$$h'^{\lambda t'_\lambda \pm}_{J v_\lambda j_\lambda \Omega_\lambda} = \sum_{j''_\lambda} \int_0^{\pi/2} D_{j_\lambda \Omega_\lambda}^{\nu\lambda} (\gamma_\lambda) G'^{\lambda t'_\lambda \pm}_{J v_\lambda j''_\lambda \Omega_\lambda} (\gamma_\lambda) \sin \gamma_\lambda \, d\gamma_\lambda \tag{4.35}$$

where Eq. 4.29 is to be used in evaluating Eq. 4.35. Note that the indices $v_\lambda j_\lambda \Omega_\lambda$ in Eqs. 4.32 - 4.35 can assume only N/2 values (from the discussion above) whereas the indices $v'_\lambda j'_\lambda \Omega'_\lambda$ scan N values. This implies that the matrices $h_{\underset{\approx}{J}}^\lambda$ and $h_{\underset{\approx}{J}}'^\lambda$ have dimensions N/2 x N.

We now consider the expansion of the wave function $\overline{\chi}_{J\Omega_\nu}^{\nu t'_\nu \pm}$ obtained from the integration in arrangement channel region ν on $\pi_{\nu\lambda}$ in a manner analogous to that for $\overline{\chi}_{J\Omega_\lambda}^{\lambda t'_\lambda \pm}$. The expressions for the wave functions are given by Eqs. 4.24 and 4.25 with ν replacing

λ everywhere. To find the normal derivatives, the lower line of Eq. 4.26 is used with the resulting expression given by Eqs. 4.27 and 4.28 where ν is replaced by λ and where the function $G'{}^{\nu t'\nu\pm}_{Jv_\nu j_\nu \Omega_\nu}$ is given by

$$G'{}^{\nu t'\nu\pm}_{Jv_\nu j_\nu \Omega_\nu} = -(-1)^{j_\nu - \Omega_\nu}[\tfrac{1}{2}\mathcal{P}^{\Omega_\nu}_{j_\nu}(\cos\gamma_\lambda)\frac{dg^{\nu t'\nu\pm}_{Jv_\nu j_\nu \Omega_\nu}(\eta_\nu(\gamma_\lambda))}{d\eta_\nu}$$

$$- \cot\alpha_{\nu\lambda}\, g^{\nu t'\nu\pm}_{Jv_\nu j_\nu \Omega_\nu}(\eta_\nu(\gamma_\lambda))\{j_\nu\cos\gamma_\lambda\mathcal{P}^{\Omega_\nu}_{j_\nu}(\cos\gamma_\lambda) \qquad (4.36)$$

$$- [\frac{2j_\nu + 1}{2j_\nu + 3}]^{\frac{1}{2}}[(j_\nu + 1)^2 - \Omega_\nu^2]^{\frac{1}{2}}\mathcal{P}^{\Omega_\nu}_{j_\nu+1}(\cos\gamma_\lambda)\}]$$

Note that Eq. 4.10 has been used in Eq. 4.36 (along with the property $\mathcal{P}^m_j(-x) = (-1)^{j+m}\mathcal{P}^m_j(x)$) to express all quantities in terms of γ_λ. The relation between η_ν and γ_λ on $\pi_{\nu\lambda}$ is obtained from Eqs. 4.12 and 4.13.

The expansions analogous to Eqs. 4.32 and 4.33 are given by

$$\Phi^{\nu t'\nu\pm}_{J\Omega_\nu} = \sum_{v_\nu j_\nu} f^{\nu t'\nu\pm}_{Jv_\nu j_\nu \Omega_\nu}\, T^{\nu\lambda}_{v_\nu j_\nu \Omega_\nu}(\zeta, \gamma_\lambda) \qquad (4.37)$$

$$\Phi'{}^{\nu t'\nu\pm}_{J\Omega_\nu} = \sum_{v_\nu j_\nu} f'{}^{\nu t'\nu\pm}_{Jv_\nu j_\nu \Omega_\nu}\, T^{\nu\lambda}_{v_\nu j_\nu \Omega_\nu}(\zeta, \gamma_\lambda) \qquad (4.38)$$

where

$$f_{Jv_\nu j_\nu \Omega_\nu}^{\nu t'_\nu \pm} = \sum_{j''_\nu} (-1)^{j''_\nu - \Omega_\nu} \int_0^{\pi/2} D_{j_\nu \Omega_\nu}^{\nu \lambda} (\gamma_\lambda) \mathscr{P}_{j''_\nu}^{\Omega_\nu} (\cos \gamma_\lambda)$$

$$\times g_{Jv_\nu j''_\nu \Omega_\nu}^{\nu t'_\nu \pm} (\eta_\nu(\gamma_\lambda)) \sin \gamma_\lambda \, d\gamma_\lambda \tag{4.39}$$

$$f'^{\nu t'_\nu \pm}_{Jv_\nu j_\nu \Omega_\nu} = \sum_{j''_\nu} \int_0^{\pi/2} D_{j_\nu \Omega_\nu}^{\nu \lambda} (\gamma_\lambda) G'^{\nu t'_\nu \pm}_{Jv_\nu j''_\nu \Omega_\nu} (\gamma_\lambda) \sin \gamma_\lambda \, d\gamma_\lambda \tag{4.40}$$

with Eq. 4.36 being used to evaluate Eq. 4.40. All expansions are made in terms of the coordinate γ_λ to facilitate later manipulations.

For atom plus homonuclear diatom collisions, the coefficients $f_{Jj_\lambda v_\lambda \Omega_\lambda}^{\lambda t'_\lambda \pm}$ obtained in the $\pi_{\lambda\kappa}$ matching can be related to the $h_{Jj_\lambda v_\lambda \Omega_\lambda}^{\lambda t'_\lambda \pm}$ of the $\pi_{\nu\lambda}$ matching by noting in Eq. 4.39 (with λ substituted for ν and κ for λ) that $g_{Jv_\lambda j''_\lambda \Omega_\lambda}^{\lambda t'_\lambda \pm} = 0$ [44] for $j''_\lambda - j'_\lambda = $ odd and therefore that $(-1)^{j''_\lambda} = (-1)^{j'_\lambda}$ for the non-vanishing terms. For collisions with a homonuclear diatom, $m_\nu = m_\kappa$ so $\beta_{\lambda\kappa} = \beta_{\nu\lambda}$ (from Eq. 2.4), and the mathematical expressions analogous to Eqs. 4.12 - 4.16 for $\pi_{\lambda\kappa}$ are identical to those equations. Therefore, from Eqs. 4.34 and 4.39 (transformed to $\pi_{\lambda\kappa}$), we have

$$f_{Jv_\lambda j_\lambda \Omega_\lambda}^{\lambda t'_\lambda \pm} = (-1)^{j'_\lambda - \Omega_\lambda} h_{Jv_\lambda j_\lambda \Omega_\lambda}^{\lambda t'_\lambda \pm} \tag{4.41}$$

By similar arguments for the derivative equations, Eqs. 4.35 and 4.40, using Eqs. 4.29 and 4.36, we find

$$f'^{\lambda t'_\lambda \pm}_{Jv_\lambda j_\lambda \Omega_\lambda} = -(-1)^{j'_\lambda - \Omega_\lambda} h'^{\lambda t'_\lambda \pm}_{Jv_\lambda j_\lambda \Omega_\lambda} \tag{4.42}$$

4.3 The Matching Equations

We now wish to find the appropriate linear combinations of the $\overline{\chi}$'s and $\dfrac{\partial \overline{\chi}}{\partial n_{\nu\lambda}}$'s of Eqs. 4.24 and 4.27 in channels λ and ν which give smoothly matched solutions χ and $\dfrac{\partial \chi}{\partial n_{\nu\lambda}}$ satisfying Eq. 4.20 and its normal derivative on $\pi_{\nu\lambda}$. Accordingly, we write

$$\chi_{\lambda J\Omega_\lambda}^{(i)t} = \sum_{t'_\lambda} \{ \overline{\chi}_{J\Omega_\lambda}^{\lambda t'_\lambda +} C_{J\lambda t'_\lambda}^{(i)t+} + \overline{\chi}_{J\Omega_\lambda}^{\lambda t'_\lambda -} C_{J\lambda t'_\lambda}^{(i)t-} \} \tag{4.43}$$

where the coefficients $C_{J\lambda}$ in Eq. 4.43 are to be determined by evaluating Eq. 4.20 and its normal derivative on $\pi_{\nu\lambda}$, and analogous equations on $\pi_{\kappa\nu}$ and $\pi_{\lambda\kappa}$. The indices $(i)t \equiv (i)vj\Omega$ denote different linearly independent matched solutions, with t assuming N values and $i = 1, 2$ or 3 for a total of $3N$ solutions. This is equal to the number of linearly independent scattering solutions possible as was discussed in I (Section 5.2). The normal derivative of Eq. 4.43 is:

$$\frac{\partial \chi_{\lambda J\Omega_\lambda}^{(i)t}}{\partial n_{\nu\lambda}} = \sum_{t'_\lambda} \{ \frac{\partial \overline{\chi}_{J\Omega_\lambda}^{\lambda t'_\lambda +}}{\partial n_{\nu\lambda}} C_{J\lambda t'_\lambda}^{(i)t+} + \frac{\partial \overline{\chi}_{J\Omega_\lambda}^{\lambda t'_\lambda -}}{\partial n_{\nu\lambda}} C_{J\lambda t'_\lambda}^{(i)t-} \} \tag{4.44}$$

The normal derivative of Eq. 4.20 is in general a complicated quantity, but for the particular choice of matching surface specified by Eq. 2.5a, we have the important relation[19]

$$\left(\frac{\partial \Delta_{\nu\lambda}}{\partial n_{\nu\lambda}} \right)_{\text{on } \pi_{\nu\lambda}} = 0 \tag{4.45}$$

which implies

$$\frac{\partial \chi_{\lambda J\Omega_\lambda}^{(i)t}}{\partial n_{\nu\lambda}} = \sum_{\Omega_\nu} d_{\Omega_\nu \Omega_\lambda}^{J}(\Delta_{\nu\lambda}) \frac{\partial \chi_{\nu J\Omega_\nu}^{(i)t}}{\partial n_{\nu\lambda}} \qquad (4.46)$$

Let us now substitute Eqs. 4.43 and its counterpart for channel ν into Eq. 4.20, as well as 4.44 and its ν counterpart into 4.46; utilizing Eqs. 4.24 and 4.27 (and their ν counterparts) along with Eq. 4.12. We obtain

$$\sum_{t'_\lambda} \{ \Phi_{J\Omega_\lambda}^{\lambda t'_\lambda +} C_{J\lambda t'_\lambda}^{(i)t+} + \Psi_{J\Omega_\lambda}^{\lambda t'_\lambda -} C_{J\lambda t'_\lambda}^{(i)t-} \} = \sum_{\Omega_\nu} d_{\Omega_\nu \Omega_\lambda}^{J}(\Delta_{\nu\lambda})$$

$$\times \sum_{t'_\nu} \{ \Phi_{J\Omega_\nu}^{\nu t'_\nu +} C_{J\nu t'_\nu}^{(i)t+} + \Phi_{J\Omega_\nu}^{\nu t'_\nu -} C_{J\nu t'_\nu}^{(i)t-} \} \qquad (4.47)$$

with a similar equation involving Φ' resulting from the matching of the normal derivatives. If we now substitute Eqs. 4.32, 4.33, 4.37 and 4.38 into Eq. 4.47 and its equivalent for the derivatives, then multiply by the $T_{v_\lambda j_\lambda \Omega_\lambda}^{\nu\lambda}$ (defined by Eq. 4.30) and integrate using the orthonormality properties of the $T^{\nu\lambda}$, we obtain:

$$\sum_{t'_\lambda} \{ h_{Jv_\lambda j_\lambda \Omega_\lambda}^{\lambda t'_\lambda +} C_{\lambda J t'_\lambda}^{(i)t+} + h_{Jv_\lambda j_\lambda \Omega_\lambda}^{\lambda t'_\lambda -} C_{\lambda J t'_\lambda}^{(i)t-} \} = \sum_{v_\nu j_\nu \Omega_\nu} (s_{\nu\lambda}^{J})_{v_\lambda j_\lambda \Omega_\lambda}^{v_\nu j_\nu \Omega_\nu}$$

$$\times \sum_{t'_\nu} \{ f_{Jv_\nu j_\nu \Omega_\nu}^{\nu t'_\nu +} C_{\nu J t'_\nu}^{(i)t+} + f_{Jv_\nu j_\nu \Omega_\nu}^{\nu t'_\nu -} C_{\nu J t_\nu}^{(i)t-} \} \qquad (4.48)$$

The derivative equation is analogous with h' and f' substituted for h and f above. The quantity $(s_{\nu\lambda}^{J})_{v_\lambda j_\lambda \Omega_\lambda}^{v_\nu j_\nu \Omega_\nu}$ is defined as

$$(s_{\nu\lambda}^{J})_{v_\lambda j_\lambda \Omega_\lambda}^{v_\nu j_\nu \Omega_\nu} = S_{v_\lambda v_\nu}^{\nu\lambda} \int_0^{\pi/2} D_{j_\lambda \Omega_\lambda}^{\nu\lambda} (\gamma_\lambda) \, d_{\Omega_\nu \Omega_\lambda}^{J} (\Delta_{\nu\lambda}(\gamma_\lambda))$$

$$\times \, D_{j_\nu \Omega_\nu}^{\nu\lambda} (\gamma_\lambda) \sin \gamma_\lambda \, d\gamma_\lambda$$

(4.49)

where

$$S_{v_\lambda v_\nu}^{\nu\lambda} = \int_0^\infty \phi_{v_\lambda}^{\lambda} (\zeta) \, \phi_{v_\nu}^{\nu} (\zeta) \, d\zeta$$

(4.50)

If we regard $\underset{\approx}{s}_{\nu\lambda}^{J}$ as a matrix and use the Davydov definition of $d_{\Omega_\nu \Omega_\lambda}^{J}$,[33] then provided that the $T_{v_\lambda j_\lambda \Omega_\lambda}^{\nu\lambda}$ form a complete set of functions, we can rewrite $\underset{\approx}{s}_{\nu\lambda}^{J}$ as

$$\underset{\approx}{s}_{\nu\lambda}^{J} = \exp (i \underset{\approx}{\Delta}_{\nu\lambda}^{J})$$

(4.51)

where

$$(\Delta_{\nu\lambda}^{J})_{v_\lambda j_\lambda \Omega_\lambda}^{v_\nu j_\nu \Omega_\nu} = \langle j_\lambda \Omega_\lambda | \Delta_{\nu\lambda} | j_\nu \Omega_\nu \rangle \langle J\Omega_\lambda | J_y | J\Omega_\nu \rangle$$

(4.52)

From Eq. 4.51 it is immediately obvious that $\underset{\approx}{s}_{\nu\lambda}^{J}$ is unitary if the T are complete, and since the $d_{\Omega_\nu \Omega_\lambda}^{J}$ are real, Eq. 4.49 indicates that $\underset{\approx}{s}_{\nu\lambda}^{J}$ is orthogonal. Let us now write Eq. 4.48 as a matrix equation by regarding the h, f and C appearing there as the elements of matrices, obtaining

$$\underset{\approx}{h}_{J}^{\lambda+} \underset{\approx}{C}_{\lambda J}^{(i)+} + \underset{\approx}{h}_{J}^{\lambda-} \underset{\approx}{C}_{\lambda J}^{(i)-} = \underset{\approx}{s}_{\nu\lambda}^{J} \{ \underset{\approx}{f}_{J}^{\nu+} \underset{\approx}{C}_{\nu J}^{(i)+} + \underset{\approx}{f}_{J}^{\nu-} \underset{\approx}{C}_{\nu J}^{(i)-} \}$$

(4.53)

According to the arguments of the previous section, the matrices $\underset{\approx}{h}_{J}^{\lambda\pm}$ and $\underset{\approx}{f}_{J}^{\nu\pm}$ should be of dimension N/2 x N while $\underset{\approx}{s}_{\nu\lambda}^{J}$ should be

N/2 x N/2 and the C's are N x N matrices. The corresponding derivative equation is obtained from Eq. 4.53 by substituting h' and f' for h and f. We can combine function and derivative equations into a single matrix equation involving only N x N matrices by defining the augmented N x N matrices $\hat{\underset{\approx}{h}}_J^{\lambda\pm}$, $\hat{\underset{\approx}{f}}_J^{\nu\pm}$ and $\hat{\underset{\approx}{s}}_{\nu\lambda}^J$ as

$$\hat{\underset{\approx}{h}}_J^{\lambda\pm} = \begin{pmatrix} \underset{\approx}{h}_J^{\lambda\pm} \\ \\ \underset{\approx}{h}_J'^{\lambda\pm} \end{pmatrix} \tag{4.54}$$

$$\hat{\underset{\approx}{f}}_J^{\nu\pm} = \begin{pmatrix} \underset{\approx}{f}_J^{\nu\pm} \\ \\ \underset{\approx}{f}_J'^{\nu\pm} \end{pmatrix} \tag{4.55}$$

$$\hat{\underset{\approx}{s}}_{\nu\lambda}^J = \begin{pmatrix} \underset{\approx}{s}_{\nu\lambda}^J & \underset{\approx}{0} \\ \\ \underset{\approx}{0} & \underset{\approx}{s}_{\nu\lambda}^J \end{pmatrix} \tag{4.56}$$

where $\underset{\approx}{0}$ is an N/2 x N/2 matrix of zeros. The resulting matching equation for $\pi_{\nu\lambda}$ is

$$\hat{\underset{\approx}{h}}_J^{\lambda+} \underset{\approx}{C}_{\lambda J}^{(i)+} + \hat{\underset{\approx}{h}}_J^{\lambda-} \underset{\approx}{C}_{\lambda J}^{(i)-} = \hat{\underset{\approx}{s}}_{\nu\lambda}^J \{ \hat{\underset{\approx}{f}}_J^{\nu+} \underset{\approx}{C}_{\nu J}^{(i)+} + \hat{\underset{\approx}{f}}_J^{\nu-} \underset{\approx}{C}_{\nu J}^{(i)-} \} \tag{4.57}$$

Following the same arguments as were used in I (Section 5.2), we now combine Eq. 4.57 and its counterparts for $\pi_{\kappa\nu}$ and $\pi_{\lambda\kappa}$ into a single 3N x 3N equation which can then be solved for the coefficients $\underset{\approx}{C}_J^{\pm}$ which determine the matched solutions. The final result is

$$\underset{\approx}{C}_J^+ (\underset{\approx}{C}_J^-)^{-1} = - (\underset{\approx}{N}_J^+)^{-1} \underset{\approx}{N}_J^- \tag{4.58}$$

where

$$\underset{\sim}{N}_J^{\pm} = \begin{pmatrix} \hat{\underset{\sim}{h}}_J^{\lambda\pm} & -\hat{\underset{\sim}{s}}_{\nu\lambda}^J\,\hat{\underset{\sim}{f}}_J^{\nu\pm} & \underset{\hat{}}{0} \\ \underset{\hat{}}{0} & \hat{\underset{\sim}{h}}_J^{\nu\pm} & -\hat{\underset{\sim}{s}}_{\kappa\nu}^J\,\hat{\underset{\sim}{f}}_J^{\kappa\pm} \\ -\hat{\underset{\sim}{s}}_{\lambda\kappa}^J\,\hat{\underset{\sim}{f}}_J^{\lambda\pm} & \underset{\hat{}}{0} & \hat{\underset{\sim}{h}}_J^{\kappa\pm} \end{pmatrix} \qquad (4.59)$$

and

$$\underset{\sim}{C}_J^{\pm} = \begin{pmatrix} \underset{\sim\lambda J}{C}^{1\pm} & \underset{\sim\lambda J}{C}^{2\pm} & \underset{\sim\lambda J}{C}^{3\pm} \\ \underset{\sim\nu J}{C}^{1\pm} & \underset{\sim\nu J}{C}^{2\pm} & \underset{\sim\nu J}{C}^{3\pm} \\ \underset{\sim\kappa J}{C}^{1\pm} & \underset{\sim\kappa J}{C}^{2\pm} & \underset{\sim\kappa J}{C}^{3\pm} \end{pmatrix} \qquad (4.60)$$

$\underset{\hat{}}{0}$ here represents an N x N matrix of zeros.

Eq. 4.58 can now be used in conjunction with the asymptotic analysis of the next section to determine the 3N x 3N coefficient matrices $\underset{\sim}{C}_J^{\pm}$ which will provide wave functions which are both smooth and continuous everywhere and which also satisfy the proper scattering boundary conditions. Note that our procedure for matching simultaneously combines the primitive solutions in channels λ, ν and κ to yield solutions which are smoothly continuous throughout all of configuration space. This contrasts with the analogous procedures of Wyatt and coworkers[16] and of Light and coworkers[15] which seem not to include the coupling between channels ν and κ (here represented by the $\pi_{\kappa\nu}$ matching equation) explicitly when dealing with collisions originating in channel λ. They may have included such coupling implicitly by utilizing the symmetry of the H_3 system. However, if A_ν and A_κ are different atoms we believe that the $\nu-\kappa$ coupling must be included explicitly.

5. ASYMPTOTIC ANALYSIS

5.1 The Reactance and Scattering Matrices

In this section we define the reactance and scattering solutions and relate these to the matched solutions of the previous section so as to complete the determination of the coefficient matrices $\underset{\approx}{C}_J^{\pm}$ and also the reactance and scattering matrices $\underset{\approx}{R}_J$ and $\underset{\approx}{S}_J$. In I we proved that the R and S matrices (which are physically dimensionless) can be equivalently defined in the scaled variables $\hat{r}_\lambda$, $\hat{R}_\lambda$ or in the "physical" ones $\bar{r}_\lambda$, $\bar{R}_\lambda$. Here, for simplicity, we use the scaled coordinates in all definitions except that of the scattering amplitudes (Section 5.2).

If we use Eqs. 2.13, 2.18, 2.30 and 3.3 to express the matched asymptotic wave function (of Eqs. 4.17, 4.18 and 4.43) in each arrangement channel, we find

$$\Psi_{JM}^{(i)t} \sim \sum_\lambda \sum_{t_\lambda} D_{M\Omega_\lambda}^J (\phi_\lambda, \theta_\lambda, 0)\, Y_{j_\lambda \Omega_\lambda} (\gamma_\lambda, \psi_\lambda)$$

$$\frac{\phi_{v_\lambda j_\lambda}(r_\lambda)}{r_\lambda R_\lambda}\; e_{\lambda J t_\lambda}^{(i)t} (R_\lambda) \tag{5.1}$$

where

$$e_{\lambda J t_\lambda}^{(i)t} = \sum_{t_\lambda'} \{ g_{J t_\lambda}^{\lambda t_\lambda' +}\, C_{\lambda J t_\lambda'}^{(i)t+} + g_{J t_\lambda}^{\lambda t_\lambda' -}\, C_{\lambda J t_\lambda'}^{(i)t-} \} \tag{5.2}$$

Here we have dropped the superscript (a) as it will be implicit throughout Section 5. The sum over arrangement channels serves as a convenient notation for expressing the asymptotic wavefunction in all three arrangement channels simultaneously and is made possible by the fact that asymptotically there is no overlap between the separated atom plus diatom wavefunctions in different arrangement channels. An equation analogous to Eq. 5.1 for the derivative

$$\frac{1}{R_\lambda} \frac{\partial}{\partial R_\lambda} R_\lambda \, \Psi_{JM}^{(i)t} \quad \text{can be obtained by replacing} \quad g_{Jt_\lambda}^{\lambda t'_\lambda \pm} \quad \text{by}$$

$$\frac{dg_{Jt_\lambda}^{\lambda t'_\lambda \pm}}{dR_\lambda} \quad \text{in Eq. 5.2.}$$

The reactance and scattering body-fixed solutions are defined to have the asymptotic form

$$\Psi_{JM}^{\lambda' t'_\lambda} [R \text{ or } S] \underset{R_\alpha, R_\beta, R_\gamma \to \infty}{\sim} \sum_\lambda \sum_{t_\lambda} D_{M\Omega_\lambda}^{J} (\phi_\lambda, \theta_\lambda, 0) Y_{j_\lambda \Omega_\lambda} (\gamma_\lambda, \psi_\lambda)$$

$$\times \frac{\phi_{v_\lambda j_\lambda}^\lambda (r_\lambda)}{r_\lambda R_\lambda} b_{\lambda J t_\lambda}^{\lambda' t'_\lambda} [R \text{ or } S] \tag{5.3}$$

where, in the far asymptotic region (in which both potential coupling and the centrifugal coupling of Eq. 3.6 have become negligible), for the R solution,

$$
b_{\lambda J t_\lambda}^{\lambda' t_\lambda'}[R] = \left(\left| V_{v_\lambda j_\lambda}^{\lambda} \right|\right)^{-\frac{1}{2}}
\begin{cases}
\sin\left(k_{v_\lambda j_\lambda}^{\lambda} R_\lambda - (J+j_\lambda)\frac{\pi}{2}\right)\delta_{\lambda t_\lambda}^{\lambda' t_\lambda'} \\[2mm]
\quad + \cos\left(k_{v_\lambda j_\lambda}^{\lambda} R_\lambda - (J+j_\lambda)\frac{\pi}{2}\right) R_{J\lambda' v_\lambda' j_\lambda' -\Omega_\lambda'}^{\lambda v_\lambda j_\lambda \Omega_\lambda} \\[2mm]
\qquad\qquad\qquad\qquad\qquad \text{(open channels)} \\[3mm]
e^{\left|k_{v_\lambda j_\lambda}^{\lambda}\right|R_\lambda}\delta_{\lambda t_\lambda}^{\lambda' t_\lambda'} - e^{-\left|k_{v_\lambda j_\lambda}^{\lambda}\right|R_\lambda} R_{J\lambda' v_\lambda' j_\lambda' -\Omega_\lambda'}^{\lambda v_\lambda j_\lambda \Omega_\lambda} \\[2mm]
\qquad\qquad\qquad\qquad\qquad \text{(closed channels)} \quad (5.4)
\end{cases}
$$

and, for the S solution[32]

$$
b_{\lambda J t_\lambda}^{\lambda' t_\lambda'}[S] = \left(\left| V_{v_\lambda j_\lambda}^{\lambda} \right|\right)^{-\frac{1}{2}}
\begin{cases}
e^{-i\left(k_{v_\lambda j_\lambda}^{\lambda} R_\lambda - (J+j_\lambda)\frac{\pi}{2}\right)}\delta_{\lambda t_\lambda}^{\lambda' t_\lambda'} \\[2mm]
\quad - e^{i\left(k_{v_\lambda j_\lambda}^{\lambda} R_\lambda - (J+j_\lambda)\frac{\pi}{2}\right)} S_{J\lambda' v_\lambda' j_\lambda' -\Omega_\lambda'}^{\lambda v_\lambda j_\lambda \Omega_\lambda} \\[2mm]
\qquad\qquad\qquad\qquad\qquad \text{(open channels)} \\[3mm]
e^{\left|k_{v_\lambda j_\lambda}^{\lambda}\right|R_\lambda}\delta_{\lambda t_\lambda}^{\lambda' t_\lambda'} - e^{-\left|k_{v_\lambda j_\lambda}^{\lambda}\right|R_\lambda} S_{J\lambda' v_\lambda' j_\lambda' -\Omega_\lambda'}^{\lambda v_\lambda j_\lambda \Omega_\lambda} \\[2mm]
\qquad\qquad\qquad\qquad\qquad \text{(closed channels)} \quad (5.5)
\end{cases}
$$

$V_{v_\lambda j_\lambda}^{\lambda}$ is the velocity (in scaled variables)

$$
V_{v_\lambda j_\lambda}^{\lambda} = \hbar k_{v_\lambda j_\lambda}^{\lambda}/\mu \qquad\qquad\qquad (5.6)
$$

and the primed variables $v'_\lambda j'_\lambda \Omega'_\lambda$ in Eqs. 5.4 and 5.5 define the reagent state in the λ' arrangement channel. (Note our use of the abbreviation $\lambda' t'_\lambda \equiv \lambda' t'_{\lambda'}$.) $\underset{\approx}{R}_J$ and $\underset{\approx}{S}_J$ are the partial wave reactance and scattering matrices and, for exact solutions of the Schrödinger equation, they are symmetric.[45]

Note that $-\Omega'_\lambda$ rather than Ω'_λ appears in the definition of $\underset{\approx}{R}_J$ and $\underset{\approx}{S}_J$. This choice allows the open channel part of the scattering matrix to become the identity matrix in the limit of zero interaction potential (as will be evident from the partial wave expression for the scattering amplitude in Section 5.2). The phase factors $i^{\pm(J+j_\lambda)}$ appearing in Eqs. 5.4 and 5.5 are arbitrary but will prove convenient later on. The open channel sub-blocks of $\underset{\approx}{R}_J$ and $\underset{\approx}{S}_J$ are labelled $\underset{\approx}{R}^0_J$ and $\underset{\approx}{S}^0_J$, and from Eqs. 5.4 and 5.5, one can easily show[46] that

$$\underset{\approx}{S}^0_J = (\underset{\approx}{I} + i\underset{\approx}{R}^0_J)\,(\underset{\approx}{I} - i\underset{\approx}{R}^0_J)^{-1} \qquad (5.7)$$

where $\underset{\approx}{I}$ is the identity matrix. In addition to being symmetric, $\underset{\approx}{R}^0_J$ is real and $\underset{\approx}{S}^0_J$ is unitary. From the unitarity of $\underset{\approx}{S}^0_J$ one can prove flux conservation and from its symmetry, microscopic reversibility results.[45]

In an actual calculation, we wish to use the R and S solutions of the Schrödinger equation at a finite R_λ for which the potential coupling has become negligible but the centrifugal coupling in Eq. 3.6 has not. These solutions can be obtained by taking the appropriate linear combinations of space-fixed Bessel functions which appeared in Eq. 3.9 so that the far asymptotic behavior in Eqs. 5.3

and 5.4 is obtained in that limit. In other words, as soon as potential coupling has become negligible (but not the centrifugal one) the b in Eq. 5.3 can be written according to Eq. 3.9 as

$$b_{\lambda J t_\lambda}^{\lambda' t'_\lambda}[R] = (|V_{v_\lambda j_\lambda}^{\lambda}|)^{-\frac{1}{2}} \sum_{\lambda'' t''_\lambda} \{ I_{J\lambda t_\lambda}^{\lambda'' t''_\lambda}[R] \, \delta_{\chi'' t''_\lambda}^{\lambda' t'_\lambda} + O_{J\lambda t_\lambda}^{\lambda'' t''_\lambda}[R] \, R_{J\lambda' v'_\lambda j'_\lambda -\Omega'_\lambda}^{\lambda'' t''_\lambda} \}$$

$$(5.8)$$

$$b_{\lambda J t_\lambda}^{\lambda' t'_\lambda}[S] = (|V_{v_\lambda j_\lambda}^{\lambda}|)^{-\frac{1}{2}} \sum_{\lambda'' t''_\lambda} \{ I_{J\lambda t_\lambda}^{\lambda'' t''_\lambda}[S] \, \delta_{\chi'' t''_\lambda}^{\lambda' t'_\lambda} - O_{J\lambda t_\lambda}^{\lambda'' t''_\lambda}[S] \, S_{J\lambda' v'_\lambda j'_\lambda -\Omega'_\lambda}^{\lambda'' t''_\lambda} \}$$

$$(5.9)$$

where, for both R and S matrix solutions,

$$\binom{I}{O}_{\lambda t_\lambda}^{\lambda' t'_\lambda} = \delta_{\lambda v_\lambda j_\lambda}^{\lambda' v'_\lambda j'_\lambda} (-1)^{\Omega'_\lambda - \Omega_\lambda} \sum_{\ell_\lambda} C(J j_\lambda \ell_\lambda ; \Omega'_\lambda, -\Omega'_\lambda, 0)$$

$$\times C(J j_\lambda \ell_\lambda ; \Omega_\lambda, -\Omega_\lambda, 0) \binom{\mathcal{I}_{J v_\lambda j_\lambda \ell_\lambda}}{\mathcal{O}_{J v_\lambda j_\lambda \ell_\lambda}}$$

$$(5.10)$$

For the R solution,

$$\mathcal{I}_{Jv_\lambda j_\lambda \ell_\lambda}[R] = |k^\lambda_{v_\lambda j_\lambda}| R_\lambda \begin{cases} y_{\ell_\lambda}(k^\lambda_{v_\lambda j_\lambda} R_\lambda) \sin(J + j_\lambda - \ell_\lambda)\frac{\pi}{2} \\ \\ + j_{\ell_\lambda}(k^\lambda_{v_\lambda j_\lambda} R_\lambda) \cos(J + j_\lambda - \ell_\lambda)\frac{\pi}{2} \\ \\ \qquad \text{(open channels)} \\ \\ 2 i_{\ell_\lambda}(|k^\lambda_{v_\lambda j_\lambda}| R_\lambda) \\ \\ \qquad \text{(closed channels)} \end{cases}$$

$$(5.11a)$$

$$\mathcal{O}_{Jv_\lambda j_\lambda \ell_\lambda}[R] = |k^\lambda_{v_\lambda j_\lambda}| R_\lambda \begin{cases} - y_{\ell_\lambda}(k^\lambda_{v_\lambda j_\lambda} R_\lambda) \cos(J + j_\lambda - \ell_\lambda)\frac{\pi}{2} \\ \\ + j_{\ell_\lambda}(k^\lambda_{v_\lambda j_\lambda} R_\lambda) \sin(J + j_\lambda - \ell_\lambda)\frac{\pi}{2} \\ \\ \qquad \text{(open channels)} \\ \\ k_{\ell_\lambda}(|k^\lambda_{v_\lambda j_\lambda}| R_\lambda) \\ \\ \qquad \text{(closed channels)} \end{cases}$$

$$(5.11b)$$

while, for the S solution,

$$\mathcal{I}_{Jv_\lambda j_\lambda \ell_\lambda}[S] = |k^\lambda_{v_\lambda j_\lambda}| R_\lambda \begin{cases} e^{i(J + j_\lambda - \ell_\lambda)\frac{\pi}{2}} \, h^{(-)}_{\ell_\lambda}(k^\lambda_{v_\lambda j_\lambda} R_\lambda) \\ \\ \qquad \text{(open channels)} \\ \\ 2 i_{\ell_\lambda}(|k^\lambda_{v_\lambda j_\lambda}| R_\lambda \\ \\ \qquad \text{(closed channels)} \end{cases}$$

$$(5.12a)$$

$$\mathcal{O}_{Jv_\lambda j_\lambda \ell_\lambda}[S] = |k^\lambda_{v_\lambda j_\lambda}| R_\lambda \begin{cases} e^{-i(J+j_\lambda-\ell_\lambda)\frac{\pi}{2}} h^{(+)}_{\ell_\lambda}(k^\lambda_{v_\lambda j_\lambda} R_\lambda) \\ \qquad\qquad \cdot \quad \text{(open channels)} \\ k_{\ell_\lambda}(|k^\lambda_{v_\lambda j_\lambda}| R_\lambda) \\ \qquad\qquad \cdot \quad \text{(closed channels)} \end{cases}$$

(5.12b)

where

$$h^{(\pm)}_{\ell_\lambda} = -y_{\ell_\lambda} \pm ij_{\ell_\lambda}$$

(5.13)

where y_{ℓ_λ}, j_{ℓ_λ}, i_{ℓ_λ} and k_{ℓ_λ} are the spherical Bessel functions

introduced in Section 3.2.1. To show that Eqs. 5.8 and 5.9 do indeed

reduce respectively to Eqs. 5.4 and 5.5 in the far asymptotic limit,

one simply uses Eqs. 3.10 and 3.11. We may use Eq. A.14 to

relate the usual space-fixed S matrix $\hat{\underset{\approx}{S}}_J$ to the body-fixed $\underset{\approx}{S}_J$.

We obtain the R_λ independent unitary transformation

$$\hat{\underset{\approx}{S}}_J = \underset{\approx}{T}^\dagger \underset{\approx}{S}_J \underset{\approx}{T}$$

(5.14)

where

$$(\underset{\approx}{T})^{\lambda' v'_\lambda j'_\lambda \ell'_\lambda}_{\lambda v_\lambda j_\lambda \Omega_\lambda} = \delta^{\lambda' v'_\lambda j'_\lambda}_{\lambda v_\lambda j_\lambda} C(Jj_\lambda \ell'_\lambda|\Omega_\lambda, -\Omega_\lambda, 0) i^{\ell'_\lambda - j_\lambda}(-1)^{\Omega_\lambda}$$

(5.15)

In order to obtain $\underset{\approx}{R}_J$, we generate an R solution of the

Schrödinger equation satisfying the asymptotic conditions of Eqs. 5.3

or 5.8 by taking linear combinations of the matched solutions in Eq. 5.1:

$$\Psi_{JM}^{\lambda't'_\lambda}[R] = \sum_{(i)t} \Psi_{JM}^{(i)t} Q_{(i)t}^{J\lambda't'_\lambda} \tag{5.16}$$

As in I, we are free to choose $Q_{(i)t}^{\lambda't'_\lambda} = \delta_{(i)t}^{\lambda't'_\lambda}$ and require the $\underset{\approx J}{C^{\pm}}$ matrices to provide for us those linear combinations of the primitive solutions satisfying both the matching condition (Eq. 4.58) and the asymptotic conditions. If we substitute Eqs. 5.1, 5.2, 5.3 and 5.8 into Eq. 5.16 and express everything in matrix notation (involving matrices of dimension $3N \times 3N$), we get

$$\underset{\approx}{V^{-\frac{1}{2}}} (\underset{\approx J}{I_J}[R] + \underset{\approx J}{O_J}[R]\ \overline{R}_J)\ (\underset{\approx J}{C^-_J})^{-1} = \underset{\approx J}{g^+_J}\ \underset{\approx J}{C^+_J}\ (\underset{\approx J}{C^-_J})^{-1} + \underset{\approx J}{g^-_J} \tag{5.17}$$

where $\underset{\approx J}{\overline{R}_J}$ is related to $\underset{\approx J}{R_J}$ of Eq. 5.8 by

$$(\underset{\approx J}{\overline{R}_J})^{\lambda'v'_\lambda j'_\lambda \Omega'_\lambda}_{\lambda v_\lambda j_\lambda \Omega_\lambda} = (R_J)^{\lambda v_\lambda j_\lambda \Omega_\lambda}_{\lambda'v'_\lambda j'_\lambda -\Omega'_\lambda} \tag{5.18}$$

and

$$(\underset{\approx}{V})^{\lambda't'_\lambda}_{\lambda t_\lambda} = |V^\lambda_{v_\lambda j_\lambda}|\ \delta^{\lambda't'_\lambda}_{\lambda t_\lambda} \tag{5.19}$$

Note that $(\underset{\approx J}{g_J})^{\lambda't'_\lambda \pm}_{\lambda t_\lambda}$ in Eq. 5.17 is identical to $\delta_{\lambda\lambda'}$ times $g^{\lambda t'_\lambda \pm}_{Jt_\lambda}$ in Eq. 5.2. An equation analogous to Eq. 5.17 for the derivative

$$R_\lambda^{-1} \frac{\partial}{\partial R_\lambda} R_\lambda \Psi_{JM}^{\lambda' t_\lambda'} \quad \text{is easily shown to be}$$

$$V^{-\frac{1}{2}} (I_J'[R] + O_J'[R] \bar{R}_J) (C_J^-)^{-1} = g_J'^+ C_J^+ (C_J^-)^{-1} + g_J'^-$$

(5.20)

where prime denotes differentiation with respect to R_λ. The quantity $C_J^+ (C_J^-)^{-1}$ is given by Eq. 4.58. Equations 5.17, 5.20 provide therefore two simultaneous linear matrix equations for the two unknown matrices $(C_J^-)^{-1}$ and $\bar{R}_J$. Eliminating the former from these two equations and using Eq. 4.58, we get:

$$\bar{R}_J = -V^{\frac{1}{2}} W^{-1} \{ (I_J'[R] g_J^+ - I_J[R] g_J'^+) (N_J^+)^{-1} N_J^-$$

$$- (I_J'[R] g_J^- - I_J[R] g_J'^-) \} \{ (O_J'[R] g_J^+ - O_J[R] g_J'^+) (N_J^+)^{-1} N_J^-$$

$$- (O_J'[R] g_J^- - O_J[R] g_J'^-) \}^{-1} W V^{-\frac{1}{2}}$$

(5.21)

Here

$$W = O_J'[R] I_J[R] - I_J'[R] O_J[R]$$

(5.22)

is a Wronskian matrix which, as can be seen by inspection of Eqs. 5.10 and 5.11, is diagonal and independent of R_λ. The right-hand side of Eq. 5.21 involves real matrices which are obtained directly from the integration and matching steps of the calculation. Therefore, $\bar{R}_J$ and R_J are real.

With $\underset{\approx}{R}_J$ and hence $\underset{\approx}{R}^0_J$ determined, we use Eq. 5.7 to calculate $\underset{\approx}{S}^0_J$, which in turn can be related to the scattering amplitude by the formulas of the next section. In addition, the scattering matrix is related to the probability of transition from initial arrangement channel λ' and quantum state $v'_\lambda j'_\lambda \Omega'_\lambda$ to final channel λ and state $v_\lambda j_\lambda \Omega_\lambda$ by[47]

$$P^{\lambda v_\lambda j_\lambda \Omega_\lambda}_{J \lambda' v'_\lambda j'_\lambda \Omega'_\lambda} = \left| S^0 {}^{\lambda v_\lambda j_\lambda \Omega_\lambda}_{J\lambda' v'_\lambda j'_\lambda \Omega'_\lambda} \right|^2 \tag{5.23}$$

The scattering matrix may also be related to the opacity function as discussed in the next section.

5.2. Scattering Amplitudes and Cross Sections

We now define the scattered plane wave solution and relate it to the scattering solution of the previous section so as to express the scattering amplitude in terms of the open parts of the partial wave scattering matrices. Our analysis will be done using the helicity representation[48] in which the axis of quantization of the incoming and outgoing rotational states is chosen to coincide with the direction of the incident and final wave vectors respectively. The helicity formalism is very closely related to the use of body-fixed coordinate systems of the type described in Section 2.2 and leads to a particularly simple relation between the helicity scattering amplitudes and body-fixed S matrices.

We define the helicity representation scattered plane wave solution by

$$\bar{\Psi}^{\lambda' \hat{t}_\lambda}[P] \sim e^{i\bar{k}^{\lambda'}_{v'_\lambda j'_\lambda}(\bar{R}_{\lambda'})_z} \frac{\bar{\phi}^{\lambda'}_{v'_\lambda j'_\lambda}(\bar{r}_{\lambda'})}{\bar{r}_{\lambda'}} Y_{j'_\lambda m'_{j_\lambda}}(\theta_{r_{\lambda'}}, \phi_{r_{\lambda'}})$$

$$+ \sum_{\lambda \hat{t}_\lambda} \frac{e^{i\bar{k}^\lambda_{v_\lambda j_\lambda}\bar{R}_\lambda}}{\bar{R}_\lambda} \frac{\bar{\phi}^\lambda_{v_\lambda j_\lambda}(\bar{r}_\lambda)}{\bar{r}_\lambda} \cdot Y_{j_\lambda m_{j_\lambda}}(\gamma_\lambda, \psi_\lambda) f^{\lambda \hat{t}_\lambda}_{\lambda' \hat{t}'_\lambda}(\theta_\lambda, \phi_\lambda)$$

(5.24)

where the sum over final states includes both open and closed channels. For closed channel solutions (which we shall ignore below), $\bar{k}_{v_\lambda j_\lambda}$ is pure imaginary so $\exp(i\bar{k}_{v_\lambda j_\lambda}\bar{R}_\lambda)$ decreases exponentially. Note that the physical coordinates $\bar{R}_\lambda, \bar{r}_\lambda$ and wave vectors $\bar{k}_{v_\lambda j_\lambda} = a_\lambda k_{v_\lambda j_\lambda}$ have been used in Eq. 5.24. In addition, we have introduced the global index $\hat{t}$ to denote the quantum numbers vjm_j. (We will relate m_j to Ω and hence $\hat{t}$ to t below). For simplicity the space-fixed z axis has been chosen to be in the direction of the incident wave vector. It then follows (by inspection of Fig. 3) that the space-fixed and body-fixed z axes will point in opposite directions initially (i.e., for $(\bar{R}_{\lambda'})_z \rightarrow -\infty$). The outgoing body-fixed z'_λ axis points in the same direction as the outgoing wave vector thus allowing us to use $Y_{j_\lambda m_{j_\lambda}}(\gamma_\lambda, \psi_\lambda)$ instead of $Y_{j_\lambda m_{j_\lambda}}(\theta_{r_\lambda}, \phi_{r_\lambda})$ in the summation appearing in Eq. 5.24.

The differential scattering cross section is defined as the ratio of the outgoing radial flux per unit solid angle to the incoming plane wave flux and, from Eq. 5.24, is related to the scattering amplitude $\bar{f}$ by

$$\sigma^{\lambda t_\lambda}_{\chi' \hat{t}'_\lambda} = \frac{\bar{V}^\lambda_{v_\lambda j_\lambda}}{\bar{V}^\lambda_{v'_\lambda j'_\lambda}} \mid \bar{f}^{\lambda \hat{t}_\lambda}_{\chi' \hat{t}'_\lambda} \mid^2 \tag{5.25}$$

for $\lambda v_\lambda j_\lambda \Omega_\lambda$ and $\chi' v'_\lambda j'_\lambda \Omega'_\lambda$ representing open channels. Here $\bar{V}^\lambda_{v_\lambda j_\lambda}$ is the physical velocity

$$\bar{V}^\lambda_{v_\lambda j_\lambda} = \frac{1}{a_\lambda} V^\lambda_{v_\lambda j_\lambda} = \left(\frac{2(E - \epsilon^\lambda_{v_\lambda j_\lambda})}{\mu_{\lambda, \nu \kappa}} \right)^{\frac{1}{2}} \tag{5.26}$$

In order to relate $\bar{f}$ to the scattering matrices, it is desirable to first define a scattering solution analogous to Eq. 5.24 in terms of the scaled coordinates of Eq. 2.1. This is easily done by removing the "bars" on all symbols containing them in Eq. 5.24. By comparing the plane wave parts, we see that the resulting $\Psi^{\chi' \hat{t}'_\lambda} [P]$ is proportional to $\bar{\Psi}^{\chi' \hat{t}'_\lambda} [P]$ with a proportionality constant $a_\lambda^{\frac{3}{2}}$. Comparison of the outgoing wave parts of Ψ and $\bar{\Psi}$ then yields

$$\bar{f}^{\lambda t_\lambda}_{\chi' \hat{t}'_\lambda} = a_\lambda^{-1} f^{\lambda t_\lambda}_{\chi' \hat{t}'_\lambda} \left(\frac{a_\lambda}{a_{\chi'}} \right)^{\frac{1}{2}} \tag{5.27}$$

which will be useful below.

One now expands the plane wave part of $\Psi^{\chi'\ell'_{\chi}}_{\chi}[P]$ in terms of a series of products of Legendre polynomials $P_{\ell'_{\chi}}(\cos\theta_{\chi'})$ times spherical Bessel functions $j_{\ell'_{\chi}}(k^{\chi'}_{v'_{\chi}j'_{\chi}}R_{\chi'})$, takes the asymptotic limit $(R_{\chi'}\to\infty)$ and converts the result to the body-fixed variables $r_{\chi}\gamma_{\chi}\psi_{\chi}$ and $R_{\chi}\theta_{\chi}\phi_{\chi}$ following the procedure outlined by Pack,[32] obtaining

$$e^{ik^{\chi'}_{v'_{\chi}j'_{\chi}}(\hat{R}_{\chi'})_z}\left(\frac{\phi^{\chi'}_{v'_{\chi}j'_{\chi}}(r_{\chi'})}{r_{\chi'}}\right)Y_{j'_{\chi}m'_{j_{\chi}}}(\theta_{r_{\chi'}},\phi_{r_{\chi'}})$$

$$\sim\frac{1}{2k^{\chi'}_{v'_{\chi}j'_{\chi}}R_{\chi'}}\left(\frac{\phi^{\chi'}_{v'_{\chi}j'_{\chi}}(r_{\chi'})}{r_{\chi'}}\right)\sum_{JM\Omega'_{\chi}}\delta_{Mm'_{j_{\chi}}}D^{J}_{M\Omega'_{\chi}}(\phi'_{\chi'},\theta_{\chi'},0)$$

$$\times Y_{j'_{\chi}\Omega'_{\chi}}(\gamma_{\chi},\psi_{\chi})(2J+1)\,i^{J+j'_{\chi}+1}\{e^{-i[k^{\chi'}_{v'_{\chi}j'_{\chi}}R_{\chi'}-(J+j'_{\chi})\frac{\pi}{2}]}$$

$$\times\delta_{M-\Omega'_{\chi}}-e^{i[k^{\chi'}_{v'_{\chi}j'_{\chi}}R_{\chi'}-(J+j'_{\chi})\frac{\pi}{2}]}\delta_{M\Omega'_{\chi}}\}\qquad(5.28)$$

In analogy to Eq. 2.11, the scattered plane wave solution $\Psi^{\chi'v'_{\chi}j'_{\chi}m'_{j_{\chi}}}_{\chi}[P]$ may be expanded in terms of the scattering solutions $\Psi^{\chi'v'_{\chi}j'_{\chi}m'_{j_{\chi}}}_{\chi}[S]$ as

$$\Psi^{\lambda' v'_{\lambda} j'_{\lambda} m'_{j_{\lambda}}}[P] = \sum_{JM\Omega'_{\lambda}} C_{JM}^{\lambda' v'_{\lambda} j'_{\lambda} m'_{j_{\lambda}} \Omega'_{\lambda}} \Psi_{JM}^{\lambda' v'_{\lambda} j'_{\lambda} \Omega'_{\lambda}}[S] \qquad (5.29)$$

Using Eq. 5.28 to express $\Psi[P]$ in terms of body-fixed quantities, Eqs. 5.3 and 5.5 for the asymptotic form of $\Psi_{JM}^{\lambda' t'_{\lambda'}}[S]$, and equating coefficients of the incoming spherical wave parts, one finds:

$$C_{JM}^{\lambda' v'_{\lambda} j'_{\lambda} m'_{j_{\lambda}} \Omega'_{\lambda}} = \delta_{M,-\Omega'_{\lambda}} \, \delta_{Mm'_{j_{\lambda}}} \left(\frac{\hbar}{\mu}\right)^{\frac{1}{2}} \frac{2J+1}{2} \, i^{J+j'_{\lambda}+1} \qquad (5.30)$$

Note that Eq. 5.30 implies $m'_{j_{\lambda}} = -\Omega'_{\lambda}$ thus relating $\hat{t}'_{\lambda}$ and t'_{λ} for the reagent states. If we now equate coefficients of outgoing spherical wave parts and use Eq. 5.30 to simplify, we get

$$f_{\lambda' \hat{t}'_{\lambda}}^{\lambda \hat{t}_{\lambda}} = \left(\frac{v_{v'_{\lambda} j'_{\lambda}}^{\lambda'}}{v_{v_{\lambda} j_{\lambda}}^{\lambda}}\right)^{\frac{1}{2}} \frac{e^{im_{j_{\lambda}}\phi_{\lambda}}}{2k_{v'_{\lambda} j'_{\lambda}}^{\lambda'}} i^{j'_{\lambda}-j_{\lambda}+1} \sum_{J=0}^{\infty} d_{m'_{j_{\lambda}} m_{j_{\lambda}}}^{J}(\theta_{\lambda}) \, T_{J\lambda' \hat{t}'_{\lambda'}}^{\lambda \hat{t}_{\lambda}}$$

$$(5.31)$$

where

$$\underset{\approx}{T}_J = \underset{\approx}{I} - \underset{\approx}{S}_J^0 \qquad (5.32)$$

is the transition matrix[32] and $m_{j_{\lambda}} = \Omega_{\lambda}$ for the product states so that $\hat{t}_{\lambda}$ and t_{λ} are identical. Equation 5.31 shows that the helicity amplitude and body-fixed scattering matrix are related by a single

sum reminiscent of the analogous result for potential scattering. This illustrates one of the primary advantages of the use of helicity amplitudes in conjunction with body-fixed coordinates such as those depicted in Fig. 3. Combining Eqs. 5.31 and 5.27, and using Eq. 5.26 and its counterpart for the wave numbers $\bar{k}^{\lambda}_{v_{\lambda}j_{\lambda}}$ and $k^{\lambda}_{v_{\lambda}j_{\lambda}}$, we find that the physical scattering amplitude $f^{-\lambda\hat{t}_{\lambda}}_{\lambda'\hat{t}'_{\lambda'}}$ is given by an expression identical to Eq. 5.31 with all velocities and wave numbers "barred". Substituting this into Eq. 5.25, we find

$$\sigma^{\lambda\hat{t}_{\lambda}}_{\lambda'\hat{t}'_{\lambda'}}(\theta_{\lambda}) = \frac{1}{4\bar{k}^{\lambda'2}_{v_{\lambda}j_{\lambda}}} \left| \sum_{J=0}^{\infty} (2J+1)\, d^{J}_{m'_{j_{\lambda}}, m_{j_{\lambda}}}(\theta_{\lambda})\, T^{\lambda\hat{t}_{\lambda}}_{J\lambda'\hat{t}'_{\lambda'}} \right|^{2} \quad (5.33)$$

which demonstrates that the differential cross section is independent of ϕ_{λ}.[49] The integral cross section $Q^{\lambda\hat{t}_{\lambda}}_{\lambda'\hat{t}'_{\lambda'}}$ is obtained by integrating Eq. 5.33 over θ_{λ} and ϕ_{λ}, and using the orthonormality property of the d^{J} functions.[33] This yields the remarkably simple expression

$$Q^{\lambda\hat{t}_{\lambda}}_{\lambda'\hat{t}'_{\lambda'}} = \frac{\pi}{\bar{k}^{\lambda'2}_{v_{\lambda}j_{\lambda}}} \sum_{J=0}^{\infty} (2J+1) \left| T^{\lambda\hat{t}_{\lambda}}_{J\lambda'\hat{t}'_{\lambda'}} \right|^{2} \quad (5.34)$$

Both $\sigma^{\lambda\hat{t}_{\lambda}}_{\lambda'\hat{t}'_{\lambda'}}$ and $Q^{\lambda\hat{t}_{\lambda}}_{\lambda'\hat{t}'_{\lambda'}}$ may be averaged over initial $m'_{j_{\lambda}}$ and summed over final $m_{j_{\lambda}}$ to give the degeneracy averaged quantities $\sigma^{\lambda v_{\lambda}j_{\lambda}}_{\lambda'v'_{\lambda}j'_{\lambda}}$ and $Q^{\lambda v_{\lambda}j_{\lambda}}_{\lambda'v'_{\lambda}j'_{\lambda}}$ respectively. The latter of these two can be

written as[32]

$$Q^{\lambda v_\lambda j_\lambda}_{\lambda v'_\lambda j'_\lambda} = \frac{\pi}{k^{\lambda'\, 2}_{v'_\lambda j'_\lambda}} \sum_{J=0}^{\infty} (2J+1)\, P^{v_\lambda j_\lambda}_{J v'_\lambda j'_\lambda} \qquad (5.35)$$

where the opacity function P_J is

$$P^{v_\lambda j_\lambda}_{J v'_\lambda j'_\lambda} = (2j'_\lambda + 1)^{-1} \sum_{m_{j_\lambda}} \sum_{m'_{j_\lambda}} P^{\lambda \hat{t}_\lambda}_{J \lambda \hat{t}'_\lambda} \qquad (5.36)$$

and the limits on the sums are $\left| m_{j_\lambda} \right| \le \min{(j_\lambda, J)}$ and

$\left| m'_{j_\lambda} \right| \le \min{(j'_\lambda, J)}$.

In an application to the $H + H_2$ reaction, the number of different distinguishable atom scattering amplitudes and cross sections may be greatly reduced by considering the symmetries involved. This was done in I and the derivations are essentially unchanged in 3D. First, the scattering amplitudes are invariant to a cyclic permutation of arrangement channel indices so that (suppressing the t_λ, t'_λ) $f^\lambda_\lambda = f^\nu_\nu = f^\kappa_\kappa$, $f^\nu_\lambda = f^\kappa_\nu = f^\lambda_\kappa$ and $f^\lambda_\nu = f^\nu_\kappa = f^\kappa_\lambda$. Second, f^κ_λ and f^ν_λ are related by[19]

$$f^{\kappa v' j' m'_j}_{\lambda v_j m_j} = (-1)^{j+j'}\, f^{\nu v' j' m'_j}_{\lambda v j m_j} \qquad (5.37)$$

and the non-reactive f^λ_λ satisfy

$$f_{\lambda v_j m_j}^{\lambda v' j' m'_j} = 0 \quad \text{if} \quad j - j' = \text{odd} \qquad (5.38)$$

These statements imply that f_λ^λ and f_λ^ν are the only distinct scattering amplitudes and that many components of f_λ^λ are zero. These symmetry relations also apply to the scattering matrix $\underset{\approx}{S}_J$ so that the entire distinguishable atom cross section calculation can be considerably streamlined. It should be mentioned that although the cyclic permutational symmetry is built into the calculation if the integration is done in only one of the three equivalent arrangement channel regions, Eqs. 5.37 and 5.38 will only hold rigorously if $\underset{\approx}{s}_{\nu\lambda}^J$ defined by Eq. 4.49 is orthogonal, and this will only be the case if the matching surface basis functions given by Eq. 4.30 form a sufficiently complete set. This provides a test of convergence of the method as long as the symmetries of Eqs. 5.37 and 5.38 are not built in.

To convert these distinguishable atom scattering amplitudes into the corresponding indistinguishable ones when two or three of the atoms are identical, the standard technique of post-antisymmetrization[50] may be used. Application to $H + H_2$ was given in I and is unchanged in the three-dimensional treatment. In the notation of this paper we obtain the following expressions for the antisymmetrized differential cross sections:

(a) para → para (j, j′ = even)

$$\sigma^{p\hat{t}}_{p\hat{t}'} = \frac{\bar{V}_{vj}}{\bar{V}_{v'j'}} \; | \; \bar{f}^{\lambda\hat{t}}_{\lambda\hat{t}'} - \bar{f}^{\nu\hat{t}}_{\lambda\hat{t}'} \; |^2 \tag{5.39a}$$

(b) para → ortho (j′ = even, j = odd)

$$\sigma^{o\hat{t}}_{p\hat{t}'} = 3 \frac{\bar{V}_{vj}}{\bar{V}_{v'j'}} \; | \; \bar{f}^{\nu\hat{t}}_{\lambda\hat{t}'} \; |^2 \tag{5.39b}$$

(c) ortho → para (j′ = odd, j = even)

$$\sigma^{p\hat{t}}_{o\hat{t}'} = \frac{\bar{V}_{vj}}{\bar{V}_{v'j'}} \; | \; \bar{f}^{\nu\hat{t}}_{\lambda\hat{t}'} \; |^2 \tag{5.39c}$$

(d) ortho → ortho (j, j′ = odd)

$$\sigma^{o\hat{t}}_{o\hat{t}'} = \frac{\bar{V}_{vj}}{\bar{V}_{v'j'}} \; \{ \; | \; \bar{f}^{\lambda\hat{t}}_{\lambda\hat{t}'} + \bar{f}^{\nu\hat{t}}_{\lambda\hat{t}'} \; |^2 + 2 \; | \; \bar{f}^{\nu\hat{t}}_{\lambda\hat{t}'} \; |^2 \} \tag{5.39d}$$

where Eqs. 5.27 and 5.31 are to be used in evaluating Eqs. 5.39a-d. The expressions for the antisymmetrized integral reaction cross sections are:

(a) para → para

$$Q^{p\hat{t}}_{p\hat{t}'} = \frac{\pi}{k^2_{v'j'}} \sum_J (2J+1) \; | \; \delta^{\hat{t}}_{\hat{t}'} - S^{o\lambda\hat{t}}_{J\lambda\hat{t}'} + S^{o\nu\hat{t}}_{J\lambda\hat{t}'} \; |^2 \tag{5.40a}$$

(b) para → ortho

$$Q_{p\hat{t}'}^{o\hat{t}} = 3 \frac{\pi}{\bar{k}_{v'j'}^2} \sum_J (2J+1) \left| S_{J\lambda\hat{t}'}^{o\nu\hat{t}} \right|^2 \tag{5.40b}$$

(c) ortho → para

$$Q_{o\hat{t}'}^{p\hat{t}} = \frac{\pi}{\bar{k}_{v'j'}^2} \sum_J (2J+1) \left| S_{J\lambda\hat{t}'}^{o\nu\hat{t}} \right|^2 \tag{5.40c}$$

(d) ortho → ortho

$$Q_{o\hat{t}'}^{o\hat{t}} = \frac{\pi}{\bar{k}_{v'j'}^2} \sum_J (2J+1) \left\{ \left| \delta_{\hat{t}'}^{\hat{t}} - S_{J\lambda\hat{t}'}^{o\lambda\hat{t}} - S_{J\lambda\hat{t}'}^{o\nu\hat{t}} \right|^2 \right.$$
$$\left. + 2 \left| S_{J\lambda t'}^{o\nu t} \right|^2 \right\} \tag{5.40d}$$

As was pointed out in Section 3.3, parity symmetry may be used in both the integration and matching procedures for any chemical reaction to reduce the number of states coupled in these stages of the calculation. One may also define parity scattering matrices, but the plane wave solution of Eq. 5.24 does not have parity symmetry so that these two decoupled parity S matrices must be recoupled before performing the calculation of the scattering amplitude in Eq. 5.31. This procedure is outlined in Appendix B.

6. Discussion

The method we have outlined in Sections 2-5 has a number of limitations or restrictions which we shall now consider. First, we have considered the reactive collision of an atom with a diatomic molecule on a single electronically adiabatic surface. The extension to multisurface reactions is straightforward and would follow the general format previously developed for collinear reactions.[51] All three reactive arrangement channels are assumed to be energetically accessible and the diatom in each arrangement channel is assumed to be in a $^1\Sigma$ electronic state. A straightforward modification of the matching procedure which simplifies it appropriately is required for single reaction path systems (for which one of the three arrangement channels is closed). This was discussed in I. For diatoms having electronic states other than $^1\Sigma$ (such as $^1\Lambda$ with $\Lambda \neq 0$), the rotational states $Y_{j_\lambda m_{j_\lambda}}(\theta_{r_\lambda}, \phi_{r_\lambda})$ must be modified[33] to $D^{j_\lambda}_{m_{j_\lambda}\Lambda}(\theta_{r_\lambda}, \phi_{r_\lambda}, 0)$ and electronic-vibration-rotation coupling must be considered, but the basic integration and matching procedures are unchanged. One basic restriction of the method is its inability to treat dissociative or break-up channels. This is not a serious limitation for many important chemical reactions at thermal energies. A procedure for treating both dissociative and reactive collisions is is currently being developed in this laboratory.

The integration procedure outlined in Section 3 may be applied

to any reaction for which the criteria of the preceding paragraph apply, however, the matching procedure (and hence the choice of coordinate system in the matching region) is strongly dependent on our choice of matching surfaces (Eqs. 2.5). Other choices will require significant modifications in the details of Section 4, although the basic concepts involved in matching will still be applicable. The matching surfaces considered in Eqs. 2.5 should be useful for many chemical reactions but may not always be ideal for obtaining rapidly convergent close coupling expansions. In particular, if the reaction has a low barrier for $\gamma_\lambda = \pi/2$ configurations, the expansion of the wave function in terms of matching surface basis functions $T^{\nu\lambda}$ (Section 4.2) may be slowly convergent. Conversely, too strong an anisotropy favoring collinear reactions over perpendicular ones leads to an ill conditioned close coupling problem. These and related restrictions on the matching surfaces were outlined in I.

The asymptotic analysis of Section 5 is quite general and should be applicable to those chemical reactions which fit the criteria of the first paragraph of this section. The anti-symmetrized results presented in Section 5 are only applicable to a collision system of three identical spin $\frac{1}{2}$-particles. Other combinations of identical particles and spins may be treated by post antisymmetrization procedures analogous to that in Appendix D of I.

The final criteria regarding the applicability of the method is computational efficiency. The large number of open rotational channels present in any 3D atom-diatom system makes the application

of any coupled channel method a large computational project. Much effort has however been spent in designing the method so that a minimum number of such channels are needed for convergence of the results. We therefore feel that this method should provide a computationally feasible procedure for studying simple chemical reactions. The first application of this procedure (to 3D $H + H_2$[24]) supports this statement.

APPENDIX A: ANGULAR MOMENTUM OPERATORS AND THE SCHRODINGER EQUATION IN SPACE-FIXED AND BODY-FIXED COORDINATE SYSTEMS

In this Appendix we will establish the relations between the rotational and total angular momentum operators in the space-fixed and body-fixed coordinate systems defined in Section 2.2 and Fig. 3.

We first consider the space-fixed coordinate system Oxyz. If we use the variables ϕ_{r_λ}, θ_{r_λ}, ϕ_λ and θ_λ (Section 2.2) to describe the various components of the operators $\underset{\sim}{j}_\lambda$ and $\underset{\sim}{\ell}_\lambda$ we obtain the usual expressions for these angular momentum operators in spherical polar coordinates.

$$j_{\lambda z} = -i\hbar \frac{\partial}{\partial \phi_{r_\lambda}} \tag{A.1a}$$

$$j_{\lambda x} = -i\hbar \left(-\cos\phi_{r_\lambda} \cot\theta_{r_\lambda} \frac{\partial}{\partial \phi_{r_\lambda}} - \sin\phi_{r_\lambda} \frac{\partial}{\partial \theta_{r_\lambda}} \right) \tag{A.1b}$$

$$j_{\lambda y} = -i\hbar \left(-\sin\phi_{r_\lambda} \cot\theta_{r_\lambda} + \cos\phi_{r_\lambda} \frac{\partial}{\partial \theta_{r_\lambda}} \right) \tag{A.1c}$$

with a similar expression for the components of $\underset{\sim}{\ell}_\lambda$ with $\phi_\lambda, \theta_\lambda$ substituted for $\phi_{r_\lambda}, \theta_{r_\lambda}$. Expressions for the components of $\underset{\sim}{J}$ are trivially obtained by the addition $\underset{\sim}{J} = \underset{\sim}{\ell}_\lambda + \underset{\sim}{j}_\lambda$. The eigenfunctions of the operators j_λ^2 and ℓ_λ^2 appearing in Eq. 2.9 (and also $j_{\lambda z}$ and $\ell_{\lambda z}$) are the spherical harmonics $Y_{j_\lambda m_{j_\lambda}}(\theta_{r_\lambda}, \phi_{r_\lambda})$ and

$Y_{\ell_\lambda m_{\ell_\lambda}}(\theta_\lambda, \phi_\lambda)$. We shall define the spherical harmonic Y_{jm_j} by the expression

$$Y_{jm_j}(\theta, \phi) = \frac{e^{im_j\phi}}{\sqrt{2\pi}} \mathscr{P}_j^{m_j}(\cos\theta) \tag{A.2}$$

where

$$\mathscr{P}_j^{m_j}(\cos\theta) = P_j^{|m_j|}(\cos\theta) \left(\frac{(j-|m_j|)!}{(j+|m_j|)!} \frac{2j+1}{2} \right)^{\frac{1}{2}} \begin{cases} (-1)^{m_j} & m_j > 0 \\ 1 & m_j \leq 0 \end{cases}$$

$$\tag{A.3}$$

In the space-fixed formalism of Arthurs and Dalgarno,[29] the full wavefunction is expanded in terms of a set of functions $\mathscr{Y}_{\ell_\lambda j_\lambda}^{JM}(\theta_\lambda, \phi_\lambda; \theta_{r_\lambda}, \phi_{r_\lambda})$ which are simultaneous eigenfunctions of J^2, J_z, ℓ_λ^2 and j_λ^2. These $\mathscr{Y}_{\ell_\lambda j_\lambda}^{JM}$ are obtained from the $Y_{j_\lambda m_{j_\lambda}}$ and $Y_{\ell_\lambda m_{\ell_\lambda}}$ via

$$\mathscr{Y}_{j_\lambda \ell_\lambda}^{JM}(\theta_\lambda, \phi_\lambda; \theta_{r_\lambda}, \phi_{r_\lambda}) = \sum_{m_{j_\lambda}, m_{\ell_\lambda}} C(j_\lambda \ell_\lambda J; m_{j_\lambda} m_{\ell_\lambda} M)$$

$$\times Y_{j_\lambda m_{j_\lambda}}(\theta_{r_\lambda}, \phi_{r_\lambda}) Y_{\ell_\lambda m_{\ell_\lambda}}(\theta_\lambda, \phi_\lambda) \tag{A.4}$$

where the notation of Rose[37] is used for the Clebsch Gordon coefficient C. The full space-fixed wavefunction is then written as

$$\Psi_{JM}(\underset{\sim}{r}_\lambda, \underset{\sim}{R}_\lambda) = \sum_{\ell_\lambda j_\lambda} \mathscr{Y}_{\ell_\lambda j_\lambda}^{JM}(\theta_\lambda, \phi_\lambda; \theta_{r_\lambda}, \phi_{r_\lambda}) G_{j_\lambda \ell_\lambda}^{JM}(r_\lambda, R_\lambda) \tag{A.5}$$

and the space-fixed coupled Schrödinger equation for $G_{j_\lambda \ell_\lambda}^{JM}$ is[29]

$$\left\{ - \frac{\hbar^2}{2\mu} \left[\frac{1}{R_\lambda} \frac{\partial^2}{\partial R_\lambda^2} R_\lambda + \frac{1}{r_\lambda} \frac{\partial^2}{\partial r_\lambda^2} r_\lambda \right] + \frac{j_\lambda(j_\lambda + 1)\hbar^2}{2\mu r_\lambda^2} \right.$$

$$\left. + \frac{\ell_\lambda(\ell_\lambda + 1)\hbar^2}{2\mu R_\lambda^2} - E \right\} G_{j_\lambda \ell_\lambda}^{JM} + \sum_{j'_\lambda \ell'_\lambda} \langle j_\lambda \ell_\lambda | V | j'_\lambda \ell'_\lambda \rangle G_{j'_\lambda \ell'_\lambda}^{JM} = 0.$$

$$\text{(A.6)}$$

We now consider the transformation to the body-fixed

coordinate systems $X_\lambda Y_\lambda Z_\lambda$ and $x'_\lambda y'_\lambda z'_\lambda$ of Section 2.2

convenient representation of angular momentum operators in these

coordinate systems involves choosing the operators $\vec{J}$ and $\vec{j}_\lambda$ as

as independent and expressing the ℓ_λ^2 of Eq. 2.9 by the expansion

$$\ell_\lambda^2 = | \underset{\sim}{J} - \underset{\sim}{j}_\lambda |^2 = J^2 + j_\lambda^2 - (\underset{\sim}{J} \cdot \underset{\sim}{j}_\lambda + \underset{\sim}{j}_\lambda \cdot \underset{\sim}{J}) . \qquad \text{(A.7)}$$

To convert the operators $\underset{\sim}{j}_\lambda$ and $\underset{\sim}{J}$, and thus the Hamiltonian of

Eq. 2.9 to the body-fixed systems requires first a change from the

variables $\theta_\lambda \phi_\lambda \theta_{r\lambda} \phi_{r\lambda}$ to $\theta_\lambda \phi_\lambda \gamma_\lambda \psi_\lambda$ as defined in Section 2.2,

followed by successive rotations of the components of the operators.

These rotational transformations may be accomplished by using the

general expression[37]

$$J_{k'} = R(\alpha\beta\gamma)^{-1} J_k R(\alpha\beta\gamma) \qquad \text{(A.8)}$$

where J_k refers to the kth component of any angular momentum

operator $\underset{\sim}{J}$ in an initial system and

$$R\,(\alpha\beta\gamma) = e^{i\gamma J_z}\,e^{i\beta J_y}\,e^{i\alpha J_z} \tag{A.9}$$

$J_{k'}$ refers to the k'^{th} component of $\underset{\sim}{J}$ in a transformed coordinate system which is obtained through rotations by Euler angles $\alpha\beta\gamma$ from the initial system. One important point to note in the application of Eq. A.8 to the body-fixed coordinate systems $X_\lambda Y_\lambda Z_\lambda$ or $x'_\lambda y'_\lambda z'_\lambda$ is that the components J_k and $(j_\lambda)_k$ of the operators $\underset{\sim}{J}$ and $\underset{\sim}{j}_\lambda$ will in general operate upon one or more of the Euler angles $\phi_\lambda, \theta_\lambda$ and ψ_λ of the transformations, and thus great care must be taken in properly commuting the operators. In Table I we express the components of the resulting operators $\underset{\sim}{J}$ and $\underset{\sim}{j}_\lambda$ as well as various combinations thereof in terms of the coordinates $\theta_\lambda \phi_\lambda \gamma_\lambda \psi_\lambda$ in the three coordinate systems $Oxyz$, $OX_\lambda Y_\lambda Z_\lambda$ and $Ox'_\lambda y'_\lambda z'_\lambda$. Some of the relations in that table have been given previously by Vezzetti and Rubinow,[52] by Morse and Feshbach[53] and by Curtiss, Hirschfelder and Adler.[31] One very useful point to notice about $j_{\lambda X_\lambda}$, $j_{\lambda Y_\lambda}$ and $j_{\lambda Z_\lambda}$ is that their expressions in terms of $\gamma_\lambda, \psi_\lambda$ in Table I have the same functional form as the corresponding $j_{\lambda x}$, $j_{\lambda y}$ and $j_{\lambda z}$ in Eqs. A.1. This implies that the rotational angular momentum eigenfunctions in the $X_\lambda Y_\lambda Z_\lambda$ coordinate system will simply be the spherical harmonics $Y_{j_\lambda \Omega_\lambda}(\gamma_\lambda, \psi_\lambda)$ where, as is explained in Section 2.2, Ω_λ is the quantum number associated with $j_{\lambda Z_\lambda}$.

In terms of the coordinate system $X_\lambda Y_\lambda Z_\lambda$, the Hamiltonian of Eq. 2.9 may be written as

$$H = -\frac{\hbar^2}{2\mu} \left[\frac{1}{R_\lambda} \frac{\partial^2}{\partial R_\lambda^2} R_\lambda + \frac{1}{r_\lambda} \frac{\partial^2}{\partial r_\lambda^2} r_\lambda \right] + \frac{j_\lambda^2}{2\mu r_\lambda^2}$$

$$+ \frac{1}{2\mu R_\lambda^2} \left[J^2 + j_\lambda^2 - 2j_{\lambda Z_\lambda} J_{Z_\lambda} - (j_\lambda^- J^+ + j_\lambda^+ J^-) \right] + V^\lambda (r_\lambda, R_\lambda, \gamma_\lambda)$$

$$(A.10)$$

where the raising and lowering operators are defined in terms of the X_λ and Y_λ components of $\underset{\sim}{J}$ and $\underset{\sim}{j}_\lambda$ in the usual way.[37] In order to express the Schrödinger equation in $X_\lambda Y_\lambda Z_\lambda$ coordinates, we must also rotate the wavefunction as is done in Eq. 2.13. Substituting this expression, along with Eq. A.10 into Eq. 2.9, and using the normal raising and lowering properties of the rotation matrix,[33] i.e.,

$$J^\pm D_{M\Omega_\lambda}^J = \hbar \left(J(J+1) - \Omega_\lambda (\Omega_\lambda \mp 1) \right)^{\frac{1}{2}} D_{M\Omega_\lambda +1}^J \qquad (A.11)$$

(where the $\pm$ components refer to the body-fixed system), we obtain the following coupled equations for $\Psi_{J\Omega_\lambda}^\lambda$:

$$\left\{ -\frac{\hbar^2}{2\mu} \left[\frac{1}{R_\lambda} \frac{\partial^2}{\partial R_\lambda^2} R_\lambda + \frac{1}{r_\lambda} \frac{\partial^2}{\partial r_\lambda^2} r_\lambda \right] + \frac{j_\lambda^2}{2\mu r_\lambda^2} \right.$$

$$+ \frac{1}{2\mu R_\lambda^2} \left[J(J+1)\hbar^2 + j_\lambda^2 - 2\hbar \Omega_\lambda j_{\lambda Z_\lambda} \right] + V^\lambda (r_\lambda, R_\lambda, \gamma_\lambda)$$

$$\left. - E \right\} \Psi_{J\Omega_\lambda}^\lambda - \frac{\hbar}{2\mu R_\lambda^2} \left(J(J+1) - \Omega_\lambda (\Omega_\lambda +1) \right)^{\frac{1}{2}} j_\lambda^- \Psi_{J\Omega_\lambda +1}^\lambda$$

$$- \frac{\hbar}{2\mu R_\lambda^2} \left(J(J+1) - \Omega_\lambda (\Omega_\lambda -1) \right)^{\frac{1}{2}} j_\lambda^+ \Psi_{J\Omega_\lambda -1}^\lambda = 0 \qquad (A.12)$$

Since the rotational eigenfunctions in the $X_\lambda Y_\lambda Z_\lambda$ coordinate system are the $Y_{j_\lambda \Omega_\lambda} (\gamma_\lambda, \psi_\lambda)$, the rotationally coupled body-fixed solutions analogous to Eq. A.5 are given by

$$\Psi_{JM} (\underset{\sim}{r}_\lambda, \underset{\sim}{R}_\lambda) = \sum_{j_\lambda \Omega_\lambda} D^J_{M\Omega_\lambda} (\phi_\lambda, \theta_\lambda, 0) Y_{j_\lambda \Omega_\lambda} (\gamma_\lambda, \psi_\lambda) w^\lambda_{Jj_\lambda \Omega_\lambda} (r_\lambda, R_\lambda)$$

(A.13)

which is a combination of Eqs. 2.18 and 2.13. The body-fixed and space-fixed representations may be related by using the equality

$$D^J_{M\Omega_\lambda} (\phi_\lambda, \theta_\lambda, 0) Y_{j_\lambda \Omega_\lambda} (\gamma_\lambda, \psi_\lambda) = (\frac{4\pi}{2J+1})^{\frac{1}{2}} \sum_{\ell_\lambda} (-1)^{j_\lambda - \Omega_\lambda}$$

$$\times C (Jj_\lambda \ell_\lambda | \Omega_\lambda - \Omega_\lambda 0) \mathcal{Y}^{JM}_{j_\lambda \ell_\lambda} (\theta_\lambda, \phi_\lambda ; \theta_{\underset{\sim}{\lambda}} \phi_{\underset{\sim}{\lambda}})$$

(A.14)

Equation A.14 will be of great utility to us in the asymptotic analysis. A further modification of the rotationally coupled Schrödinger equation is given in Section 2.4.

APPENDIX B: PARITY DECOUPLING

In this Appendix we consider the decoupling that occurs when eigenfunctions of the parity (or inversion) operator $\hat{\mathscr{I}}$ are used in the close coupling expansion. This operator inverts all atoms through the system's center of mass. For the three-particle system we are considering,

$$\hat{\mathscr{I}} \; \Psi(\underset{\sim}{r}_\lambda, \underset{\sim}{R}_\lambda) \; = \; \Psi \, (-\underset{\sim}{r}_\lambda, \; -\underset{\sim}{R}_\lambda) \tag{B.1}$$

where Ψ is any wave function describing the system. $\hat{\mathscr{I}}$ commutes with $\nabla^2_{\underset{\sim}{R}_\lambda}$ and $\nabla^2_{\underset{\sim}{r}_\lambda}$. In addition, the internal configuration of the system before and after inversion is the same and consequently the potential energy is not changed by the parity operation. We conclude that $\hat{\mathscr{I}}$ commutes with the hamiltonian in Eq. 2.7 for any triatomic system.

If we express $\underline{R}_\lambda$ and $\underset{\sim}{r}_\lambda$ in body-fixed variables, we find that

$$\hat{\mathscr{I}} \; \Psi \, (r_\lambda, \gamma_\lambda, \psi_\lambda, R_\lambda, \theta_\lambda, \phi_\lambda) \; = \; \Psi \, (r_\lambda, \gamma_\lambda, \pi - \psi_\lambda, R_\lambda, \pi - \theta_\lambda, \pi + \phi_\lambda)$$

$$\tag{B.2}$$

The body-fixed wavefunction we are considering is given, from Eqs. 2.13, 2.18, 2.30 and 3.3, by

$$\Psi_{JM}(\underset{\sim}{r}_\lambda, \underset{\sim}{R}_\lambda) = \sum_{v_\lambda j_\lambda \Omega_\lambda} D^J_{M\Omega_\lambda}(\phi_\lambda, \theta_\lambda, 0) \, Y_{j_\lambda \Omega_\lambda}(\gamma_\lambda, \psi_\lambda)$$

$$\times \frac{\phi^\lambda_{v_\lambda j_\lambda}(r_\lambda)}{r_\lambda R_\lambda} \, g^\lambda_{Jv_\lambda j_\lambda \Omega_\lambda}(R_\lambda) \qquad (B.3)$$

Since $\hat{\mathscr{J}}$ leaves the scalars R_λ and r_λ unchanged, all derivations of this Appendix are independent of which of the four regions of each arrangement channel region we are concerned with, so we shall omit any explicit reference to them, using the general form for Ψ_{JM} in region I or II. Let us now apply $\hat{\mathscr{J}}$ to Eq. B.3, using the relations[33] $D^J_{M\Omega_\lambda}(\phi_\lambda + \pi, \pi - \theta_\lambda, 0) = (-1)^J \times D^J_{M-\Omega_\lambda}(\phi_\lambda, \theta_\lambda, 0)$ and $Y_{j_\lambda \Omega_\lambda}(\gamma_\lambda, \pi - \psi_\lambda) = Y_{j_\lambda -\Omega_\lambda}(\gamma_\lambda, \psi_\lambda)$. By changing the sign of Ω_λ in Eq. B.3 and remembering that its summation limits in that equation are invariant with respect to a sign change, we find

$$\hat{\mathscr{J}}\Psi_{JM}(\underset{\sim}{r}_\lambda, \underset{\sim}{R}_\lambda) = (-1)^J \sum_{v_\lambda j_\lambda \Omega_\lambda} D^J_{M\Omega_\lambda}(\phi_\lambda, \theta_\lambda, 0) Y_{j_\lambda \Omega_\lambda}(\gamma_\lambda, \psi_\lambda)$$

$$\times \frac{\phi^\lambda_{v_\lambda j_\lambda}(r_\lambda)}{r_\lambda R_\lambda} \, g^\lambda_{Jv_\lambda j_\lambda -\Omega_\lambda}(R_\lambda) \qquad (B.4)$$

which indicates that Ψ^λ_{JM} is not an eigenfunction of the parity operator $\hat{\mathscr{J}}$ unless $J = 0$ (since Ω must equal zero as well in that case). Since $\hat{\mathscr{J}}$ commutes with the Hamiltonian, we should be able to linearly combine the Ψ_{JM}'s so as to produce simultaneous eigen-

functions of $\hat{\mathcal{J}}$ and H. Let us consider the linear combinations

$$\overline{\Psi}^{\pm}_{JM} (\underline{r}_\lambda, \underline{R}_\lambda) = \frac{1}{\sqrt{2}} \left\{ \Psi_{JM} (\underline{r}_\lambda, \underline{R}_\lambda) \pm (-1)^J \Psi_{JM} (-\underline{r}_\lambda, -\underline{R}_\lambda) \right\}$$

(B.5)

By substituting Eqs. B.3 and B.4 and rearranging, we find that

$$\overline{\Psi}^{\pm}_{JM} (\underline{r}_\lambda, \underline{R}_\lambda) = \sum_{v_\lambda j_\lambda \Omega_\lambda} D_{M\Omega_\lambda} (\phi_\lambda, \theta_\lambda, 0) \, Y_{j_\lambda \Omega_\lambda} (\gamma_\lambda, \psi_\lambda) \frac{\phi^\lambda_{v_\lambda j_\lambda} (r_\lambda)}{r_\lambda R_\lambda}$$

$$\times \left\{ \begin{array}{c} \dfrac{1}{\sqrt{2}} (g^\lambda_{Jv_\lambda j_\lambda \Omega_\lambda} + g_{Jv_\lambda j_\lambda -\Omega_\lambda}) \\[2ex] \dfrac{1}{\sqrt{2}} (g_{Jv_\lambda j_\lambda \Omega_\lambda} - g_{v_\lambda j_\lambda -\Omega_\lambda}) \end{array} \right\}$$

(B.6)

where the upper term in brackets refers to the plus solution and the lower to the minus solution. From Eq. B.4, it should be apparent that

$$\hat{\mathcal{J}} \, \overline{\Psi}^{\pm}_{JM} (\underline{r}_\lambda, \underline{R}_\lambda) = \pm (-1)^J \, \overline{\Psi}^{\pm}_{JM} (\underline{r}_\lambda, \underline{R}_\lambda)$$

(B.7)

Since the basis functions $D^J_{M\Omega_\lambda} Y_{j_\lambda \Omega_\lambda} \phi_{v_\lambda j_\lambda}$ in Eq. B.6 are unchanged from those in Eq. B.3, the equations of Sections 2-4 may be converted to the corresponding ones involving parity solutions by simply linearly combining the g's according to the expression in brackets in Eq. B.6. To facilitate this, we define a new function $\overline{g}$ via[54]

$$\bar{g}^{\lambda}_{Jv_{\lambda}j_{\lambda}\Omega_{\lambda}}(R_{\lambda}) = \begin{cases} \dfrac{1}{\sqrt{2}} (g^{\lambda}_{Jv_{\lambda}j_{\lambda}\Omega_{\lambda}} + g^{\lambda}_{Jv_{\lambda}j_{\lambda}-\Omega_{\lambda}}) \\ \qquad\qquad\qquad\qquad \text{for } \Omega_{\lambda} > 0 \\ g^{\lambda}_{v_{\lambda}j_{\lambda}\Omega_{\lambda}} \qquad \text{for } \Omega_{\lambda} = 0 \\ \\ \dfrac{1}{\sqrt{2}} (-g^{\lambda}_{Jv_{\lambda}j_{\lambda}\Omega_{\lambda}} + g^{\lambda}_{Jv_{\lambda}j_{\lambda}-\Omega_{\lambda}}) \\ \qquad\qquad\qquad\qquad \text{for } \Omega_{\lambda} < 0 \end{cases}$$

(B.8)

or in the matrix notation of Section 3.1,

$$\bar{\underline{g}}^{\lambda}_{J}(R_{\lambda}) = \underset{\approx}{T}_{\lambda}\, \underline{g}^{\lambda}_{J}(R_{\lambda}) \qquad\qquad\qquad\qquad (B.9)$$

where the orthogonal matrix $\underset{\approx}{T}_{\lambda}$ is given by

$$(\underset{\approx}{T}_{\lambda})^{v'_{\lambda}j'_{\lambda}\Omega'_{\lambda}}_{v_{\lambda}j_{\lambda}\Omega_{\lambda}} = \delta^{v'_{\lambda}j'_{\lambda}}_{v_{\lambda}j_{\lambda}} \begin{cases} \dfrac{1}{\sqrt{2}} (\delta_{\Omega_{\lambda}\Omega'_{\lambda}} + \delta_{\Omega_{\lambda}-\Omega'_{\lambda}}) \text{ for } \Omega_{\lambda} > 0 \\ \\ \delta_{\Omega_{\lambda}\Omega'_{\lambda}} \qquad\qquad\qquad \text{for } \Omega_{\lambda} = 0 \\ \\ \dfrac{1}{\sqrt{2}} (-\delta_{\Omega_{\lambda}\Omega'_{\lambda}} + \delta_{\Omega_{\lambda}-\Omega'_{\lambda}}) \text{ for } \Omega_{\lambda} < 0 \end{cases}$$

(B.10)

If we include initial conditions of the proper symmetry to form the

matrix $\bar{\underline{g}}^{\lambda}_{J}$, we find that

$$\overline{\underset{\approx}{g}}{}_J^\lambda (R_\lambda) = \underset{\approx\lambda}{T} \; \underset{\approx}{g}{}_J^\lambda (R_\lambda) \; \overset{\sim}{\underset{\approx\lambda}{T}} \tag{B.11}$$

To convert the equations of Section 3 to the corresponding expressions involving parity solutions, we need only to use Eq. B.11 to transform them into expressions for $\overline{\underset{\approx}{g}}{}_J^\lambda$ rather than $\underset{\approx}{g}{}_J^\lambda$. For example, the fully coupled Schrödinger equation (Eq. 3.18) becomes

$$\frac{d^2 \overline{\underset{\approx}{g}}{}_J^{\lambda\pm}}{dR_\lambda^2} = \overline{\underset{\approx}{U}}{}_J^\lambda \; \overline{\underset{\approx}{g}}{}_J^{\lambda\pm} \tag{B.12}$$

where

$$\overline{\underset{\approx}{U}}{}_J^\lambda = \underset{\approx\lambda}{T} \; \underset{\approx}{U}{}_J^\lambda \; \underset{\approx\lambda}{T} \tag{B.13}$$

$\overline{\underset{\approx}{U}}{}_J$ is identical to $\underset{\approx}{U}{}_J^\lambda$ in all terms of Eq. 3.19 except those off diagonal in Ω_λ (i.e., in $\underset{\approx c}{U}{}_J^\lambda$). From Eqs. 3.15 and B. 10, we find that

$$(\overline{\underset{\approx c}{U}}{}_J^\lambda)_{t_\lambda}^{t'_\lambda} = \frac{\delta_{v_\lambda j_\lambda}^{v'_\lambda j'_\lambda}}{R_\lambda^2} \{ \delta_{\Omega_\lambda \Omega'_\lambda} [J(J+1) - 2\Omega_\lambda^2$$

$$+ j_\lambda(j_\lambda+1)] - A_{\Omega_\lambda} \delta_{\Omega_\lambda+1, \Omega'_\lambda} \xi_+(J,\Omega_\lambda) \xi_+(j_\lambda,\Omega_\lambda)$$

$$- B_{\Omega_\lambda} \delta_{\Omega_\lambda-1,\Omega'_\lambda} \xi_-(J,\Omega'_\lambda) \xi_-(j_\lambda,\Omega_\lambda) \} \tag{B.14}$$

where

$$A_{\Omega_\lambda} = \begin{cases} 1 & \text{for } \Omega_\lambda \geq 1 \quad \text{and} \quad \Omega_\lambda < -1 \\ \sqrt{2} & \text{for } \Omega_\lambda = 0 \\ 0 & \text{for } \Omega_\lambda = -1 \end{cases} \quad \cdot \tag{B.15}$$

and

$$B_{\Omega_\lambda} = \begin{cases} 1 & \text{for } \Omega_\lambda > 1 \quad \text{and} \quad \Omega_\lambda \leq -1 \\ \sqrt{2} & \text{for } \Omega_\lambda = 1 \\ 0 & \text{for } \Omega_\lambda = 0 \end{cases} \tag{B.16}$$

An examination of the structure of $\underset{\approx}{\overline{U}}{}^\lambda_{cJ}$ indicates that it contains no elements which couple states whose Ω_λ is positive or zero to those whose Ω_λ is negative. Since only $\underset{\approx}{\overline{U}}{}^\lambda_{cJ}$ provides off-diagonal Ω_λ coupling in Eq. B.12, we see that our coupled Schrödinger equations have been separated into two uncoupled sets--those with $\Omega_\lambda \geq 0$ (of parity $(-1)^J$) and those with $\Omega_\lambda < 0$ (parity $-(-1)^J$). This uncoupling is preserved throughout the integration in a given arrangement channel region since the only Ω_λ dependent coupling appearing anywhere in this process occurs in centrifugal terms identical to Eq. B. 14. Thus by constructing parity eigenfunctions, we can separate our integration problem into two smaller ones (each of which can be further separated into two parts for homonuclear targets (Section 3.3)).

Parity is also preserved in the matching procedure because the parity operation is invariant to which arrangement channel coordinate system one is considering (by inspection of Fig. 1). This means that solutions of the same parity symmetry but expressed in different arrangement channel coordinates should be related to

each other by a transformation which does not mix in solutions of the opposite parity. To show this, we must first transform the coefficient matrices $\underset{\approx}{h}{}_J^\lambda$, $\underset{\approx}{h}'{}_J^\lambda$, $\underset{\approx}{f}{}_J^\nu$ and $\underset{\approx}{f}'{}_J^\nu$ of Section 4.2 to the representation involving parity eigenfunctions. This requires a transformation similar to Eq. B.11

$$\overline{\underset{\approx}{h}}{}_J^\lambda = \underset{\approx}{T}'_{\nu\lambda} \; \underset{\approx}{h}{}_J^\lambda \; \underset{\approx}{\widetilde{T}}_\lambda \tag{B.17}$$

where $\underset{\approx}{T}'_{\nu\lambda}$ is an $N/2 \times N/2$ matrix (N = total number of solutions of both parities) whose precise mathematical form is identical to $\underset{\approx}{T}_\lambda$ in Eq. B.10, but whose actual structure is different because the set of indices $v_\lambda j_\lambda$ involving the matching surface basis functions of Eq. 4.30 will assume only half the number of values that the asymptotic solutions do (as discussed in Section 4.3). Note that we still right-multiply $\underset{\approx}{h}{}_J^\lambda$ by $\underset{\approx}{T}_\lambda$ in Eq. B.17 because right multiplication corresponds to linearly combining different initial conditions, and the number of these is always N. By writing equations analogous to Eq. B.17 for $\underset{\approx}{f}{}_J^\nu$, $\underset{\approx}{f}'{}_J^\nu$ and $\underset{\approx}{h}'{}_J^\lambda$, substituting these into Eq. 4.57 (using Eqs. 4.54, 4.55, 4.56) and simplifying, we obtain

$$\overline{\underset{\approx}{h}}{}_J^{\lambda+} \overline{\underset{\approx}{C}}{}_{\lambda J}^{(i)+} + \overline{\underset{\approx}{h}}{}_J^{\lambda-} \overline{\underset{\approx}{C}}{}_{\lambda J}^{(i)-} = \overline{\underset{\approx}{s}}{}_{\nu\lambda}^J \left\{ \overline{\underset{\approx}{f}}{}_J^{\nu+} \overline{\underset{\approx}{C}}{}_{\nu J}^{(i)+} + \overline{\underset{\approx}{f}}{}_J^{\nu-} \overline{\underset{\approx}{C}}{}_{\nu J}^{(i)-} \right\} \tag{B.18}$$

where the circumflex symbol implies definitions analogous to Eqs. 4.54, 4.55 and 4.56 for "barred" (i.e., parity) quantities, and

$$\overline{\underset{\approx}{s}}{}_{\nu\lambda}^J = \underset{\approx}{T}'_{\nu\lambda} \; \underset{\approx}{s}{}_{\nu\lambda}^J \; \underset{\approx}{\widetilde{T}}'_{\nu\lambda} \tag{B.19}$$

From Eq. 4.49 we can rewrite $\underset{\approx}{\bar{s}}{}^J_{\nu\lambda}$ as

$$
(\underset{\approx}{\bar{s}}{}^J_{\nu\lambda})^{v'_\lambda j'_\lambda \Omega'_\lambda}_{v_\lambda j_\lambda \Omega_\lambda} = S^{\lambda\lambda'}_{v_\lambda v'_\lambda} \int D^{\nu\lambda}_{j_\lambda \Omega_\lambda}(\gamma_\lambda)
$$

$$
\times D^{\nu\lambda}_{j'_\lambda \Omega'_\lambda}(\gamma_\lambda) \left\{ \begin{array}{c} (d^J_{\Omega'_\lambda \Omega_\lambda} + d^J_{\Omega'_\lambda -\Omega_\lambda}) \\[2ex] (d^J_{\Omega'_\lambda \Omega_\lambda} - d^J_{\Omega'_\lambda -\Omega_\lambda}) \end{array} \right\} f_{\Omega_\lambda \Omega'_\lambda} \sin\gamma_\lambda \, d\gamma_\lambda
$$

$$\tag{B.20}$$

where

$$
f_{\Omega_\lambda \Omega'_\lambda} = \left\{ \begin{array}{ll} \dfrac{1}{\sqrt{2}} & \text{for } \Omega_\lambda = 0 \text{ or } \Omega'_\lambda = 0 \\[2ex] \tfrac{1}{2} & \text{for } \Omega_\lambda = \Omega'_\lambda = 0 \\[2ex] 1 & \text{for both } \Omega_\lambda, \Omega'_\lambda > 0 \text{ or } < 0 \\[2ex] 0 & \text{otherwise} \end{array} \right.
$$

and the upper term in the brackets is used for $\Omega_\lambda, \Omega'_\lambda \geqslant 0$ and the lower term for $\Omega_\lambda, \Omega'_\lambda < 0$. It should be evident from Eq. B.21 that $\underset{\approx}{\bar{s}}{}^J_{\nu\lambda}$ does not couple terms of different parity nor does any part of Eq. B.18; this implies that the matching procedure can be done separately for solutions of each parity. It should also be noted that for a complete set of matching surface functions, the two sub-blocks of $\bar{s}^J_{\nu\lambda}$ corresponding to solutions of different parity are separately orthogonal.

A convenient procedure for extracting the asymptotic information from the matched solutions involves first a calculation

of reactance and scattering matrices which are defined in terms of parity eigenfunctions. This is followed by a coupling transformation in which the positive and negative parity S_J matrices are combined to yield the body-fixed S_J matrix of Eq. 5.5. From that point onward: the formulas of Section 5.2 must be used, since the plane wave scattering solution is not an eigenfunction of $\hat{\mathcal{P}}$ (as seen by inspection of Eq. 5.24). The parity scattering and reactance matrix solutions are defined by equations identical in form to Eqs. 5.4 and 5.5, or to Eqs. 5.8 and 5.9, but the incoming and outgoing solutions $\underset{\approx}{I}_J$ and $\underset{\approx}{O}_J$ of Eq. 5.10 must be parity eigenfunctions and hence satisfy Eq. B.12 asymptotically. One can find these solutions by actually diagonalizing the asymptotic Hamiltonian obtained from Eq. B.12, or by performing transformations analogous to Eq. B.11 on $\underset{\approx}{I}_J$ and $\underset{\approx}{O}_J$. Both procedures lead to expressions for $\underset{\approx}{I}_J$ and $\underset{\approx}{O}_J$ identical to Eq. 5.8 except for the following two changes:

(a) the sum over ℓ_λ in that equation includes only those ℓ_λ of the same parity as is specified by the signs of Ω_λ and Ω'_λ appearing in that equation. (The only non-zero terms will always involve Ω_λ and Ω'_λ of the same signs.) In other words, when $\Omega_\lambda, \Omega'_\lambda \geq 0$, $\ell_\lambda = J + j_\lambda$, $J + j_\lambda - 2, \cdots, |J - j_\lambda|$ and when $\Omega_\lambda, \Omega'_\lambda < 0$, $\ell_\lambda = J + j_\lambda - 1, \cdots, |J - j_\lambda| + 1$.

(b) Eq. 5.10 is to be multiplied by $\bar{f}_{\Omega_\lambda \Omega'_\lambda}$ where

$$\bar{f}_{\Omega_\lambda,\Omega'_\lambda} = \begin{cases} \sqrt{2} & \text{for } \Omega_\lambda = 0 \text{ or } \Omega'_\lambda = 0 \\ 1 & \text{for } \Omega_\lambda = \Omega'_\lambda = 0 \\ 2 & \text{for both } \Omega_\lambda \text{ and } \Omega_\lambda \geq 0\,; \text{ or } < 0 \\ 0 & \text{otherwise} \end{cases}$$

$$(B.22)$$

This form of $\bar{f}_{\Omega_\lambda,\Omega'_\lambda}$ leads to block diagonal $\underset{\approx}{I}_J$ and $\underset{\approx}{O}_J$ matrices thus decoupling the reactance and scattering matrix analysis for solutions of different parities.

When these expressions for $\underset{\approx}{I}_J$ and $\underset{\approx}{O}_J$ are substituted into Eq. 5.21 along with the parity expressions for $\underset{\approx}{g}_J^\pm$, $\underset{\approx}{g}'^\pm_J$ and $\underset{\approx}{C}_J^\pm$, the correct parity reactance matrix $\underset{\approx}{\bar{R}}'_J$ (analogous to $\underset{\approx}{\bar{R}}_J$ of Eq. 5.18) is obtained (where we consider $\underset{\approx}{\bar{R}}'_J$ to contain the even and odd parity reactance matrices as separate sub-blocks). This may be subsequently converted to $\underset{\approx}{\bar{S}}'_J$ via an equation analogous to Eq. 5.6. Finally, the rows and columns of the parity scattering matrix may be rearranged to form the body-fixed scattering matrix $\underset{\approx}{\bar{S}}_J$ via

$$\underset{\approx}{\bar{S}}_J = \underset{\approx}{\tilde{T}}\ \underset{\approx}{\bar{S}}'_J\ \underset{\approx}{T} \tag{B.23}$$

where

$$(\underset{\approx}{\bar{S}}_J)^{\lambda'v'_\lambda\Omega'_\lambda}_{\lambda v_\lambda j_\lambda \Omega_\lambda} = (S_J)^{\lambda v_\lambda j_\lambda \Omega_\lambda}_{\lambda' v'_\lambda j'_\lambda -\Omega'_\lambda} \tag{B.24}$$

and the $3N \times 3N$ $\underset{\approx}{T}$ is obtained from the $N \times N$ matrices $\underset{\approx}{T}_\lambda$, $\underset{\approx}{T}_\nu$, $\underset{\approx}{T}_\kappa$ (whose definitions are analogous to Eq. B. 10), by

$$T = \begin{pmatrix} \underset{\approx}{T}_\lambda & \underset{\approx}{O} & \underset{\approx}{O} \\ \underset{\approx}{O} & \underset{\approx}{T}_\nu & \underset{\approx}{O} \\ \underset{\approx}{O} & \underset{\approx}{O} & \underset{\approx}{T}_\kappa \end{pmatrix} \qquad (B.25)$$

$\underset{\approx}{O}$ is an $N \times N$ matrix of zeros.

Table 1. Angular Momentum Operators in Space-Fixed and Body-Fixed Coordinate Systems*

$Oxyz$	$OX_\lambda Y_\lambda Z_\lambda$	$Ox'_\lambda y' z'_\lambda$
$J_x = -i\hbar(-\cos\phi\cot\theta\frac{\partial}{\partial\phi}$ $-\sin\phi\frac{\partial}{\partial\theta}+\frac{\cos\phi}{\sin\theta}\frac{\partial}{\partial\psi})$	$J_{X_\lambda} = -i\hbar(-\frac{1}{\sin\theta}\frac{\partial}{\partial\phi}+\cot\theta\frac{\partial}{\partial\psi})$	$J_{x'_\lambda} = -i\hbar(-\frac{\cos\psi}{\sin\theta}\frac{\partial}{\partial\phi}$ $+\sin\psi\frac{\partial}{\partial\theta}+\cot\theta\cos\psi\frac{\partial}{\partial\psi})$
$J_y = -i\hbar(-\sin\phi\cot\theta\frac{\partial}{\partial\phi}$ $+\cos\phi\frac{\partial}{\partial\theta}+\frac{\cos\phi}{\sin\theta}\frac{\partial}{\partial\psi})$	$J_{Y_\lambda} = -i\hbar\frac{\partial}{\partial\theta}$	$J_{y'} = -i\hbar(\frac{\sin\psi}{\sin\theta}\frac{\partial}{\partial\phi}$ $+\cos\psi\frac{\partial}{\partial\theta}-\cot\theta\sin\psi\frac{\partial}{\partial\psi})$
$J_z = -i\hbar\frac{\partial}{\partial\phi}$	$J_{Z_\lambda} = -i\hbar\frac{\partial}{\partial\psi}$	$J_{z'} = -i\hbar\frac{\partial}{\partial\psi}$
$j_{\lambda x} = -i\hbar[(\cos\phi\sin\theta+\sin\phi\sin\psi\cot\gamma$ $-\cos\phi\cos\theta\cos\psi\cot\gamma)\frac{\partial}{\partial\psi}$ $-(\sin\phi\cos\psi+\cos\phi\cos\theta\sin\psi)\frac{\partial}{\partial\gamma}]$	$j_{\lambda X_\lambda} = -i\hbar(-\cos\psi\cot\gamma\frac{\partial}{\partial\psi}$ $-\sin\psi\frac{\partial}{\partial\gamma})$	$j_{\lambda x'_\lambda} = -i\hbar(-\cot\gamma\frac{\partial}{\partial\psi})$
$j_{\lambda y} = -i\hbar[(\sin\phi\sin\theta-\cos\phi\sin\psi\cot\gamma$ $-\sin\phi\cos\theta\cos\psi\cot\gamma)\frac{\partial}{\partial\psi}$ $+(\cos\phi\cos\psi-\sin\phi\cos\theta\sin\psi)\frac{\partial}{\partial\gamma}]$	$j_{\lambda Y_\lambda} = -i\hbar(-\sin\psi\cot\gamma\frac{\partial}{\partial\psi}$ $+\cos\psi\frac{\partial}{\partial\gamma})$	$j_{\lambda y'} = -i\hbar\frac{\partial}{\partial\gamma}$
$j_{\lambda z} = -i\hbar[(\cos\theta+\sin\theta\cos\psi\cot\gamma)\frac{\partial}{\partial\psi}$ $+\sin\theta\sin\psi\frac{\partial}{\partial\gamma}]$	$j_{\lambda Z_\lambda} = -i\hbar\frac{\partial}{\partial\psi}$	$j_{\lambda z'_\lambda} = i\hbar\frac{\partial}{\partial\psi}$
$J^2 = J_x^2 + J_y^2 + J_z^2$ $= -\hbar^2[\frac{\partial^2}{\partial\theta^2}+\cot\theta\frac{\partial}{\partial\theta}$ $+\frac{1}{\sin^2\theta}(\frac{\partial^2}{\partial\phi^2}+\frac{\partial^2}{\partial\psi^2})-\frac{2\cos\theta}{\sin^2\theta}\frac{\partial^2}{\partial\phi\partial\psi}]$	$J^2 = J_{X_\lambda}^2 + J_{Y_\lambda}^2 + J_{Z_\lambda}^2$ $-i\hbar\cot\theta J_{Y_\lambda}$	$J^2 = J_{x'_\lambda}^2 + J_{y'}^2 + J_{z'_\lambda}^2$
$j_\lambda^2 = j_{\lambda x}^2 + j_{\lambda y}^2 + j_{\lambda z}^2$ $= -\hbar^2(\frac{\partial^2}{\partial\gamma^2}+\cot\gamma\frac{\partial}{\partial\gamma}+\frac{1}{\sin^2\gamma}\frac{\partial^2}{\partial\psi^2})$	$j_\lambda^2 = j_{\lambda X_\lambda}^2 + j_{\lambda Y_\lambda}^2 + j_{\lambda Z_\lambda}^2$	$j_\lambda^2 = j_{\lambda x'_\lambda}^2 + j_{\lambda y'}^2 + j_{\lambda z'_\lambda}^2$ $-i\hbar\cot\gamma\, j_{\lambda y'}$
$\underline{j}_\lambda \cdot \underline{J} = j_{\lambda z}J_z + j_{\lambda x}J_x + j_{\lambda y}J_y$ $= -\hbar^2[\frac{\cos\psi\cot\gamma}{\sin\theta}\frac{\partial^2}{\partial\psi\partial\phi}+\frac{\sin\psi}{\sin\theta}\frac{\partial^2}{\partial\gamma\partial\phi}$ $-\sin\psi\cot\theta\frac{\partial^2}{\partial\psi\partial\gamma}-\sin\psi\cot\gamma\frac{\partial^2}{\partial\psi\partial\theta}$ $+\cos\psi\frac{\partial^2}{\partial\gamma\partial\theta}+(1-\cos\psi\cot\gamma\cot\theta)\frac{\partial^2}{\partial\psi^2}]$	$\underline{j}_\lambda \cdot \underline{J} = j_{\lambda Z_\lambda}J_{Z_\lambda}+j_{\lambda X_\lambda}J_{X_\lambda}$ $+j_{\lambda Y_\lambda}J_{Y_\lambda}$	$\underline{j}_\lambda \cdot \underline{J} = j_{\lambda z'_\lambda}J_{z'_\lambda}+j_{\lambda x'_\lambda}J_{x'_\lambda}$ $+j_{\lambda y'}J_{y'}-i\hbar\cot\gamma J_{y'}$

*The subscript λ has been omitted on the symbols θ, ϕ, γ, ψ.

Note that the expressions for J^2, j_λ^2 and $\underline{j}_\lambda \cdot \underline{J}$ in terms of θ, ϕ, γ, ψ are independent of coordinate system.

REFERENCES

*Research supported in part by the United States Air Force Office of Scientific Research.

†Work performed in partial fulfillment of the requirements for the Ph.D. in Chemistry at the California Institute of Technology.

‡Contribution No.

REFERENCES

[1] D. J. Diestler and V. McKoy, J. Chem. Phys. $\underline{48}$, 2951 (1968).

[2] D. J. Diestler, J. Chem. Phys. $\underline{54}$, 4547 (1971).

[3] E. M. Mortenson and K. S. Pitzer, Chem. Soc. (London) Spec. Publ. $\underline{16}$, 57 (1962); J. Chem. Phys. $\underline{48}$, 4029 (1968).

[4] D. J. Truhlar and A. Kuppermann, J. Chem. Phys. $\underline{52}$, 3841 (1970); ibid. $\underline{56}$, 2232 (1972).

[5] A. Kuppermann, Proceedings of the Conference on Potential Energy Surfaces in Chemistry, U. C. Santa Cruz, W. A. Lester, Ed., (August, 1970) p. 121; Electronic and Atomic Collisions, Proceedings of VII ICPEAC, North Holland, Amsterdam, 1971, p. 3.

[6] G. C. Schatz, J. Bowman and A. Kuppermann, J. Chem. Phys. $\underline{58}$, 4023 (1973); J. M. Bowman, G. C. Schatz and A. Kuppermann, Chem. Phys. Lett. $\underline{24}$, 378 (1974); G. C. Schatz, J. M. Bowman and A. Kuppermann, J. Chem. Phys., $\underline{63}$, 674, 685 (1975).

[7] C. C. Rankin and J. Light, J. Chem. Phys. $\underline{51}$, 1701 (1969); G. Miller and J. C. Light, J. Chem. Phys. $\underline{54}$, 1635 (1971); ibid., $\underline{54}$, 1643 (1971).

[8] B. R. Johnson, Chem. Phys. Lett. $\underline{13}$, 172 (1972).

[9] S. F. Wu and R. D. Levine, Mol. Phys. $\underline{22}$, 881 (1971).

[10] E. Shipley, J. Chem. Phys. $\underline{58}$, 232 (1973).

[11] J. T. Adams, R. L. Smith and E. F. Hayes, J. Chem. Phys. $\underline{61}$, 2193 (1974).

[12] M. Baer and D. J. Kouri, Chem. Phys. Lett. $\underline{24}$, 37 (1974); M. Baer, J. Chem. Phys. $\underline{60}$, 1057 (1974); A. Persky and M. Baer,

J. Chem. Phys. 60, 133 (1974); M. Baer, U. Halavee and

A. Persky, J. Chem. Phys. 61, 5122 (1974).

[13] P. B. Middleton and R. E. Wyatt, J. Chem. Phys. 56, 2720 (1972);

E. A. McCollough and R. E. Wyatt, J. Chem. Phys. 54, 3578

(1971); ibid., 54, 3592 (1971).

[14] M. Baer and D. J. Kouri, Chem. Phys. Lett. 11, 238 (1971);

J. Chem. Phys. 56, 1758 (1972); ibid., 57, 3991 (1972).

[15] R. P. Saxon and J. C. Light, J. Chem. Phys. 56, 3874 (1972);

56, 3885 (1972); A. Altenberger-Siczek and J. C. Light, J. Chem.

Phys. 61, 4373 (1974).

[16] (a) A. B. Elkowitz and R. E. Wyatt, J. Chem. Phys. 62, 2504

(1975); 62, 3683 (1975); (b) S. A. Harms and R. E. Wyatt, J.

Chem. Phys. 62, 3162 (1975); 62, 3173 (1975).

[17] G. Wolken and M. Karplus, J. Chem. Phys. 60, 351 (1974).

[18] W. H. Miller, J. Chem. Phys. 50, 407 (1969).

[19] A. Kuppermann, G. C. Schatz and M. Baer, Mol. Phys., in

preparation.

[20] A. Kuppermann, G. C. Schatz and M. Baer, J. Chem. Phys. 61,

4362 (1974).

[21] G. C. Schatz and A. Kuppermann, in preparation.

[22] A. Kuppermann and G. C. Schatz, J. Chem. Phys. 62, 2502 (1975).

[23] G. C. Schatz and A. Kuppermann, in preparation.

[24] G. C. Schatz and A. Kuppermann, in preparation.

[25] L. M. Delves, Nucl. Phys. 9, 391 (1959); 20, 275 (1960).

[26] D. Jepsen and J. O. Hirschfelder, Proc. Nat. Acad. Sci. 45, 249

(1959).

[27] F. Smith, J. Math. Phys. **3**, 735 (1962).

[28] A. Kuppermann, Chem. Phys. Lett., in press; J. Chem. Phys., to be published.

[29] A. M. Arthurs and A. Dalgarno, Proc. R. Soc. London, **A256**, 540 (1960).

[30] J. O. Hirschfelder and E. P. Wigner, Proc. Nat. Acad. Sci. **21**, 113 (1935).

[31] C. F. Curtiss, J. O. Hirschfelder and F. T. Adler, J. Chem. Phys. **18**, 1638 (1950).

[32] R. T. Pack, J. Chem. Phys. **60**, 633 (1974).

[33] A. S. Davydov, Quantum Mechanics (trans. I. V. Schensted). NEO Press, Ann Arbor, 1966, Chap. VI.

[34] P. McGuire and D. J. Kouri, J. Chem. Phys. **60**, 2488 (1974).

[35] R. B. Walker and J. C. Light, Chem. Phys. **7**, 84 (1975).

[36] It can be shown that the McGuire-Kouri approximation is equivalent to replacing ℓ_λ^2 in body-fixed coordinates (involving the four angles $\theta_\lambda, \phi_\lambda, \gamma_\lambda, \psi_\lambda$) by its expression in space-fixed coordinates (involving only the angles $\theta_\lambda, \phi_\lambda$). This approximate body-fixed ℓ_λ^2 commutes with the approximate body-fixed hamiltonian resulting from its use. Simultaneous eigenfunctions of these two approximate operators can be written as $Y_{\ell_\lambda m_{\ell_\lambda}}(\theta_\lambda, \phi_\lambda) \times \Psi_{\ell_\lambda}^\lambda(R_\lambda, r_\lambda, \gamma_\lambda, \psi_\lambda)$, in terms of which any eigenfunction of the approximate hamiltonian may be expanded. An expansion of the $\Psi_{\ell_\lambda}^\lambda$ in terms of the $Y_{j_\lambda \Omega_\lambda}(\gamma_\lambda, \psi_\lambda)$ leads to coefficients $W_{j_\lambda \Omega_\lambda}^{\lambda \ell_\lambda}(r_\lambda, R_\lambda)$ which satisfy an

equation similar to Eq. 2.19 with the off diagonal Ω_λ terms missing and the factor multiplying $\hbar^2/2\mu R_\lambda^2$ in Eq. 2.20 replaced by $\ell_\lambda(\ell_\lambda + 1)$.

[37] M. E. Rose, Elementary Theory of Angular Momentum, Wiley, New York, 1957.

[38] Handbook of Mathematical Functions (M. Abramowitz and I. A. Stegun, Eds.), National Bureau of Standards, Washington, D.C., 1964, Chaps. 9 and 10.

[39] R. N. Porter and M. Karplus, J. Chem. Phys. 40, 1105 (1964).

[40] $i_n(x) = (\pi/2x)^{\frac{1}{2}} I_{n+\frac{1}{2}}(x)$ and $k_n(x) = (\pi/2x)^{\frac{1}{2}} K_{n+\frac{1}{2}}(x)$ where I_m and K_m are the modified cylindrical Bessel functions described by Abramowitz and Stegun[38] p. 374.

[41] The row indices designate the different tumbling and vibration rotation basis functions and the column indices the different linearly independent solutions.

[42] R. Gordon, J. Chem. Phys. 51, 14 (1969).

[43] These asymptotic solutions are simply the non integer order spherical Bessel functions which solve Eq. 3.6 when the $\xi_\pm$ terms are set equal to zero. Note that in the R and S matrix determination outlined in Section 5, the complications arising from these truncated basis expansions are ignored. In actual calculations[24] these effects have, however, been correctly included.

[44] As noted in Section 3.3, the even and odd j_λ solutions are not coupled for atom plus homonuclear diatomic arrangement channels. We are accordingly allowed (but not required) to set the components

of g_J connecting even and odd rotational quantum numbers equal to zero. This results in scattering solutions of the correct homonuclear symmetry and allows us to considerably decouple the problem as described in Section 3.3

[45] A. M. Lane and R. G. Thomas, Rev. Mod. Phys. 30, 257 (1958).

[46] N. S. F. Mott and H. S. W. Massey, The Theory of Atomic Collisions (3rd Ed.) Clarendon Press, Oxford, 1965.

[47] The transition probability is defined as the ratio of the outgoing radial flux in a specified product channel to the incoming radial flux in a specified reagent channel. Equation 5.23 easily follows from application of this definition to Eqs. 5.3 and 5.5.

[48] M. Jacob and G. C. Wick, Annals of Physics, 7, 404 (1959).

[49] This lack of dependence of σ on ϕ is a simple consequence of our choice of incident quantization axis as being the direction of the incident wave vector. This results in an "initial" probability density which is cylindrically symmetric about that axis (from Eq. 5.24) which implies that the "final" probability density must be symmetric as well in the absence of external fields.

[50] L. I. Schiff, Quantum Mechanics (3rd edition), McGraw-Hill, New York, 1968, p. 384-395.

[51] J. M. Bowman, Ph.D. Thesis, California Institute of Technology (unpublished), 1974.

[52] D. J. Vezzetti and S. I. Rubinow, Ann. Phys. 35, 373 (1965).

[53] P. M. Morse and H. Feshbach, Methods of Theoretical Physics (Part II), McGraw-Hill, New York, 1953, p. 1721.

[54]A factor of $\sqrt{2}$ has been omitted in the $\Omega_\lambda = 0$ solution. This is always permitted because the integrated solutions are undetermined to within an overall constant multiplicative factor. This choice has the advantage of making the $\underset{\approx}{T}_\lambda$ defined by Eq. B.10 orthogonal.

FIGURE CAPTIONS

FIG. 1. Vectors used to specify the location of the three atoms A, B and C relative to the center of mass G. G_{BC}, G_{AC} and G_{AB} denote the locations of the centers of mass of the diatoms BC, AC and AB, respectively. The vectors $\bar{\underset{\sim}{R}}_\alpha$, $\bar{\underset{\sim}{r}}_\alpha$, $\bar{\underset{\sim}{R}}_\beta$, $\bar{\underset{\sim}{r}}_\beta$, $\bar{\underset{\sim}{R}}_\gamma$, $\bar{\underset{\sim}{r}}_\gamma$ are defined in text.

FIG. 2. Plot of potential contours for the $H + H_2$ reaction in a space $OX_\lambda Y_\lambda Z_\lambda$ such that a point P has the spherical polar coordinates ζ, ω_λ, γ_λ defined in the text after Eq. 2.3. In (a) we depict contours for the fixed values of $\gamma_\lambda = 0°$ and $180°$, while in (b) we consider $\gamma_\lambda = 45°$ and $225°$, and in (c) $90°$ and $270°$. In (a) we also depict the lines of inter- section of the $\gamma_\lambda = 0$, $180°$ plane with the half planes $\pi_{\nu\lambda}$, $\pi_{\kappa\nu}$ and $\pi_{\lambda\kappa}$ of Eq. 2.5, which are used to divide configuration space into three arrangement channel regions λ, ν, κ. For each figure, OW_λ is the intersection of the half plane determined by OZ_λ and the corresponding smallest γ_λ with the $OX_\lambda Y_\lambda$ plane.

FIG. 3. Space-fixed coordinate system $Oxyz$ and body-fixed systems $OX_\lambda Y_\lambda Z_\lambda$ and $Ox'_\lambda y'z'_\lambda$ (Section 2.2) in relation to the triatomic collision system and to each other.

FIG. 4. Division of the R_λ, r_λ space into four regions I, II, III and IV. The contours are equipotentials of the matrix element $V_0^\lambda (r_\lambda, R_\lambda)$ (see Eq. 3.4) in eV for the Porter Karplus $H + H_2$ potential energy function. The dashed line L is the line of steepest ascents for V_0^λ. The locations of the points P_0', P_0 and P_1 are discussed in Section 3.1 of the text. Q is the origin of this space.

FIG. 5. The polar coordinates $\rho_\lambda, \varphi_\lambda$ and ζ, η_λ and their inter-relationship in R_λ, r_λ configuration space.
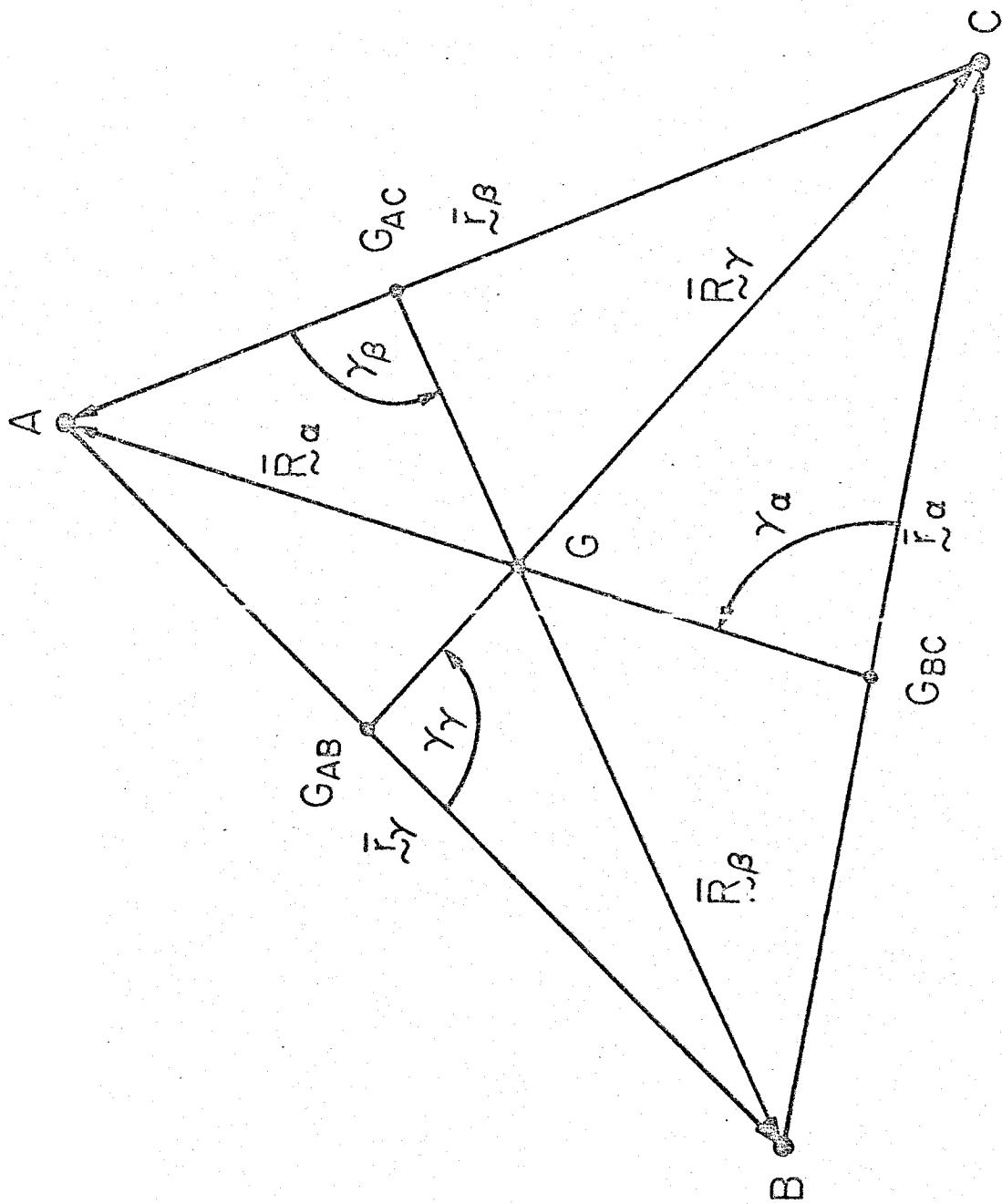
Figure 1
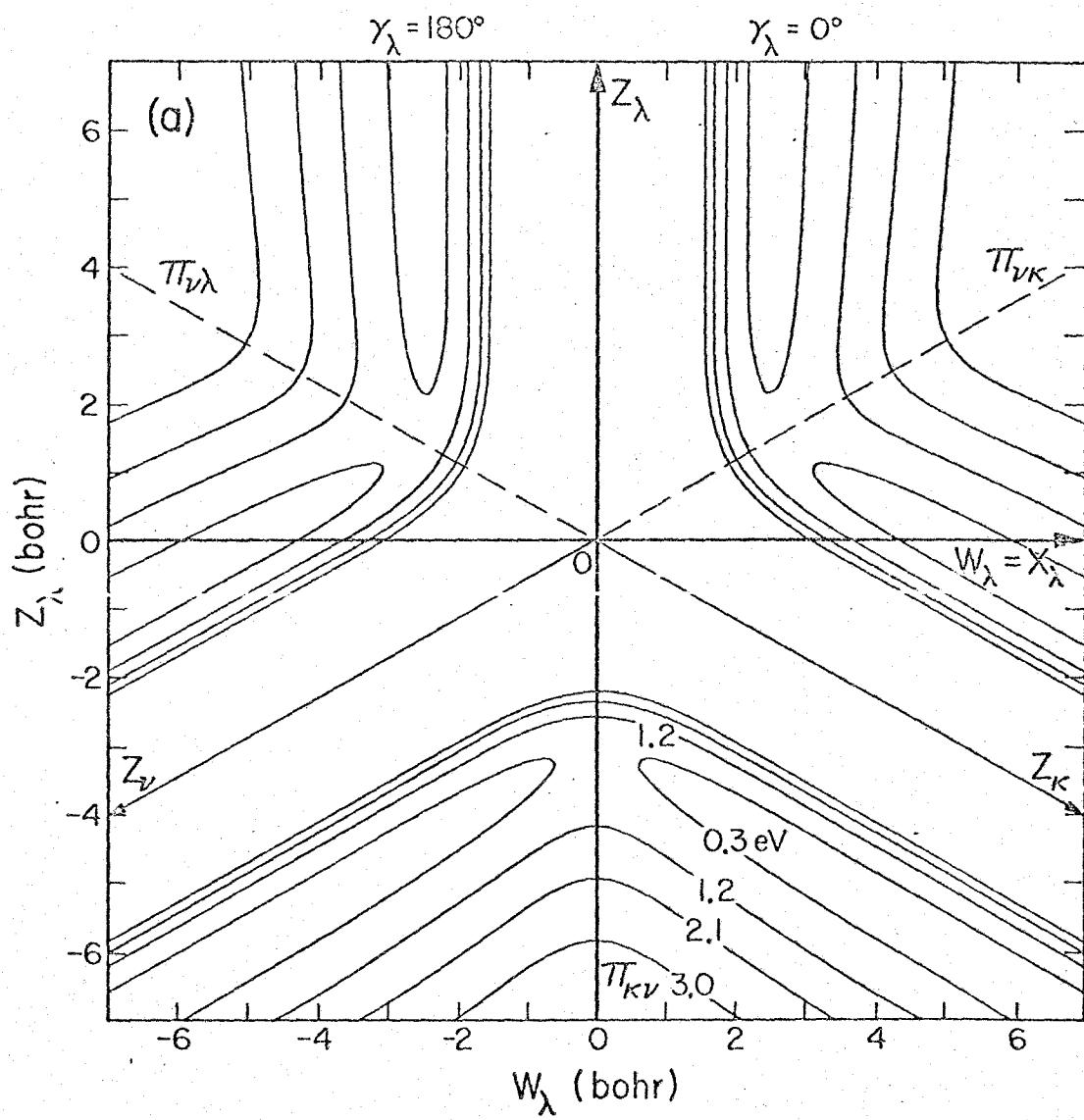
Figure 2a
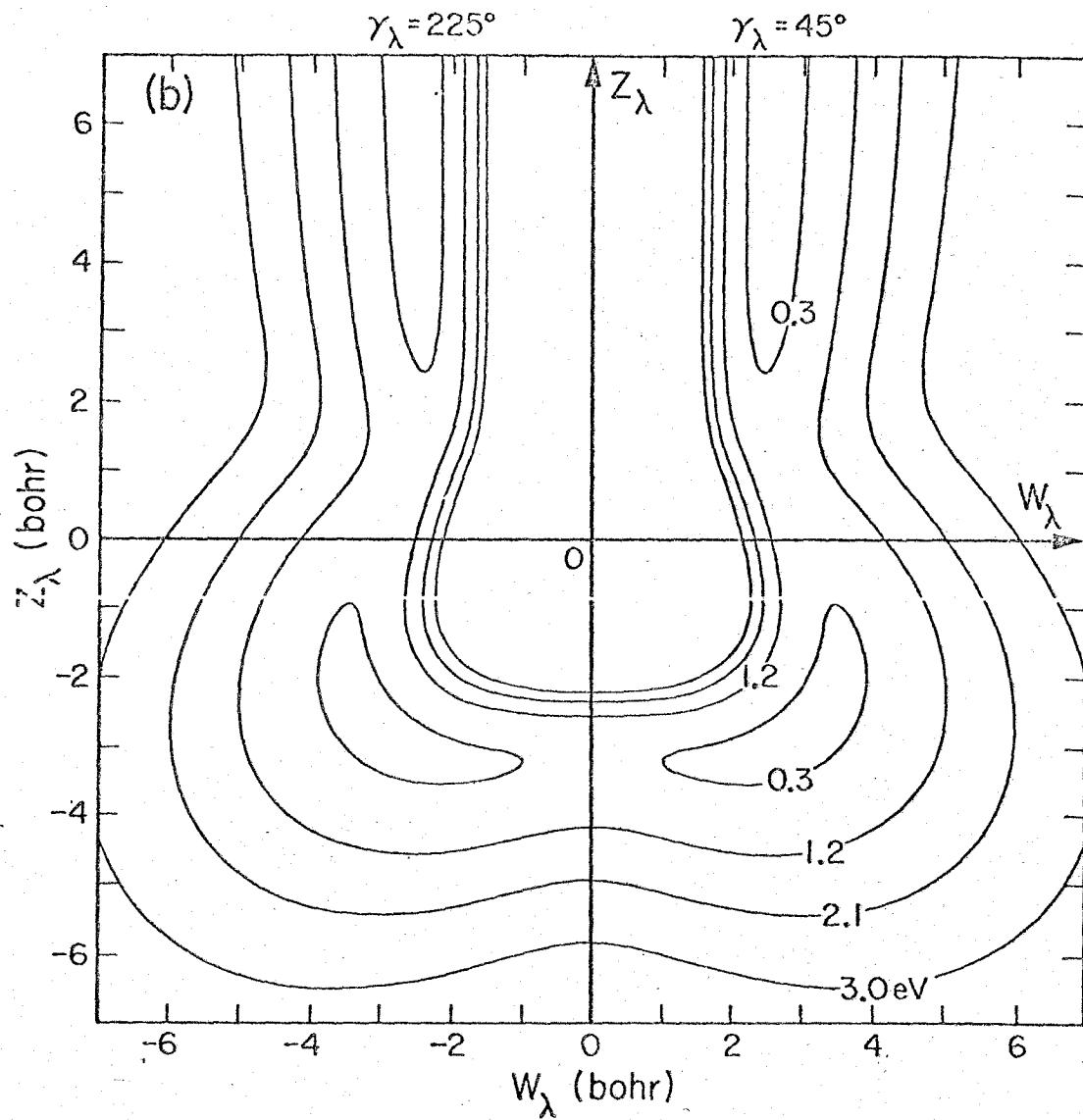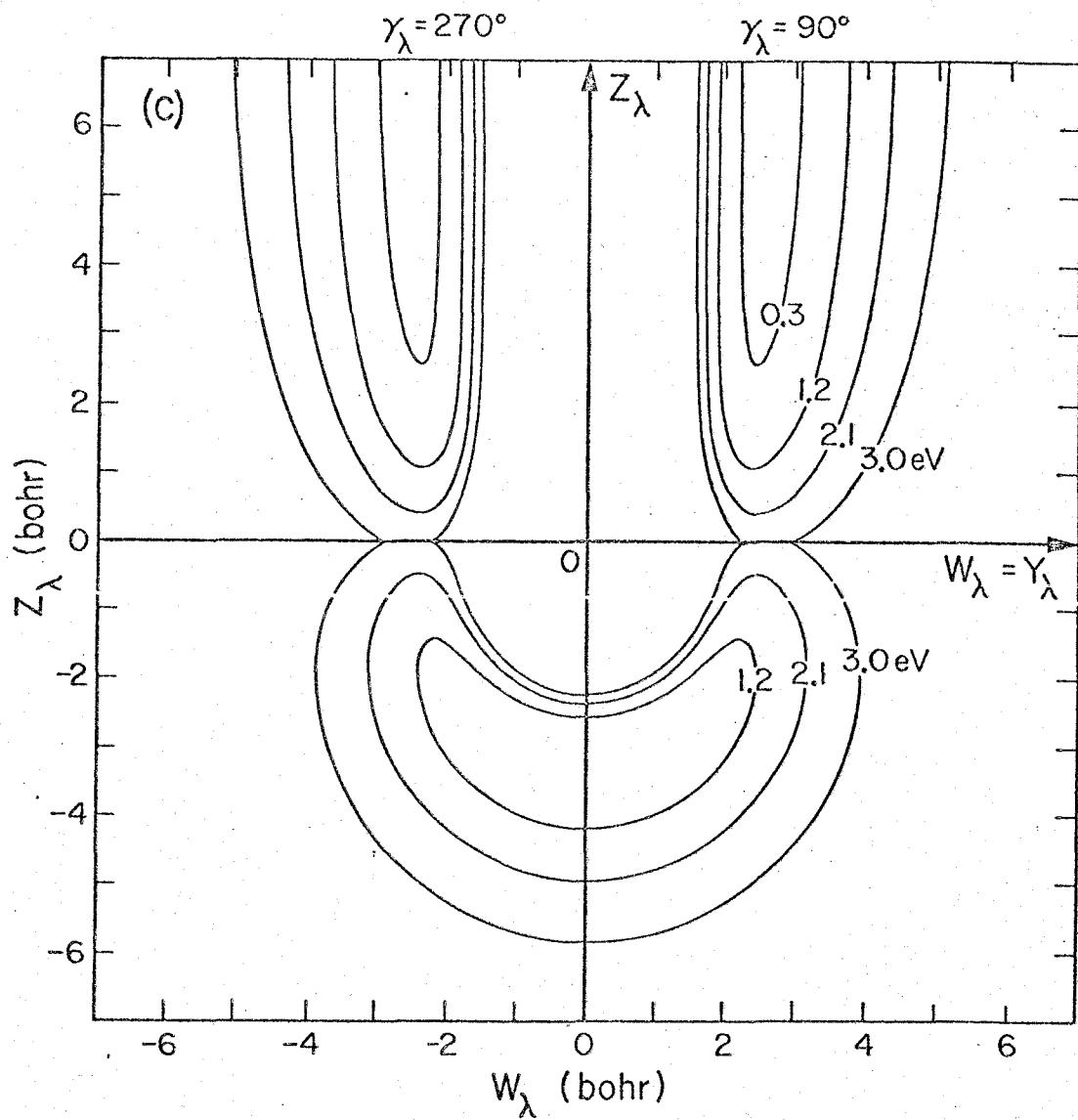
Figure 2b

Figure 2c
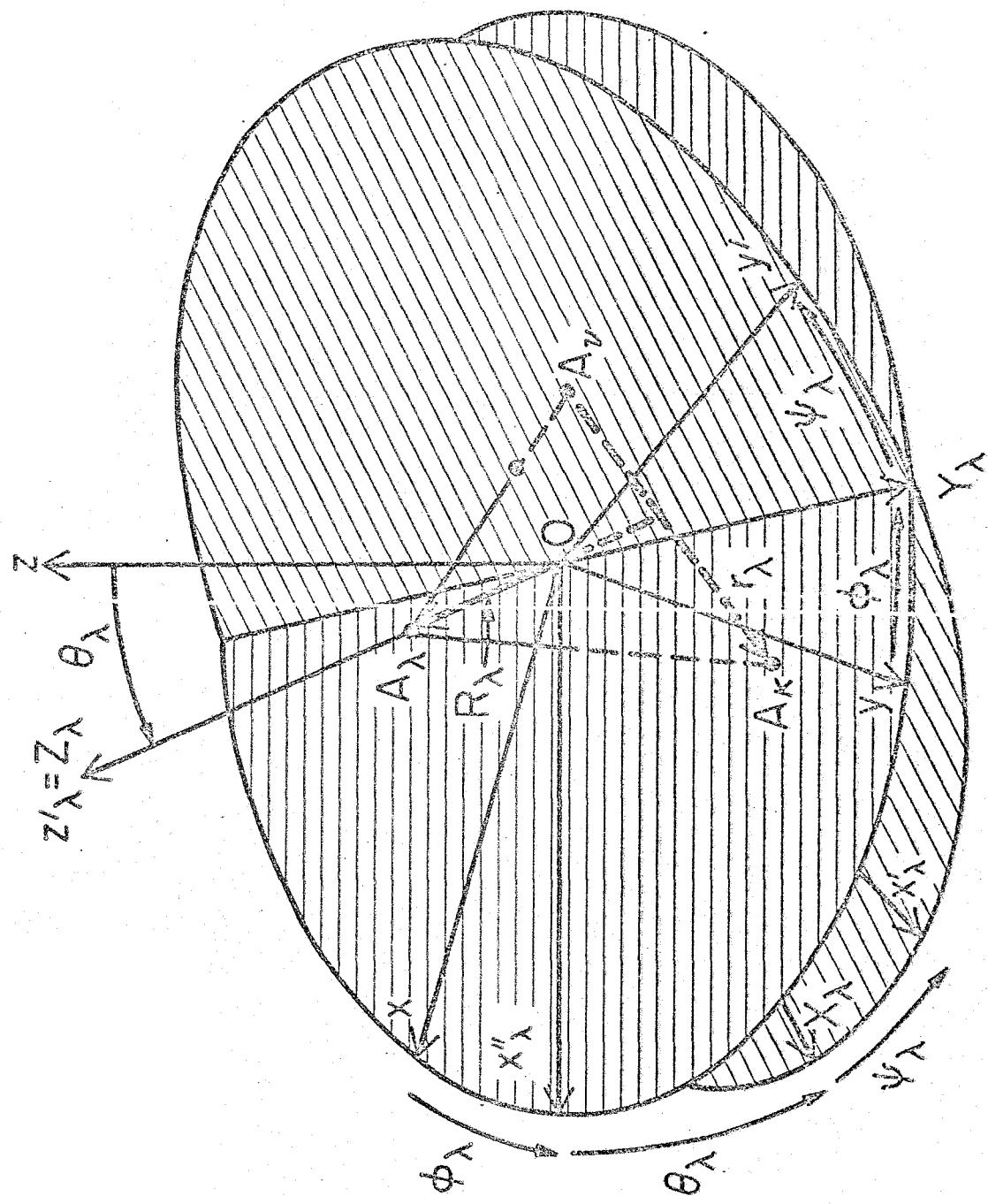
Figure 3
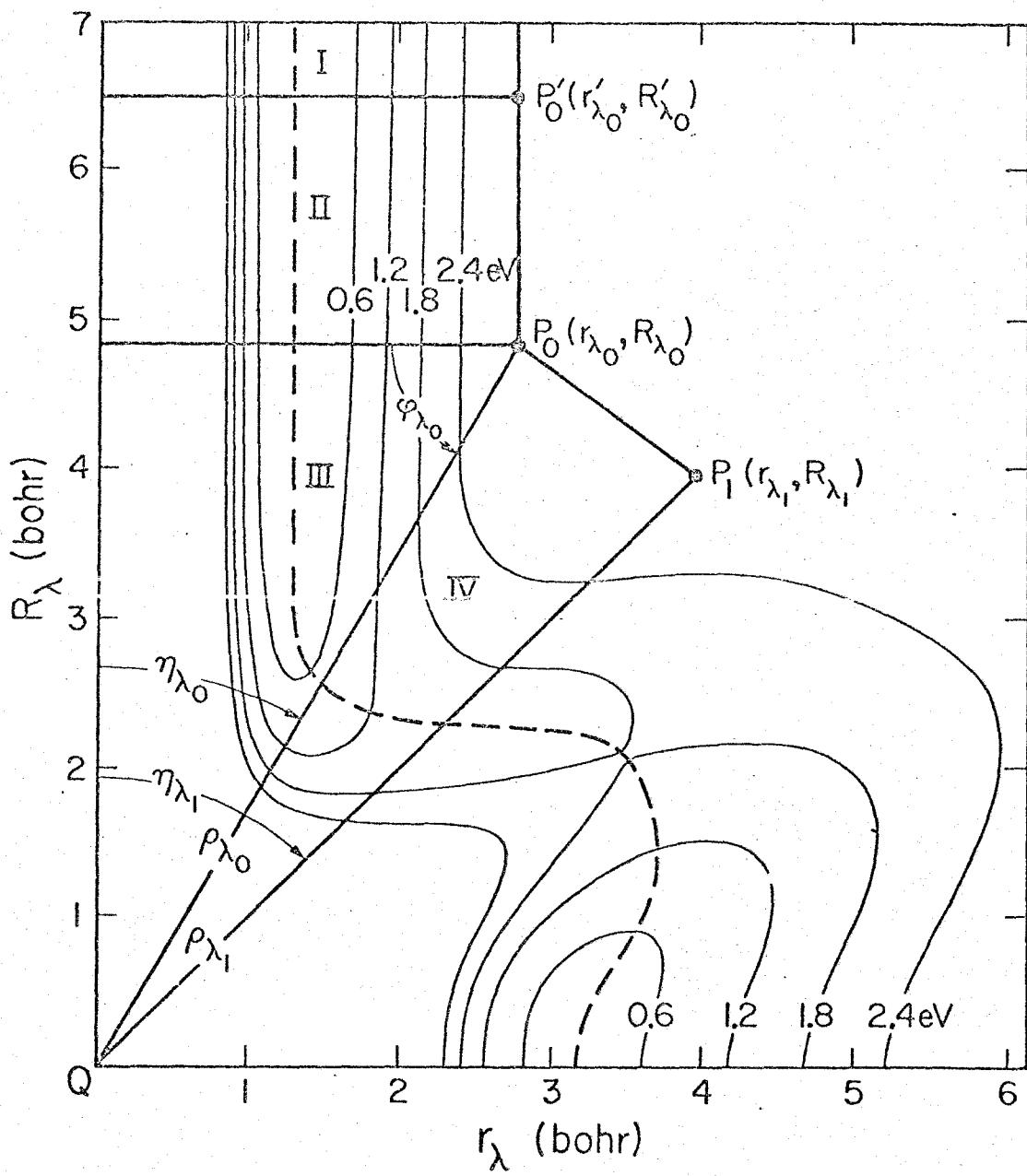
Figure 4
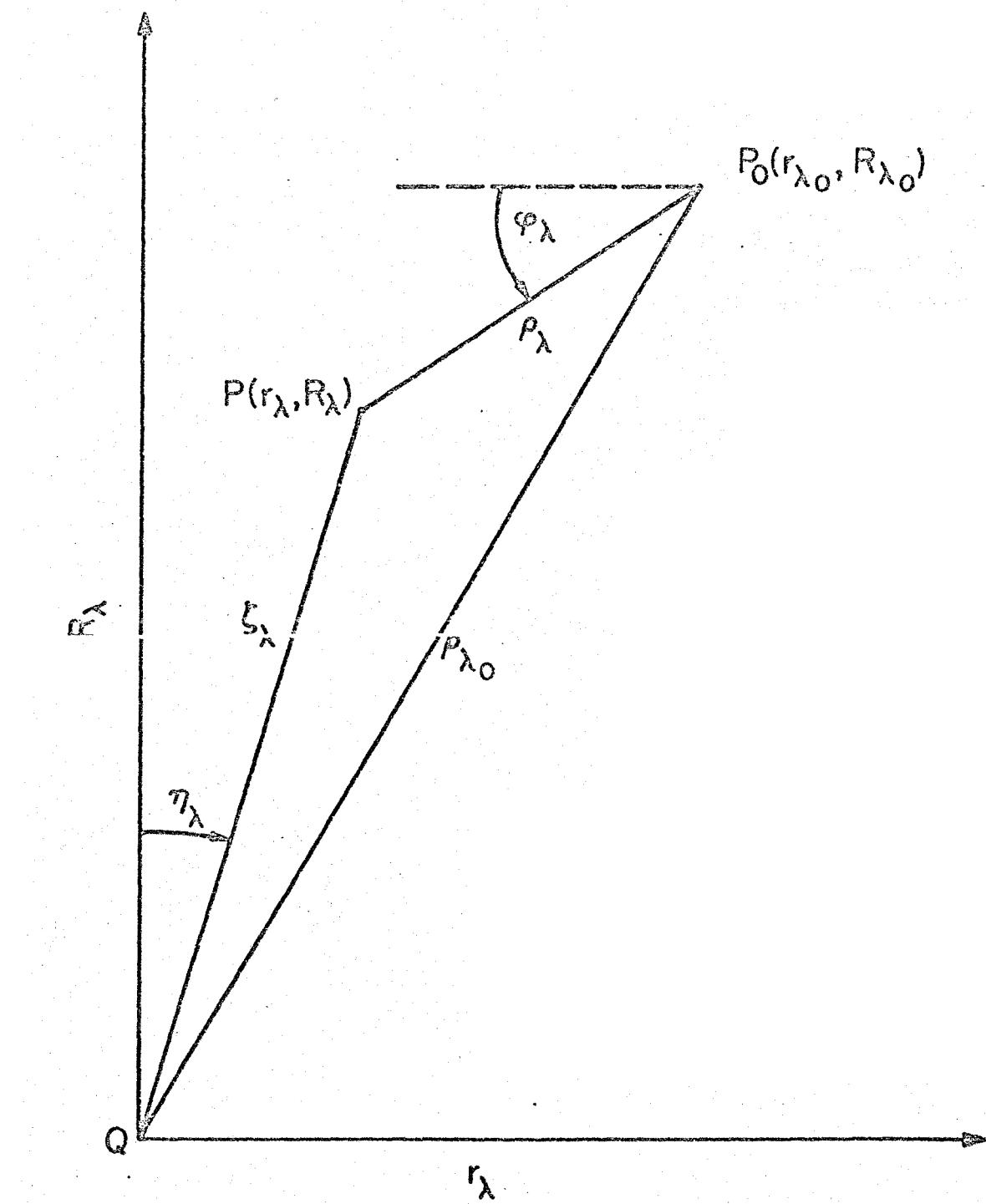
Figure 5

7. QUANTUM MECHANICAL REACTIVE SCATTERING FOR THREE DIMENSIONAL ATOM PLUS DIATOM SYSTEMS: II. ACCURATE CROSS SECTIONS FOR 3D H + H_2

Quantum mechanical reactive scattering for three dimensional atom plus diatom systems: II. Accurate cross sections for 3D H + H$_2$[*]

George C. Schatz[†] and Aron Kuppermann

Arthur Amos Noyes Laboratory of Chemical Physics,

Division of Chemistry and Chemical Engineering[‡],

California Institute of Technology, Pasadena, California 91125

Accurate three dimensional reactive and nonreactive quantum mechanical cross sections for the H + H$_2$ exchange reaction on the Porter-Karplus potential energy surface are presented. Tests of convergence in the calculations indicate a probable accuracy of better than 5% for most of the results in the energy range considered (0.3 to 0.7 eV total energy). The reactive differential cross sections are exclusively backward peaked with peak widths of about 32° at 0.4 eV changing to 51° at 0.7 eV. Nonreactive (inelastic) differential cross sections show backwards to sidewards peaking, while elastic cross sections are strongly forward peaked with a nearly monotonic decrease with increasing scattering angle. Some oscillations due to interferences between the direct and exchange amplitudes are obtained in the para to para and ortho to ortho (antisymmetrized) cross sections above the (effective) threshold for reaction. The reactive cross sections show significant rotational angular momentum polarization with the $m_j = m_{j'} = 0$ transition dominating for low j. In contrast, the (degeneracy averaged) rotational distributions can be fitted to tempera-

ture-like expressions to a high degree of accuracy. The integral cross sections have an effective threshold energy of about 0.55 eV, and differences of this quantity with the corresponding 1D and 2D results can largely be interpreted as resulting from bending motions in the transition state. In comparing these results with those of previous approximate dynamical calculations, we find best overall agreement between our reactive integral and differential cross sections and the quasi-classical ones of Karplus, Porter and Sharma [J. Chem. Phys. 43, 3259 (1965)] (at energies above the quasi-classical effective thresholds). This results in the near equality of the quantum and quasi-classical thermal rate constants at 600 K. At lower temperatures the effects of tunnelling become very important with the quantum rate constant larger than the quasi-classical one by factors of 3.2 and 18 at 300 K and 200 K, respectively.

1. INTRODUCTION

The H + H$_2$ hydrogen atom exchange reaction has been of fundamental theoretical interest in the field of chemical dynamics ever since the beginning of quantum mechanics. Great progress in our understanding of this simplest of chemical reactions has been made both in the accurate determination of the electronically adiabatic potential energy surface,[1] and in the calculation of accurate cross sections and other dynamical information.[2-13] A long sought objective of the dynamical studies has been the accurate quantum mechanical treatment of the three dimensional collision dynamics. Such an accurate ab initio understanding of H + H$_2$ is important, for this system has served as a prime example in the development and testing of approximate reaction dynamic theories such as quasi-classical methods,[2,10c] semi-classical methods[5,10d] and approximate quantum methods.[3,4,6,7,10,11] In addition, H + H$_2$ has been valuable in the development of transition state theory,[14,15] in the characterization of tunnelling[13a,16] and the concept of vibrational adiabaticity,[17] and in analyzing the effects of changes in the potential energy surface on the reaction dynamics.[18] Much of our understanding of the influence initial rotational[2] and vibrational[13a] state on the dynamics comes from studies on this system as does our knowledge concerning the influence of varying impact parameter[2,10c] or total angular momentum,[4,6,10ab] of resonance and direct reaction mechanisms,[2,19-21] and other dynamical effects. Nonreactive elastic and inelastic H + H$_2$ collisions have also been of theoretical interest in the analysis of rotational excitation and deactivation processes,[10,12,22,23,24,25]

and in examining the nature of the competition and interference between reactive and nonreactive processes.[10a,12b] A number of reactive and nonreactive experimental studies of H + H_2 and its isotopic counterparts have been done ranging from kinetic rate constant determinations,[26] to hot atom[27] and molecular beam[28] experiments. The interaction of theory and experiment has been of mutual benefit throughout their respective evolutionary developments.

In a previous paper[29] we presented a method for accurately solving the Schrödinger equation for the dynamics of the three dimensional collision of an atom with a diatomic molecule on a single electronically adiabatic potential energy surface. This method was an extension of an earlier coplanar method[30] which has since been used extensively to study 2D H + H_2.[12a,b] In this paper we present the results of an application of this 3D procedure to H + H_2. The results include reactive and nonreactive transition probabilities, integral and differential cross sections, and reagent and product rotational state distributions. These results will be thoroughly compared with those of earlier 3D approximate reactive and nonreactive calculations, and with 1D and 2D accurate ones. Some of the 2D - 3D comparisons were considered in preliminary communications,[8,21] and we shall elaborate upon them here by developing simple dynamical models for relating results of different dimensionality. Additional topics considered include the effects of indistinguishability of particles, angular momentum decoupling approximations, and thermal rate constants. In most calculations, we use the semi-empirical Porter-Karplus[1c] potential surface. This surface has been used in several

earlier studies, thus enabling comparisons of these results and ours without ambiguity being introduced by the use of different potentials. Some additional results for the more accurate surface of Liu[1f] (as parametrized by us) will also be given.

Section 2 provides a brief outline of the procedure used, and computational considerations governing convergence and accuracy of the results obtained. The results for the Porter-Karplus potential energy surface are given in Section 3, and Section 4 includes a summary of the more significant results presented. In Appendix A we examine the results of one very simple angular momentum decoupling approximation and in Appendix B we present some results for the Liu potential surface.

2. THE CALCULATION

2.1 General Description of the Method

The method used to solve the Schrödinger equation for three dimensional reactive and nonreactive $H + H_2$ collisions has been extensively described elsewhere.[29] The wave function describing the scattering process is first partial wave expanded and then transformed to a representation involving body fixed coordinates. The coordinates involved in this transformation are pictured in Fig. 1. The body fixed coordinates $Ox_\lambda'y'z_\lambda'$ are obtained from the space fixed $Oxyz$ by rotation through the Euler angles $\alpha = \phi_\lambda$, $\beta = \theta_\lambda$, $\gamma = \psi_\lambda$ where θ_λ, ϕ_λ are the polar coordinates of the vector $\underset{\sim}{R}_\lambda$ between the incident atom A_λ and diatomic molecule $A_\nu A_k$ (in arrangement channel coordinates λ). ψ_λ indicates the angle of rotation of the diatom (about $O z_\lambda'$) with

respect to the X_λ Z_λ plane in Fig. 1. In the body fixed system, the diatomic internuclear vector $\underset{\sim}{r}_\lambda$ between A_ν and A_k is referenced relative to $\underset{\sim}{R}_\lambda$ rather than to space fixed directions. (Note that we are not using scaled coordinates in this paper in contrast to Ref. 29). Rotational motion is described by quantum numbers j_λ and Ω_λ where the tumbling quantum number Ω_λ is associated with the component of rotational angular momentum along the $z_\lambda{}'$ (body fixed) axis. As shown in Ref. 29, the component of the orbital angular momentum about $z_\lambda{}'$ is zero, so Ω_λ is also associated with the projection of the total angular momentum along that axis. In order to simultaneously satisfy both criteria, Ω_λ must obey the inequality

$$\Omega_\lambda \leq \min (J, j_\lambda) \tag{2.1}$$

where J is the total angular momentum quantum number.

Of crucial significance in the body fixed coordinate system of Fig. 1 is the fact[29] that the kinetic energy operator couples vibration rotation states with different Ω_λ quantum numbers but the same vibrational and rotational ones $(v_\lambda j_\lambda)$, while the potential energy coupling is diagonal in Ω_λ but not in $v_\lambda j_\lambda$. This allows for the approximate separation of effects due to tumbling of the three atom plane about $z_\lambda{}'$ versus those due to potential interactions, and we shall examine this separation in Section 3. In addition, it provides for the natural development of centrifugal decoupling schemes, one of which is analyzed in Appendix A. Once the body fixed fully coupled Schrödinger equations are set up, they are then solved in two steps. The first one involves a numerical integration of these coupled equa-

tions through each arrangement channel region in coordinates appropriate to that region. This is followed by a second step in which the solutions thus generated in each of the three arrangement channel regions are smoothly matched to one another on a set of three surfaces which separate these regions. The resulting solutions, which should be smooth and continuous everywhere are then linearly combined to yield the appropriate reactance and scattering matrix solutions and these solutions for different partial waves are then combined to form the plane wave scattering solutions. By using helicity representation scattering amplitudes, we obtain a very simple relationship between these amplitudes and the body fixed scattering matrix $\underset{\approx}{S}_J$, namely (from Eq. 5.31 of Ref. 29),

$$
f^{\lambda'v'_\lambda j'_\lambda m'_{j_\lambda}}_{\lambda v_\lambda j_\lambda m_{j_\lambda}} = \left(\frac{V^\lambda_{v_\lambda j_\lambda}}{V^{\lambda'}_{v'_\lambda j'_\lambda}} \right)^{\frac{1}{2}} \frac{1}{2k^\lambda_{v_\lambda j_\lambda}} (i)^{j_\lambda - j'_\lambda + 1}
$$

$$
\times \sum_{J=0}^{\infty} d^J_{m_{j_\lambda} m'_{j_\lambda}} (\theta_{\lambda'}) (\delta^{\lambda'v'_\lambda j'_\lambda m'_{j_\lambda}}_{\lambda v_\lambda j_\lambda m_{j_\lambda}} \tag{2.2}
$$

$$
- S^{\lambda'v'_\lambda j'_\lambda m'_{j_\lambda}}_{J\lambda v_\lambda j_\lambda m_{j_\lambda}})
$$

where the reagent state has $m_{j_\lambda} = M = -\Omega_\lambda$ and the product state has $m'_{j_\lambda} = \Omega'_\lambda$. $V^\lambda_{v_\lambda j_\lambda}$ and $k^\lambda_{v_\lambda j_\lambda}$ represent the appropriate (unscaled) velocities and wave numbers and $d^J_{m_{j_\lambda} m'_{j_\lambda}} (\theta_\lambda)$ is a Wigner rotation function (in the notation of Davydov[31]) with $\theta_{\lambda'}$ the scattering angle.

For $H + H_2$, the problem can be simplified considerably because of arrangement channel symmetry and even-odd decoupling within each arrangement channel (as described in Ref. 29). A major consequence of these symmetry properties is that only two scattering amplitudes between a given initial state vjm_j and final state $v'j'm'_j$ (where m'_j is an abbreviation for $m'_{j'}$) need be considered, the non-reactive one (labelled N) and the reactive one (labelled R). Thus all the arrangement channel indices λ and λ' in Eq. 2.3 may be dropped as long as the symbols N or R are included as appropriate. As an additional consequence, nonreactive transitions between even and odd rotational states are forbidden. From the reactive and nonreactive scattering amplitudes f^N and f^R, one may then calculate differential (distinguishable atom) cross sections via:

$$\sigma^{N,R}_{vjm_j \to v'j'm'_j}(\theta) = \frac{V_{v'j'}}{V_{vj}} \left| f^{N,R}_{vjm_j \to v'j'm'_j} \right|^2 \tag{2.3}$$

so that the integral cross section is given by

$$Q^{N,R}_{vjm_j \to v'j'm'_j} = \frac{\pi}{k_{vj}^2} \sum_{J=0}^{\infty} (2J+1) \left| T^{N,R}_{J,vjm_j \to v'j'm'_j} \right|^2 \tag{2.4}$$

where

$$T^{N}_{J,vjm_j \to v'j'm'_j} = \delta^{v'j'm'_j}_{vjm_j} - S^{N}_{J,vjm_j \to v'j'm'_j} \tag{2.5a}$$

and

$$T^{R}_{J,vjm_j \to v'j'm'_j} = -S^{R}_{J,vjm_j \to v'j'm'_j} \tag{2.5b}$$

The transition probability $P^{N,R}_{J,vjm_j \to v'j'm'_j}$ is given by

$$P_{J, vjm_j \rightarrow v'j'm'_j}^{N,R} = \left| S_{J, vjm_j \rightarrow v'j'm'_j}^{N,R} \right|^2 \qquad (2.6)$$

Inclusion of parity symmetry in the calculation leads to the relation

$$\sigma_{vjm_j \rightarrow v'j'm'_j}^{N,R} = \sigma_{vj-m_j \rightarrow v'j'-m'_j}^{N,R} \qquad (2.7)$$

with analogous expressions valid for Q and P_J. The angle θ (or θ_{λ}) of Eq. 2.2 refers to the direction of the scattered H atom with respect to the reagent H atom beam. For reactive collisions, a more customary angle to use is θ_R which is the angle of the product H_2 with respect to the incident H, and is the supplement of θ (i.e., $\theta_R = \pi - \theta$).

For H + H_2, the physically measurable cross sections must be obtained from wave functions which have been properly antisymmetrized with respect to interchange of any two identical nuclei. This can be done by the technique of post-antisymmetrization as was detailed in Ref. 29, and leads to the following indistinguishable atom differential cross sections (labelled by the symbol A):

$$\sigma^A_{vjm_j \to v'j'm'_j} = \frac{V_{v'j'}}{V_{vj}} \times \begin{cases} \left| f^N_{vjm_j \to v'j'm'_j} - f^R_{vjm_j \to v'j'm'_j} \right|^2 \\ \quad (j, j' \text{ even, para} \to \text{para}) \\[6pt] 3 \left| f^R_{vjm_j \to v'j'm'_j} \right|^2 \\ \quad (j \text{ even, } j' \text{ odd, para} \to \text{ortho}) \\[6pt] \left| f^R_{vjm_j \to v'j'm'_j} \right|^2 \\ \quad (j \text{ odd, } j' \text{ even, ortho} \to \text{para}) \\[6pt] \{ \left| f^N_{vjm_j \to v'j'm'_j} + f^R_{vjm_j \to v'j'm'_j} \right|^2 \\ \quad + 2 \left| f^R_{vjm_j \to v'j'm'_j} \right|^2 \} \\ \quad (j, j' \text{ odd, ortho} \to \text{ortho}) \end{cases} \tag{2.8}$$

For even j to odd j (odd j to even j) transitions, the antisymmetrized and reactive cross sections are proportional, with a multiplicative factor of 3 (1), so either quantity gives equivalent information. For other transitions, there will be interference between direct and exchange amplitudes as is implied in Eq. 2.8.

Since the rotational sublevels for a given vibration-rotation state are degenerate, we may define both integral and differential degeneracy averaged cross sections by (valid for R, N or A transitions):

$$\sigma_{vj \to v'j'} = \frac{1}{2j+1} \sum_{m_j} \sum_{m'_j} \sigma_{vjm_j \to v'j'm'_j} \tag{2.9}$$

and

$$Q_{vj \to v'j'} = \frac{1}{2j+1} \sum_{m_j} \sum_{m'_j} Q_{vjm_j \to v'j'm'_j} \qquad (2.10)$$

We may also sum these cross sections over all final states, obtaining

$$\sigma^N_{vj} \to \sum_{v'j'} \sigma^N_{vj \to v'j'} \qquad (2.11)$$

$$\sigma^R_{vj} = 2 \sum_{v'j'} \sigma^R_{vj \to v'j'} \qquad (2.12)$$

$$\sigma^A_{vj \to (\text{para, ortho})} = \sum_{v'} \sum_{j'} \sigma^A_{vj \to v'j'} \qquad (2.13)$$

$$(j' \text{ even (para)})$$

$$(j' \text{ odd (ortho)})$$

with analogous expressions holding for the integral cross sections with Q substituted for σ. The factor of 2 in Eq. 2.11 arises from a sum over the two equivalent reactive arrangement channels (in a distinguishable atom sense). The final state sum in Eq. 2.12 refers specifically to final ortho or para states as is appropriate.

2.2 Convergence and Accuracy Tests, Details of the Calculation

In order to establish the reliability of the results of these calculations, a number of convergence and accuracy tests were performed, including (a) tests of flux conservation and microscopic reversibility, (b) tests of invariance of the results with respect to the inclusion of additional vibrational or rotational basis functions in the close coupling expansion, (c) tests of invariance of the results with respect to a change in the number of terms used to expand the potential (see Eq. 2.14 below), and (d) tests of invariance of the results with

respect to a change in the nature of the reference potential $V_{ref}(r_\lambda, R_\lambda)^{29}$ used to generate vibrational basis functions for the integration. Two additional tests are (e) of invariance with respect to a change in the matching surface basis functions, and (f) of the effects of lack of completeness of these matching surface functions on the ortho to para nonreactive transition probabilities. These latter two tests were not performed, but the analogous planar tests[12b] indicated that both effects were not important in that calculation. Since comparable planar and 3D vibration rotation basis sets were used in the two sets of calculations, we have assumed that the matching surface basis functions of Eq. 4.28 of Ref. 29 will produce adequate (5% or better) convergence of the 3D results.

Conservation of flux and microscopic reversibility may be tested by examining the probability matrices for each partial wave, an example of which is given in Table I for total energy E = 0.6 eV and J = 0. Flux conservation requires that the sum of each row or column of $\underset{\sim}{P}_J$ should equal unity, while microscopic reversibility requires that $\underset{\sim}{P}_J$ be symmetric. In the table we see that both of these properties are well satisfied (0.18% maximum deviation from flux conservation and < 3% from symmetry for those probabilities > 1 x 10^{-4}). In the results presented in this paper, we consider the energy range 0.3 to 0.7 eV. For energies E in the range 0.3 eV to 0.6 eV, we find maximum deviations from flux conservation of 1% and from symmetry 10% (for non-negligible probabilities). Between 0.6 and 0.7 eV we find 4% deviations from flux conservation and 15% from symmetry. In order to obtain results of this quality, we used

the vibration rotation basis sets specified in Table II. For $J = 0$, Eq. 2.1 greatly reduces the number of channels coupled, thus reducing computation time, allowing us to use more complete basis sets. This leads to excellent results for the $J = 0$ probabilities (similar or better than those in Table I at all energies considered). However, for larger J, the number of projections Ω increases greatly. This leads to prohibitively large computation times if basis sets analogous to those for $J = 0$ are used. The ones actually used are those described in Table II. The above mentioned accuracy limits were obtained with them.

Convergence with respect to the inclusion of additional vibrational or rotational channels is examined in Table III. In part (A) of that table, we examine several important transition probabilities at $E = 0.65$ eV, $J = 1$ for three different rotational basis sets (all with four vibrations). Upon changing from a $j_{max} = 5$ to $j_{max} = 6$ basis set, we find changes of less than 1% in all probabilities. In part (B) we examine several 0.65 eV, $J = 0$ probabilities with 4 and 5 vibrations (all with $j_{max} = 7$). Here we find 4% maximum change. An examination of the nature of the convergence properties with respect to the inclusion of additional basis functions was examined in greater detail in the planar calculation[12b] where we found that typically 4 vibrations and $j_{max} = 5$ were required for 5% convergence. A less extensive study of the three dimensional results indicates similar convergence properties and the results of Table III are in agreement with this statement.

The two criteria (c) and (d) mentioned at the beginning of this section refer to changes in the representation of the potential

$V^{\lambda}(r_{\lambda}, R_{\lambda}, \gamma_{\lambda})$ (where γ_{λ} is the angle between R_{λ} and r_{λ} (Fig. 1)), and in the character of the reference potential $V^{\lambda}_{ref}(r_{\lambda}, R_{\lambda})$ used to generate the vibrational eigenfunctions. As detailed in Ref. 29, the potential is expanded in a series of Legendre polynomials

$$V^{\lambda}(r_{\lambda}, R_{\lambda}; \gamma_{\lambda}) = \sum_{k=0}^{\infty} V^{\lambda}_k(r_{\lambda}, R_{\lambda}) P_k(\cos \gamma_{\lambda}) \qquad (2.14)$$

where, for an atom plus homonuclear diatomic molecule system like $H + H_2$, the sum on k includes only even terms. In an actual calculation, Eq. 2.14 is truncated after n terms (such as n = 3). This procedure is justified if the resulting probabilities are not significantly changed when an additional term is added. To evaluate the effects of changing n, we compare in Table IV the results of calculations with n = 2, 3, 4 and 5 [32] for selected transition probabilities at two different energies. Although the n = 2 results are often significantly in error (by as much as 30%), we find less than 7% changes in going from n = 3 to n = 4 and virtually no change at all in going from n = 4 to n = 5. All calculations of this paper other than those whose results are presented in Table IV used n = 3. The reference potential V^{λ}_{ref} which is used to numerically generate the vibrational basis functions according to the procedure of Ref. 29 suffers from a lack of uniqueness in the interaction region due to nonseparability of vibrational motions from translational or rotational ones. In the coplanar calculations, two different choices of the reference potential $(V^{\lambda}_{ref} = V(r_{\lambda}, R_{\lambda}, \gamma_{\lambda} = 0)$ and $V^{\lambda}_{ref} = V^{\lambda}_0(r_{\lambda}, R_{\lambda}))$ were used. A comparison of these calculations indicated that for basis sets with four or

more vibrations, the results changed by less than 5% between the two

reference potentials. A limited number of three dimensional calcula-

tions indicates that behavior is comparable to the planar case.

3. RESULTS FOR THREE DIMENSIONAL $H + H_2$

3.1 Transition Probabilities

In this section we examine the J dependence of the reactive

and inelastic transition probabilities in the energy range 0.3 to 0.7 eV.

Figures 2a and 3a present the reactive probabilities $P^R_{J,00 \to 01}$ (summed

over final m'_j). These figures indicate that the probability is a rapidly

decreasing function of J with a peak near J = 0 for all but the highest

energy considered. If we define J_{MAX} as the lowest value of J for

which $P^R_{J,vj \to v'j'}$ has decreased to less than 1% of its maximum value,

then J_{MAX} = 4 at 0.3 eV and increases monotonically to about 10 at

0.7 eV. The contributions of these transition probabilities to the

integral reaction cross sections are weighted by the factor 2J + 1

(see Eqs. 2.5 to 2.7). Figures 2b and 3b depict the product (2J + 1) ×

$P^R_{J,00 \to 01}$, and we see that the partial wave which gives the largest

contribution to $Q^R_{00 \to 01}$ varies from J = 1 at 0.3 eV to J = 4 at 0.7 eV.

To examine the contributions of the different projection quantum

numbers to the curves in Figs. 2a and 3a, we plot in Fig. 4 the

reaction probabilities $P^R_{J,000 \to 01m'_j}$ for m'_j = 0, ±1 (and their sum)

at E = 0.6 eV. It is apparent from the figure that m'_j = 0 makes the

dominant contribution to $P^R_{J,00 \to 01}$ for this transition at all J for which

the transition probability is non-negligible. The m'_j = ±1 probability

(which, from Eq. 2.7 is independent of the sign of m'_j) shows a peak

near J = 4 followed by a somewhat slower decrease with increasing J than is exhibited by the $m'_j = 0$ probability. An examination of other transition probabilities at 0.6 eV indicates that in general, the $m_j = 0$ to $m'_j = 0$ reaction probability is the dominant one for a given vj and v'j'. This effect becomes less important as both J, j or j' increase as is illustrated in Fig. 5 for the probability $P^R_{J, 000 \to 03m'_j}$, but it remains a general fact that the $m_j = m'_j = 0$ transition probability is the largest one for $J < J_{MAX}$ and $j \le 4$. This statement is also true for other energies considered. Its effect on the integral cross sections will be discussed in Section 3.3.

Let us now consider the meaning of this rotational projection quantum number "quasi selection rule." Recall that $\Omega = -m_j$ initially so that $m_j = 0$ implies (for nonzero j) that the direction of rotation is perpendicular to the direction of approach, as is schematically indicated in Fig. 6. In this situation, we find that twice during each diatom rotation, the three atoms are completely collinear (for zero impact parameter collisions). For the Porter-Karplus potential used,[1c] linear orientations greatly favor reaction over other orientations. (The linear barrier height is 0.396 eV while the perpendicular one is about 2.8 eV) For collisions where $m_j \ne 0$, the rotational wave function $Y_{j_\lambda m_{j_\lambda}}(\gamma_\lambda, \psi_\lambda)$ has a node at $\gamma_\lambda = 0$ so that there is zero probability density for strictly collinear zero impact parameter collisions. (All of these considerations, of course, apply before the incident atom begins perturbing the diatom target.) Thus we see that only for $m_j = 0$ can the system assume initially the linear orientation favorable to

reaction. After the collision, $m'_j = \Omega'$ so that again only for $m'_j = 0$ can we have a linear orientation after the collision (regardless of the scattering angle). We should also note that the rotational period $(2.7 \times 10^{-13}/[j(j+1)]^{\frac{1}{2}} \text{ sec})^2$ is generally larger than the interaction time (which is less than $3 \times 10^{-14} \text{ sec}^{33}$ for the energies considered here) so that the rotational motions are generally slow compared to collision times at these energies and the collision orientation does not change rapidly during the approach and departure steps. All of this indicates that the $m_j = m'_j = 0$ reaction probability should be larger than all others in agreement with our results. It also indicates why this rule becomes less rigid for large J (where nonzero impact parameter collisions can lead to linear orientations for $m_j, m'_j \neq 0$) and for large j (where the diatom rotates fast enough to change the collision orientation rapidly during the collision thus reducing the advantage of a linear orientation at any one point during the collision). As a second prediction of this model, we would expect that those transition probabilities for which $m_j = 0$ or $m'_j = 0$ (but not both) should dominate over those for which neither m_j nor m'_j are zero. We shall see in Section 3.3 that this prediction is correct. We emphasize that this projection quantum number selection rule depends on (a) a potential surface which favors linear orientations, and (b) projection quantum numbers referenced relative to the body fixed coordinate system of Fig. 1. The latter reason is important because it singles out the m_j or $m'_j = 0$ collisions as leading to a linear collision orientation with a greater probability than m_j or $m'_j \neq 0$. By rotating the quantization axis to another direction (such as perpendicular to the three atom plane

as is done for the coplanar reaction, or along a space fixed direction), we would not be able to unscramble the information as easily.

Figure 7 shows the J dependence of the phases of the scattering matrix elements $S_{J,000 \to 01m'_j}^R$ for $m'_j = 0, \pm 1$ at 0.6 eV (the same transitions considered in Fig. 4). It is important to note that the phase is most slowly varying near $J = 0$. Semi-classically this implies that the deflection angle should be small for small impact parameter collisions. This implies that a small scattering angle θ will result from these low J collisions, or, equivalently, a reactive scattering angle θ_R near $180°$.

In Fig. 8a we examine the nonreactive transition probability $P_{J,000 \to 02m'_j}^R$, and its sum over final m'_j at 0.6 eV as a function of J. Here we find $J_{MAX} = 30$ so that a much larger number of partial waves contribute to the nonreactive cross section than is the case for the reactive transitions in Figs. 2 - 5. Note that the $m'_j = 0$ transition probability is dominant only for very small J (< 6) indicating that the linear orientation rule is probably not significant here (as might be expected for a nonreactive collision where the nature of the potential in the transition state is of lesser significance than it is for reactive collisions). An examination of other nonreactive transition probabilities indicates no strong tendency for a $m_j = - m'_j$ ($\Omega = \Omega'$) selection rule as has often been assumed in rotationally inelastic scattering,[34] thus indicating that the strong coupling or sudden limit does not apply to $H + H_2$ inelastic collisions for the potential used. We shall examine this again in Appendix A for reactive collisions. The transition probabilities of Fig. 2a may also be expressed in terms of the orbital

angular momentum quantum number 1 (as might be used in a space fixed analysis) by performing a unitary transformation on the body fixed scattering matrix (see Eqs. 5.14 and 5.15 of Ref. 29). Figure 8b indicates the resulting transition probabilities (the sum over projections being an invariant). Here we again see no particular selection rule governing the transition probabilities.

3.2 Differential Cross Sections

In Figs. 9 and 10 we plot the antisymmetrized para to ortho differential cross sections $\sigma^A_{00 \rightarrow 01}$ as a function of the reactive scattering angle θ_R. From Eqs. 2.4 and 2.8 it should be apparent that these cross sections are just three times the distinguishable atom $\sigma^R_{00 \rightarrow 01}$. We see in both figures that the reactive cross section is strongly backward peaked at all energies considered in the calculation. The width of the backward peak at half maximum is $48°$, $32°$, $33°$, $41°$ and $51°$ at $E = 0.3$, 0.4, 0.5, 0.6 and 0.7 eV, respectively. At the energetic threshold of the process considered, one would normally expect isotropic scattering since only the $J = 0$ partial wave would contribute to the cross section. At 0.3 eV, Fig. 2 indicates still a very small number of significant partial waves ($J_{MAX} = 4$) so the backward peak is still rather broad. The width of this backward peak decreases above 0.3 eV to a minimum near 0.4 eV. As E increases above that, the width begins to increase, presumably as a result of increased contributions of larger impact parameter collisions (from Figs. 2, 3) to the reaction cross section.

As was the case in the coplanar reaction,[12b] the shape of the

differential cross section is a sensitive test of the accuracy of the calculation. Small fluctuations of either the magnitudes or phases of the scattering matrix elements from their correct values for any partial wave can result in spurious oscillations in the differential cross sections. In addition, premature truncation of the partial wave sum (Eq. 2.2) can lead to a spurious forward peaking. In order to avoid spurious oscillations in the cross sections, we checked convergence at several values of J (by the criteria of Section 2.2) and found that reasonably uniform convergence had been attained at all J. (Recall from Table II that the nature of the vibration rotation basis set has to be changed for each J (J $\leq$ 4).) Premature truncation of the partial wave sum was avoided by requiring that the reactive probabilities at the cutoff value J_c be at least 10^{-4} times those at J = 0. In general, we found $J_c \sim J_{MAX} + 5$. Both Figs. 9 and 10 show essentially no indication of spurious oscillations or forward peaking (typically the θ_R = 0 cross section is 200 to 1,000 times smaller than the $\theta = 180°$ result). We should also note that the appearance of Figs. 9 and 10 is quite typical of all degeneracy averaged para to ortho and ortho to para cross sections.

To examine the m_j dependence of the differential cross sections, we plot $\sigma^A_{000 \to 03m'_j}$ for m'_j = 0, ±1, ±2, ±3 . (and their sum) in Fig. 11. Here we see that only the m'_j = 0 projection gives backward scattering. As $|m'_j|$ increases from zero, we find a shift towards more forward scattering with the cross sections peaking at θ_R = 139°, 117° and 102° for $|m'_j|$ = 1, 2, 3, respectively. Much of the structure of the angular distributions in Fig. 11 can be

understood by examining Eq. 2.2 where we find[31] that $d_{0m'_j}^J(\theta)$ is proportional to $(\sin\theta)^{m'_j}$ times a polynomial in $\cos\theta$. Since $\theta_R = \pi - \theta$, the $\sigma_{000 \to 03m'_j}^A$ should have a $(\sin\theta_R)^{2m'_j}$ envelope and should consequently vanish at $\theta_R = 0°$ and $180°$. Indeed, one can qualitatively obtain the $m'_j = \pm 1$ curve by multiplying the $m'_j = 0$ curve by $\sin^2\theta_R$ and similarly for the higher m'_j curves. The vanishing of the $m'_j \neq 0$ cross sections at $\theta_R = 0°$ and $180°$ is also a consequence of angular momentum conservation. To see this, we recall that the incident plane wave solution is an eigenfunction of J_z, the operator corresponding to the projection of the total angular momentum along the space fixed z axis, with eigenvalue $M = m_j$ (since m_1 is initially zero for the plane wave solution). Since J_z commutes with the Hamiltonian[35], M will be a good quantum number. This is true for any collision, but in the particular case where $\theta_R = 0°$ (180°), the final z'_λ axis[36] will be antiparallel (parallel) to the initial z axis, so that the outgoing projection quantum number Ω must equal $-M$ (+M). From this and the discussion following Eq. 2.3, we find that $m_j = M = -\Omega' = -m'_j$ for $\theta_R = 0°$ and $m_j = M = \Omega' = m'_j$ for $\theta_R = 180°$. For $\sigma_{000 \to 03m'_j}^A$, $m'_j = 0$ is required for both $\theta_R = 0°$ or $180°$ and hence $m'_j \neq 0$ projections cannot satisfy angular momentum conservation in these two directions. Finally we should point out that the dominance of the $m'_j = 0$ component of $\sigma_{000 \to 03m'_j}^A$ in Fig. 11 is again a consequence of the favored linear transition state geometry. The $m'_j = 0$ collisions for small impact parameters have a significant probability for a linear or nearly linear collision which should lead to the observed dominant backward scattering. For

$m'_j \neq 0$, the collision configurations must be nonlinear (at least in the product arrangement channel) and we would expect to see the sidewards scattering exhibited in Fig. 11.

In Fig. 12 we plot the nonreactive differential cross sections $\sigma^N_{000 \to 02m'_j}$ ($m'_j = 0, \pm1, \pm2$ and summed) at $E = 0.6$ eV as a function of θ. Here the predominant scattering direction is approximately $90°$ although significant cross sections are obtained at all angles. The forward peaking in the $m'_j = 0$ component and forward oscillations in the remaining curves in the figure are probably spurious artifacts introduced by small errors in the phases of certain large J elements of $\underset{\approx}{S_J}$ (see related discussion of Ref. 22). Much of our previous analysis regarding the angular dependence of individual m'_j cross sections applies to Fig. 1 as well so we shall not repeat it. We note, however, that the absence of a linear or near linear orientation restriction in nonreactive collisions leads to significant cross sections at all scattering angles. Since the $j = 0$ to $j' = 2$ transition can occur by both nonreactive and reactive mechanisms, the more meaningful quantity to consider is the antisymmetrized cross section of Eq. 2.8. In Figs. 13, 14 and 15 we plot this para to para cross section $\sigma^A_{00 \to 02}$ (summed over m'_j) along with the nonreactive and reactive counterparts at $E = 0.5$, 0.6 and 0.7 eV. At the lowest energy, the reactive cross section is typically three orders of magnitude smaller than the nonreactive one, so the resulting para to para cross section is dominated by the direct amplitude and differs very little from its nonreactive counterpart. As the energy is increased, the reactive amplitude increases rapidly and begins to interfere significantly with

the nonreactive one. This results in the oscillations observed in $\sigma^A_{00 \to 02}$ in Figs. 14 and 15. The period of these quantum symmetry oscillations seems to be roughly $10 - 15°$ in both Figs. 14 and 15 for $\theta < 90°$ with a gradual increase in period with increasing θ until the oscillations wash out completely at large θ. Figures 13 to 15 also indicate that the peak in $\sigma^N_{00 \to 02}$ shifts gradually to forward scattering angles as the energy is increased. The contributions of different m'_j to the $\sigma^A_{00 \to 02}$ at 0.7 eV are shown in Fig. 16 (along with the distinguishable atom $\sigma^N_{000 \to 02m'_j}$ for comparison). We see that the $m'_j = 0$ cross section in that figure has the largest oscillations followed by $m'_j = \pm 1$ and then $m'_j = \pm 2$. This results from the dominant contribution of the $m'_j = 0$ reactive scattering amplitude (as evidenced in Fig. 11) followed by $m'_j = \pm 1$ and finally $m'_j = \pm 2$. Note also that the phases of the oscillations in Fig. 16a,b,c are not particularly coherent, so that a certain amount of cancellation occurs in the sum over projections (which is shown in Fig. 15).

3.3 Integral Cross Sections

A number of reactive, nonreactive and antisymmetrized integral cross sections are listed in Table V. Some of the reactive and para to ortho cross sections of that table are plotted as a function of energy in Fig. 17. Both logarithmic and linear scales are used to exhibit both the tunnelling and threshold regions. If we define the effective threshold energy E_T as that energy for which the cross section is 0.05 bohr^2, then $E_T = 0.545$ eV, 0.550 eV and 0.615 eV for Q^R_{00}, $Q^A_{00 \to 01}$ and $Q^A_{00 \to 03}$, respectively. Alternatively, since the high

energy dependence of the cross sections is linear, we could define an effective threshold energy E_T' as the energy to which a line fitted to these linear points extrapolates in the limit of zero cross section. From this definition, we find $E_T' = 0.568$ eV, 0.565 eV and 0.605 eV for these same cross sections. Either way we find that the threshold energies are considerably above the barrier height (0.396 eV) and this difference will be discussed in detail in Section 3.5. At energies below threshold, the effects of tunnelling give the cross section an approximately exponential behavior.

To examine the m_j dependence of the cross sections, we list in Table VI a portion of the "cross section matrix" $Q^R_{0jm_j \to 0j'm'_j}$ for $j, j' \leq 2$ at 0.6 eV. (Note that these cross sections are distinguishable reactive ones.) The table indicates that the $m_j = m'_j = 0$ cross section is typically 10 to 20 times larger than any other cross section with the same vj and $v'j'$. In addition, for a given m_j, Q is a decreasing function of increasing $|m'_j|$ (and, by microscopic reversibility, Q decreases with increasing $|m_j|$ for a given m'_j). These observations are indicative of the very significant rotational angular momentum polarization effect that can occur when only a restricted range of geometries can lead to reaction. This approximate selection effect breaks down eventually for large enough j or j'. Let us consider the cross sections $Q^R_{000 \to 0j'm'_j}$ for varying j' and m'_j at 0.6 eV. The ratio of the $m'_j = 0$ to $m'_j = \pm 1$ cross section is 22.3 for $j' = 1$ decreasing to 7.1 for $j' = 2$, 3.1 for $j' = 3$ and 1.1 for $j' = 4$. The $j' = 1$ ratio is 10.6, 24.7, 24.9, 22.3 and 14.7 at $E = 0.3$, 0.4, 0.5, 0.6 and 0.7 eV, respectively, indicating that this selection rule is most rigorously obeyed

in the intermediate range of energies just below the effective threshold energy. We shall examine the rotational energy dependence of the j and j' distributions in Section 3.6.

The nonreactive cross sections $Q_{00 \rightarrow 02}^{N}$ are listed in Table V. At 0.6 eV, the $Q_{000 \rightarrow 02m'_j}^{N}$ have values of 3.01, 3.31 and 1.67 bohr^2 for $m_{j'} = 0$, ± 1 and ± 2 indicative of the lack of strong rotational angular momentum polarization effects such as are observed with the reactive cross sections. Table V also indicates that the $Q_{00 \rightarrow 02}^{N}$ and $Q_{00 \rightarrow 02}^{A}$ are identical in magnitude except at the highest energy considered. An additional discussion of the energy dependence of these nonreactive cross sections is given in Section 3.7.

3.4 Elastic and Total Cross Sections

The calculation of converged elastic cross sections requires a large number of partial waves (up to 70 at 0.70 eV). Since the Porter-Karplus surface has a repulsive exponential long range functionality[1c] rather than the correct attractive R_λ^{-6} dependence[37] a fully coupled calculation of the elastic cross sections for the purpose of comparison with experiments[37] on this and related systems would not be worthwhile. At several energies, however, we found that a very accurate extrapolation to obtain the required large J phase shifts could be accomplished. For J large enough so that both reactive and inelastic nonreactive transition probabilities are negligible, it is often the case that the elastic phase shifts have not yet decayed to zero. Since these large J collisions correspond to large impact parameters, we would expect that only the isotropic

tail of the potential is important. In such circumstances, a central field, single channel model of the potential should suffice to predict these phase shifts. Using a standard central potential integration routine[38] with the spherically averaged potential $V_0(r_e, R)$ of Eq. 2.14 where r_e is the equilibrium internuclear distance, we have calculated the elastic $v = j = 0$ phase shifts at the energies considered in Table V. Typical results are presented in Fig. 18 where we have also plotted the phase shift of the exact scattering matrix elements ($\frac{1}{2}$ Arg $(S^N_{J,000 \to 000})$). The figure indicates that the accurate phase shifts are essentially identical to their central field counterparts for $J > 10$. Indeed, between $J = 11$ and $J = 39$ (the highest J for which a fully coupled calculation was done), the difference between these two phase shifts is always less than 0.05 rad and usually less than 0.02 rad. This is rather interesting, for the modulus of $S^N_{J,000 \to 000}$ is not even close to unity as is illustrated in Fig. 18 with a plot of the elastic transition probability $|S^N_{J,000 \to 000}|^2$. This presumably indicates that the phases of the scattering matrix elements are much less sensitive to the presence of reactive and inelastic channels than are the moduli. By using these elastic central field phase shifts, we can now extrapolate the large J behavior of the converged results and thus calculate accurate elastic cross sections.[39] Typical results for $\sigma^N_{000 \to 000}$ at $E = 0.7$ eV are plotted in Fig. 19. The elastic differential cross section shows strong forward peaking with a small oscillation near $\theta = 6°$ and otherwise decreases in a nearly monotonic manner to $\theta = 180°$. The $\theta = 110°$ to $180°$ behavior of $\sigma^N_{000 \to 000}$ is probably not accurately characterized since the small cross sections in this

region must result from extensive cancellation in the partial wave sum (Eq. 2.2) and are easily modified by small errors in the scattering matrix elements. Also plotted on the same graph are the central field elastic cross section $\sigma^E_{000 \to 000}$ and the total cross σ^T_{000} (which is the sum of the cross sections for all possible processes (N or R) starting from reagents with $v = j = m_j = 0$). We see that all three cross sections are essentially identical for $\theta < 30°$. Even for very large scattering angles σ^T_{000} and $\sigma^E_{000 \to 000}$ agree to within better than a factor of 2. Moreover, the integral cross sections Q^T_{000} and $Q^E_{000 \to 000}$ are 221.0 bohr^2 and 220.8 bohr^2 respectively indicating that Levine's conservation of total cross section rule[40] is obeyed quite accurately for this system. We should, however, point out that the above mentioned total cross section is considerably larger than the recently measured experimental one[37] (for $D + H_2$) which is about 151 bohr^2 at 0.75 eV. If the antisymmetrized cross section $\sigma^A_{000 \to 000}$ is considered, we find that quantum symmetry effects due to interference between the elastic and reactive scattering amplitudes are much less significant than they were with the inelastic transitions in Fig. 15. Nevertheless, oscillations in this cross section can result in differences between σ^A and σ^N as big as 10% of σ^N for scattering angles between 30° and 90°.

3.5 Comparison of Collinear, Coplanar and Three Dimensional Results

In the analysis of the coplanar results,[12b] it was determined that a physically meaningful comparison of the 1D and 2D results could be obtained by examining the $J = 0$ total reaction probabilities. We

extend this comparison in Figs. 20 and 21 by plotting the 1D[21,41]

2D and 3D total reaction probabilities $P_{00}^R(J = 0)$ [P_0^R for 1D] as a

function of E. Both logarithmic and linear scales are used so as to

enable examination over a wide energy range. The figures indicate a

surprisingly similar energy dependence over several orders of

magnitude of probabilities. There are, however, two important

differences both of which provide significant insight into the dynamics.

First, an energy shift of about 0.05 eV occurs in going from 1D to 2D

and again in going from 2D to 3D. In the coplanar analysis,[12b] we

explained the 1D to 2D shift as arising from additional bending energy

required in the coplanar transition state over the linear one. This

bending energy is added to the symmetric stretch energy of the collinear

transition state which, in turn, is primarily responsible for the shift

in the collinear effective threshold energy over the barrier height

energy[13] (0.396 eV). In the three dimensional case, the bending mode

of the transition state is doubly degenerate so that a second quantum

of bending energy (approximately the zero point energy which is

0.06 eV) will be required. Indeed, an examination of Fig. 20 indicates

that the 1D to 2D and 2D to 3D shifts are identical to within the

accuracy to which the probabilities can be interpolated. The second

difference between 1D, 2D and 3D results lies in the magnitudes of

the maximum probabilities in Fig. 21. The collinear probability

peaks near unity while the planar one levels off at about 0.6, and the 3D

one at roughly 0.45. The difference between the 1D and 2D plateau

values has been previously analyzed[12b] in terms of the orientation

dependence of the 2D probability. Since the potential barrier varies

from 0.396 eV at $\gamma_\lambda = 0$ to 2.8 eV at $\gamma_\lambda = 90°$ [1c], one would expect

a decreasing probability of reaction with increasing γ_λ (assuming that

we can consider the orientation of the atom with respect to the diatom

as fixed throughout the reaction). If we consider that the total reaction

probability is unity for $0 \leq \gamma_\lambda \leq \bar{\gamma}_\lambda$ and zero for $\bar{\gamma}_\lambda \leq \gamma_\lambda \leq 90°$, and use

symmetry about $90°$ for $90° \leq \gamma_\lambda \leq 180°$, then we find that $P_{00}^R(2D) =$

$2\bar{\gamma}_\lambda/\pi$ and $P_{00}^R(3D) = 1 - \cos \bar{\gamma}_\lambda$. In the 2D case, we find that $\bar{\gamma}_\lambda = 54°$

is required to give a reaction probability of 0.6. This estimate of

$\bar{\gamma}_\lambda$ is in approximate agreement with previous estimates of this angle

from a classical analysis.[2] The same angle used in the 3D formula

yields $P_{00}^R(3D) = 0.41$ which is not considerably different from the

observed value of 0.45. This indicates that the 2D and 3D orientation

dependence is probably quite similar with primarily dimensionality

considerations responsible for the difference in reaction probabilities.

At least two procedures for converting 2D integral or differential

cross sections into 3D ones have been proposed[10,42] both of which use

semi-classical arguments in making the connection. We will leave a

thorough analysis of these conversion procedures to a future publica-

tion, preferring instead to concentrate on approximate 3D procedures

which require comparable or smaller amounts of computation time

than the 2D calculation while providing 3D information directly. (See

Appendix A.) We would like to point out, however, one rather remarkable

comparison between 2D and 3D results which is obtained by examining

the differential cross sections. In Fig. 22 we plot the 2D and 3D

differential cross section $\sigma_{00 \to 01}^A$ (adjusting the respective abscissa

scales to bring them into approximate agreement at $\theta_R = 180°$). The

2D result at 0.55 eV is compared to the 3D one at 0.60 eV so as to include for any effects due to the bending energy shift. Fig. 22 indicates a remarkably similar shape in the respective angular distributions over the entire range of scattering angles. A similar comparison at other energies in the range considered usually leads to comparable agreement. This indicates that the dynamical processes involved are indeed quite similar. Such behavior is not unexpected, for the same potential is sampled in both cases and the primary difference between the two calculations is the additional centrifugal coupling resulting from tumbling of the 3 atom plane, which is present in 3D but not in 2D. The existence of a strong rotational polarization selection effect as evidenced in Table VI indicates that such coupling is weak in comparison to the potential coupling since it is the potential which is responsible for the linear geometry requirement. Thus 2D and 3D dynamics should be quite similar and conversion of 2D to 3D results could prove to be an accurate approximate technique.

3.6 Reagent and Product Rotational State Distributions

We now consider the rotational distributions of the degeneracy averaged reactive distinguishable atom cross sections (all for $v = v' = 0$). In the coplanar $H + H_2$ study,[12b] we found that a surprisingly accurate fit to this distribution could be obtained with a temperature-like expression (for a 2D system). This type of distribution can be derived from an information theoretic formalism through the assumption that the surprisal function[43] is linear in the final state rotational energy. For 3D collisions, with only one open vibrational channel, the information

theoretic expression for the degeneracy averaged cross section

between rotational states j and j' may be written as

$$Q_{j \to j'}^{R} = A_j(E) \rho(E_{j'}^{tr})(2j' + 1) e^{-E_{j'}/kT_j(E)} \tag{3.1}$$

where the pre-exponential factors comprise the reference or statistical distribution, and T_j and A_j are the two j' independent parameters of the theory. $\rho(E_{j'}^{tr})$ is the product translational density of states and is a function of the translational energy $E_{j'}^{tr}$ relative to state j'. $E_{j'}$ is the rotational energy, and we choose $E_{j'} = 0$ for j' = 0 so that $E_{j'}^{tr} = E - E_{j'} - E_0$ where E_0 is the v' = j' = 0 zero point energy. The 2j' + 1 in Eq. 3.2 is the product rotational degeneracy factor. To see how well our 3D cross sections obey Eq. 3.2, we have plotted in Fig. 23 the cross sections $Q_{0j \to 0j'}^{R}$ divided by $(2j' + 1) \times \bar{\rho}(E_{j'}^{tr})$ on a logarithmic scale as a function of $E_{j'}$ for several initial states j at 0.6 eV. $(\bar{\rho}(E_{j'}^{tr}) = \rho(E_{j'}^{tr})/\rho(0)$ so that $\bar{\rho}(0) = 1$.) If Eq. 3.2 is satisfied, then the resulting curves should be linear with slopes inversely proportional to $T_j(E)$. We see in the figure that the low j' calculated points do indeed form nearly straight lines for each j, thus indicating that the temperature-like distribution is quite accurate for describing the reactive cross sections. The temperature parameters obtained from the straight lines which connect the low j' points are 326, 326, 328, 316 and 376 K for j = 0, 1, 2, 3 and 4, respectively. The first four values are identical to the accuracy to which the points form a straight line. Actually, one can easily show by applying microscopic reversibility to Eq. 3.2 that if the rotational distribution is temperature-like for all j then $T_j(E)$ must be independent of j.

The above listed temperatures consequently should all be the same if the distributions are truly temperature-like. Only for $j = 4$ or $j' = 4$ are deviations from temperature-like behavior significant. If we now perform a similar analysis at several other energies we obtain Fig. 24 which depicts the $j = 0$ distributions between 0.45 and 0.70 eV. Temperature-like behavior is evident to a comparable extent at all energies considered. The temperature parameters obtained from the slopes of the lines in Fig. 24 vary from 228 K to 446 K as E varies from 0.45 eV to 0.70 eV in steps of roughly 40 K per 0.05 eV increase in energy.

In the coplanar study[12b] we pointed out that the existence of temperature-like rotational distributions could be a reflection of the shape of the potential energy surface near the transition state and the significant restriction in bending motions which the potential induces there. Since the transition state bending motions correlate adiabatically with asymptotic free rotor motions one might expect that the average rotational energy of the products should be related to the average energy in bending. This relation does not seem to be quantitative, however, for the average product state rotational energy is roughly equal to the temperature parameter while the bending energy, as estimated in the previous section, seems to be somewhat higher (228 - 446 K for the former and 550 K for the latter). The model explains the similarity between the coplanar and three dimensional temperature parameters (311 K for 2D[12b] versus 326 K for 3D, both at 0.6 eV) only if we further assume that only one of the two degenerate 3D bending modes becomes product rotational motion. It therefore

appears that some refinement in the model will be necessary in order to quantitatively explain the temperature-like distributions observed in Figs. 23 and 24.

3.7 Comparisons with the Results of Other Three Dimensional Calculations

In Figs. 25 and 26 we compare our integral cross sections (labelled SK) with the corresponding ones obtained by several other methods, all applied to $H + H_2$ on the Porter-Karplus potential surface. In Fig. 25 we plot the quasi-classical total reactive cross sections of Karplus, Porter and Sharma[2] (KPS) and the quantum mechanical results of Elkowitz and Wyatt[9] (EW) while Fig. 26 contains the anti-symmetrized Q_{00-01}^{A} of Tang and Karplus[4] (TK), Choi and Tang[7] (CT) and Wolken and Karplus[6] (WK). It is apparent that the best agreement in either figure is between our Q_{00}^{R} and Q_{01}^{R} and the corresponding quasi-classical quantities. Our converged quantum result and the quasi-classical cross sections are essentially identical between 0.6 and 0.7 eV to within the statistical accuracy of the classical calculation. Agreement between Q_{02}^{R}(SK) and Q_{02}^{R}(KPS) is much less quantitative but still reasonable if one considers the small cross sections involved and the inherent statistical uncertainty in the classical result. Below the classical thresholds, we observe characteristic tunnelling behavior in our quantum cross sections which will have an important effect in the comparison of classical and quantum thermal rate constants (see Section 3.8). Agreement between our results and the corresponding ones of Elkowitz and Wyatt is rather poor considering that both calculations employed extended vibration rotation basis sets. Recently, EW have discovered some errors in

their calculations[44] which put the comparison in Fig. 25 into question.
We would, however, like to point out that EW simplified their calcula-
tion in three ways,[45] one or more of which could have an appreciable
effect on the results: (a) they omitted certain Coriolis coupling terms
from the kinetic energy part of the Hamiltonian; (b) the potential was
fitted to analytic expressions so that vibration rotation coupling was
omitted; and (c) only the $v = 0, 1, 2$ vibrational states were included
in the close coupling expansion and convergence with respect to
addition of vibrational states was apparently not tested. The Tang and
Karplus distorted wave curve in Fig. 26 has a much higher effective
threshold energy than ours and consequently much smaller cross
sections at the same energy. Part of the difficulty could be the
"linear" assumption used[4] in evaluating the integrals for the transition
amplitude. When this assumption was removed, as was done by Choi
and Tang, the cross section increased significantly at the one energy
they considered. We should also note that Choi and Tang[7b] have also
observed an m'_j dependence in their $P^R_{J,000 \to 01m'_j}$ reaction proba-
bilities quite similar to Fig. 4. It would be interesting to obtain
distorted wave results such as those of CT at lower energies so that
a more direct comparison with our results may be effected. The one
vibrational basis function results of Wolken and Karplus have an
effective threshold energy much lower than ours for the same transition.
This is probably a consequence of the severely truncated basis set
used (only vibrational quantum state $v = 0$ and the $j = 0 - 3$ rotational
levels[6]). Convergence properties of severely truncated basis sets
were examined in the coplanar $H + H_2$ study,[12b] and it was determined

there that errors of several orders of magnitude in cross sections were possible in some cases if both vibrational and rotational convergence was not achieved.

The quasi-classical and quantum differential cross sections σ_{00}^{R} (at somewhat different energies) are examined in Fig. 27. Both angular distributions are backward peaked with very similar shapes. A very interesting comparison between classical and quantum dynamics would involve an examination of the classical rotational polarization effect analogous to the quantum results in Fig. 11. Such a detailed comparison of cross sections between individual quantum states (rather than summed over several as is the case in Figs. 25 and 27) would be highly desirable in establishing the general validity of the quasi-classical procedure. Fig. 28 provides a comparison of the WK, CT and SK $\sigma_{00 \to 01}^{A}$ angular distributions at similar energies. We find the distorted wave differential cross section of Choi and Tang to be very similar to ours while the Wolken and Karplus cross section differs rather substantially from either. Part of the error in the WK result could be due to an ambiguity in the interpolation of amplitudes and phases of scattering matrix elements for those partial waves they did not explicitly calculate. (Only every third partial wave was done.[6]) Indeed, we have found interpolation procedures to be extremely dangerous (especially for the phases) and for this reason, we have always computed scattering matrices at each partial wave required for convergence of the cross section. Another comparison of angular distributions is indicated in Fig. 29 where we examine the semi-classical $\sigma_{00 \to 01}^{R}$ of Doll, George and

Miller[5] (DGM) at a much lower energy than has been considered in the previous two figures. The agreement between the shapes of the quantum and semi-classical differential cross sections is excellent, but much less quantitative agreement is seen in a comparison with the DGM reaction probabilities as is seen in Fig. 30. In that figure, both methods of computing the semi-classical probability yield results which are factors of 5 to 10 larger than ours (although closer to ours than are the comparable results of Wolken and Karplus shown in the same figure. Presumably a "uniform" type of expression for evaluating the semi-classical reaction probability is required to bring those results into agreement comparable to what was obtained in the same energy range with collinear $H + H_2$.[46]

We conclude this section with a comparison of our nonreactive integral and differential cross sections with those of Wolken, Miller and Karplus.[22] The latter calculation considered the same potential surface[1c] as did we but ignored the possibility of reactive collisions. A comparison of the resulting integral cross sections $Q_{00 \to 02}^N$ is given in Fig. 31. The difference between the two curves is essentially within the accuracy of the respective calculations except perhaps at the highest energies considered. This is quite interesting, for WMK used a one vibration basis function approximation (with, however, $j_{max} = 6$[22]) in their calculation. This could indicate that the absence of closed vibrational channels is of much less significance for non-reactive collisions than it is for reactive ones. Unfortunately, a comparison between the WMK differential cross sections $\sigma_{00 \to 02}^N$ and ours (Fig. 32) shows significant disagreement with the WMK

result highly oscillatory in contrast with our very smooth result.

This disagreement is very suspicious, however, because the WMK

reaction probabilities and phase shifts are very similar to Figs. 8b

and 18, respectively, implying that the input into the respective

differential cross section calculations is very similar. We believe

that the smooth rather than oscillatory differential cross section

behavior is more reasonable because (a) it is consistent

with a direct mechanism being dominant in the collision process;

(b) it agrees qualitatively with our coplanar result at the same

energy (also plotted in Fig. 32) which is obtained from an entirely

different kind of cross section expression;[12b] and (c) it also qualita-

tively agrees with the corresponding nonreactive cross sections of

Allison and Dalgarno[23] for the same system but a different interaction

potential. Note that Fig. 32 also shows the absence of any forward

peak in the planar cross section. This is additional evidence for the

conclusion of Section 3.2 that the forward peak in the 3D result is

probably spurious.

3.8 Rate Constants

In this section we will examine the behavior of the para to

ortho rate constant for $H + H_2$. The ortho to para rate constant can

be easily obtained from $k_{p \to o}(T)$ by using the readily available

equilibrium constant.[47]

We first define the rate constant for the transition $vjm_j \to$

$v'j'm'_j$ (valid for R, N or A transitions):

$$k_{vjm_j \to v'j'm'_j} = \langle Q_{vjm_j \to v'j'm'_j} V_{vj} \rangle \tag{3.2}$$

$$= \int Q_{vjm_j \to v'j'm'_j} (V_{vj}) V_{vj} P(V_{vj}) d^3 V_{vj}$$

where the velocities V_{vj} were introduced in Section 2.1 and $P(V_{vj})$ is the Boltzman distribution function. Upon explicit substitution of this function into Eq. 3.2, we find

$$k_{vjm_j \to v'j'm'_j} = N_A \frac{8}{\pi\mu} \cdot \frac{1}{(kT)^{3/2}} \int_0^\infty E_{vj}^{tr} Q_{vjm_j \to v'j'm'_j} (E_{vj}^{tr})$$

$$\times e^{-E_{vj}^{tr}/kT} dE_{vj}^{tr} \tag{3.3}$$

where μ is the reduced mass corresponding to the motion of the atom with respect to the diatom and E_{vj} is the translational energy relative to state vj ($E_{vj}^{tr} = \frac{1}{2} \mu V_{vj}^2$). N_A is Avagadro's number so that k has units of cm^3/(mole $\times$ sec). Expressions for degeneracy averaged rate constants $k_{vj \to v'j'}$ may be obtained by using the degeneracy averaged $\sigma_{vj \to v'j'}$ in Eq. 3.3 rather than $\sigma_{vjm_j \to v'j'm'_j}$. The para to ortho cross section is then obtained from the $k_{vj \to v'j'}^A$ via:

$$k_{p\to o}(T) = \sum_{\substack{vj \\ (j\ even)}} \frac{f_j(2j+1) e^{-E_{vj}/kT}}{Q_p} \sum_{\substack{v'j' \\ (j'\ odd)}} k_{vj \to v'j'}^A(T) \tag{3.4}$$

where

$$Q_p = \sum_{\substack{vj \\ (j\ even)}} f_j(2j+1) e^{-E_{vj}/kT} \tag{3.5}$$

and E_{vj} is the vibration rotation energy of state vj ($E = E_{vj} + E_{vj}^{tr}$).
The nuclear spin degeneracy factor f_j has the value 1 for j even and 3
for j odd and thus is always unity for $k_{p \to o}$. Evaluation of Eqs. 3.3
and 3.4 may be accomplished by using the cross sections
$Q_{vj \to ortho}^{A}$ which are defined in Section 2.1. Some values of these
integral cross sections are given in Table V. By numerically evaluating
Eq. 3.3, we have calculated the para to ortho rate constants given in
the first column of Table VII. Both linear and logarithmic interpolation
were considered between the energies at which cross sections were
calculated and the results from the two methods agree to 20% or
better. (The linear results are given in Table VII.) Only temperatures
below 600 K have been used in the calculation because of substantial
errors which occur in truncating the integral in Eq. 3.3 at 0.7 eV
total energy for temperatures above 600 K.

The quantum para to ortho rate constant may also be obtained
(approximately) from distinguishable atom cross sections. The total
reactive rate constant $k^R(T)$ for distinguishable atom collisions is:[2]

$$k^R(T) = 2 \sum_{vj} \frac{f_j(2j + 1) e^{-E_{vj}/kT}}{Q} \sum_{v'j'} k_{vj \to v'j'}^{R}(T) \qquad (3.6)$$

where

$$Q = \sum_{vj} f_j(2j + 1) e^{-E_{vj}/kT} \qquad (3.7)$$

The factor of 2 at the beginning of Eq. 3.6 arises from an explicitly
performed sum over the two equivalent product arrangement channels.
Now in the limit that a large number of quantum states contribute to

the sums in Eqs. 3.4 and 3.6, we may assume that a sum of rate constants over just odd product states (or just even states) is approximately half the sum over all possible states, i.e.,

$$\sum_{\substack{v'j' \\ (j' \text{ odd})}} k^R_{vj \to v'j'}(T) \sim \frac{1}{2} \sum_{v'j'} k^R_{vj \to v'j'}(T) \qquad (3.8)$$

$$\text{or}$$
$$(j' \text{ even})$$

In addition, for high enough temperatures,

$$Q_o = \sum_{\substack{vj \\ (j \text{ odd})}} f_j(2j+1) e^{-E_{vj}/kT} \sim 3 \sum_{\substack{vj \\ (j \text{ even})}} f_j(2j+1) e^{-E_{vj}/kT}$$

$$= 3 Q_p \qquad (3.9)$$

So that

$$Q = Q_o + Q_p \sim 4 Q_p \qquad (3.10)$$

By realizing that $k_{o \to p}$ is given by an expression analogous to Eqs. 3.4 and 3.5 but with the even and odd sums interchanged, and by combining the expressions for $k_{o \to p}$ and $k_{p \to o}$, using Eqs. 3.8 - 3.10 to simplify and using the relations between antisymmetrized and distinguishable reactive rate constants implicit in the discussion following Eq. 2.8, we find

$$k^R(T) \sim k_{p \to o}(T) + k_{o \to p}(T) \qquad (3.11)$$

$$\sim k_{p \to o}(T) \left(1 + \frac{1}{K_{eq}}\right)$$

where K_{eq} is the equilibrium constant. To the same order of approximation, Eq. 3.9 implies that $K_{eq} \sim 3$ so Eq. 3.11 yields

$$k^R(T) \sim \frac{4}{3} k_{p \to o}(T) \qquad . \qquad (3.12)$$

This implies that by computing $k^R(T)$ and using Eqs. 2.11 and 3.12, we can approximately compute $k_{p \to o}(T)$. In the second column of Table VII we list these $k_{p \to o}^{dist}$ obtained from the distinguishable atom cross sections. Equation 3.11 rather than 3.12 was found to give slightly better agreement between $k_{p \to o}^{dist}$ and $k_{p \to o}$ for $T < 300$ K and was therefore used in calculating $k_{p \to o}^{dist}$ in the table. We see that for $T \geq 300$ K, $k_{p \to o}^{dist}(T)$ and $k_{p \to o}(T)$ are identical to at least 2 significant figures indicating that the approximation is quite accurate even at fairly low temperatures. Our primary reason for developing this distinguishable atom method for calculating $k_{p \to o}$ is for the purpose of comparing our results with the quasi-classical rate constants of Karplus, Porter and Sharma.[2] If we use Eq. 3.11 to convert their calculated k^R(KPS) to $k_{p \to o}$(KPS) we obtain the results in the third column of Table VII. In the fourth column we have listed the analogous transition state theory result $k_{p \to o}$(TST) [which is obtained from the formula given in Ref. 2]. Arrhenius plots of these quantum, quasi-classical and transition state theory rate constants are presented in Fig. 33. At 600 K, the quasi-classical $k_{p \to o}$(KPS) differs from $k_{p \to o}$ by only 7% while the TST result is in error by 79%. The close agreement of the quasi-classical and quantum results is an obvious consequence of the excellent agreement of the corresponding integral cross sections (above the classical thresholds) in Fig. 25

coupled with the excellent validity of Eqs. 3.11 and 3.12. Presumably, the quantum and quasi-classical rate constants will continue to be in very good agreement at temperatures above 600 K. At lower temperatures, however, tunnelling effects become extremely important with $k_{p \to o}$ (SK) a factor of 3.3 larger than $k_{p \to o}$ (KPS) at 300 K and 18 times larger at 200 K. The significant nonlinearity in the quantum curve in Fig. 31 is also apparently related to tunnelling, although we should note that previous studies on collinear H + H_2 have shown[48] that tunnelling can make significant contributions to the rate constant even at 1000 K where the Arrhenius plot is quite linear. The transition state theory rate constant deviates from $k_{p \to o}$ (SK) even more severely than $k_{p \to o}$ (KPS), with $k_{p \to o}$ (SK)/$k_{p \to o}$ (TST) being 20 at 300 K and 427 at 200 K. Part of the error in the TST result is probably due to the neglect of tunnelling corrections in the expression used[2] (i.e., a transmission coefficient of unity has been assumed). For the SSMK surface[12], Shavitt[16] has estimated one dimensional transmission coefficients of 1.769 at 600 K, 6.482 at 300 K and 44.867 at 200 K thus indicating the possibility of substantial improvement upon inclusion of these factors. On the other hand, the ratio $k_{p \to o}$ (KPS)/$k_{p \to o}$ (TST) deviates substantially from unity in Table VII despite the fact that tunnelling has been omitted from both calculations. Because of the strongly nonlinear behavior of $k_{p \to o}$ (SK) in Fig. 33, the attempt to characterize that rate constant by a single activation energy is probably not too meaningful. If one does, however, compute such a quantity by arbitrarily fitting a straight line between the 500 K and 600 K points, one finds activation energies of 6.3, 7.5 and 8.8

kcal/mole for $k_{p \to o}$ (SK), $k_{p \to o}$ (KPS) and $k_{p \to o}$ (TST), respectively. The quantum activation energy is 1.1 kcal/mole (0.048 eV) above the corresponding coplanar one (5.2 kcal/mole)[12b] and this difference is almost identical to the 0.05 eV 2D to 3D shift observed in Figs. 20 and 21 for the reaction probability curves.

Since the Porter-Karplus potential surface we used has an incorrect barrier height (0.396 eV[1c] versus 0.425 eV for the more accurate Liu surface[1e]), a comparison with experimental results of thermal rate constant measurements will be deferred until a more extensive series of results similar to those of Appendix B for the Liu surface are completed.

4. SUMMARY

Let us now summarize the significant concepts developed in this paper. First, in the analysis of the reactive transition probabilities and cross sections we found a fairly accurate rotational projection quantum number selection rule ($m_j = m'_j = 0$). Although one can find many factors which are at least partially responsible for this effect, the primary reason for this specificity and selectivity is the restriction to nearly linear geometries in the transition state as is determined by the potential energy surface. No comparable selection effect was found for the nonreactive collisions (compare, for example, Figs. 12 and 15). At higher energies, quantum symmetry interference oscillations were observed in the $j = 0$ to $j' = 2$ para to para differential cross sections. Such oscillations might be capable of interpretation in terms of parameters which characterize the potential energy surface

as has been done for the related atom-diatom and molecule-molecule elastic scattering situations.[49] The elastic cross sections revealed a lack of sensitivity of the $\theta < 30°$ angular distributions to the loss of flux into inelastic and reactive channels, and demonstrated the approximate validity of Levine's[40] conservation of total cross section rule. A comparison of the results of 1D, 2D and 3D calculations revealed the importance of bending motions in the transition state and demonstrated their connection with threshold energies. In addition, the orientation dependence of the reaction probabilities was analyzed and found to be compatible with the observed maximum values of the total reaction probabilities. The results of 1D, 2D and 3D comparisons afforded in this paper should be of great use in the improvement of 1D and 2D models so that they can be used to make quantitative predictions about 3D results. The degeneracy averaged rotational distributions were found to obey Boltzman-like expressions with a surprising degree of accuracy. A precise understanding of why this occurs remains unknown at present but an analysis of the scattering wave function at the transition state in terms of vibrationally and rotationally adiabatic wave functions may help to clarify the relation of bending energy to product state rotational energy and hence to the temperature parameter. A comparison of our integral and differential cross sections with those of several other approximate calculations indicates best agreement with the quasi-classical results. The lack of tunnelling in the classical cross sections produces important differences in the para to ortho thermal rate constant at temperatures well below 600 K but good agreement at 600 K.

The wealth of dynamical information presented here makes clear the great usefulness of these calculations. At the same time, the large expenditure of computer time indicated in Table II implies that analogous calculations will be done for only a limited number of additional systems for which a very detailed understanding of the important dynamical processes involved is highly desirable. This places prime emphasis on the development of accurate but efficient approximate techniques, and the comparisons between accurate and approximate theories given in Sections 3.5, 3.7 and Appendix A indicate that such techniques may be possible.

ACKNOWLEDGEMENT

APPENDIX A: ANGULAR MOMENTUM DECOUPLING APPROXIMA-TIONS: APPLICATION TO 3D $H + H_2$.

In Ref. 29 (Section 2.3) we described the use of angular momentum decoupling (tumbling decoupling) approximations for reactive scattering. In this Appendix, we present the results of an application of one very simple variation of these procedures to 3D $H + H_2$ using the Porter-Karplus[1c] potential surface.

The particular decoupling approximation we used can be applied in two steps. The first involves the neglect of all terms in the λ arrangement channel Hamiltonian which are off diagonal in Ω_λ. In order to elaborate upon this, we write the rotationally coupled Schrödinger equation (Eq. 2.19 of Ref. 29) as follows:

$$(t^{J\lambda j_\lambda}_{\Omega_\lambda \Omega_\lambda} - E) w^{\lambda}_{Jj_\lambda \Omega_\lambda}(r_\lambda, R_\lambda) + \sum_{j_\lambda'} V^{\lambda \Omega_\lambda}_{j_\lambda j_\lambda'} w^{\lambda}_{Jj_\lambda' \Omega_\lambda}(r_\lambda, R_\lambda)$$

$$+ t^{J\lambda j_\lambda}_{\Omega_\lambda \Omega_\lambda +1} w^{\lambda}_{Jj_\lambda \Omega_\lambda +1}(r_\lambda, R_\lambda) + t^{J\lambda j_\lambda}_{\Omega_\lambda \Omega_\lambda -1} w^{\lambda}_{Jj_\lambda \Omega_\lambda -1}(r_\lambda, R_\lambda) = 0 \tag{A.1}$$

where

$$t^{J\lambda j_\lambda}_{\Omega_\lambda \Omega_\lambda} = -\frac{\hbar^2}{2\mu} \left[\frac{1}{R_\lambda} \frac{\partial^2}{\partial R_\lambda^2} R_\lambda + \frac{1}{r_\lambda} \frac{\partial^2}{\partial r_\lambda^2} r_\lambda \right]$$

$$+ \frac{j_\lambda(j_\lambda+1)\hbar^2}{2\mu r_\lambda^2} + \frac{\hbar^2}{2\mu R_\lambda^2} [J(J+1) - 2\Omega_\lambda^2 + j_\lambda(j_\lambda + 1)] \tag{A.2}$$

$$t^{J\lambda j_\lambda}_{\Omega_\lambda \Omega_\lambda \pm 1} = -\frac{\hbar^2}{2\mu R_\lambda^2} [J(J+1) - \Omega_\lambda(\Omega_\lambda \pm 1)]^{-\frac{1}{2}}$$

$$\times [j_\lambda(j_\lambda + 1) - \Omega_\lambda(\Omega_\lambda \pm 1)]^{\frac{1}{2}} . \tag{A.3}$$

and

$$V_{j_\lambda j_\lambda'}^{\lambda \Omega_\lambda}(r_\lambda, R_\lambda) = \langle j_\lambda \Omega_\lambda | V^\lambda(r_\lambda, R_\lambda, \gamma_\lambda) | j_\lambda ' \Omega_\lambda \rangle \qquad (A.4)$$

The functions $W_{Jj_\lambda \Omega_\lambda}^\lambda$ arise from the expansion of the full wave function Ψ_{JM} in terms of the λ arrangement channel angular functions:

$$\Psi_{JM}(\underset{\sim}{r}_\lambda, \underset{\sim}{R}_\lambda) = \sum_{\Omega_\lambda} D_{M\Omega_\lambda}^J(\phi_\lambda, \theta_\lambda, \psi_\lambda) \, \chi_{J\Omega_\lambda}^\lambda(r_\lambda, R_\lambda, \gamma_\lambda)$$

$$(A.5)$$

$$= \sum_{j_\lambda \Omega_\lambda} D_{M\Omega_\lambda}^J(\phi_\lambda, \theta_\lambda, 0) \, Y_{j_\lambda \Omega_\lambda}(\gamma_\lambda, \psi_\lambda) W_{Jj_\lambda \Omega_\lambda}^\lambda(r_\lambda, R_\lambda)$$

From Eq. A.1, we see that the only terms in the Hamiltonian which are off diagonal in Ω_λ are the $t_{\Omega_\lambda \Omega_\lambda \pm 1}^{J\lambda j_\lambda}$ which come from the orbital angular momentum term $l_{\underset{\sim}{\lambda}}^2 / 2\mu R_\lambda^2$. The potential energy $V_{j_\lambda j_\lambda'}^{\lambda \Omega_\lambda}$ is diagonal in Ω_λ and hence is treated exactly in the approximation. The last term in the diagonal kinetic energy operator $t_{\Omega_\lambda \Omega_\lambda}^{J\lambda j_\lambda}$ of Eq. A.2 is not approximated in our method as has often been done in analogous nonreactive scattering calculations.[50] Rather, this term is treated exactly, necessitating the use of noninteger-order spherical Bessel functions in determining the asymptotic reactance and scattering matrix solutions. With the neglect of the last two terms in Eq. A.1, the integration of the Schrödinger equation in each arrangement channel region λ may be done separately for each Ω_λ. No additional approximations in any formulas pertaining to the integration are required. As with the fully coupled problem, the homonuclear symmetry of the H_2 target allows us to decouple even and odd rotational states. Parity decoupling does not apply, but the reactance and scattering matrices generated are invariant to the sign of Ω_λ, so only $\Omega_\lambda \geq 0$ needs to be

considered in the calculation.

The second step of the approximation refers to the matching procedure of Ref. 29. In this procedure, the wave function $\chi^{\lambda}_{J\Omega_{\lambda}}$ (Eq. A. 5) expressed in λ arrangement channel coordinates, is related to $\psi^{\nu}_{J\Omega_{\nu}}$ (in ν coordinates) via (Eq. 4.20 of Ref. 29)

$$\chi^{\lambda}_{J\Omega_{\lambda}} = \sum_{\Omega_{\nu}} d^{J}_{\Omega_{\nu}\Omega_{\lambda}} (\Delta_{\nu\lambda}) \, \chi^{\nu}_{J\Omega_{\nu}} \qquad (A.6)$$

where $\Delta_{\nu\lambda}$ is the angle between R_{λ} and R_{ν}. In the fully coupled procedure, we evaluate Eq. A.6 on a surface $\pi_{\nu\lambda}$ which separates arrangement channel regions ν and λ. Analogous equations relating the ν and κ regions, and the κ and λ regions are required to complete the matching. In the second step of our decoupling approximation, we replace $d^{J}_{\Omega_{\nu}\Omega_{\lambda}}$ in Eq. A.6 by $\delta_{\Omega_{\nu}\Omega_{\lambda}}$, thereby neglecting all Ω_{λ} and Ω_{ν} mixing that arises from the transformation between the λ and ν arrangement channel coordinate systems. Analogous approximations are made in the $\nu\kappa$ and $\kappa\lambda$ matching equations, thereby forcing the entire scattering matrix to be diagonal in the tumbling quantum numbers Ω_{λ} ($\lambda = \alpha, \beta, \gamma$), and antidiagonal in the projection quantum numbers $m_{j_{\lambda}}$ (i.e., $m'_{j_{\lambda}} = -m_{j_{\lambda}}$; see Section 5.2 of Ref. 29). We should make two additional remarks about the procedure:

(1) Because of our separation of the method into integration and matching steps, the approximate Hamiltonian is not everywhere invariant to a change in arrangement channel coordinates (say, from λ to ν) as the full one is. The λ and ν arrangement channel Hamiltonians are, however, identical at the $\pi_{\nu\lambda}$ matching surface (although possibly not smooth), so no artifacts arising from a discontinuous change in the

Hamiltonian should occur. Nevertheless, this is a major disadvantage of the method, since it leads to a dependence of the results on the position and shape of the matching surfaces. In all likelihood, in those situations where changing the matching surfaces has a significant effect on the results, it will also be true that Ω_λ mixing will be significant and hence the neglect of this mixing will be a poor approximation anyways.[51] This difficulty can be eliminated by describing the problem with the aid of a floating z_λ axis such as Wyatt and coworkers have done[45] (in which case the matching is automatically diagonal in the local tumbling quantum number Ω).

(2) The second step in the decoupling procedure, in which the matching is uncoupled actually is unnecessary, for the exact matching procedure of Ref. 29 may be used without a significant increase in computation time. One simply uses the decoupled primitive wave functions (including all possible Ω_λ) in the matching equations derived in Ref. 29 without any modification at all. Such a method will correctly include for the Ω_λ mixing which occurs in the transformation between arrangement channels and will therefore provide approximate scattering matrix elements which are off diagonal in Ω_λ ($\lambda = \alpha, \beta, \gamma$). The dependence on choice of matching surface ((1) above) is still present, but should be much less significant in this case. We shall see in the results below that the complete neglect of Ω_λ coupling is only a moderately good approximation, but that its partial inclusion through a procedure similar to that described here may improve the results substantially.

We now consider an application of this tumbling decoupling approximation. The savings in time depends on J, but for $J \geq 4$, the decoupled calculations seem to be factors of 10 to 20 faster than the fully coupled ones (for equivalent sets of quantum numbers). Additional savings may be gained by designing the program code more specifically for decoupled calculations (as was not done here).

The resulting reaction probabilities $P^R_{J,000 \to 010}$ are plotted in Fig. 34 for E = 0.50, 0.60 and 0.70 eV. For comparison, the converged probabilities are also plotted on the same graph. For J = 0, no Ω_λ coupling exists (only $\Omega_\lambda = 0$ is allowed), so the angular momentum decoupling method becomes exact. As J increases from zero, Fig. 34 indicates that the decoupled and converged probabilities separate somewhat, but they both decay to zero with similar J dependence. This contrasts with the J dependence of the decoupled and converged inelastic nonreactive probabilities $P^N_{J,000 \to 020}$, which bear little resemblance to each other for $J > 0$.[52] To examine the m_j dependence of the decoupled results, we plot in Fig. 35 the probabilities $P^R_{J,01-m_j \to 02m_j}$ as a function of J at E = 0.60 eV. The $m_j = 0$ results look quite similar to those in Fig. 34 at the same energy. The $m_j = \pm 1$ comparison indicates that both decoupled and converged probabilities are of the same order of magnitude and have good average agreement, but that the details of the J dependence are actually quite different. This conclusion is, in fact, quite generally true concerning probabilities for $m_j \neq 0$. Note that the examination of J and m_j dependence focuses upon different parts of the Hamiltonian in Eq. A.1 (with the last two terms omitted). The J dependence occurs

only in the last term of $t_{\Omega_\lambda \Omega_\lambda}^{J\lambda j_\lambda}$ (Eq. A.2) while the m_j or Ω_λ dependence arises in both that term, and in the potential (Eq. A.4). Since the probabilities change much more rapidly with m_j than with J (Fig. 35), it is apparent that the Ω_λ dependence of $V_{j_\lambda j'_\lambda}^{\lambda \Omega_\lambda}$ must be crucial to the m_j dependence of these probabilities, for the J and Ω_λ dependent contributions to $t_{\Omega_\lambda \Omega_\lambda}^{J\lambda j_\lambda}$ are quite similar and could not be responsible for such diverse behavior in the probabilities.

The decoupled and converged para to ortho differential cross sections $\sigma_{000 \to 010}^{A}$ are presented in Fig. 36 for the same transition and energies as were considered in Fig. 34. Here we find that the converged angular distributions are somewhat more strongly backward peaked than are the decoupled ones with the differences between the two being more pronounced at 0.70 eV than at 0.50 eV. When the $\sigma_{01-m_j \to 02m_j}^{A}$ are examined in Fig. 37, we find that the $m_j = 0$ decoupled and converged results are quite similar to the corresponding $\sigma_{000 \to 010}^{A}$ of Fig. 36 while the $m_j = \pm 1$ cross sections are in surprisingly quantitative and qualitative agreement over much of the angular range. Note that those cross sections having $m'_j = -m_j \neq 0$ are required to vanish at $\theta_R = 180°$ (from the discussion of Section 3.2).

The integral cross sections $Q_{000 \to 010}^{A}$ are plotted in Fig. 38. The curves in the lower part of that figure indicate that both decoupled and converged cross sections have essentially the same energy dependence, but that the decoupled result is larger than the converged cross section by a slowly varying multiplicative factor which has the values 1.74, 1.38, 1.26, 1.38 and 1.61 at 0.3, 0.4, 0.5, 0.6 and 0.7 eV, respectively. Thus it appears that the neglect of Ω_λ coupling makes the

system somewhat more reactive than its fully coupled counterpart,
but that the error arising from this omission is not strongly energy
dependent. In Table VIII, we give the cross section matrix $Q_{0jm_j \to 0j'm'_j}$
analogous to Table VI, for the decoupled results at 0.6 eV. A compari-
son of Tables VI and VIII indicates that the decoupled $m_j = m'_j = 0$ cross
sections are always larger than the converged ones (by factors of
30% to 65%), while the decoupled $m_j = -m'_j \neq 0$ results are always
smaller than the converged ones (by factors of 3 or less). In order
for us to be able to neglect those cross sections in Table VI which are
off diagonal in Ω_λ, we would generally require that the $m_j = -m'_j$ elements
in that table be much larger than all others. Unfortunately, this is
accurately satisfied only for the $m_j = -m'_j = 0$ elements. Therefore, we
really should expect that the approximation should be accurate only for
$Q^R_{0j0 \to 0j'0}$ and not for other transitions. The fact that better than an
order of magnitude agreement can be obtained for $m_j = -m'_j \neq 0$ is
quite surprising. An additional question of interest is whether or not
by simply including the full matching procedure outlined in (2) above
(rather than the decoupled matching that we used), we can improve the
accuracy of the decoupled cross sections. We think this could in fact
be possible, for the matching seems to be more important in mixing
different Ω_λ's than is the integration.[53]

To summarize the results of this Appendix, we have found that
tumbling decoupling procedures are capable of producing reductions
in computation time by factors of 10 to 20 (perhaps more) while still
predicting reasonably accurate reaction probabilities and cross sections.
The procedure used here is at best a crude approximation and it is

possible that more accurate results may be possible by using more sophisticated decoupling approximations. Finally, we note that because the potential coupling is treated exactly, these kinematic decoupling procedures are not subject to the gross inaccuracies (at least at the energies considered) which occur with the one vibrational basis function approximation.[12] As long as potential coupling dominates over angular momentum coupling, the procedure developed here should give reasonably accurate physically meaningful results.

APPENDIX B. 3D RESULTS FOR A PARAMETRIZED FIT TO THE

AB INITIO LIU SURFACE

In this Appendix, we present the results of an application

of our 3D reactive scattering procedure using the H + H_2 ab initio

surface of Liu[1f, 54] as parametrized by us. We begin by describing

this surface.

In an important recent paper[1f], Liu has presented the results

of a very extensive CI calculation on the collinear H_3 system. Liu's

calculated surface is believed to lie no more than 0.035 eV and no less

than 0.009 eV above the exact surface and should therefore have the

necessary "chemical accuracy" required for accurate reactive cross

section calculations. His collinear barrier height of 0.425 eV

(9.8 kcal/mole) has often been assumed to be the "true" barrier

height in H_3[16], and Liu gives upper and lower bounds to it of 0.446 eV

and 0.412 eV which indicate that the 0.425 eV result cannot be seriously

in error. Liu's calculations have recently been extended to nonlinear

geometries[54], and the estimated error in the results seems to be only

slightly larger (0.01 eV) than that stated for the linear calculations.[54]

In order for us to use this surface in our calculations, we need an

analytical representation of it of the form $V(r_1, r_2, r_3)$ where r_1, r_2

and r_3 are the 3 internuclear distances. Although Lester and Yates[55]

have fitted Liu's linear results to a "Porter-Karplus-like" parametrized

function, a comparison of their surface with Liu's nonlinear points

indicates that it is not particularly accurate away from collinear geo-

metries. For this reason we decided to try to incorporate Liu's data

as accurately as possible in our own fitted surface. Since Liu's

nonlinear calculations were done for varying r_1, r_2 at a fixed value of the exterior angle θ ($r_3^2 = r_1^2 + r_2^2 + 2r_1 r_2 \cos \theta$), a convenient fitting procedure for us involves (a) separate least squares fits at each θ involved, coupled with (b) an analytical interpolation between different θ for each r_1, r_2. This interpolation may be accomplished by writing the potential in terms of a series of Legendre polynomials:

$$V(r_1, r_2, r_3) = V(r_1, r_2, \theta) = V_0(r_1, r_2) P_0(\cos \theta) + V_1(r_1, r_2) P_1(\cos \theta)$$
$$+ V_2(r_1, r_2) P_2(\cos \theta) + V_3(r_1, r_2) P_3(\cos \theta) + \ldots \qquad \text{(B.1)}$$

where both even and odd $P_k(\cos \theta)$ must be used because V is not symmetric about $\theta = 90°$. We solve for the coefficients $V_k(r_1, r_2)$ by requiring Eq. B.1 to be exact for each r_1, r_2 at the values of θ considered, thereby forming a set of algebraic equations for the coefficients. Since Liu considered $\theta = 0°$, $30°$, $60°$, and $90°$ in his calculations, we can solve for the first four V_k ($k = 0 - 3$) as follows:

$$
\begin{pmatrix} V_0(r_1,r_2) \\ V_1(r_1,r_2) \\ V_2(r_1,r_2) \\ V_3(r_1,r_2) \end{pmatrix} =
\begin{pmatrix}
-6.79743 & 11.77350 & -6.79743 & 2.82137 \\
15.42102 & -25.90171 & 16.02102 & -5.54034 \\
-13.59487 & 23.54700 & -13.59486 & 3.64273 \\
5.97128 & -9.41880 & 4.37128 & -0.92376
\end{pmatrix}
\begin{pmatrix} V(r_1,r_2, \theta = 0°) \\ V(r_1,r_2, \theta = 30°) \\ V(r_1,r_2, \theta = 60°) \\ V(r_1,r_2, \theta = 90°) \end{pmatrix}
\qquad (B.2)
$$

After using Eq. B.2 to solve for the $V_k(r_1, r_2)$ (k = 0 - 3), we then substitute these into Eq. B.3 to interpolate for $V(r_1, r_2, \theta)$ at any θ. Such a procedure is not necessarily particularly accurate, but similar interpolation procedures on related $H + H_2$ potential functions have been quite accurate[12b] and we shall assume that this is also true here.

Now we consider the fitting of $V(r_1, r_2, \theta)$ for fixed values of θ and variable r_1, r_2. This problem has been examined previously by Shavitt et al.[1d] and by Liu[1f]. For most r_1, r_2, we shall use Liu's analytical fitting function, which has the form (for $H + H_2$)

$$V(r_1, r_2, \theta) = -1.5 + [V_{H_2}(r_1) + 1] + [V_{H_2}(r_2) + 1]$$

$$+ \exp[-\gamma(\theta)(r_1 + r_2)] \qquad \text{(B.3)}$$

$$\times \sum_{k=0}^{n} \sum_{j=0}^{[k/2]} C_{k-j,j}(\theta)[r_1^{k-j} r_2^{j} + r_1^{j} r_2^{k-j}]$$

where all energies are in Hartrees and all distances in bohr. $V_{H_2}(r)$ is the H_2 diatomic potential, which is expanded in the form

$$V_{H_2}(r) = -1 + \exp(-\alpha r) \sum_{i=0}^{n} a_i r^i \qquad \text{(B.4)}$$

The coefficients α and a_i (i = 0 - 8) have been tabulated by Liu[1f]. For linear geometries, Liu has fitted Eq. B.3 to his 137 calculated points through a nonlinear least squares fitting procedure. Using n = 14 in Eq. B.3, he was able to fit all calculated points to better than 0.002 eV. The required coefficients C_{ij} and γ ($\theta = 0$) are tabulated in Ref. 1f and will not be repeated here. In fitting the $\theta = 30°$, $60°$ and $90°$ surfaces[56], we used Eq. B.4 with n = 8. The resulting

coefficients C_{ij} are given in Table IX and the $\gamma(\theta)$ are listed in the first column of Table X. The accuracy of all three nonlinear surfaces is comparable, with maximum deviations between the ab initio points and fitted points less than 0.03 eV everywhere, and 0.01 eV or less for points near the saddle point. A more accurate fit was not attempted because: (a) an insufficient number of ab initio points were available (40 for $\theta = 30°$, 50 for 60°, and 32 for 90°) to increase n in Eq. B.3 significantly, (b) the existing fit was within the accuracy of the ab initio surface (see also Ref. 56), and (c) the interpolation procedure of Eq. B.1 was known to be a larger source of error than any errors in these least squares fits (see below). For r_1 (or r_2) outside the range considered in the ab initio calculation, the analytical formula (Eq. B.3) gave very inaccurate results. To correct this, the large r_1 surfaces were replaced by the following:

(1) for $\theta = 0°$ and $r > r_{1max}(\theta = 0°)$;

$$V(r_1, r_2, \theta=0°) = V_{H_2}(r_2) + (V(r_{1max}(0°), r_2, \theta = 0°)$$

$$-V_{H_2}(r_2))\exp(-\lambda(0°)(r_1 - r_{1max}(0°))) \tag{B.5a}$$

(2) for $\theta = 30°$, 60°, 90° and $r > r_{1max}(\theta)$,

$$V(r_1, r_2, \theta) = V(r_1, r_2, \theta = 0°) + (V(r_{1max}(\theta), r_2, \theta)$$

$$-V(r_1, r_2, \theta=0°))\exp(-\lambda(\theta)(r_1 - r_{1max}(\theta))) \tag{B.5b}$$

where $r_{1max}(\theta)$ and $\lambda(\theta)$ are parameters. For large r_2, Eqs. B.5 are used with r_1 and r_2 interchanged. In the above formulas, $V(r_{1max}(\theta), r_2, \theta)$ is to be evaluated from the least squares expression

(Eq. B.3) so as to make the potential continuous everywhere. The functional forms in Eqs. B.5 have been chosen because they characterize the potential quite well for r_1 near to but less than r_{1max} and hence are smooth extrapolations of it for $r > r_{1max}$. In addition, Eqs. B.5 form excellent fits to the Porter-Karplus surface[1c] for large r_1. The parameters $r_{1max}(\theta)$ and $\lambda(\theta)$ for $\theta = 0°, 30°, 60°$ and $90°$ are listed in Table X.[57] From our discussion of Section 3.4 it should be apparent that the large r_1 behavior of Eqs. B.5 is still not physically correct. This is an important defect of our fitted surface, but, as has previously been demonstrated by Wolken, Miller and Karplus[22], it should not strongly effect the reactive and inelastic cross sections.

Probably the major error in our fitted 3D surface arises from the angular interpolation procedure. Some indication of this can be gained by examining the $\theta = 120°$ potential. From Liu's calculations[54], this potential should have a saddle point energy of 2.75 eV near $r_1 = r_2 = 2.0$ bohr. Unfortunately, the fitted surface predicts a saddle point of 2.29 eV occurring at the same $r_1 = r_2$. Although this high energy region is not sampled at the collision energies to be considered below, and the configurations considered are a rather extreme test of Eq. B.2, this example does indicate that the interpolation procedure suffers from important inaccuracies. Fortunately, the most important $\theta = 0$ configuration is treated essentially exactly by our procedure so that the saddle point parameters as well as other properties of the potential surface except the bending energy are identical to those previously given by Liu.[1f] In Liu's more recent results, he determined the bending force constant A_{22} to have the

value 0.021 a.u. [54]. The fitted surface has a saddle point bending force constant of 0.024 a.u. which is a significant improvement over the Lester Yates[55] value of 0.030 a.u. For the remainder of this Appendix, we will refer to our fitted surface as simply the Liu surface.

We now consider the results of a calculation using this surface. The details of the procedure used are identical to those described for the Porter-Karplus surface in Section 2 above, with one exception. We found that truncation of the expansion of the potential in a series of Legendre polynomials $P_k(\cos \gamma)$ (Eq. 2.14) at 3 terms did not produce adequate convergence of the results, but 4 terms did, so 4 terms were included in all calculations. As an example of this, at 0.60 eV, the reaction probability $P_{J,000 \rightarrow 010}^R (J = 0)$ has the value 0.00524 with 3 terms, 0.00803 with 4 and 0.00797 with 5. At 0.55 eV, $P_{J,010 \rightarrow 010}^R (J = 0) = 0.819 \times 10^{-3}$ with 3 terms, 0.00121 with 4 and 0.00119 with 5. These results are typical of the convergence behavior obtained. Other convergence criteria such as flux conservation, microscopic reversibility, and convergence with respect to addition of closed rotational or vibrational channels is comparable to that obtained with the Porter-Karplus (PK) results in Section 2.2.

The resulting total reaction probability $P_{00}^R (J = 0)$ is plotted in Figs. 39 and 40. For comparison, we also have plotted the corresponding Porter-Karplus probability. The figure indicates that the Liu surface results above 0.45 eV are shifted upwards in energy by about 0.05 eV from the Porter-Karplus ones. If we recall that the barrier heights of the Liu and Porter-Karplus surfaces are 0.425 eV

and 0.396 eV respectively, then we see that the shift in energy between the two curves is more than the shift in barrier heights. This difference is probably due to the difference in shapes of the barriers since the Liu barrier is broader than the PK one (i.e., the Liu value of A_{33}, the asymmetric force constant, is -0.058 a.u., while the PK value is -0.124 a.u.). This difference in shape is also probably responsible for the slightly different energy dependence of the two curves in Fig. 39. At low energies, the Liu probability actually becomes larger than the PK one. This is very likely a manifestation of the longer range exponential tail of the PK surface over the Liu one.[1f] At the higher energies in the figures, the Liu probability levels off at a somewhat lower value (0.35) than does the PK result (0.44). According to our earlier arguments (Section 3.5), this implies that the range of orientations which lead to reaction with a significant probability is more restricted for the Liu surface than for the PK surface. The dependence of the reaction probability on J is examined in Figs. 41 for the transition $P_{J, 00 \to 01}^{R}$. Both the Liu and the Porter-Karplus probabilities have similar values of J_{MAX} (defined in Section 3.1) but the Liu result is more highly peaked at low J. This result if typical for the $E \geq 0.50$ eV probabilities. For $E < 0.50$ eV, the Liu and PK probabilities have very similar J dependence, even at low J.

The Liu and Porter-Karplus differential cross sections $\sigma_{00 \to 01}^{A}$ at $E = 0.4$, 0.5 and 0.6 eV are plotted in Figs. 42, 43, and 44. All cross sections are strongly backward peaked with comparable half widths. The Liu cross sections at 0.50 eV and 0.60 eV are

slightly more highly peaked in the backward direction than are the PK ones, but the reverse behavior is found at E = 0.40 eV. The Liu differential cross sections for different projection quantum numbers show polarization behavior essentially identical to the Porter-Karplus cross sections (as, for example, in Fig. 11).

Table XI summarizes a number of important reactive integral cross sections for the Liu surface. Most cross sections have an energy dependence similar to Q_{00}^R, which is plotted in Fig. 45. The comparison between the Liu and PK cross sections in that figure is very much analogous to the probability comparison in Figs. 39 and 40. When the cross sections $Q_{000 \to 0j'm'_j}^R$ are examined for different j' and m'_j, we find that the ratio of $m'_j = 0$ to $m'_j = 1$ cross sections has the value 24.2 for j' = 1, 7.4 for j' = 2, 3.0 for j' = 3 and 2.0 for j' = 4 all at 0.60 eV. These numbers are quite close to the analogous Porter-Karplus ones given in Section 3.3. The values of the j' = 1 ratio at 0.4, 0.5 and 0.6 eV are 14.5, 18.9 and 24.2, which implies a somewhat different energy dependence than for the PK cross sections. An analysis of the rotational distributions of the degeneracy averaged cross sections is presented in Fig. 46 for E = 0.60 eV. Here, we find highly linear plots indicating good agreement with the predictions of a temperature-like distribution. The temperature parameters obtained from the slopes of the straight lines in Fig. 46 are 412, 415, 412, 420 and 423 K for j = 0, 1, 2, 3, 4 respectively. As we showed in Section 3.6, microscopic reversibility forces all these numbers to be the same for truly temperature-like distributions, so the differences between the above numbers are indicative of the deviations

from temperature-like behavior. The temperature parameters for the j = 0 distributions are 187, 301, 412 and 537 K at 0.4, 0.5, 0.6 and 0.7 eV, respectively. There is roughly a 55 K increase in T(E) for each 0.05 eV increase in the total energy. This rate of increase of T(E) with E is somewhat larger than it is for the Porter-Karplus surface (Section 3.6). Since the Liu and PK temperatures coincide near E = 0.4 eV, we see that for energies above this, the Liu rotational distribution is broader than the Porter-Karplus one. Note that the transition state bending force constant of the fitted surface is basically identical to that[1c] of the Porter-Karplus surface so that the corresponding bending zero point energies should be the same.

If the final state rotational energies were just a function of the transition state bending energies, then we would predict that the Liu and PK temperature parameters should be the same. The fact that they are somewhat different is an indication that our model is overly simplistic.

Let us summarize the differences and similarities between the Liu and Porter-Karplus results. First, the reaction probabilities and integral reaction cross sections for the Liu surface have their effective thresholds shifted upwards in energy from the PK results by about 0.05 eV. At very low energies, the Liu cross sections are larger than the PK ones, apparently a result of the longer exponential tail of the PK surface. Details of the nature of the potential surface in the transition state region are apparently responsible for such subtle differences in the Liu - PK comparison as broader Liu rotational distributions and the narrower Liu angular distributions (above 0.4 eV). The general features of the Liu and PK reactive cross sections are

basically the same, and even such detailed quantities as the degree of rotational angular momentum polarization is quantitatively unchanged in going from one surface to the other. Still remaining to be completed for this surface is a detailed comparison of the thermal rate constants, which we shall leave to a future publication.

TABLE I. Nonreactive (N) and reactive (R) transition probability matrices for E = 0.60 eV, J = 0.*

(v'j') / (vj)	(00)	(01)	(02)	(03)	(04)	(05)	(06)
				N			
(00)	0.0538	0	0.739	0	0.0195	0	0.398(−8)
(01)	0	0.460	0	0.226	0	0.215(−3)	0
(02)	0.741	0	0.0690	0	0.0303	0	0.761(−8)
(03)	0	0.226	0	0.742	0	0.219(−2)	0
(04)	0.0196	0	0.0304	0	0.948	0	0.822(−7)
(05)	0	0.222(−3)	0	0.219(−2)	0	0.998	0
(06)	0.328(−8)	0	0.642(−8)	0	0.867(−7)	0	1.000
				R			
(00)	0.0249	0.0422	0.0219	0.425(−2)	0.251(−3)	0.249(−5)	0.334(−9)
(01)	0.0415	0.0713	0.0361	0.694(−2)	0.410(−3)	0.393(−5)	0.558(−9)
(02)	0.0220	0.0368	0.0183	0.331(−2)	0.177(−3)	0.172(−5)	0.279(−9)
(03)	0.421(−2)	0.699(−2)	0.327(−2)	0.537(−3)	0.273(−4)	0.338(−6)	0.544(−10)

TABLE I. (Cont.)

(v'j') (vj)	(00)	(01)	(02)	R (03)	(04)	(05)	(06)
(04)	0.257(−3)	0.411(−3)	0.183(−3)	0.280(−4)	0.177(−5)	0.462(−7)	0.431(−11)
(05)	0.280(−5)	0.451(−5)	0.202(−5)	0.406(−6)	0.601(−7)	0.215(−8)	0.116(−12)
(06)	0.197(−9)	0.318(−9)	0.147(−9)	0.285(−10)	0.337(−11)	0.113(−12)	0.767(−17)
SUMS‡	1.0005	1.0018	0.9981	0.9997	1.0000	1.0000	1.0000

* All projection quantum numbers m_j and m'_j are zero. Numbers in parentheses indicate power of ten by which number preceding it should be multiplied.

‡ Sum of probabilities from a given initial state over all possible final states and arrangement channels.

TABLE II. Basis sets used and associated computation times for each partial wave.

J	No. of Vibrations	j_{max}[a]	Total No. of Rotational States	N[b]	Times (IBM 370/158) Integration[c]	Total[c]
0	4 to 6	7 to 11	8 to 12	32 – 60	11 min.	14 min. (40)
1	4 or 5	5 or 6	14 or 18	56 – 90	42	54 (90)
2	4	5	22	88	37	48 (88)
3	4	4 or 5	20 or 26	92[d]	36	47 (92)
≥4	4	4 or 5	20 or 30	100[e]	47	61 (100)

[a] j_{max} is the largest value of j within each rotational manifold.

[b] Total number of channels included in each arrangement channel.

[c] Computation times are for the number of channels in parentheses and apply to computations for which both ortho para and parity decoupling are used. The difference between the total time and the integration time includes that for the matching procedure and asymptotic analysis.

[d] Refers to a basis with 26 rotational states for v = 0, 1 and 20 for v = 2, 3.

[e] Refers to a basis with 30 rotational states for v = 0, 1 and 20 for v = 2, 3.

TABLE III. Nonreactive and reactive transition probabilities for
E = 0.65 eV.

Transition	Reactive or	Basis Set		
$(vj \rightarrow v'j')$	Nonreactive	a (N = 56)	b (N = 72)	c (N = 64)
(A) $J = 1$, $m_j = m'_j = 0$				
$00 \rightarrow 02$	N	0.531	0.527	0.531
$01 \rightarrow 03$	N	0.193	0.186	0.186
$00 \rightarrow 00$	R	0.0404	0.0408	0.0402
$00 \rightarrow 01$	R	0.0740	0.0741	0.0739
$01 \rightarrow 01$	R	0.134	0.135	0.134
		d (N = 32)	e (N = 40)	
(B) $J = 0$, $m_j = m'_j = 0$				
$00 \rightarrow 02$	N	0.517	0.512	
$01 \rightarrow 03$	N	0.223	0.216	
$00 \rightarrow 00$	R	0.0432	0.0434	
$00 \rightarrow 01$	R	0.0780	0.0802	
$01 \rightarrow 01$	R	0.145	0.150	

Basis Sets:[*]

a. 4 vibrations, 14 rotations/vibration ($j_{max} = 5$).

b. 4 vibrations, 18 rotations/vibration ($j_{max} = 6$).

c. 4 vibrations, 18 rotations for $v = 0, 1$; 14 for $v = 3, 4$.

d. 4 vibrations, 8 rotations/vibration ($j_{max} = 7$).

e. 5 vibrations, 8 rotations/vibration ($j_{max} = 7$).

TABLE III. (Cont.)

* In each basis set, all values of the projection quantum numbers compatible with angular momentum restrictions and with matching restrictions were included (see Section 2.1 and Ref. 29).

TABLE IV. Convergence of selected[†] nonreactive and reactive transition probabilities with respect to number of terms included in expansion of $V(r_\lambda, R_\lambda, \gamma_\lambda)$.[*]

Energy	(vj) → (v'j')	Reactive or Nonreactive	Number of Terms			
			2	3	4	5
0.55 eV	00 → 02	N	0.737	0.707	0.706	0.706
	01 → 03	N	0.153	0.161	0.161	0.161
	00 → 00	R	0.720(-2)	0.483(-2)	0.511(-2)	0.514(-2)
	00 → 01	R	0.0119	0.811(-2)	0.839(-2)	0.847(-2)
	01 → 01	R	0.0206	0.0130	0.0135	0.0135
0.625 eV	00 → 02	N	0.605	0.642	0.629	0.624
	01 → 02	N	0.206	0.225	0.224	0.220
	00 → 00	R	0.0400	0.0353	0.0372	0.0377
	00 → 01	R	0.0726	0.0641	0.0655	0.0673
	01 → 01	R	0.128	0.115	0.117	0.120

* The expansion is given in Eq. 2.13.

TABLE IV. (Cont.)

† Only $J = m_j = m'_j = 0$ transition probabilities are considered in this comparison. Notation is analogous to Table I.

TABLE V. Integral cross sections at selected total energies. [a]

Cross Section	E = 0.30 eV	0.35	0.40	0.45	0.50	0.55	0.60	0.65	0.70
Q_{00-01}^A	0.388(-13)	0.360(-8)	0.200(-5)	0.141(-3)	0.372(-2)	0.0400	0.234	0.571	0.905
Q_{00-03}^A	b	b	0.410(-8)	0.241(-5)	0.166(-3)	0.346(-2)	0.0295	0.104	0.222
$Q_{00-ortho}^A$	0.388(-13)	0.360(-8)	0.201(-5)	0.144(-3)	0.390(-2)	0.0435	0.264	0.676	1.13
$Q_{02-ortho}^A$	b	0.916(-10)	0.149(-6)	0.183(-4)	0.628(-3)	0.910(-2)	0.0632	0.209	0.423
$Q_{04-ortho}^A$	b	b	b	0.289(-8)	0.218(-5)	0.478(-3)	0.131(-2)	0.0155	0.0269
Q_{00}^R	0.156(-12)	0.480(-8)	0.252(-5)	0.184(-3)	0.501(-2)	0.0574	0.352	0.933	1.52
Q_{01}^R	0.232(-13)	0.205(-8)	0.130(-5)	0.106(-3)	0.306(-2)	0.0372	0.228	0.648	1.11
Q_{02}^R	b	0.120(-9)	0.186(-6)	0.234(-4)	0.806(-3)	0.0120	0.0843	0.291	0.575
Q_{03}^R	b	b	0.333(-8)	0.145(-5)	0.908(-4)	0.196(-2)	0.0166	0.0677	0.160
Q_{04}^R	b	b	b	0.371(-8)	0.289(-5)	0.700(-3)	0.179(-2)	0.0224	0.0484
Q_{00-02}^N	b	d	3.00	d	8.82	d	13.0	d	13.2
Q_{00-02}^R	b	0.595(-10)	0.114(-6)	0.142(-4)	0.473(-3)	0.643(-2)	0.0437	0.130	0.220
Q_{00-02}^A	b	d	3.00	d	8.82	d	13.0	d	13.5
Q_{00-00}^N	299[c]	d	260[c]	d	234[c]	d	217[c]	d	205[c]

530

TABLE V. (Cont.)

a In bohr^2. All cross sections have been degeneracy averaged. Those para to ortho cross sections which have been summed over final states are only summed over those final states of the correct spin symmetry.

b Transition is energetically forbidden.

c Obtained by the extrapolation procedure of Section 3.4.

d Calculation not done.

TABLE VI. Integral reactive cross sections $Q^R_{0jm_j \to 0j'm'_j}$ between specified rotational sublevels, E = 0.60 eV.[a]

v'j'm'_j vjm_j	000	011	010	01-1	022	021	020	02-1	02-2
000	0.0432	0.00322	0.0717	0.00322	0.227(-3)	0.00474	0.0338	0.00474	0.227(-3)
011	0.00337	0.549(-3)	0.00596	0.835(-3)	0.488(-4)	0.709(-3)	0.00261	0.00127	0.774(-4)
010	0.0751	0.00596	0.128	0.00596	0.380(-3)	0.00812	0.0578	0.00812	0.380(-3)
01-1	0.00337	0.835(-3)	0.00596	0.549(-3)	0.774(-4)	0.00127	0.00261	0.709(-3)	0.488(-4)
022	0.262(-3)	0.538(-4)	0.419(-3)	0.855(-4)	0.111(-4)	0.811(-4)	0.209(-3)	0.134(-3)	0.146(-4)
021	0.00549	0.783(-3)	0.00897	0.00140	0.811(-4)	0.00113	0.00407	0.00228	0.134(-3)
020	0.0391	0.00288	0.0638	0.00288	0.209(-3)	0.00407	0.0286	0.00407	0.209(-3)
02-1	0.00549	0.00140	0.00897	0.783(-3)	0.134(-3)	0.00228	0.00407	0.00113	0.811(-4)
02-2	0.262(-3)	0.855(-4)	0.419(-3)	0.538(-4)	0.146(-4)	0.134(-3)	0.209(-3)	0.811(-4)	0.111(-4)

TABLE VI. (Cont.)

a Tabulated is $Q^R_{vjm_j \to v'j'm'_j}$ in bohr^2 for the transitions indicated. All reactance and scattering matrices have been symmetrized (see Ref. 13a) before the above cross sections were calculated.

TABLE VII. Para to ortho thermal rate constants for $H + H_2$[a]

T(K)	$k_{p \to o}(SK)$	$k_{p \to o}^{dist}(SK)$	$k_{p \to o}(KPS)$[b]	$k_{p \to o}(TST)$[b]
100	0.270(4)	0.341(4)	0.783(-2)	0.405(-5)
200	0.688(7)	0.722(7)	0.375(6)	0.161(5)
250	0.753(8)	0.773(8)	0.127(8)	0.125(7)
300	0.442(9)	0.449(9)	0.136(9)	0.225(8)
400	0.486(10)	0.490(10)	0.268(10)	0.833(9)
500	0.224(11)	0.224(11)	0.168(11)	0.737(10)
600	0.640(11)	0.640(11)	0.595(11)	0.322(11)

[a] All rate constants are in units of cm^3/(mole x sec). Quantum rate constants are believed accurate to 20%.

[b] Results of Ref. 2.

TABLE VIII. Decoupled integral cross sections $Q_{0jm_j \to 0j'm'_j}$ at 0.60 eV.[a]

$v'j'm'_j$ $\backslash$ vjm_j	000	011	010	01-1	022	021	020	02-1	02-2
000	0.0576	0	0.0986	0	0	0	0.0494	0	0
011	0	0	0	0.527(-3)	0	0	0	0.913(-3)	0
010	0.103	0	0.172	0	0	0	0.0877	0	0
01-1	0	0.527(-3)	0	0	0	0.913(-3)	0	0	0
022	0	0	0	0	0	0	0	0	0.422(-5)
021	0	0	0	0.00101	0	0	0	0.00176	0
020	0.0571	0	0.0968	0	0	0	0.0473	0	0
02-1	0.	0.00101	0	0	0	0.00176	0	0	0
02-2	0	0	0	0	0.422(-5)	0	0	0	0

a. All cross sections are in bohr^2. Notation is analogous to Table VI.

534

TABLE IX. Coefficients for the least squares fit to Liu's $\theta = 30°$, 60° and 90° surfaces.[a]

i	j	$C_{ij}(30°)$	$C_{ij}(60°)$	$C_{ij}(90°)$
0	0	5.67326	6.93856	5.87575
1	0	-2.17052	-3.24026	-1.94989
2	0	-3.06358	-3.35290	-6.04608
1	1	-0.43655	-0.61999	3.00608
3	0	0.95542	1.08790	-1.02272
2	1	0.81781	1.17948	1.81834
4	0	2.01484	2.01433	2.55290
3	1	1.54708	1.82541	1.41960
2	2	1.59424	1.62723	1.85699
5	0	0.05805	0.08883	0.60984
4	1	0.48219	0.41435	0.70763
3	2	0.78556	0.73016	0.57707
6	0	-1.14517	-1.14989	-1.27928
5	1	-1.07526	-1.05852	-0.89655
4	2	0.17417	-0.07773	0.21171
3	3	0.28048	0.53834	0.12530
7	0	0.37777	0.36052	0.23299
6	1	0.81861	0.90191	0.79935
5	2	0.30192	0.10197	0.30292
4	3	-1.07400	0.92003	-1.00811
8	0	-0.05473	-0.05276	-0.02291
7	1	0.03868	0.03533	0.09464

TABLE IX. (Cont.)

i	j	$C_{ij}(30°)$	$C_{ij}(60°)$	$C_{ij}(90°)$
6	2	-0.48780	-0.47006	-0.63252
5	3	0.00096	-0.03835	-0.05382
4	4	0.69364	0.71595	0.85941

[a]See text for definition of the C_{ij}. All distances are expressed in bohr and energies in Hartrees when using these coefficients in the analytical formulas.

TABLE X. Parameters of the fitted 3D H + H_2 surface[a]

θ	γ	r_{1max}	λ
0	1.53906	4.33	0.82
30	1.88123	3.4	1.07
60	1.88264	3.4	1.07
90	1.87689	3.2	1.07

[a]See text for definition of the parameters. γ and λ are in $(bohr)^{-1}$ and r_{1max} is in bohr.

TABLE XI. Integral cross sections for the Liu surface.[a]

Cross Section	E = 0.30 eV	0.35 eV	0.40 eV	0.45 eV	0.50 eV	0.55 eV	0.60 eV	0.65 eV	0.70 eV
$Q_{00\to01}^A$	0.528(-11)	0.510(-8)	0.343(-6)	0.894(-5)	0.182(-3)	0.286(-2)	0.0317	0.182	0.465
$Q_{00\to03}^A$	b	b	0.468(-8)	0.485(-6)	0.205(-4)	0.511(-3)	0.821(-2)	0.0602	0.189
$Q_{00\to ortho}^A$	0.528(-11)	0.510(-8)	0.348(-6)	0.943(-5)	0.202(-3)	0.337(-2)	0.0399	0.243	0.655
$Q_{02\to ortho}^A$	b	0.280(-9)	0.380(-7)	0.171(-5)	0.493(-4)	0.103(-2)	0.0140	0.0950	0.273
$Q_{04\to ortho}^A$	b	b	b	0.611(-8)	0.505(-6)	0.179(-4)	0.694(-3)	0.649(-2)	0.0282
Q_{00}^R	0.106(-10)	0.649(-8)	0.418(-6)	0.122(-4)	0.260(-3)	0.439(-2)	0.0527	0.323	0.880
Q_{01}^R	0.231(-11)	0.305(-8)	0.244(-6)	0.776(-5)	0.180(-3)	0.320(-2)	0.03916	0.244	0.656
Q_{02}^R	b	0.344(-9)	0.478(-7)	0.221(-5)	0.631(-4)	0.133(-2)	0.0185	0.126	0.368
Q_{03}^R	b	b	0.373(-8)	0.329(-6)	0.133(-4)	0.341(-3)	0.568(-2)	0.0436	0.144
Q_{04}^R	b	b	b	0.786(-8)	0.640(-6)	0.233(-4)	0.914(-3)	0.869(-2)	0.0382

[a] In bohr^2, analogous to Table V.

[b] Transition is energetically forbidden.

[1] (a) F. London, Z. Electrochem. 35, 552 (1929); H. Eyring and M. Polanyi, Z. Physik Chemie B12, 279 (1931); (b) S. Sato, J. Chem. Phys. 23, 592 (1955); (c) R. N. Porter and M. Karplus, J. Chem. Phys. 40, 1105 (1964); (d) I. Shavitt, R. M. Stevens, F. L. Minn and M. Karplus, J. Chem. Phys. 48, 2700 (1968); (e) H. Conroy and B. Bruner, J. Chem. Phys. 42, 4047 (1965); ibid. 47, 921 (1967); (f) B. Liu, J. Chem. Phys. 58, 1925 (1973); (g) see also C. Edmiston and M. Krauss, J. Chem. Phys. 49, 192(1968) and references therein.

[2] M. Karplus, R. N. Porter, and R. D. Sharma, J. Chem. Phys. 43, 3259 (1965).

[3] D. Micha, Arkiv Fysik 30, 427 (1965).

[4] M. Karplus and K. T. Tang, Disc. Far. Soc. 44, 56 (1967); K. T. Tang and M. Karplus, Phys. Rev. A4, 1844 (1971).

[5] J. D. Doll, T. F. George and W. H. Miller, J. Chem. Phys. 58, 1343 (1973).

[6] G. Wolken and M. Karplus, J. Chem. Phys. 60, 351 (1974).

[7] (a) B. H. Choi and K. T. Tang, J. Chem. Phys. 61, 2462 (1974); (b) ibid., 61, 5147 (1974).

[8]A. Kuppermann and G. C. Schatz, J. Chem. Phys. 62, 2502 (1975).

[9]A. B. Elkowitz and R. E. Wyatt, J. Chem. Phys. 62, 2504 (1975).

[10](a) R. P. Saxon and J. C. Light, J. Chem. Phys. 56, 3874 (1972);
ibid., 56, 3885 (1972); (b) A. Altenberger-Siczek and J. C. Light,
J. Chem Phys. 61, 4373 (1974); (c) R. P. Saxon and J. C. Light,
J. Chem. Phys. 57, 2758 (1972); (d) J. J. Tyson, R. P. Saxon and
J. C. Light, J. Chem. Phys. 59, 363 (1973).

[11]R. B. Walker and R. E. Wyatt, J. Chem. Phys. 61, 4839 (1974).

[12](a) A. Kuppermann, G. C. Schatz and M. Baer, J. Chem. Phys.
61, 4362 (1974);(b) G. C. Schatz and A. Kuppermann, in preparation.

[13](a)D. G. Truhlar and A. Kuppermann, J. Chem. Phys. 56, 2232
(1972); and references therein.

[14]H. Eyring, J. Chem. Phys. 3, 107 (1935); H. Pelzer and E. Wigner,
Z. physik. chem. B15, 445 (1932).

[15]H. S. Johnston, Gas Phase Reaction Rate Theory, (The Ronald Press
Co., New York, 1966) Chap. 10.

[16]I. Shavitt, J. Chem. Phys. 49, 4048 (1969).

[17]J. M. Bowman, A. Kuppermann, J. T. Adams and D. G. Truhlar,
Chem. Phys. Lett. 20, 229 (1973); J. M. Bowman, Ph. D. thesis,
California Institute of Technology (unpublished), 1974.

[18]D. J. Diestler, J. Chem. Phys. 56, 2092 (1972).

[19](a) R. D. Levine and S. F. Wu, Chem. Phys. Lett. 11, 557 (1971);
S. F. Wu and R. D. Levine, Mol. Phys. 22, 881 (1971).

[20]G. C. Schatz and A. Kuppermann, J. Chem. Phys. 59, 964 (1973).

[21]G. C. Schatz and A. Kuppermann, Phys. Rev. Lett., submitted.

[22] G. Wolken, W. H. Miller and M. Karplus, J. Chem. Phys. 56, 4930 (1972).

[23] A. C. Allison and A. Dalgarno, Proc. Phys. Soc. 90, 609 (1967).

[24] K. T. Tang, Phys. Rev. 187, 122 (1969).

[25] E. F. Hayes, C. A. Wells and D. J. Kouri, Phys. Rev. A4, 1017 (1971).

[26] A. A. Westenberg and N. de Haas, J. Chem. Phys. 47, 1393 (1967); D. N. Mitchell and D. J. LeRoy, J. Chem. Phys. 58, 3449 (1973); see Ref. 15 for earlier references.

[27] A. Kuppermann and J. M. White, J. Chem. Phys. 44, 4352 (1966).

[28] J. Geddes, H. F. Krause and W. L. Fite, J. Chem. Phys. 52, 3296 (1970); ibid., 56, 3298 (1972); ibid., 59, 566 (1973); G. H. Kwei, V. W. S. Lo and E. A. Entemann, J. Chem. Phys. 59, 3421 (1973); S. Datz and E. H. Taylor, J. Chem. Phys. 39, 1896 (1963).

[29] G. C. Schatz and A. Kuppermann, "Quantum Mechanical Reactive Scattering: Theory for Three Dimensional Atom Diatom Collisions," in preparation.

[30] A. Kuppermann, G. C. Schatz and M. Baer, "Quantum Mechanical Reactive Scattering: Theory for Planar Atom Diatom Collisions," in preparation.

[31] A. S. Davydov, Quantum Mechanics (trans. I. V. Schensted) (NEO Press, Ann Arbor, 1966) Chap. VI.

[32] The various potential matrix elements V_k^λ of Eq. 2.14 were evaluated using a procedure outlined in Ref. 12b in which the n term truncated expansion in Eq. 2.14 is required to be exactly satisfied

at n values of γ_λ and the V_{jk}^λ are solved for algebraically.

[33] This number can be obtained from a time delay analysis of the scattering matrix. See G. C. Schatz, Ph. D. thesis, California Institute of Technology (unpublished), 1975.

[34] R. T. Pack, J. Chem. Phys. 60, 633 (1974); P. McGuire and D. J. Kouri, J. Chem. Phys. 60, 2488 (1974).

[35] This can be verified by examining the expressions for J_z and H given in Ref. 29.

[36] This follows from (a) the assumption of Ref. 29 (which is implicit in Eq. 2.3) that the initial relative velocity vector is parallel to the space fixed z axis, (b) the definition of the angle θ (or θ_λ of Fig. 1), which is the angle between the outgoing z_λ' axis and the space fixed z axis, and (c) the relation $\theta_R = 180 - \theta$ of Section 2.1.

[37] For example, R. Gengenback, C. Hahn and J. P. Toennies, J. Chem. Phys. 62, 3620 (1975); M. A. Fluendy, R. M. Martin, E. E. Muschlitz and D. R. Herschbach, J. Chem. Phys. 46, 2172 (1967) (1967); W. C. Stwalley, A. Niehaus and D. R. Herschbach, J. Chem. Phys. 51, 2287 (1969).

[38] R. Gordon, J. Chem. Phys. 51, 14 (1969).

[39] Some ambiguity still exists because of the small difference (< 0.05 rad) between the single channel and converged phase shifts.

[40] R. D. Levine, Chem. Phys. Lett. 4, 309 (1969); J. Chem. Phys. 57, 1015 (1972).

[41] D. J. Diestler, J. Chem. Phys. 54, 4547 (1971).

[42] R. B. Walker and R. E. Wyatt, Mol. Phys. 28, 101 (1974).

[43] A. Ben-Shaul, R. D. Levine and R. B. Bernstein, Chem. Phys. Lett. 15, 160 (1972); J. Chem. Phys. 57, 5427 (1972).

[44] R. Wyatt, private communication.

[45] A. B. Elkowitz and R. E. Wyatt, "Three Dimensional Natural Coordinate Asymmetric Top Theory of Reactions: Application to $H + H_2$," J. Chem. Phys., in press.

[46] J. M. Bowman and A. Kuppermann, J. Chem. Phys. 59, 6524 (1973); W. H. Miller and T. F. George, J. Chem. Phys. 57, 2458 (1972).

[47] A. Farkas, Orthohydrogen, Parahydrogen and Heavy Hydrogen (Cambridge Univeristy Press, 1935), p. 13.

[48] J. T. Adams, J. M. Bowman and A. Kuppermann, unpublished results.

[49] For examples, see: J. M. Farrar and J. T. Lee, J. Chem. Phys. 56, 5801 (1972); P. E. Siska, J. M. Parson, T. P. Schaefer and Y. T. Lee, J. Chem. Phys. 55, 5762 (1971); J. M. Farrar and Y. T. Lee, J. Chem. Phys. 57, 5492 (1972).

[50] These approximations usually involve the replacement of $J(J + 1)$ $-2\Omega_\lambda^2 + j_\lambda(j_\lambda + 1)$ by $J(J + 1)$, or by $l_\lambda(l_\lambda + 1)$ as is done in Ref. 34. (See also Ref. 29.)

[51] This is true because the degree of mixing is to a certain extent a reflection of the extent of changes in the Hamiltonian which occur upon changing from λ to ν arrangement channel coordinate systems. If mixing is weak, then the λ to ν transformation does not have a major effect, and it is logical to assume that a change in the position of the matching surface, and hence the position of the transformation

will not be important.

[52] The converged $P_{J, 000 \to 020}^{N}$ at 0.60 eV decreases rapidly from 0.74 at J = 0, to 0.025 at J = 10 (Fig. 8), while the decoupled result increases from 0.74 at J = 0 to 0.76 at J = 3 and thereafter decreases slowly to 0.41 at J = 10.

[53] The neglected angular momentum coupling terms in Eq. A.1 are typically 50 to 100 times smaller (for, say, $J \le 4$) than the corresponding potential coupling (which is diagonal in Ω_λ) in the strong interaction region which is important in determining the reaction cross section. This is presumably a much less efficient mechanism for causing transitions between states of different Ω_λ than is the matching (Eq. A.6) which has off diagonal Ω_λ coupling elements which are often of the same order of magnitude as the diagonal elements.

[54] B. Liu, private communication.

[55] A. C. Yates and W. A. Lester, Chem. Phys. Lett. 24, 305 (1974).

[56] Note that the H_2 dissociation energy in Liu's nonlinear calculations is 0.173308 a.u.[54] while that for the more accurate linear results is 0.173704 a.u. In order to relate the linear and nonlinear surfaces, it was assumed that the difference in accuracy of the two calculations is the same at all internuclear distances, and equal to the difference in the dissociation energies. Accordingly, 0.000396 a.u. (0.0108 eV) has been subtracted from all of Liu's nonlinear points before the fitting procedure was applied.

[57]The r_{1max} values are approximately equal to the maximum values of r_1 considered in the ab initio calculations. The $\lambda(\theta)$ parameters are obtained by examining the asymptotic exponential decay of the Porter-Karplus surface, and assuming that it is unchanged for the Liu surface.

FIG. 1. Space fixed coordinate system Oxyz, body fixed system $Ox_\lambda'y'z_\lambda'$ and their relation to the triatomic collision system and to each other. The origin is chosen to lie at the center of mass of the three atoms. z_λ' lies along the vector from A_λ to the center of mass of $A_\nu A_\kappa$, y' is perpendicular to the three atom plane and x_λ' lies in that plane so that $x_\lambda'y'z_\lambda'$ form a right handed system. The auxiliary body fixed system $OX_\lambda Y_\lambda Z_\lambda$ is obtained from Oxyz by Euler rotations $\alpha = \phi_\lambda$, $\beta = \theta_\lambda$, $\gamma = 0$ so that $Z_\lambda = z_\lambda'$ and Y_λ lies in the space fixed xy plane.

FIG. 2. (a) Reaction probability $P_{J,00\to01}^R$ (summed over final m_j') as a function of J for total energies E = 0.30, 0.35, 0.40 and 0.45 eV. (b) These same reaction probabilities multiplied by 2J + 1.

FIG. 3. (a) Reaction probability $P_{J,00\to01}^R$ analogous to Fig. 2, but at E = 0.50, 0.55, 0.60, 0.65 and 0.70 eV. (b) 2J + 1 times these reaction probabilities.

FIG. 4. Reaction probability $P_{J,000\to01m_j'}^R$ versus J for m_j' = 0, ± 1 at 0.60 eV total energy (E_0 = 0.328 eV). Curve labelled sum is the sum of the probabilities over m_j'.

FIG. 5. Reaction probability $P_{J,000\to03m_j'}^R$ versus J for m_j' = 0, ± 1, ± 2, ± 3 at 0.60 eV total energy, analogous to Fig. 5.

FIG. 6. Influence of projection quantum number m_j (j > 0) on the allowed relative orientations of atom (A) with respect to diatom (BC) for zero impact parameter collisions: (a) m_j = 0 initially so that

rotational angular momentum vector is perpendicular to direction of relative motion; (b) $m_j > 0$ initially so that the j vector lies in a cone about the relative motion vector and makes an acute angle with it. In both (a) and (b) the rotation plane of the diatom is indicated by a small ellipse.

FIG. 7. Phases of $S_{J,000 \to 01m'_j}^{R}$ for $m'_j = 0, \pm 1$ as a function of J at $E = 0.60$ eV.

FIG. 8. (a) Nonreactive transition probability $P_{J,000 \to 02m'_j}^{N}$ at 0.60 eV total energy for $m'_j = 0, \pm 1, \pm 2$. Curve labelled sum is the degeneracy averaged $P_{J,00 \to 02}^{N}$. (b) Analogous space fixed probabilities for the three orbital angular momenta $l' = J, J + 2, J - 2$. The sum is invariant to the use of body fixed or space fixed representations.

FIG. 9. Differential cross sections $\sigma_{00 \to 01}^{A}$ as a function of the reactive scattering angle θ_R at the same energies as were considered in Fig. 2.

FIG. 10. Differential cross sections $\sigma_{00 \to 01}^{A}$, as in Fig. 9 for the same energies considered in Fig. 3.

FIG. 11. Differential cross section $\sigma_{000 \to 03m'_j}^{A}$ for $m'_j = 0, \pm 1, \pm 2, \pm 3$ at $E = 0.60$ eV. Curve labelled sum is the degeneracy averaged $\sigma_{00 \to 03}^{A}$.

FIG. 12. Differential nonreactive cross section $\sigma^N_{000 \to 02m'_j}$ for $m'_j = 0, \pm 1, \pm 2$ at $E = 0.60$ eV. Curve labelled sum is the degeneracy averaged $\sigma^N_{00 \to 02}$.

FIG. 13. Degeneracy averaged differential cross sections $\sigma^N_{00 \to 02}$, $\sigma^A_{00 \to 02}$ and $\sigma^R_{00 \to 02}$ at $E = 0.50$ eV ($E_0 = 0.228$ eV). The nonreactive and antisymmetrized curves are essentially identical for $\theta > 20°$. Note the use of θ rather than θ_R for plotting the reactive differential cross section.

FIG. 14. Degeneracy averaged $\sigma^N_{00 \to 02}$, $\sigma^A_{00 \to 02}$ and $\sigma^R_{00 \to 02}$ analogous to Fig. 13 but at $E = 0.60$ eV.

FIG. 15. Degeneracy averaged $\sigma^N_{00 \to 02}$, $\sigma^A_{00 \to 02}$ and $\sigma^R_{00 \to 02}$ analogous to Fig. 13 but at 0.70 eV ($E_0 = 0.428$ eV).

FIG. 16. Differential cross sections $\sigma^A_{000 \to 02m'_j}$ (solid lines labelled A) and $\sigma_{000 \to 02m'_j}$ (dashed lines labelled N) for (a) $m'_j = 0$, (b) $m'_j = \pm 1$, and (c) $m'_j = \pm 2$ at $E = 0.70$ eV. The sum of the three solid curves and of the three dashed curves is shown in Fig. 15.

FIG. 17. Integral cross sections Q^R_{00}, $Q^A_{00 \to 01}$ and $Q^A_{00 \to 03}$ (degeneracy averaged) as a function of the total energy E and translational energy E_0. Arrows in abscissa indicate the energies at which the rotational states j = 2 - 7 (for v = 0) of H_2 become energetically accessible. (a) linear scale, (b) logarithmic scale.

FIG. 18.   Phase shift associated with the elastic scattering matrix element $S_{J,000 \to 000}^{N}$ (i.e., $\mathrm{Arg}\,(S_J)/2$) as a function of J for $E = 0.70$ eV.   Curve labelled converged is the coupled channel result while the central field curve is the result of a single channel calculation described in text.   Also plotted is the (converged) elastic transition probability $P_{J,000 \to 000}^{N}$ at the same energy (curve with crosses) referenced to right hand ordinate.

FIG. 19.   Elastic differential cross section $\sigma_{000 \to 000}^{N}$, total cross section σ_{000}^{T} (both from the coupled channel calculation), along with the central field elastic cross section $\sigma_{000 \to 000}^{N}$ (CF), as a function of scattering angle at $E = 0.70$ eV.

FIG. 20.   One, two and three dimensional total reaction probabilities $P_0^{\bar{R}}(1D)$, $P_{00}^{\bar{R}}(2D,\ J = 0)$ and $P_{00}^{\bar{R}}(3D,\ J = 0)$, summed over all final states, as a function of the total energy E and translational energy E_0.

FIG. 21.   1D, 2D and 3D total reaction probabilities analogous to Fig. 20 but with a linear rather than logarithmic scale.

FIG. 22.   2D and 3D differential cross sections $\sigma_{00 \to 01}^{A}(2D)$ ($\bar{\sigma}^{A}$ of Ref. 12b) and $\sigma_{00 \to 01}^{A}(3D)$.   The 3D cross section (solid curve), at 0.60 eV total energy, is referred to the left hand scale while the 2D result (circles) at 0.55 eV, is referenced to the right ordinate scale.

FIG. 23. Reactive degeneracy averaged integral cross sections $Q^R_{0j \to 0j'}$ (divided by $(2j'+1) \times \bar{\rho}(E^{tr}_{j'})$) as a function of the product rotational energy $E_{j'}$ and the product rotational quantum number j' at 0.60 eV total energy for initial rotational quantum numbers $j = 0, 1, 2, 3, 4$.

FIG. 24. Reactive degeneracy averaged integral cross sections $Q^R_{00 \to 0j'}$ (divided by $(2j'+1) \times \bar{\rho}(E^{tr}_{j'})$) as a function of the product rotational energy $E_{j'}$ analogous to Fig. 23 at 0.45, 0.50, 0.55, 0.60, 0.65 and 0.70 eV.

FIG. 25. Comparison of reactive integral cross sections from several $H + H_2$ calculations. The Q^R_{0j} (KPS) for $j = 0, 1$ and 2 are the quasi-classical results of Karplus, Porter and Sharma (indicated by dashed lines), while Q^R_{00} is the analogous total reaction cross section obtained by Elkowitz and Wyatt (indicated by squares). The present results are Q^R_{0j} (SK) with $j = 0, 1, 2$ and are connected by solid lines.

FIG. 26. Comparison of the integral cross sections $Q^R_{00 \to 01}$ as a function of E. The results labelled WK are those of Wolken and Karplus, TK denotes those of Tang and Karplus, CT the one point of Choi and Tang, and SK the present results.

FIG. 27. Comparison of the differential reaction cross section σ^R_{00} as obtained by (a) the quasi-classical trajectory method of Karplus, Porter and Sharma (the histogram labelled KPS) at E = 0.752 eV, and (b) the present coupled channel method (labelled SK) at 0.70 eV.

FIG. 28. Comparison of the differential cross section $\sigma_{00 \to 01}^{A}$ as calculated by (a) the distorted wave method of Choi and Tang (dashed curve labelled CT) at E = 0.772 eV, (b) the one vibration coupled channel method of Wolken and Karplus (dash-dotted curve labelled WK) at E = 0.773 eV, and (c) the present method (solid curve labelled SK) at 0.70 eV. The TK results in Ref. 4 have been multiplied by the necessary factor of 3 to obtain the curve plotted.

FIG. 29. Comparison of the semi-classical differential cross section $\sigma_{00 \to 01}^{A}$ of Doll, George and Miller (dashed curve labelled DGM) at 0.472 eV with the corresponding $\sigma_{00 \to 01}^{A}$ of the present work (solid curve labelled SK) at 0.45 eV. Note that both curves have been normalized to the same value at $\theta_{R} = 180°$.

FIG. 30. Reaction probability $P_{J,000 \to 000}^{R}$ for J = 0 as a function of the total energy E. Two curves labelled DGM are the semi-classical results of Doll, George and Miller using the primitive semi-classical expression (dashed) and classical semi-classical expression (dash-dotted) using the terminology of Ref. 47. The two crosses are points from the work of Wolken and Karplus (WK) and the present results (SK) are denoted by circles. The DGM and WK probabilities have been divided by 3 as described in Ref. 5 to compare with our distinguishable atom probabilities.

FIG. 31. Nonreactive integral cross section $Q_{00 \to 02}^{N}$ as a function of E. The solid curve labelled WMK is the coupled channel result of Wolken, Miller and Karplus. (The actual points calculated are denoted by squares.) The present results (SK), given by circles, are connected

by a dashed line. Arrow in abscissa indicates the energy at which

$v = 0$, $j = 2$ of H_2 becomes energetically accessible.

FIG. 32. Nonreactive differential cross section $\sigma^N_{00 \to 02}$. The dashed curve indicates the results of Wolken, Miller and Karplus (WMK) at 0.523 eV. The present result (SK) (at 0.5 eV) is denoted by a solid curve and the dash-dotted curve denotes the coplanar result (at 0.5 eV) of Ref. 12b with ordinate scale given on the right side of the graph.

FIG. 33. Arrhenius plot of the para to ortho thermal rate constant. The present quantum result is denoted by SK while the quasi-classical result of Karplus, Porter and Sharma is labelled KPS and the transition state theory result is labelled TST.

FIG. 34. Reaction probabilities $P_{J,000 \to 010}$ for decoupled and converged calculations (solid lines and dashed lines) at E = 0.50, 0.60 and 0.70 eV.

FIG. 35. Reaction probabilities $P^R_{J,01-m_j \to 02m_j}$ for decoupled and converged calculations (solid lines and dashed lines) with $m_j = 0$ and $m_j = \pm 1$.

FIG. 36. Differential cross section $\sigma^A_{000 \to 010}$ for decoupled and converged calculations analogous to those considered in Fig. 34.

FIG. 37. Differential cross section $\sigma^A_{01-m_j \to 02m_j}$ for decoupled and converged calculations analogous to those considered in Fig. 34.

FIG. 38. Integral cross section $Q^A_{000 \to 010}$ as a function of E and E_0 for decoupled and converged calculations (solid and dashed lines). (a) linear scale, (b) logarithmic scale.

FIG. 39. Three dimensional total reaction probability P^R_{00} (J = 0) for the Liu (squares) and PK (circles) surfaces as a function of the total energy E and reagent translational energy E_0.

FIG. 40. Total reaction probability P^R_{00} (J = 0) as in Fig. 39 but using linear rather than semilogarithmic scales.

FIG. 41. Reaction probability $P^R_{J,00 \to 01}$ for the Liu (squares) and PK (circles) surfaces at E = 0.60 eV as a function of J.

FIG. 42. Differential cross section $\sigma^A_{00 \to 01}$ for the Liu (solid) and PK (dashed) surfaces at E = 0.40 eV.

FIG. 43. Differential cross section $\sigma^A_{00 \to 01}$ at E = 0.50 eV analogous to Fig. 41.

FIG. 44. Differential cross section $\sigma^A_{00 \to 01}$ at E = 0.60 eV analogous to Fig. 41.

FIG. 45. Integral total cross section Q^R_{00} for the Liu (squares) and PK (circles) surfaces as a function of E and E_0, on a linear scale (a), and semilogarithmic scale (b).

FIG. 46. Reactive degeneracy averaged integral cross sections $Q^R_{0j \to 0j'}$ (divided by $(2j' + 1) \times \bar{\rho}(E^{tr}_{j'})$) for the Liu surface as a function of $E_{j'}$ and j' for j = 0, 1, 2, 3, 4 (analogous to Fig. 23).
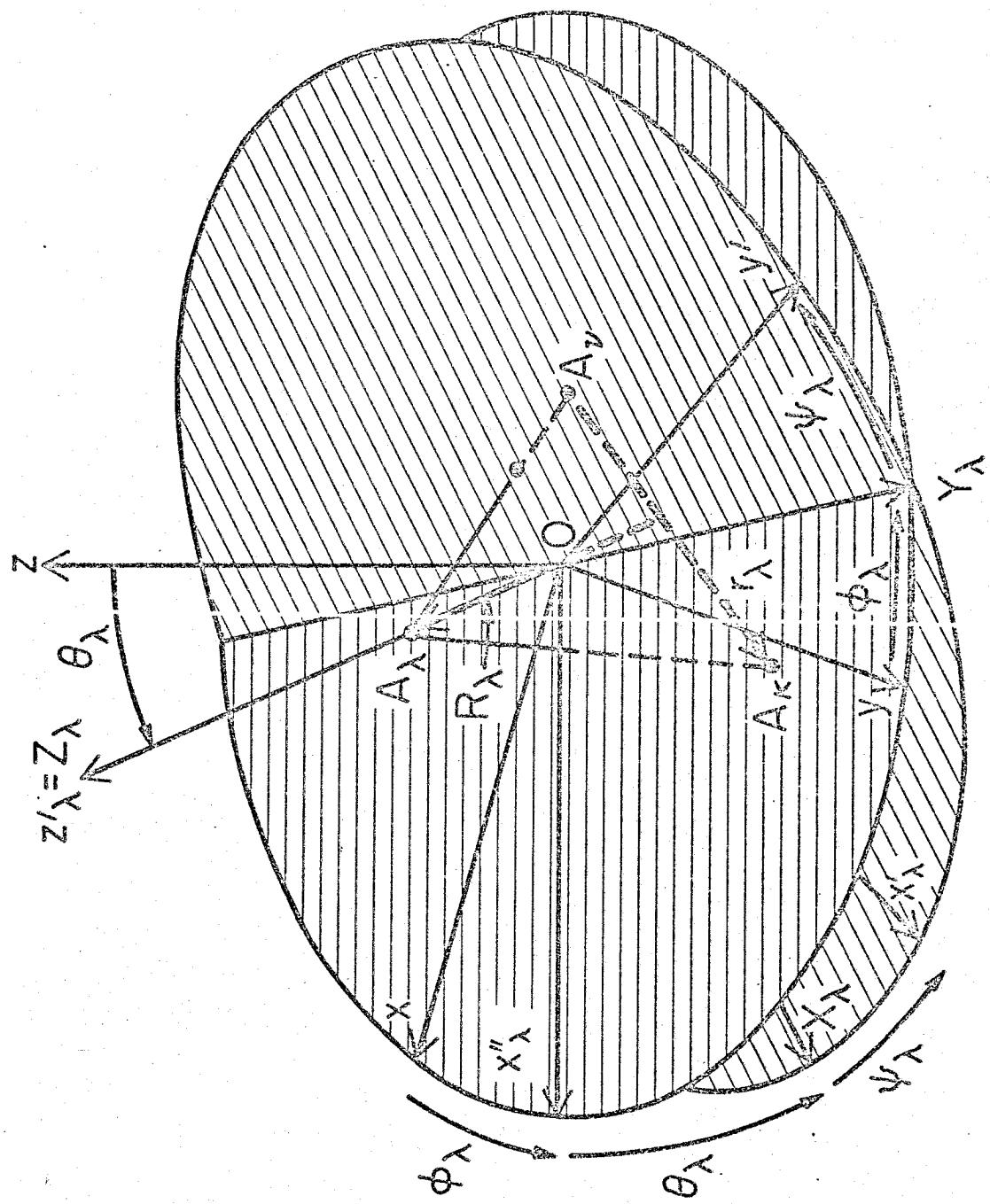
Figure 1
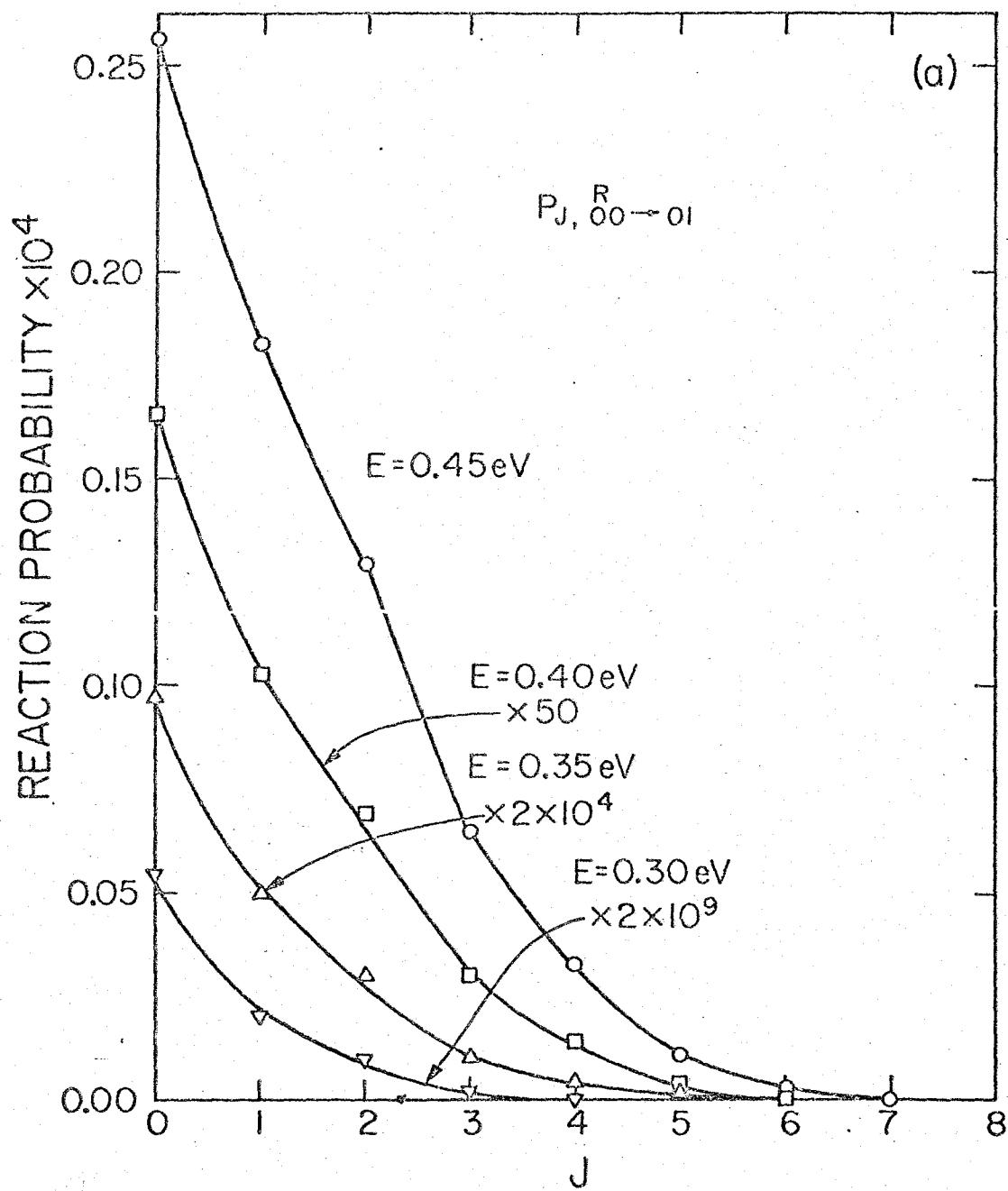
Figure 2a
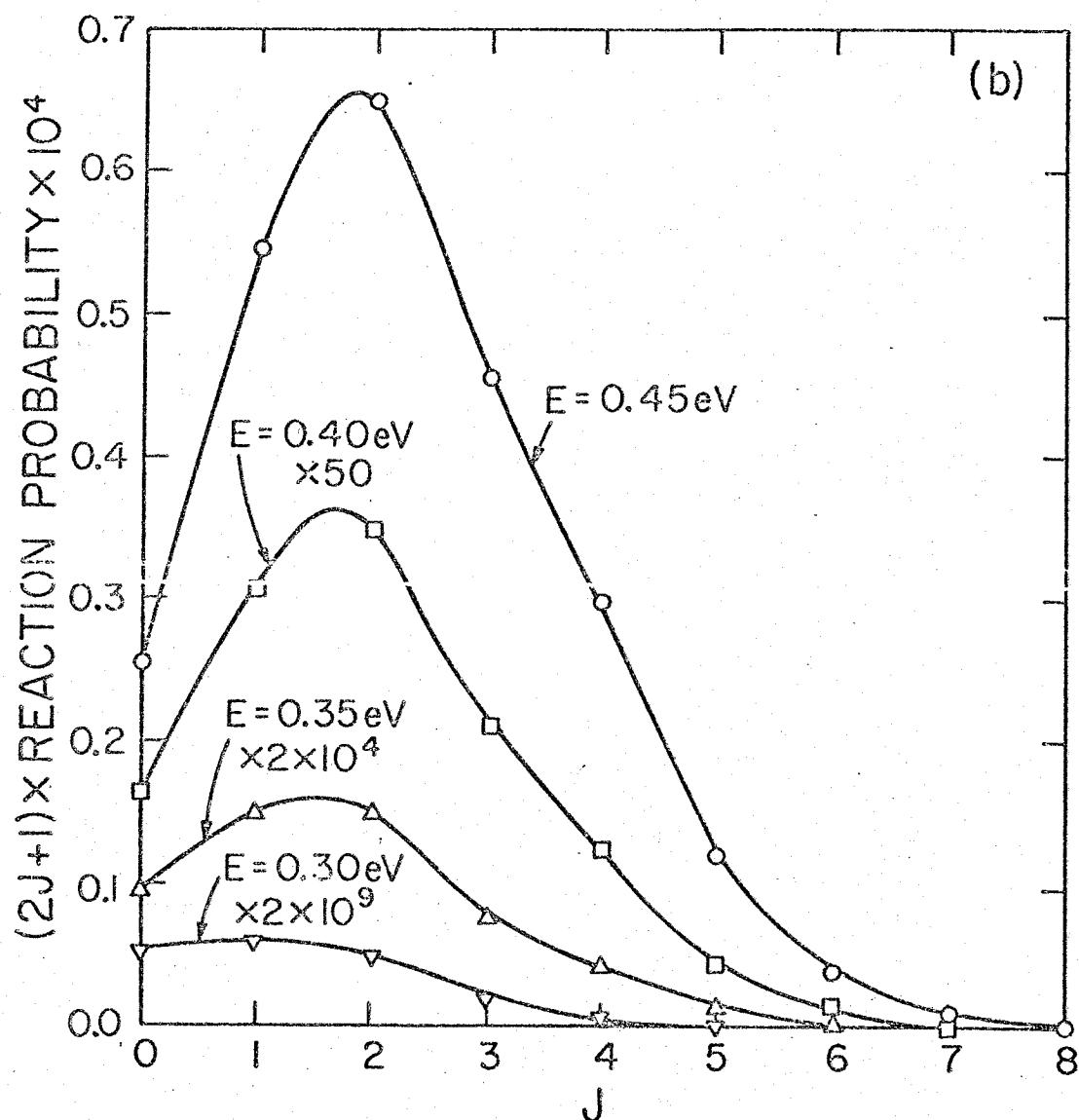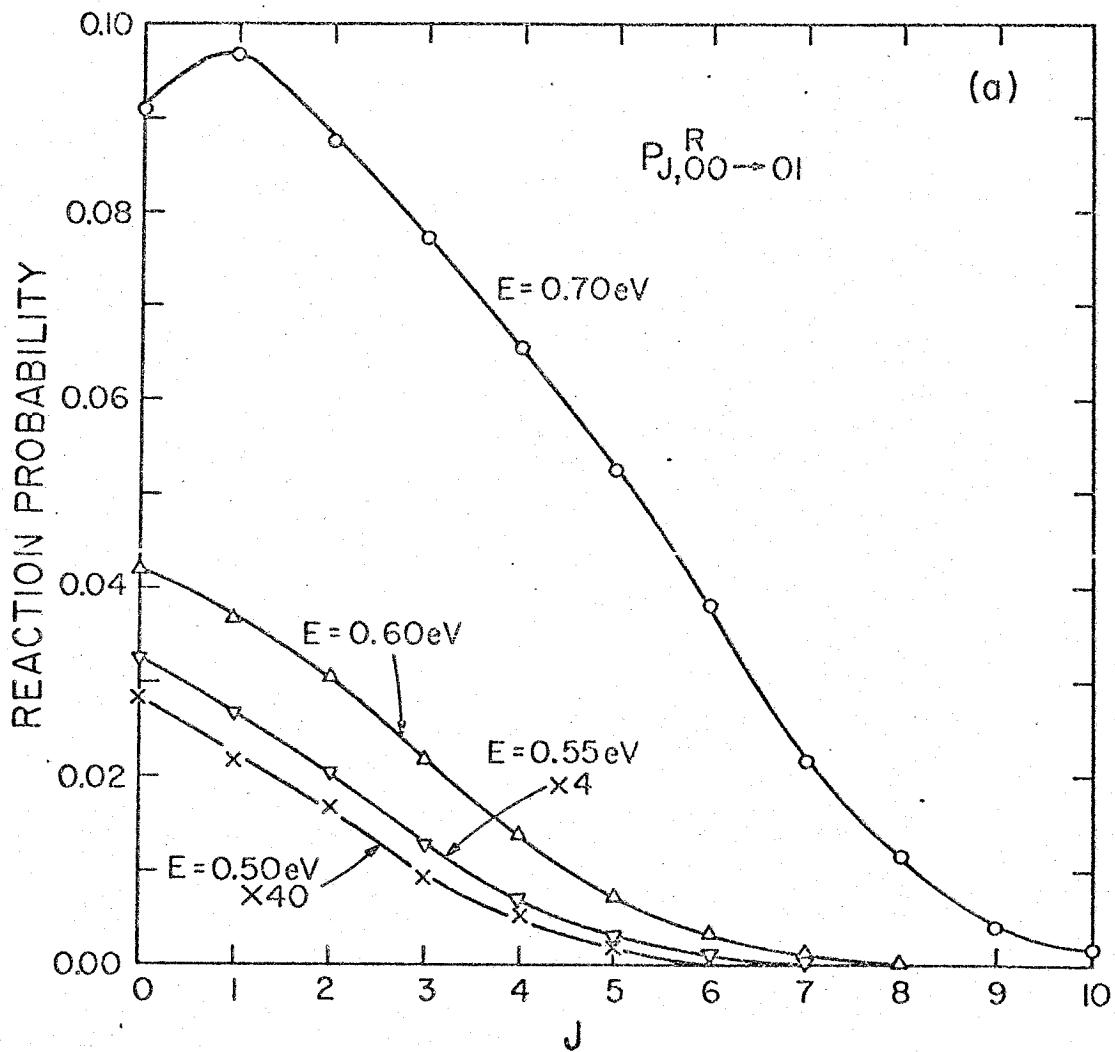
Figure 2b

Figure 3a
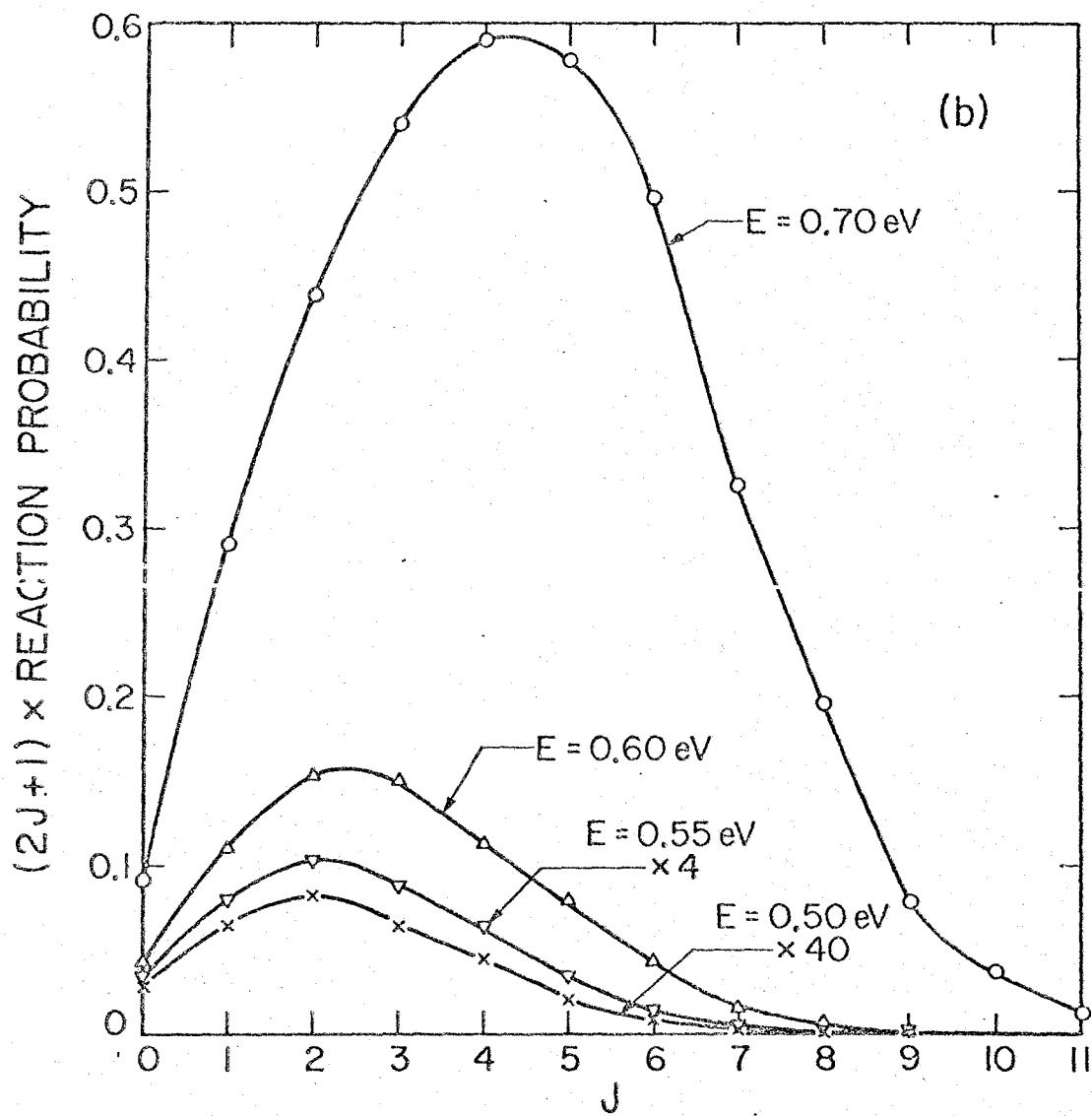
Figure 3b
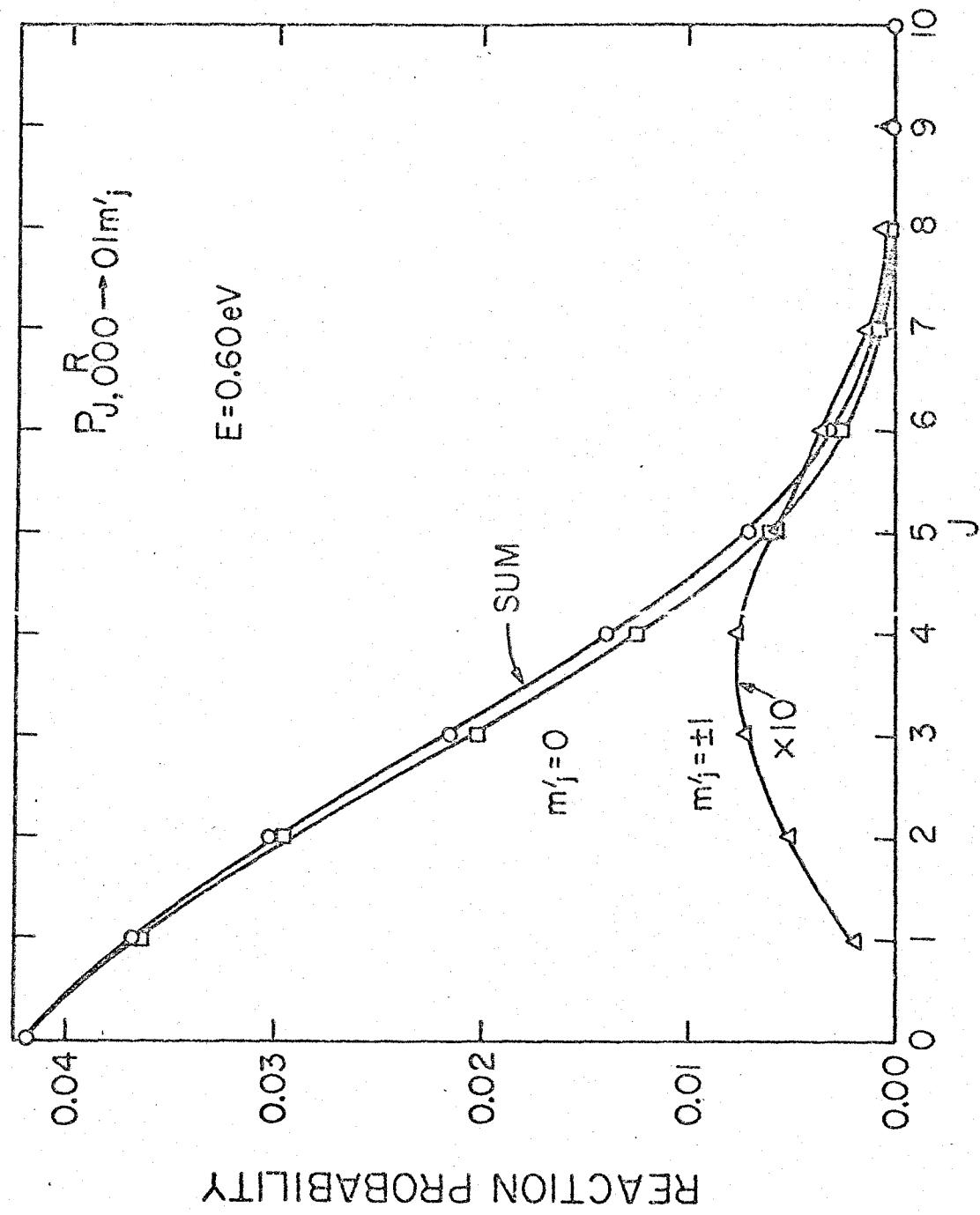
Figure 4
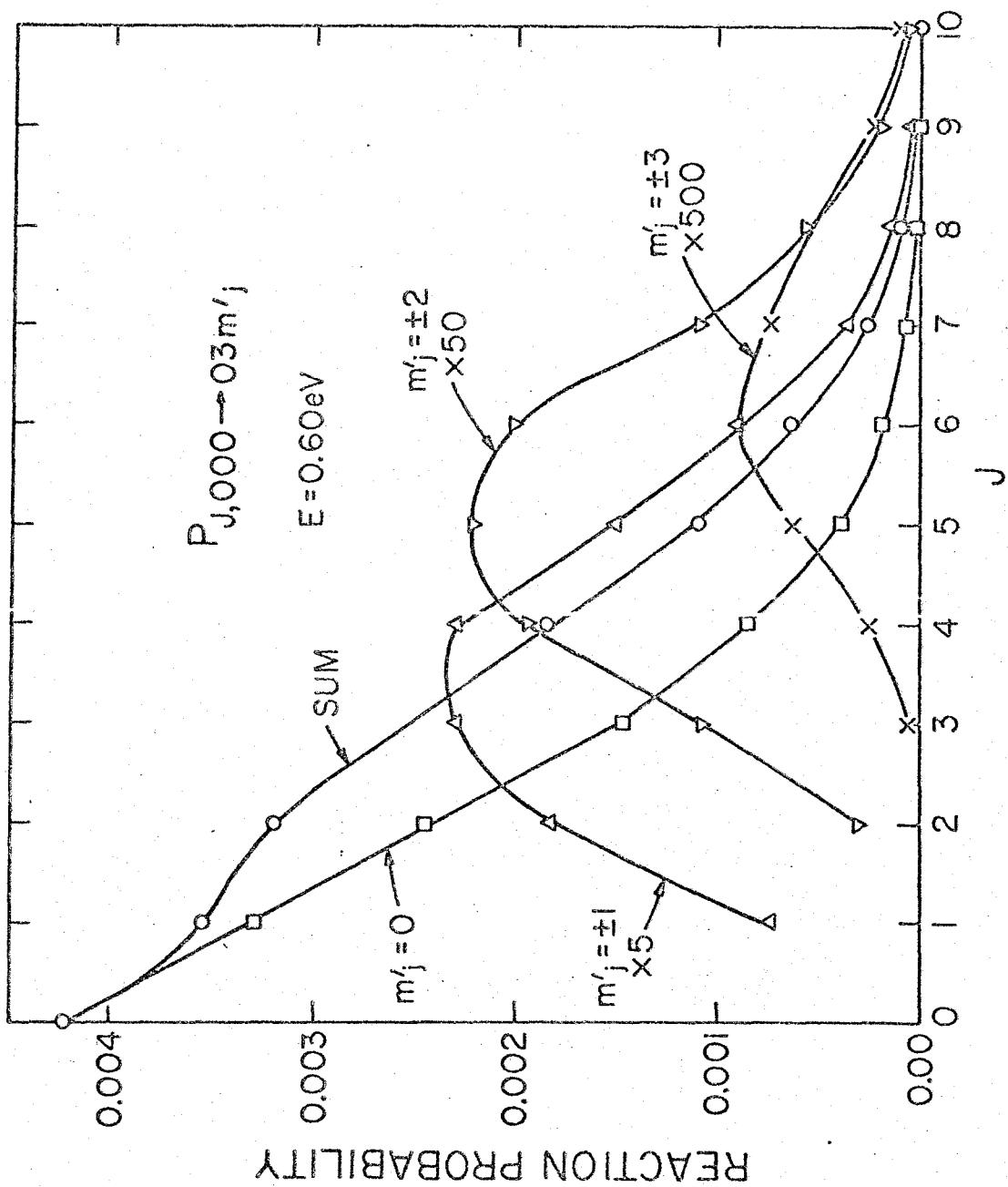
Figure 5

(a)
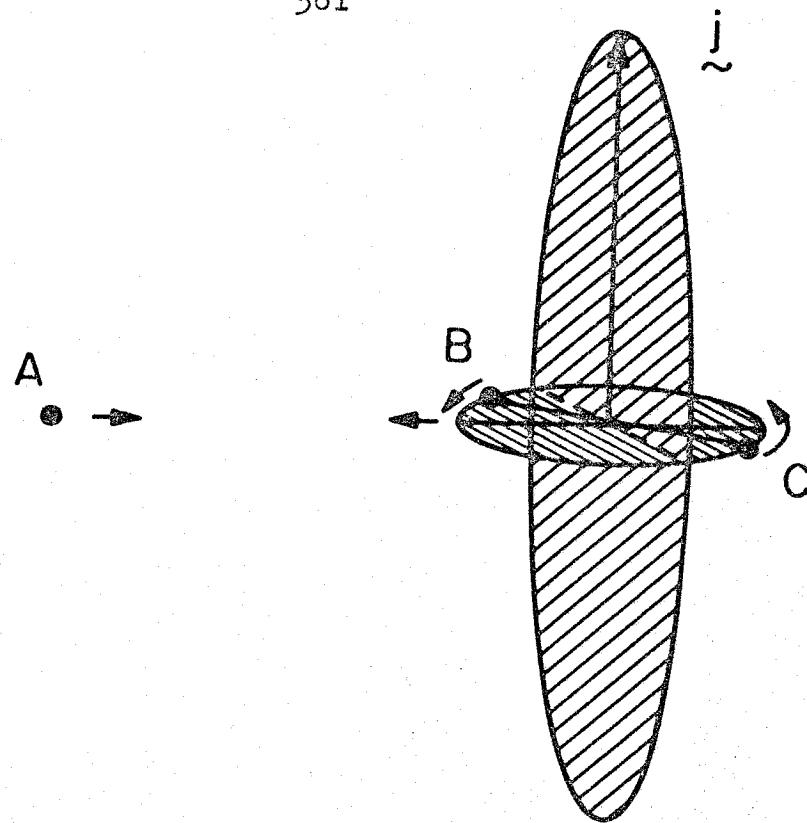
(b)
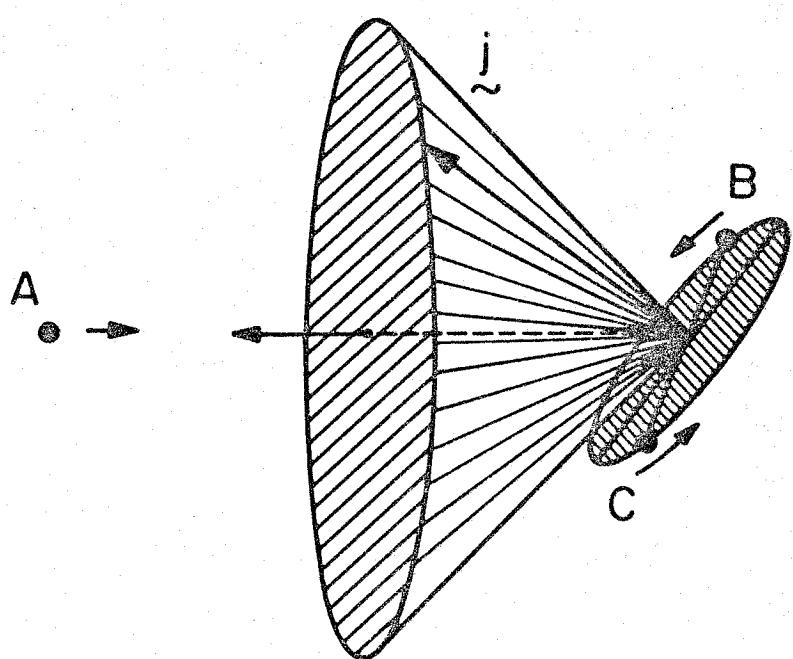
Figure 6
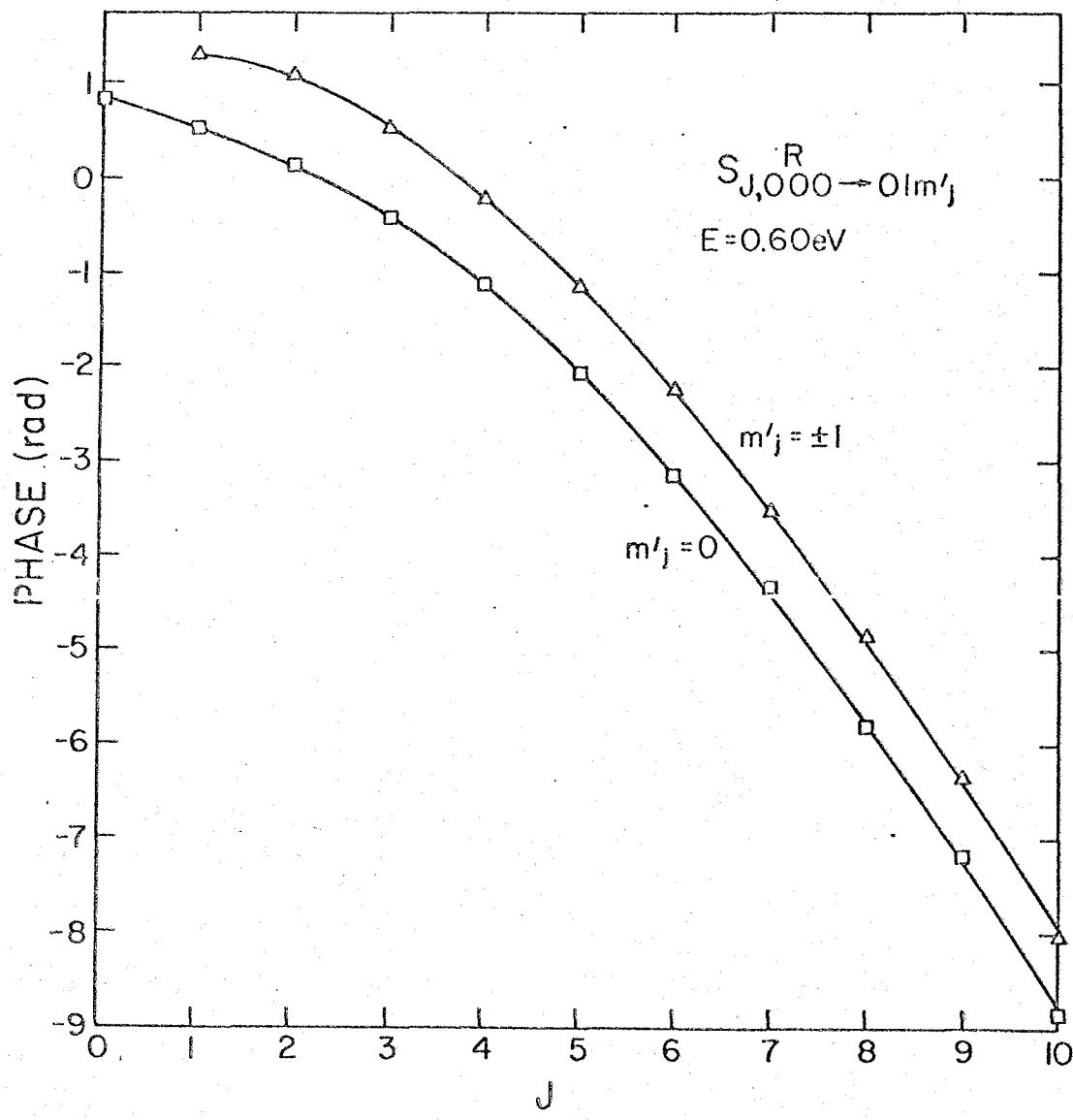
Figure 7
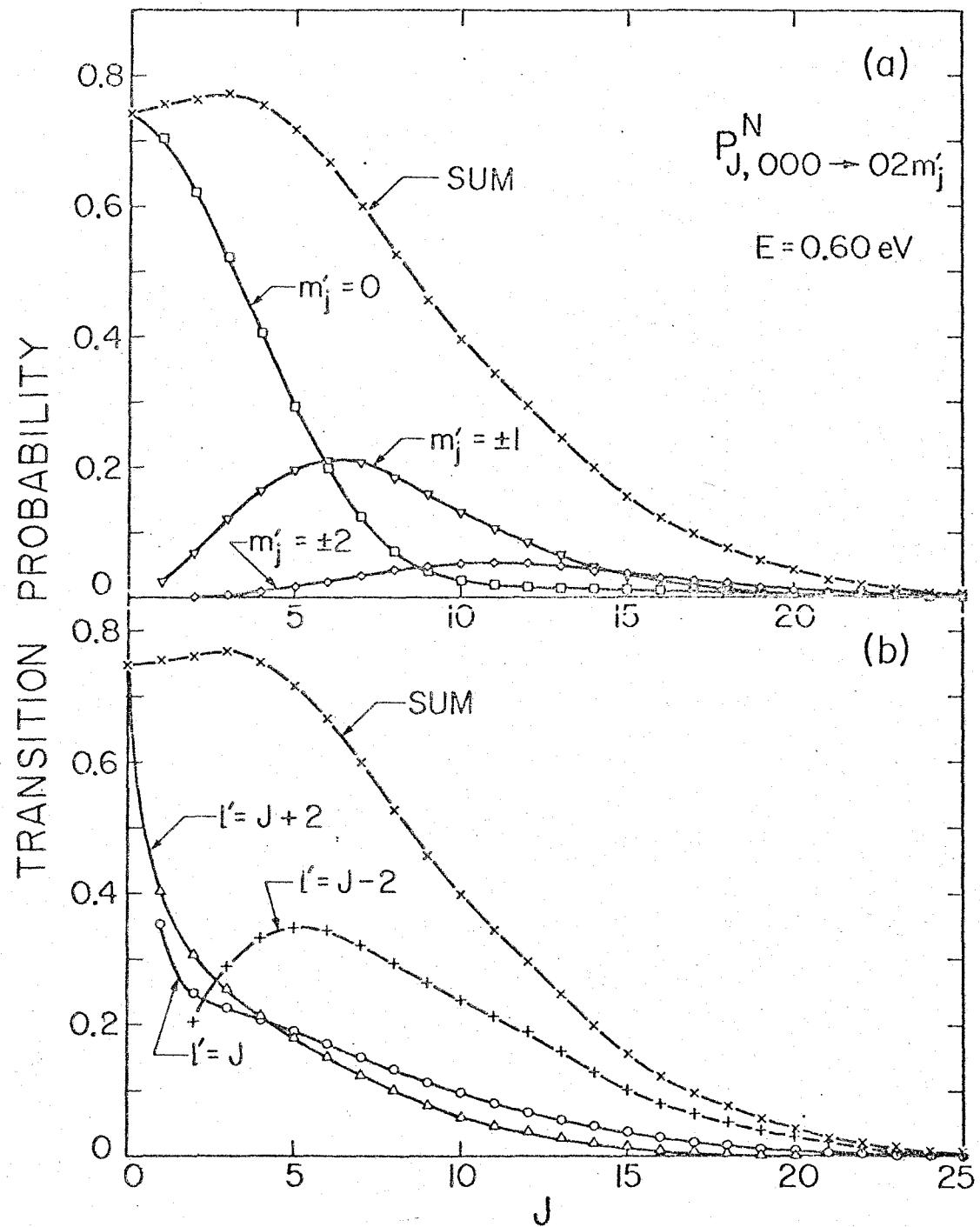
Figure 8
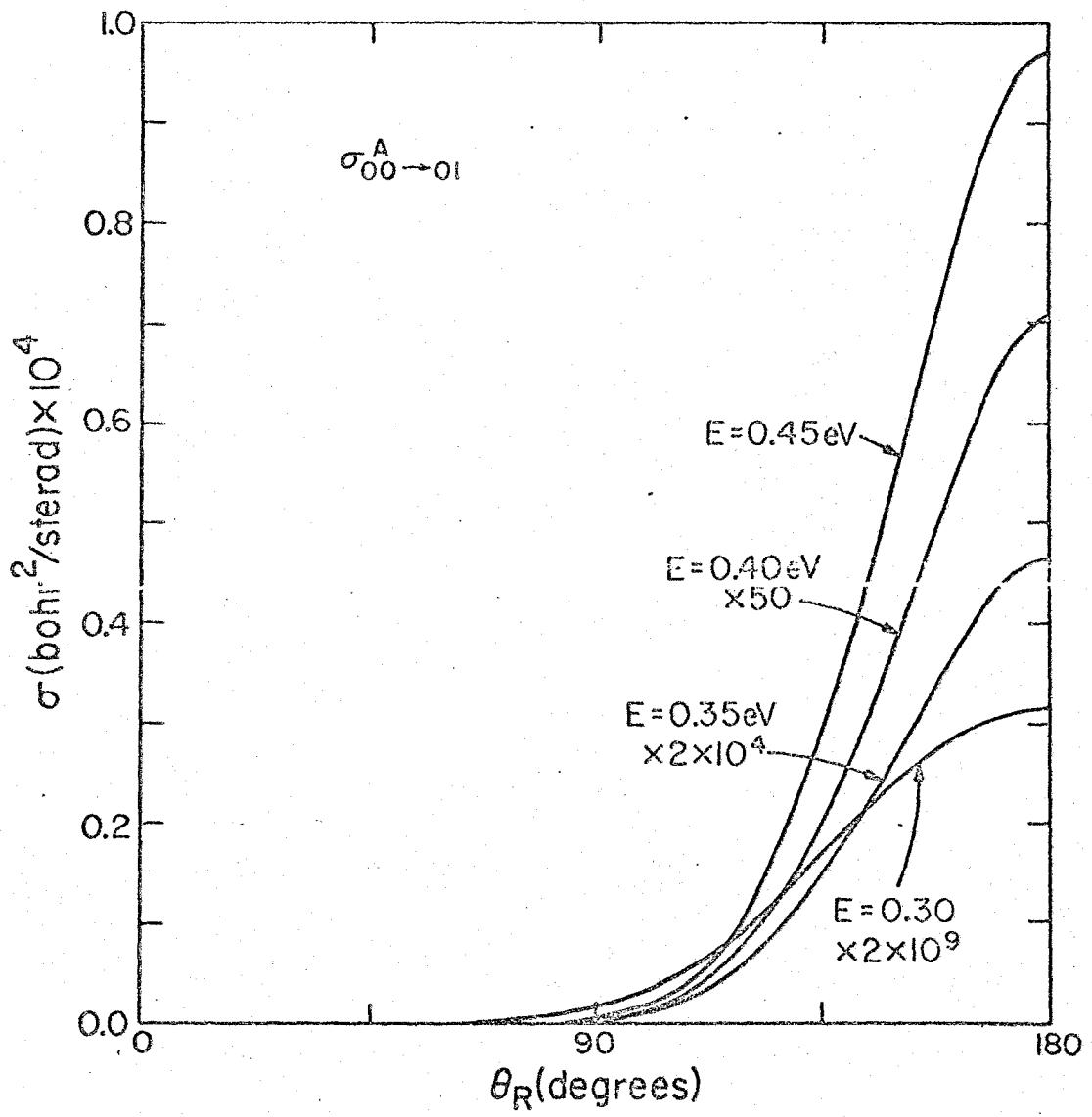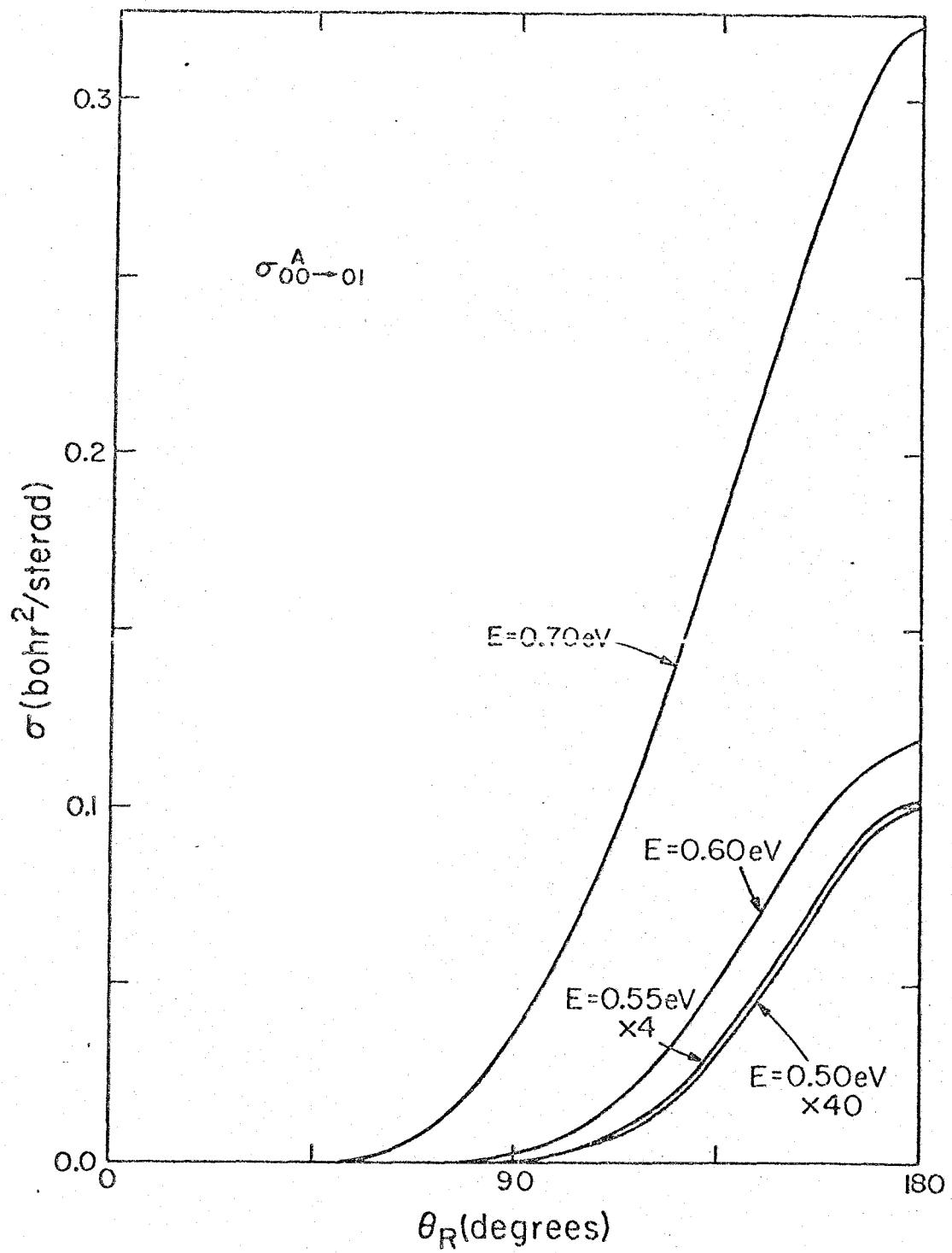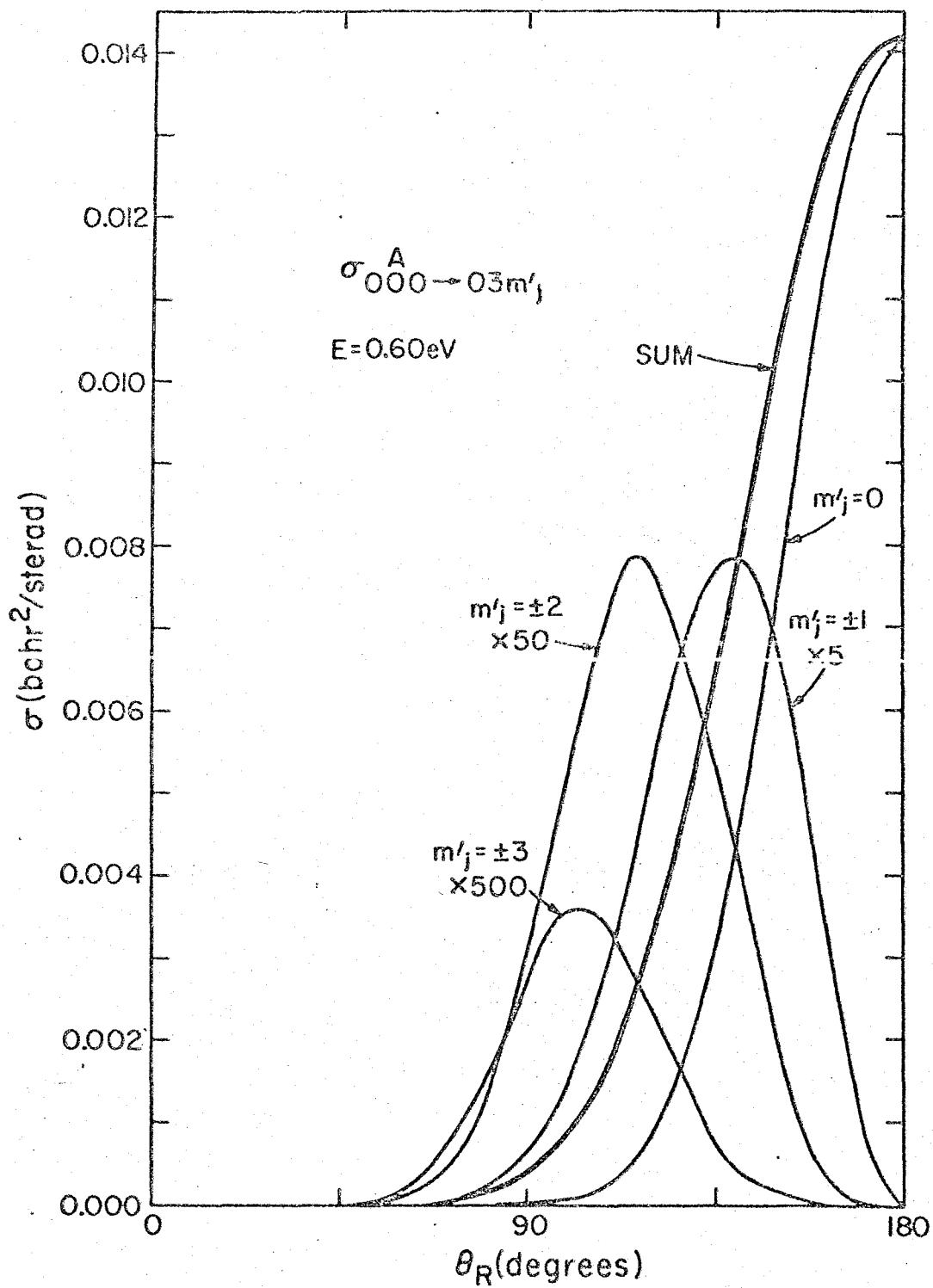
Figure 9
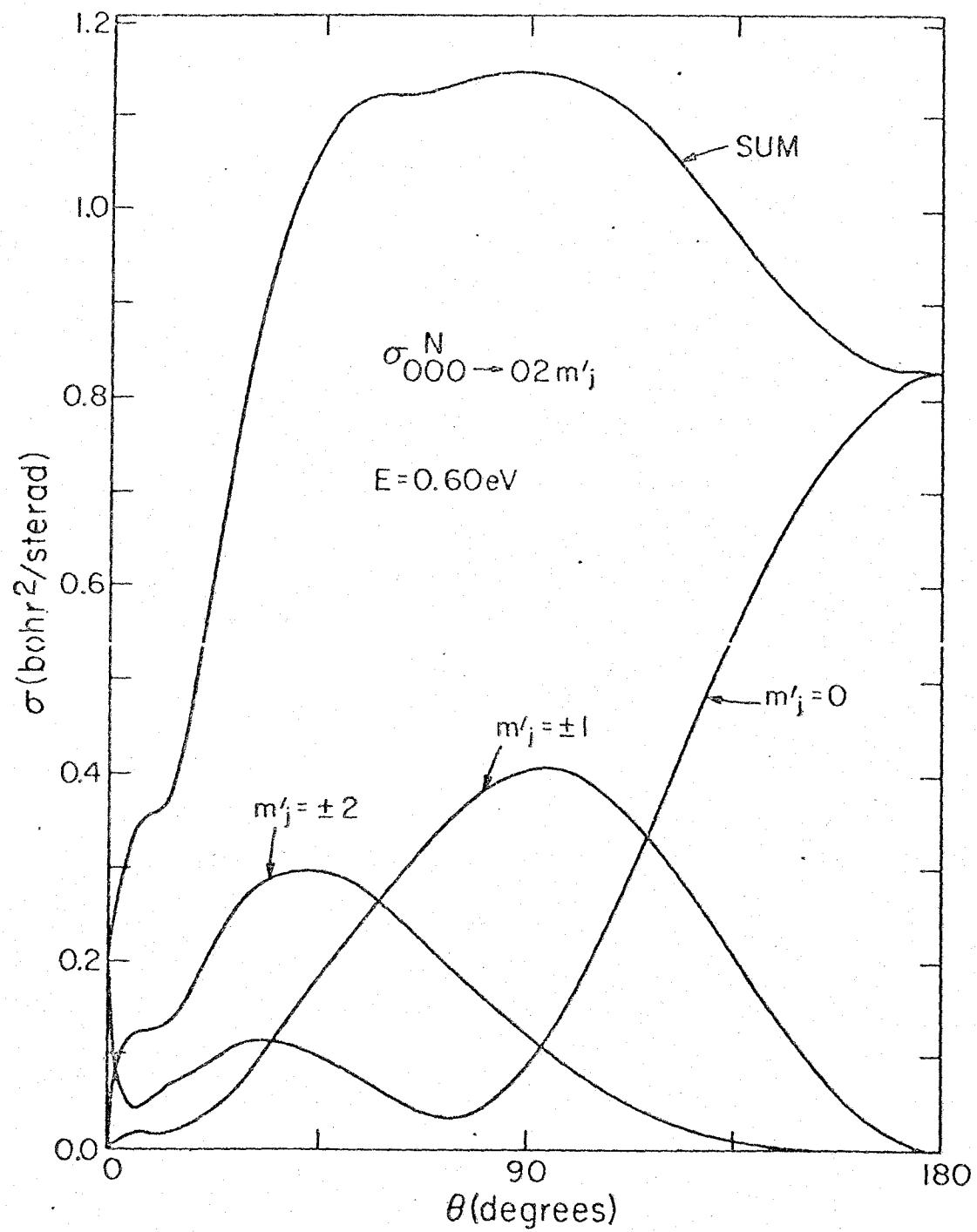
Figure 10
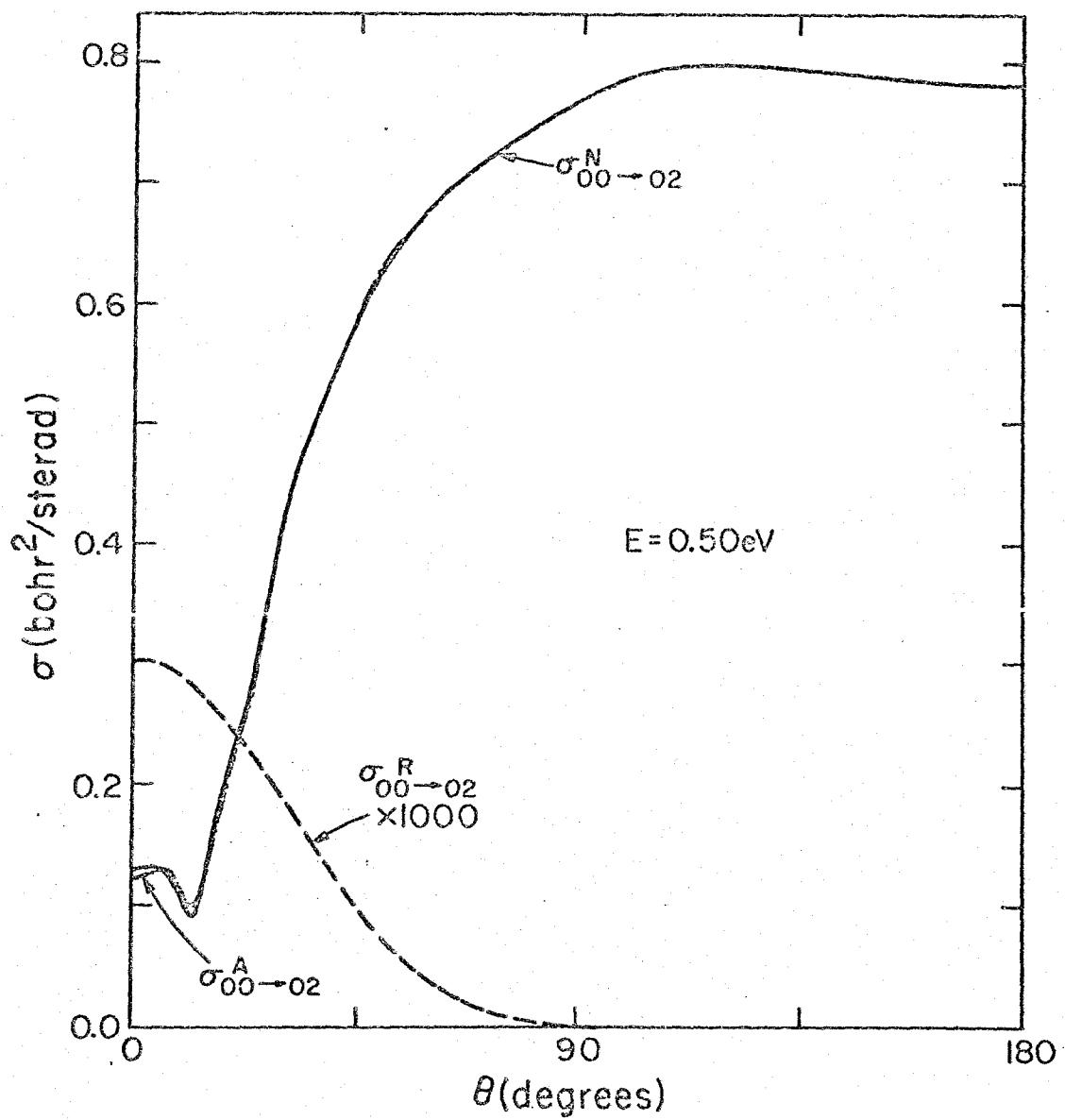
Figure 11
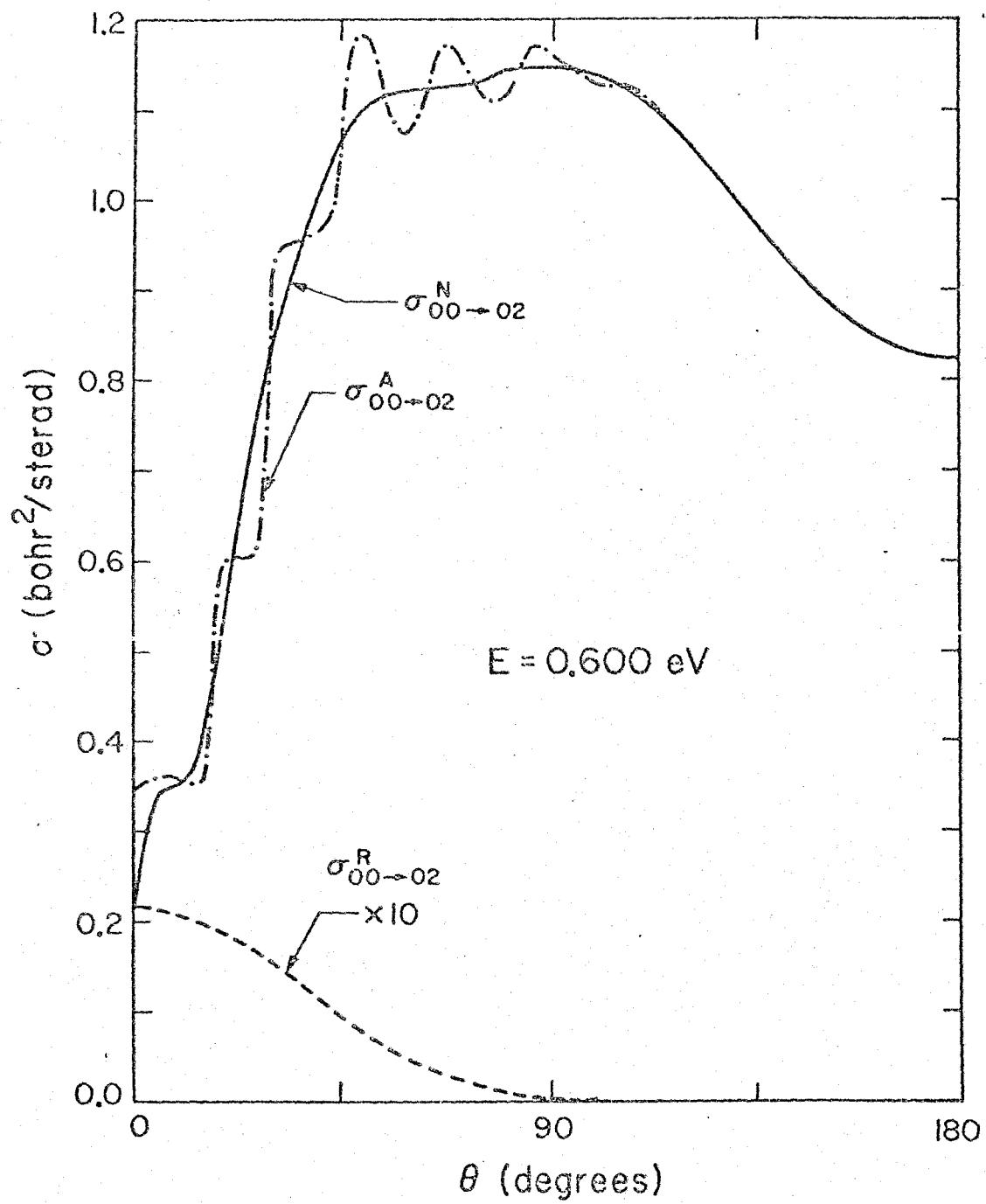
Figure 12
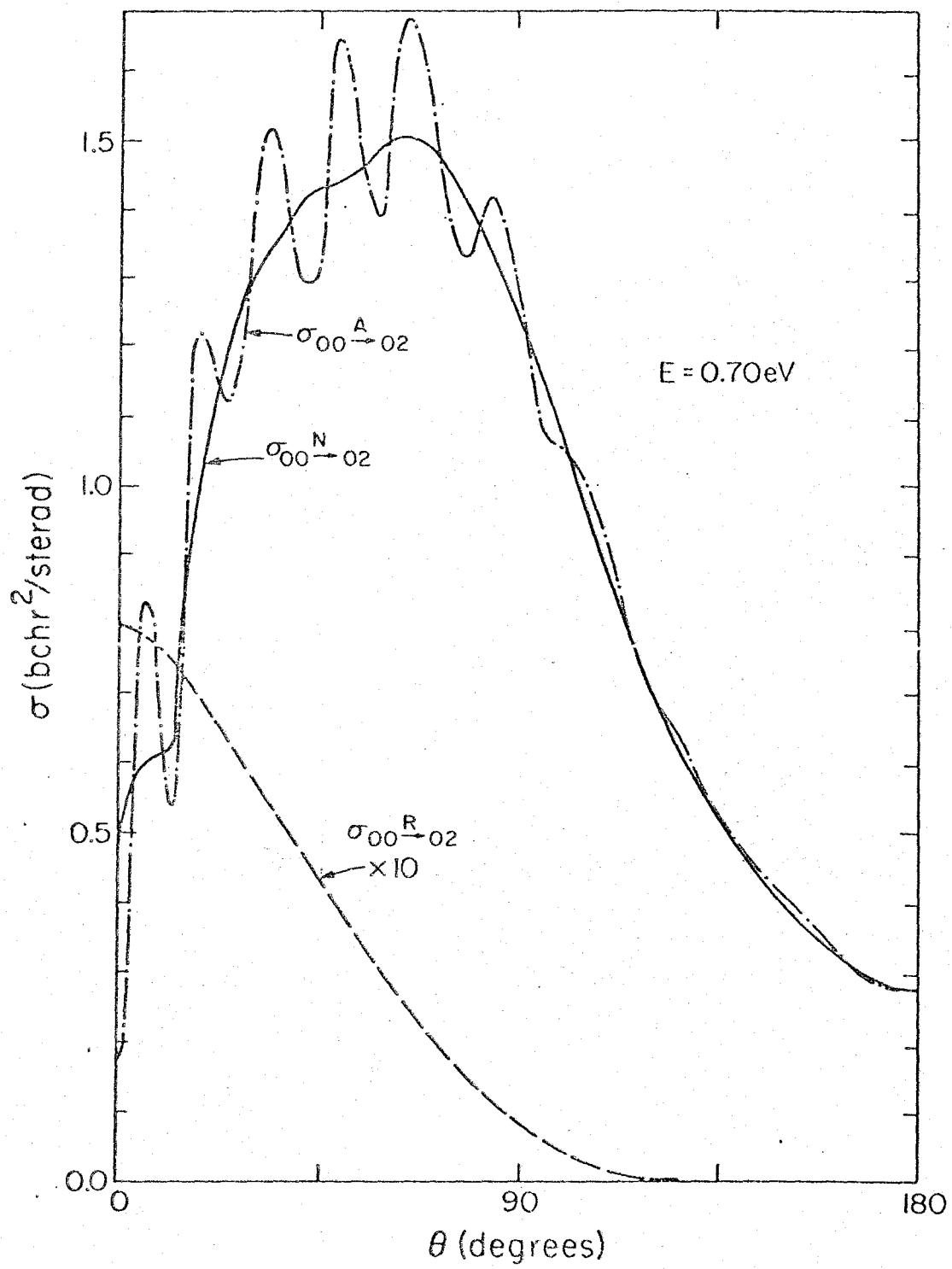
Figure 13
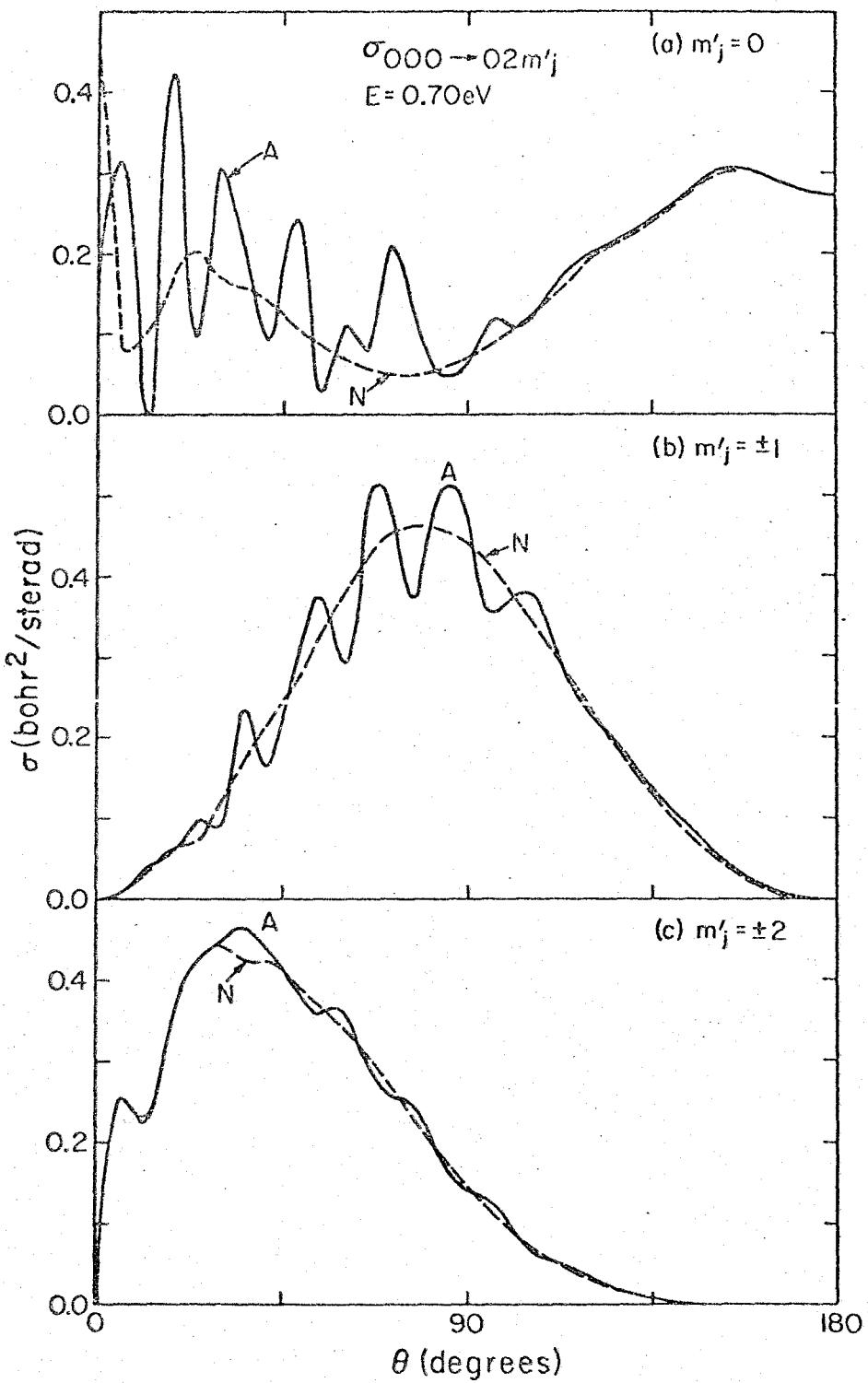
Figure 14
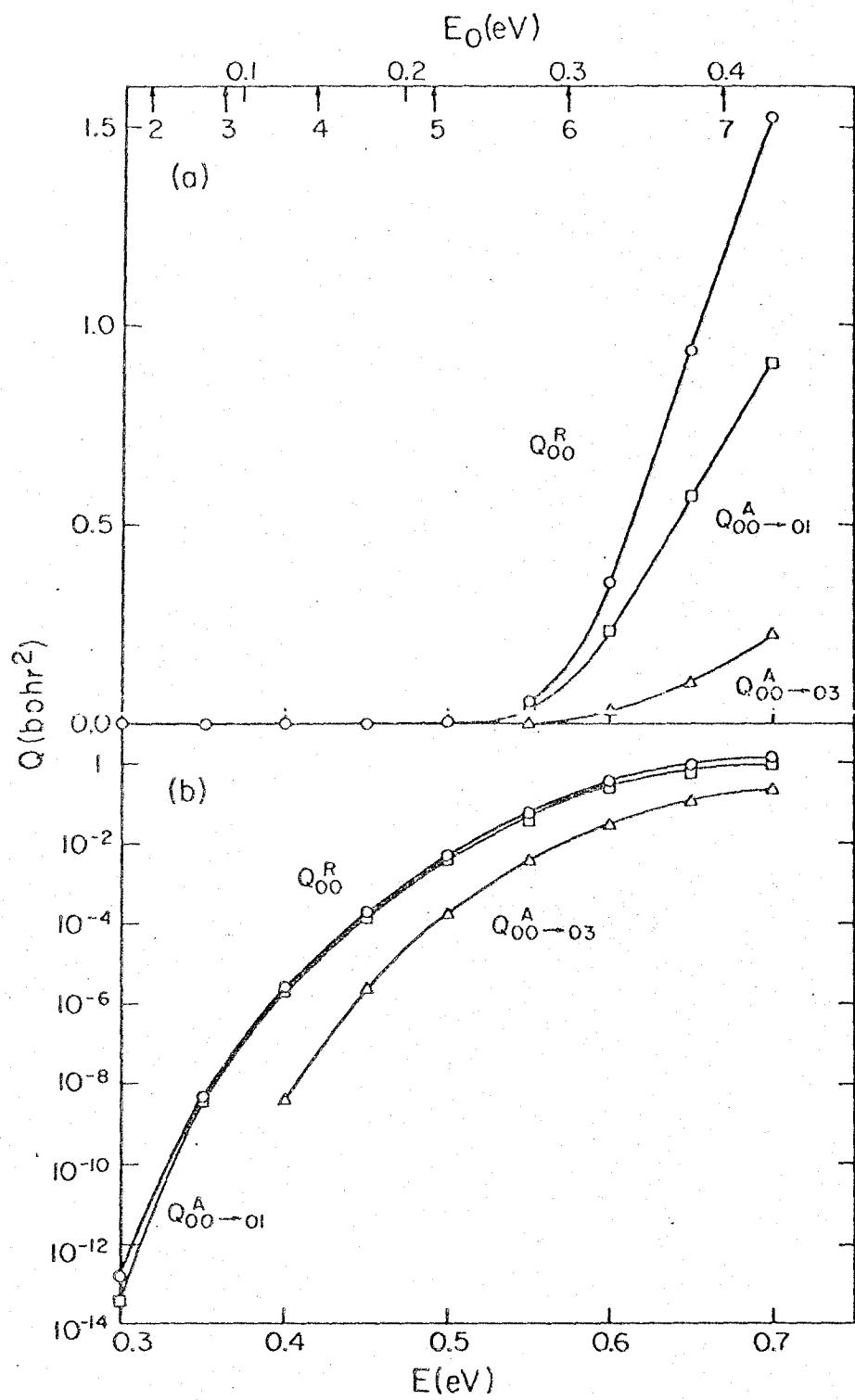
Figure 15
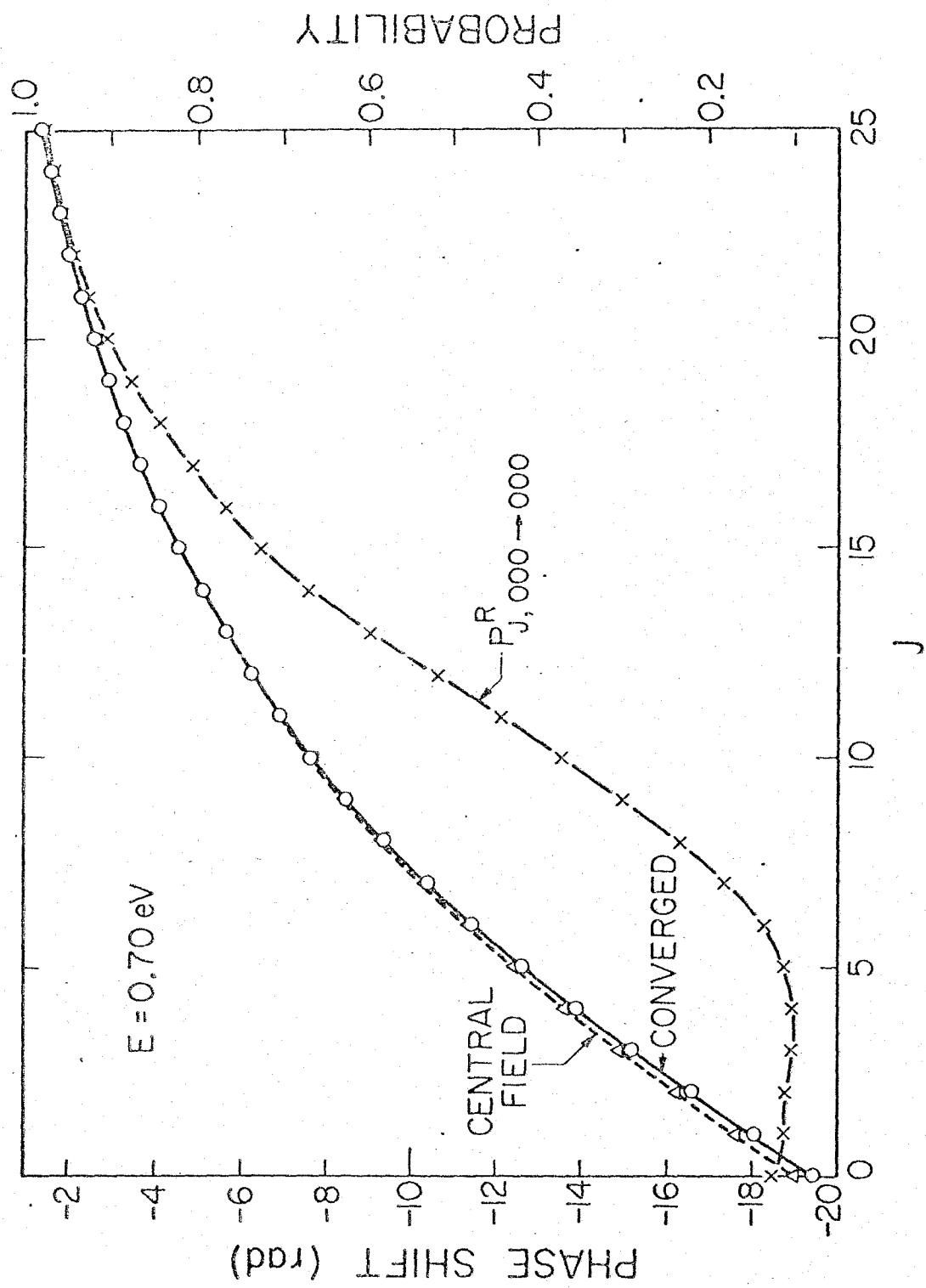
Figure 16
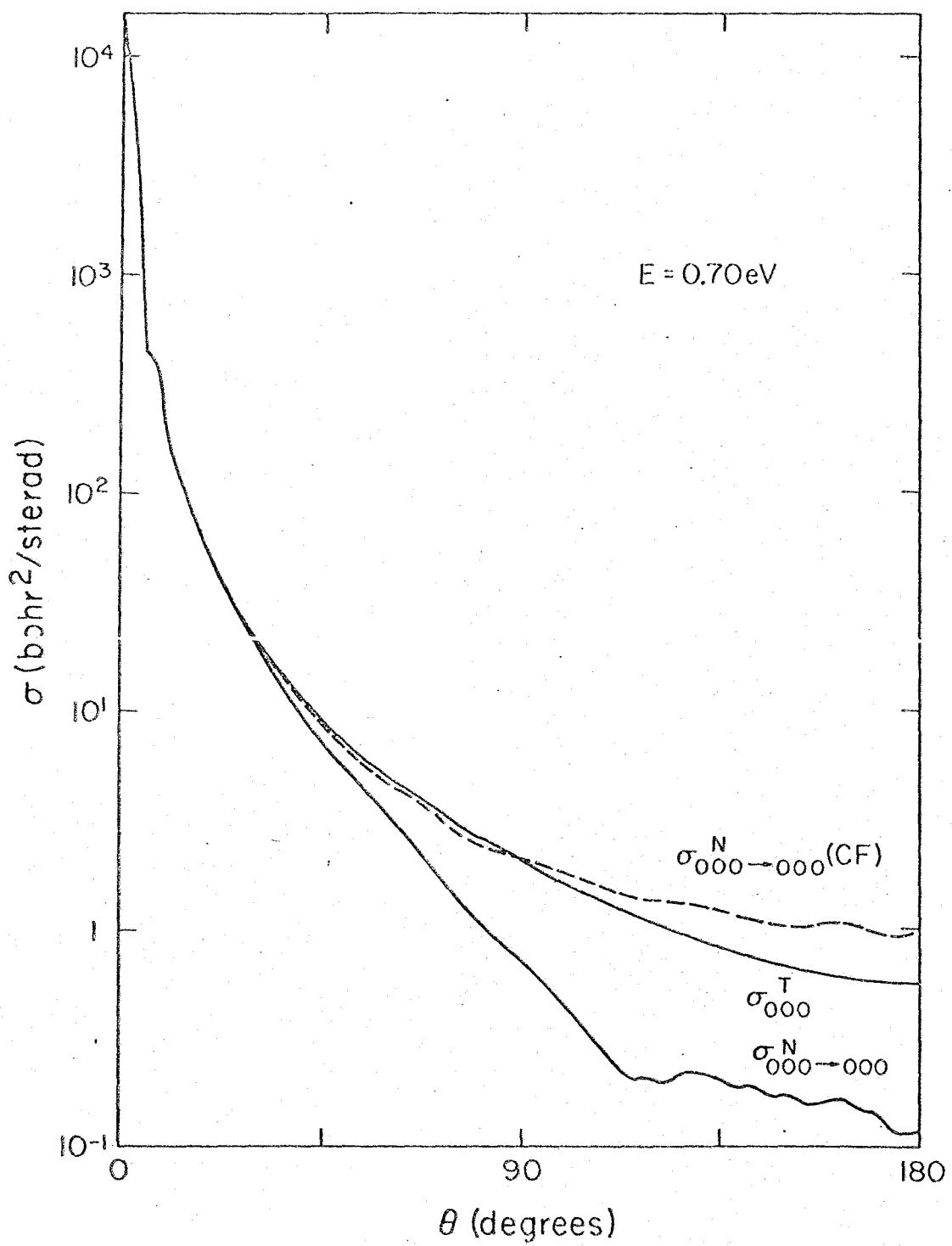
Figure 17
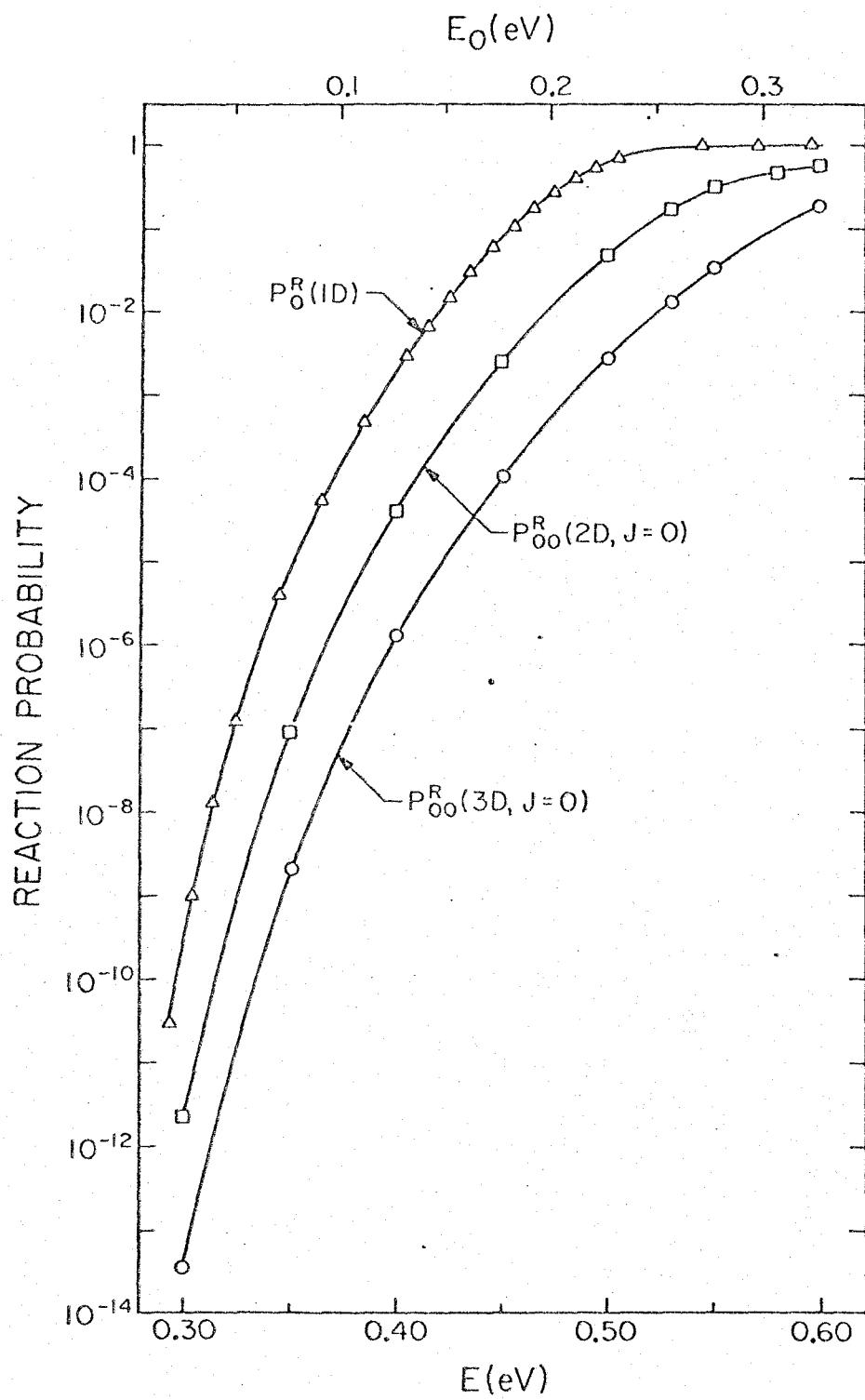
Figure 18

Figure 19

Figure 20
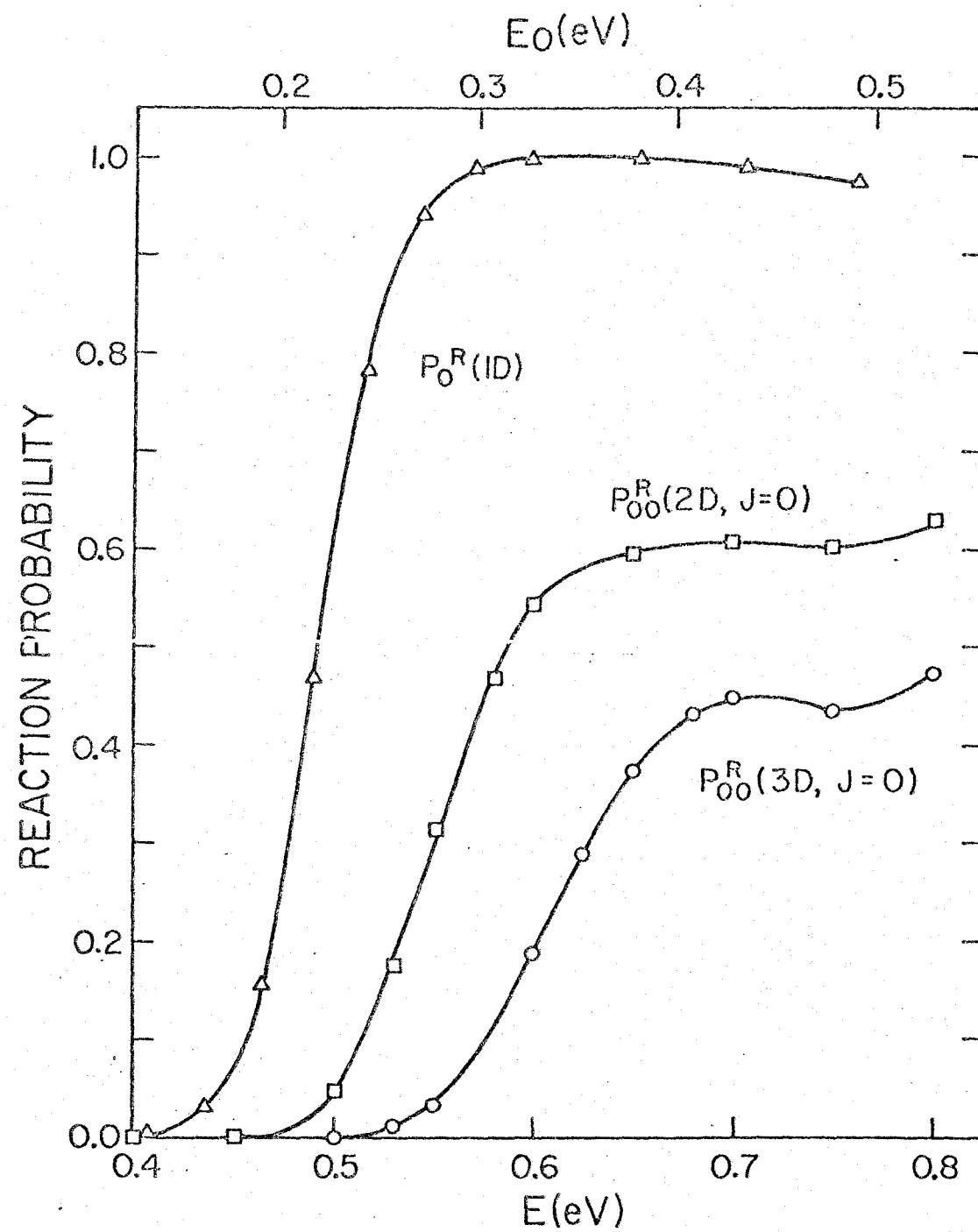
Figure 21
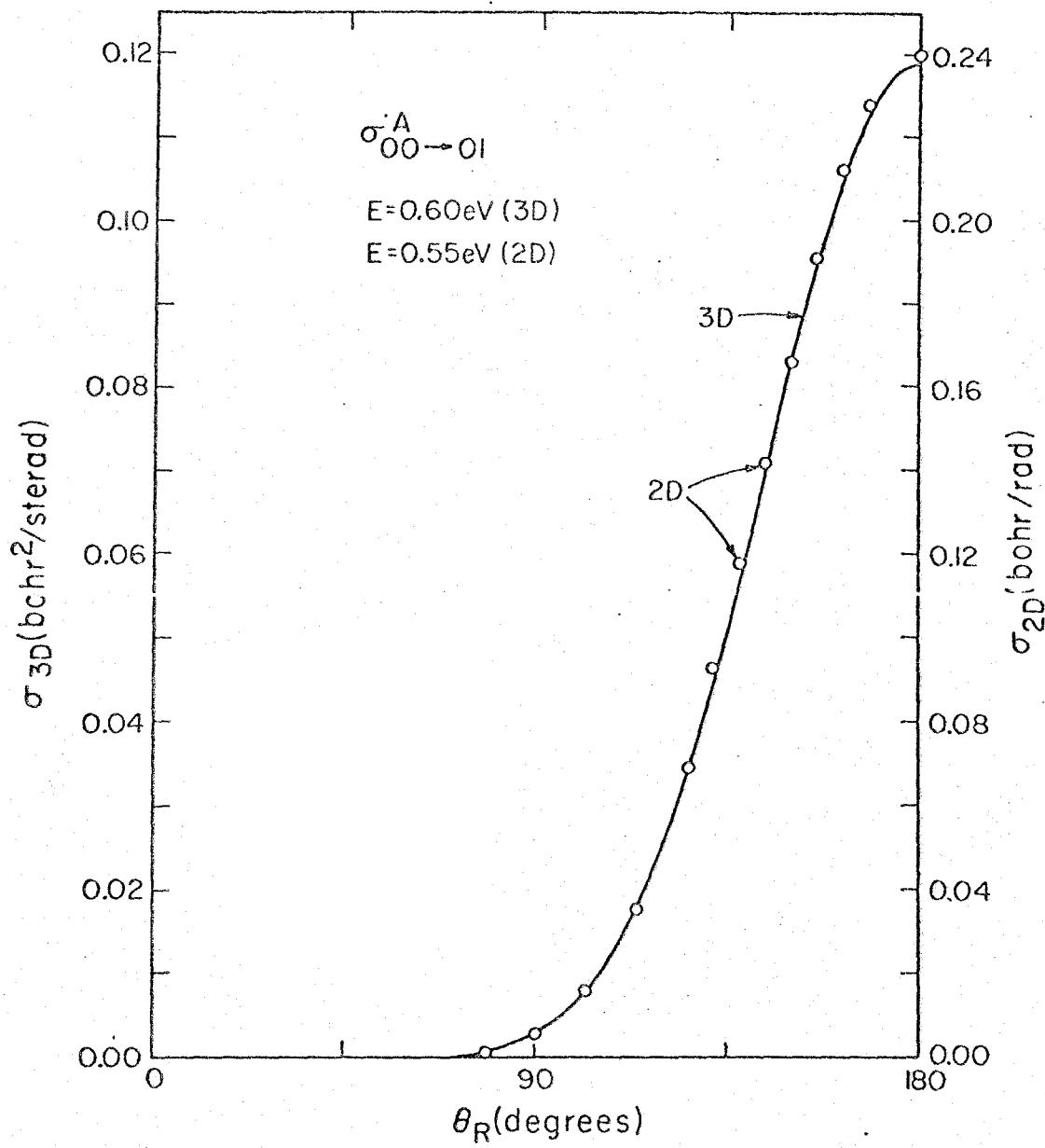
Figure 22
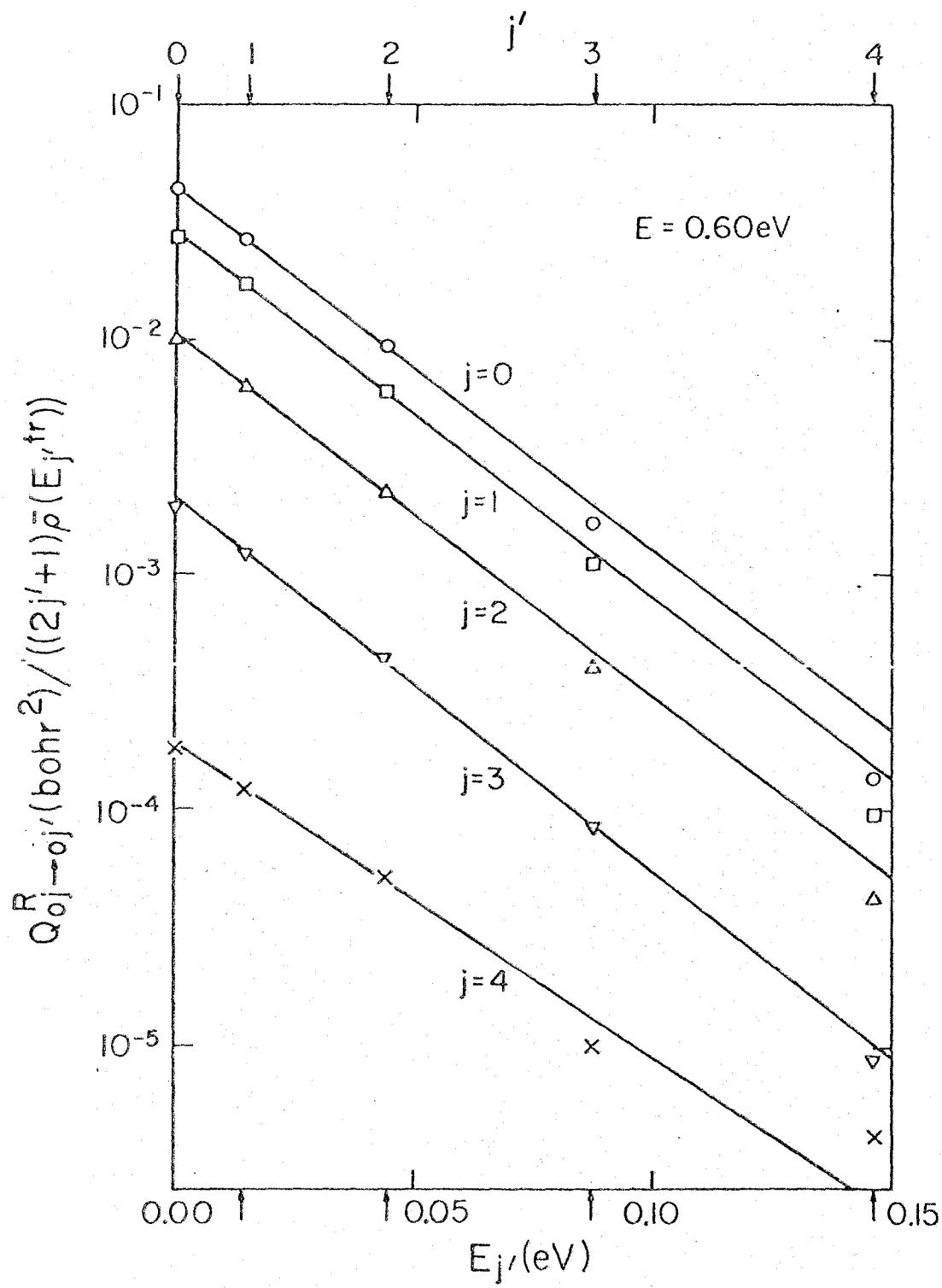
Figure 23
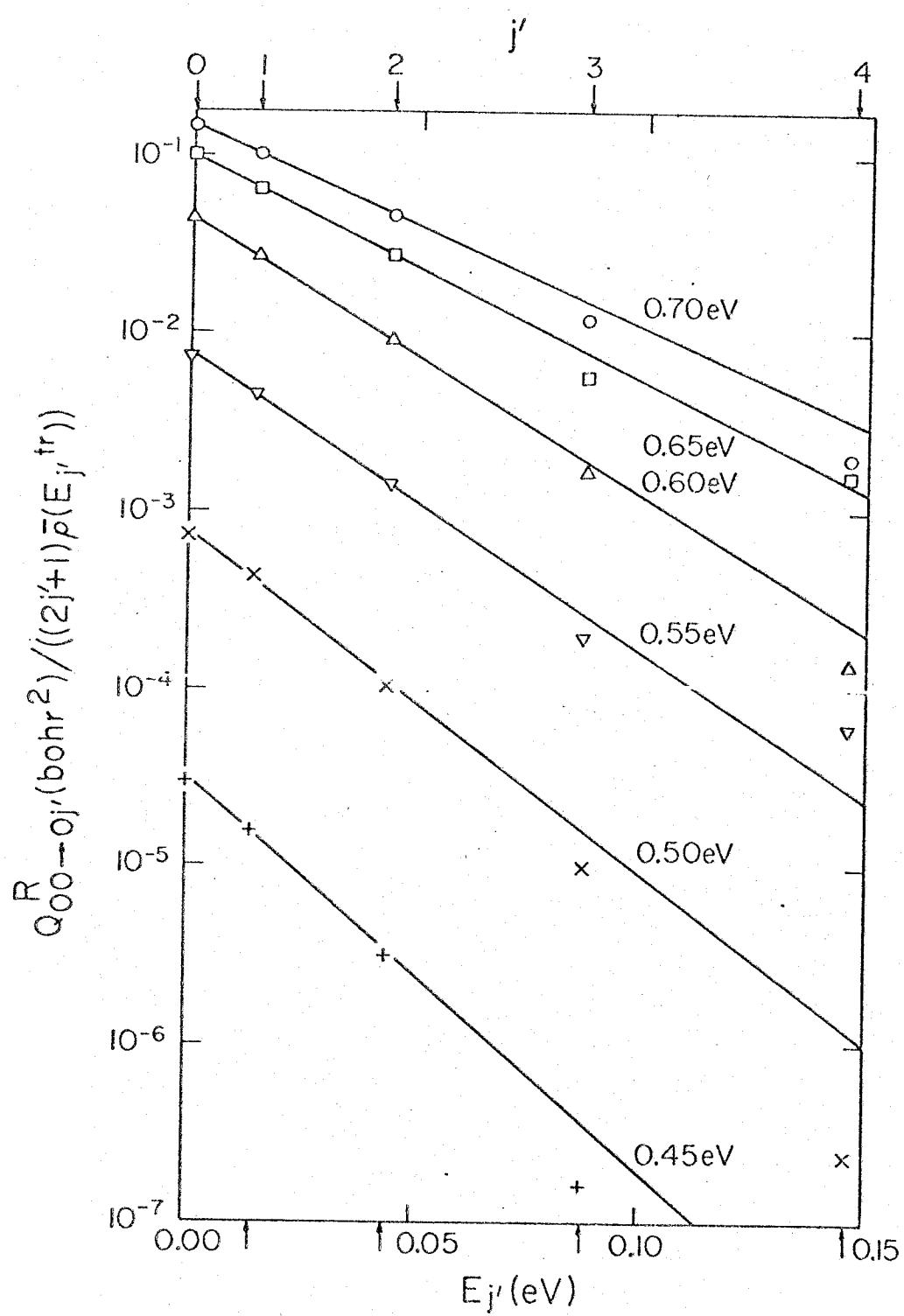
Figure 24
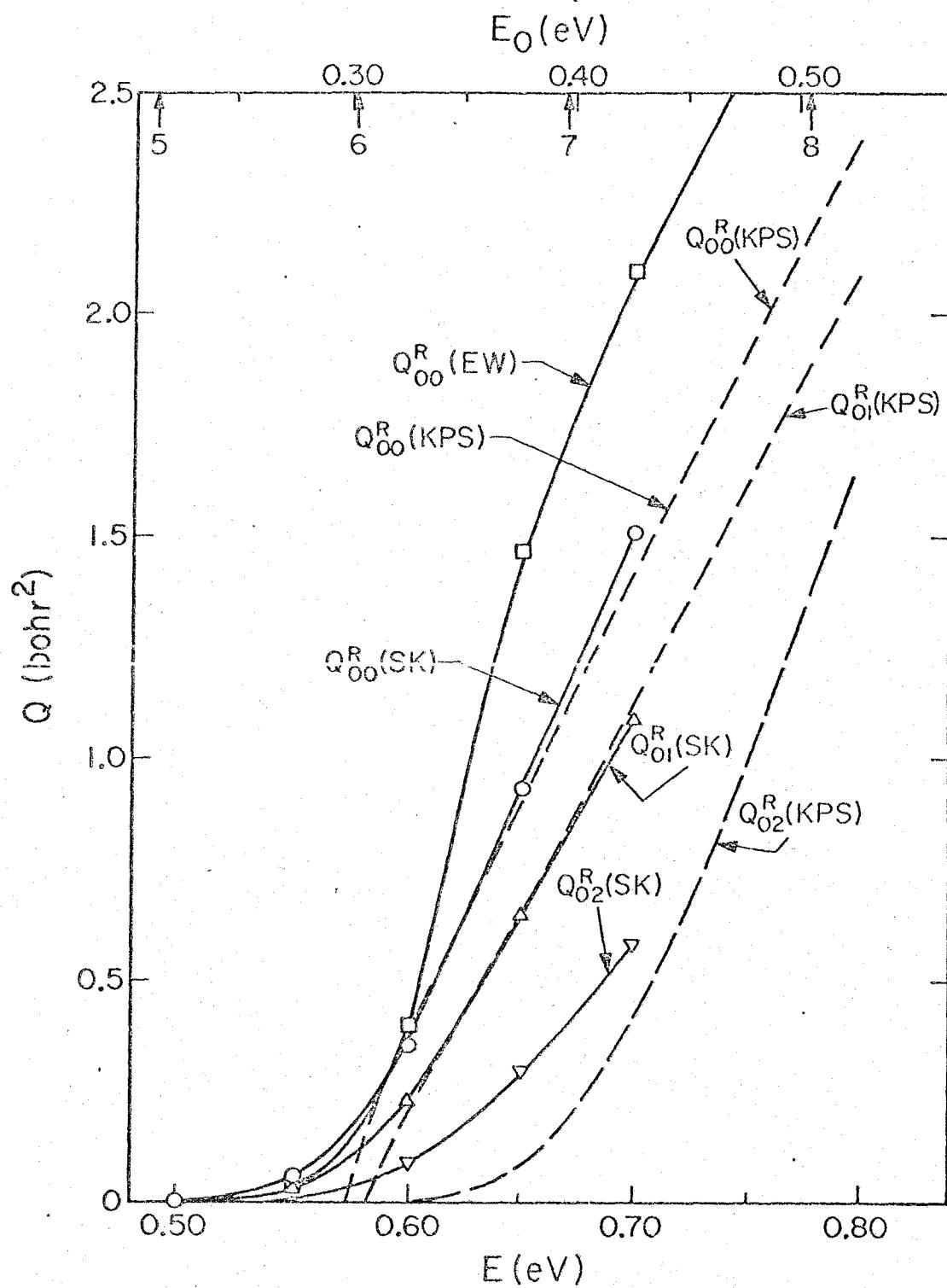
Figure 25
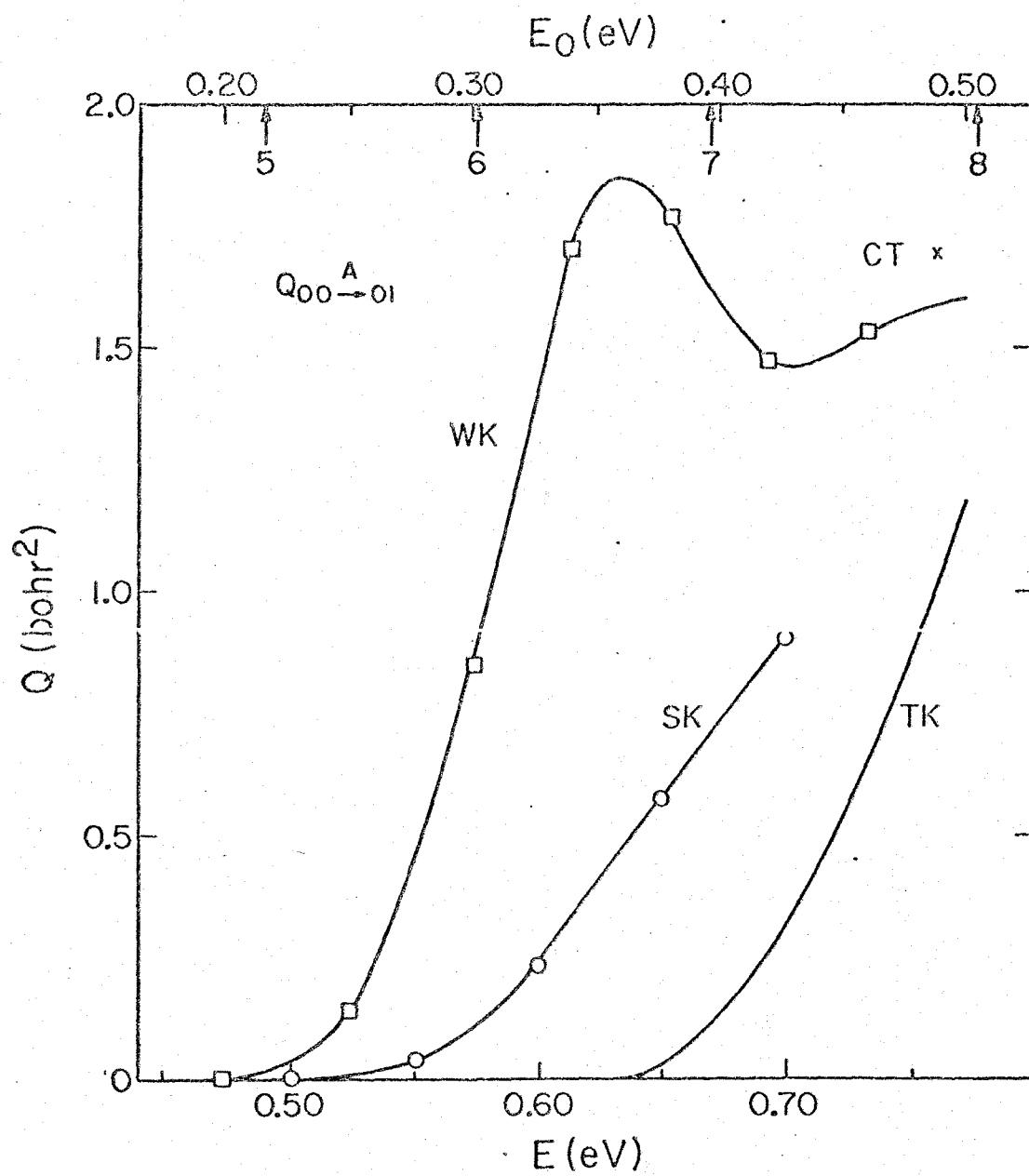
Figure 26
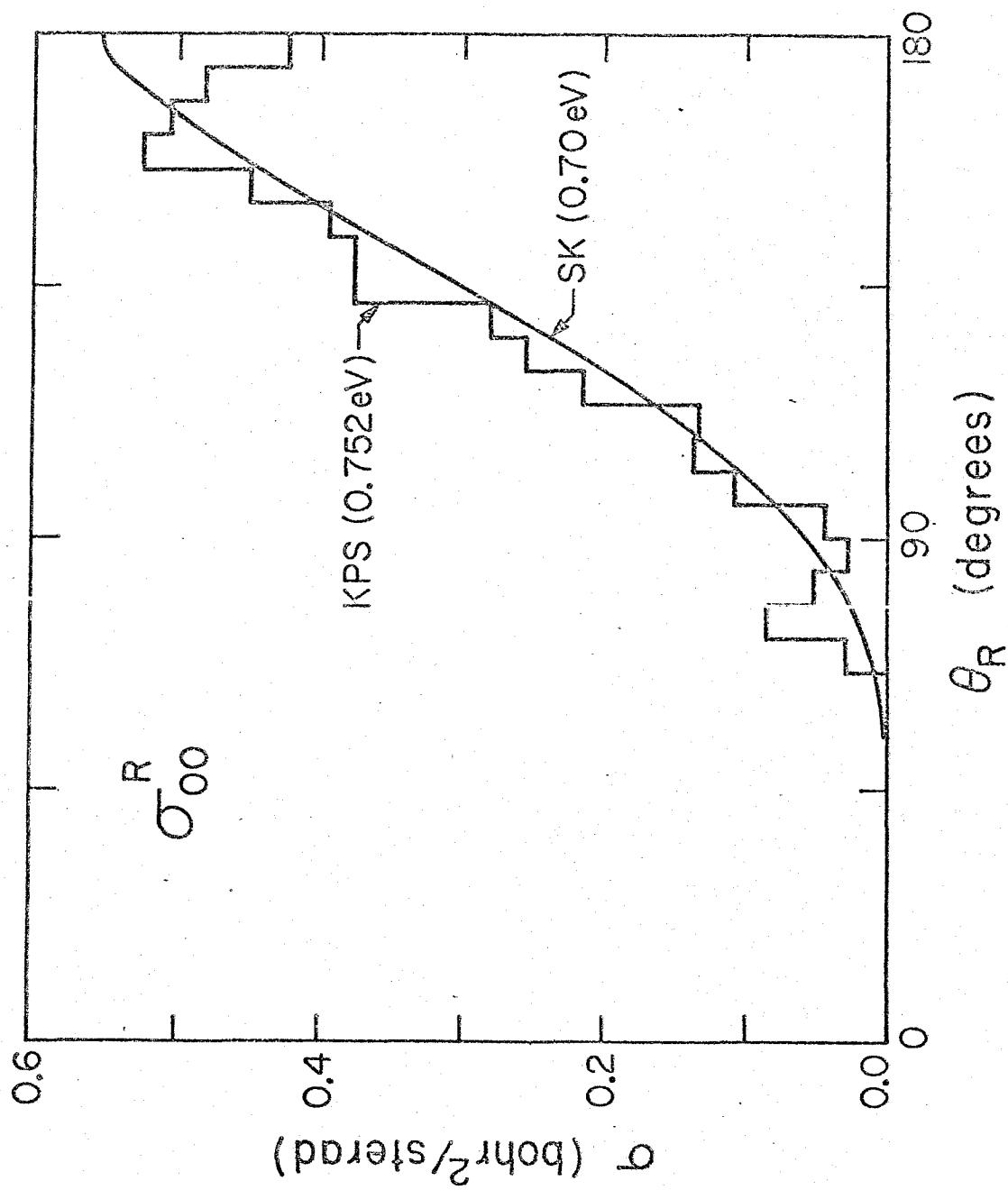
Figure 27
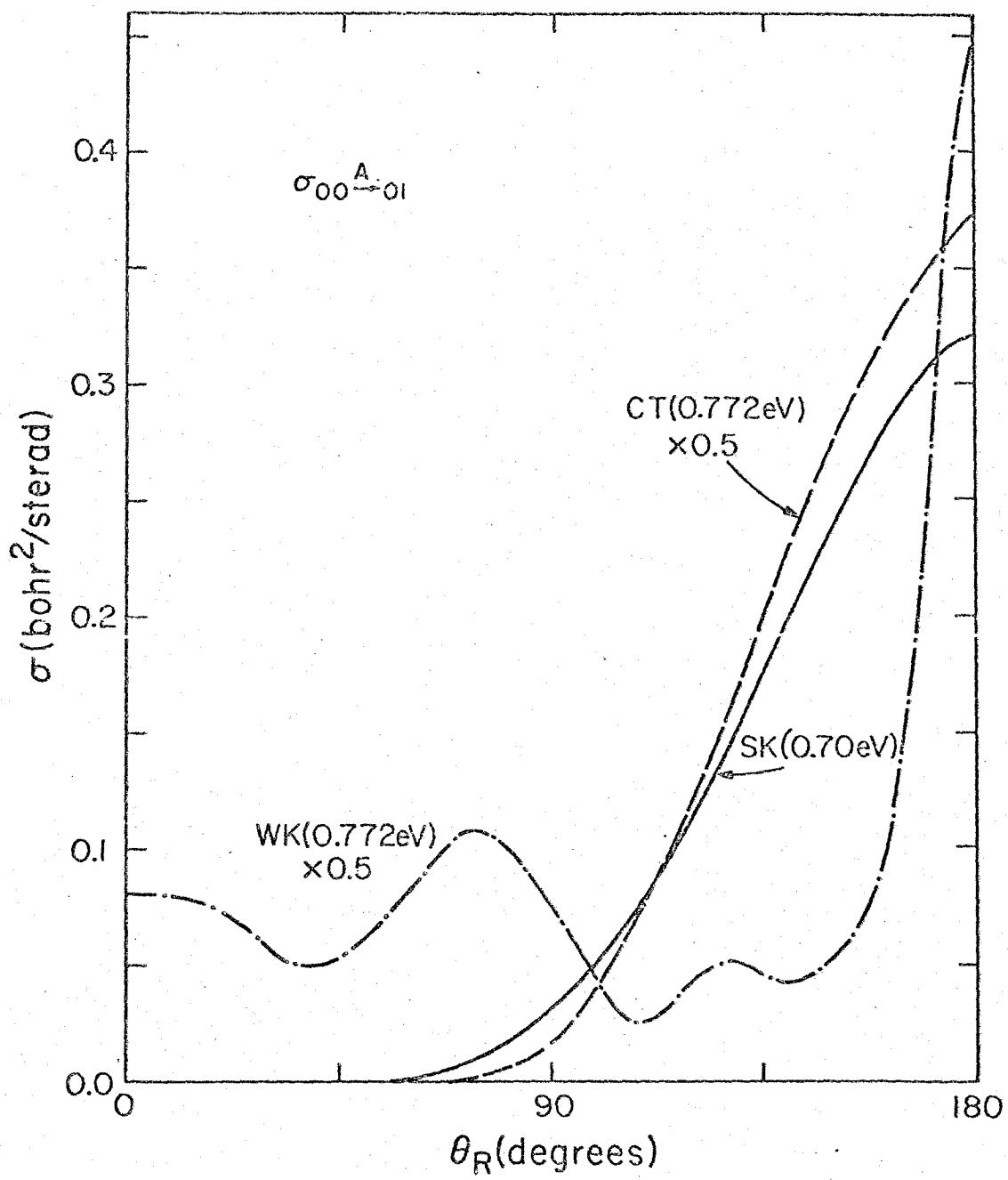
Figure 28
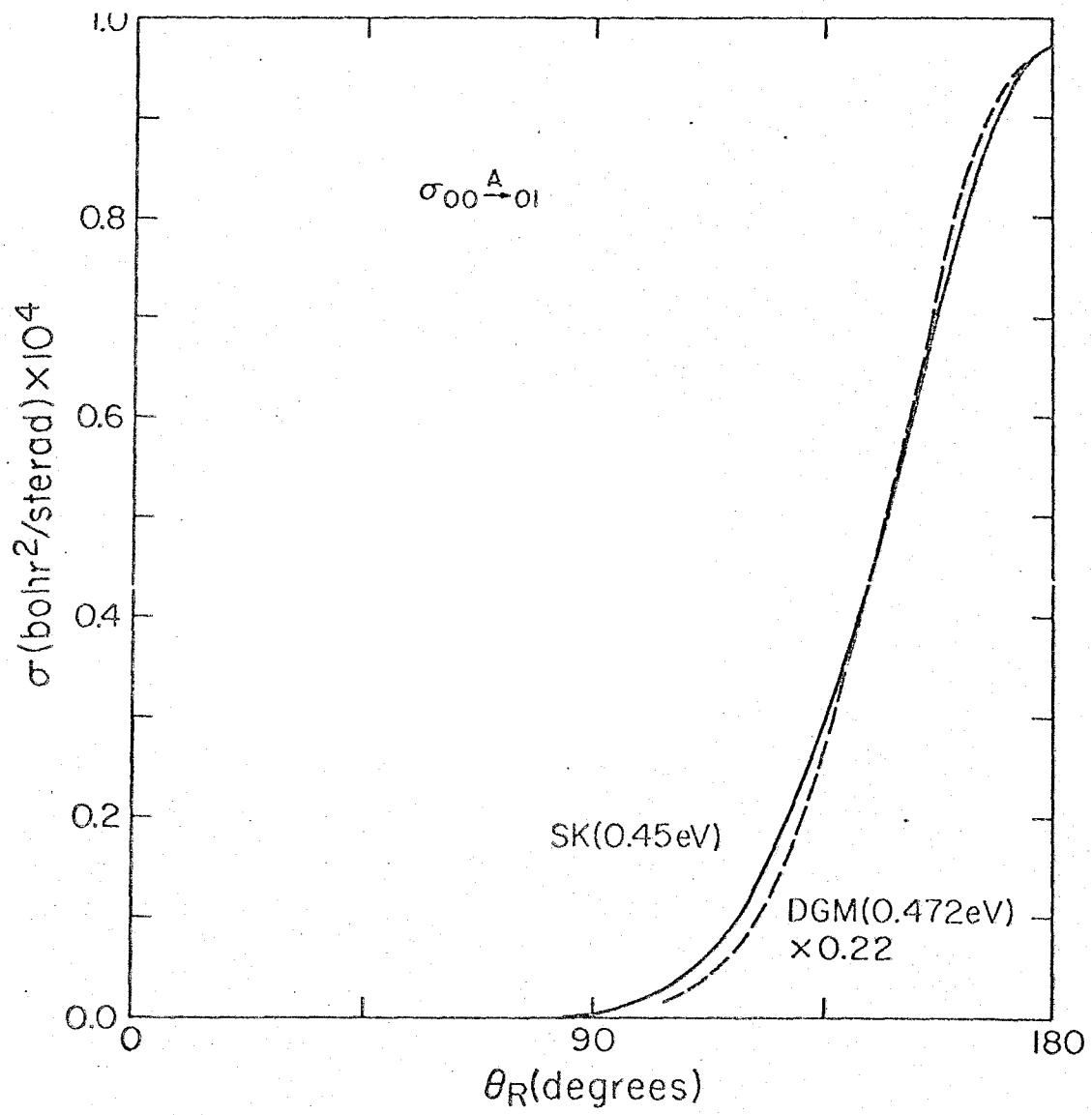
Figure 29
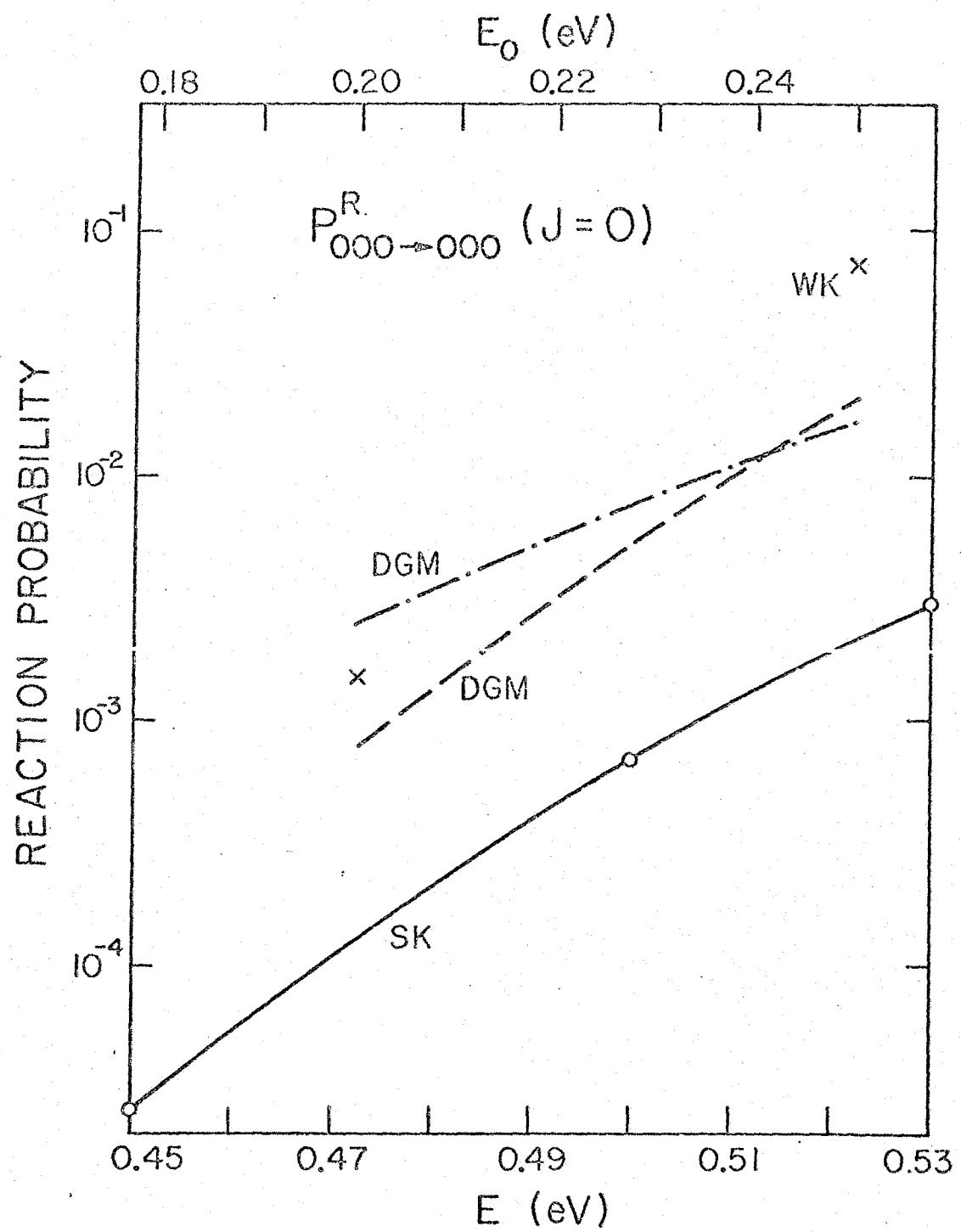
Figure 30
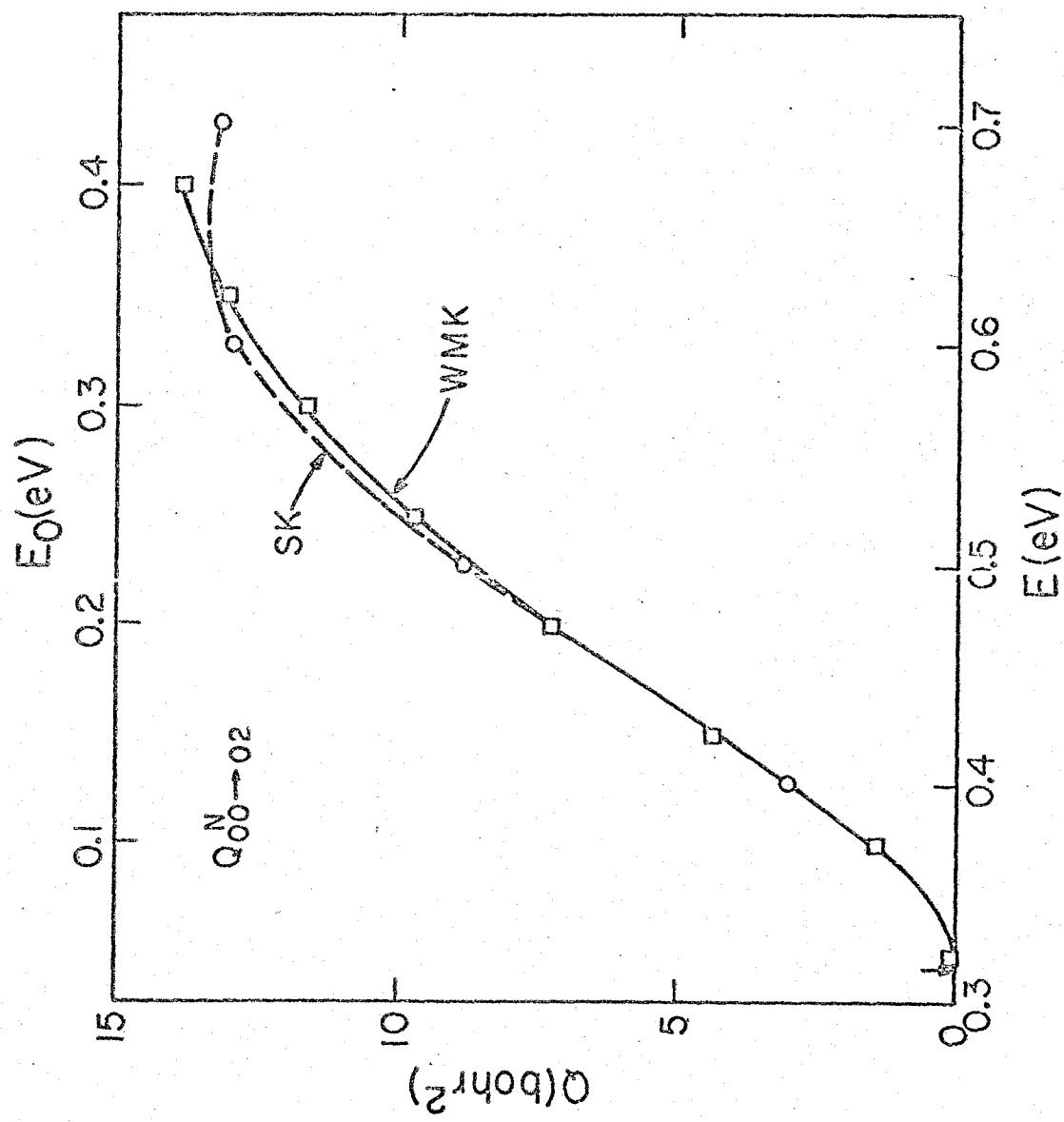
Figure 31
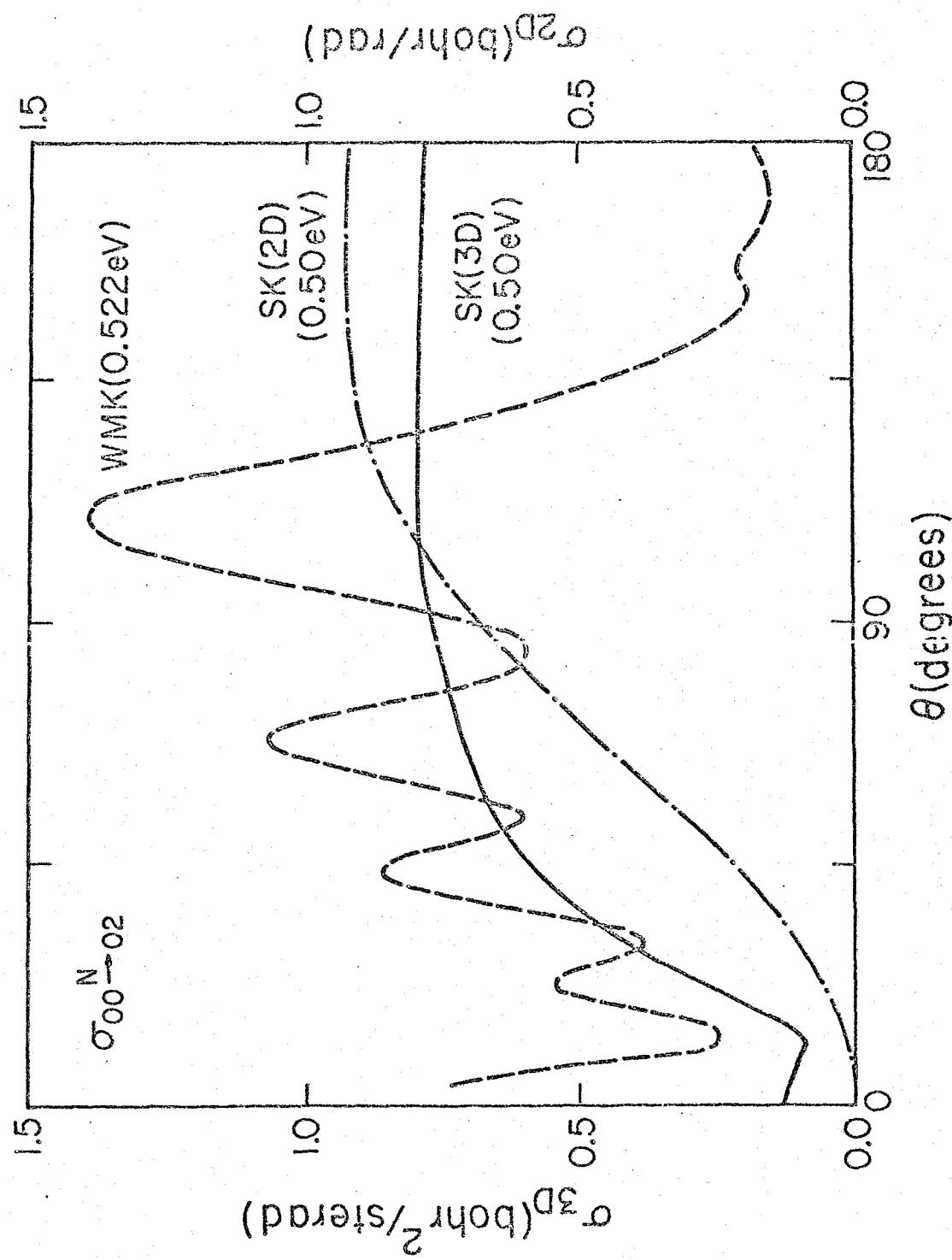
Figure 32
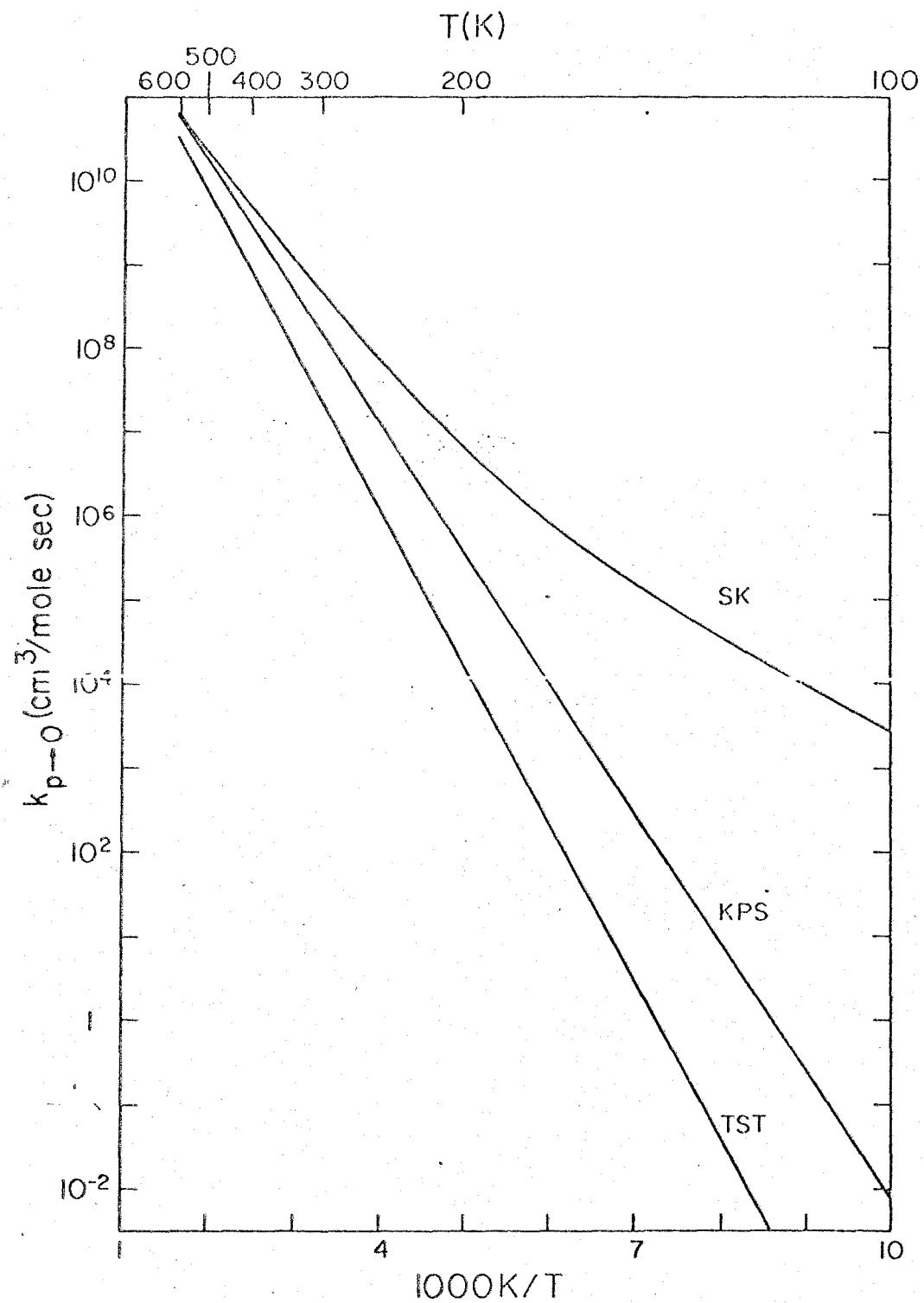
Figure 33
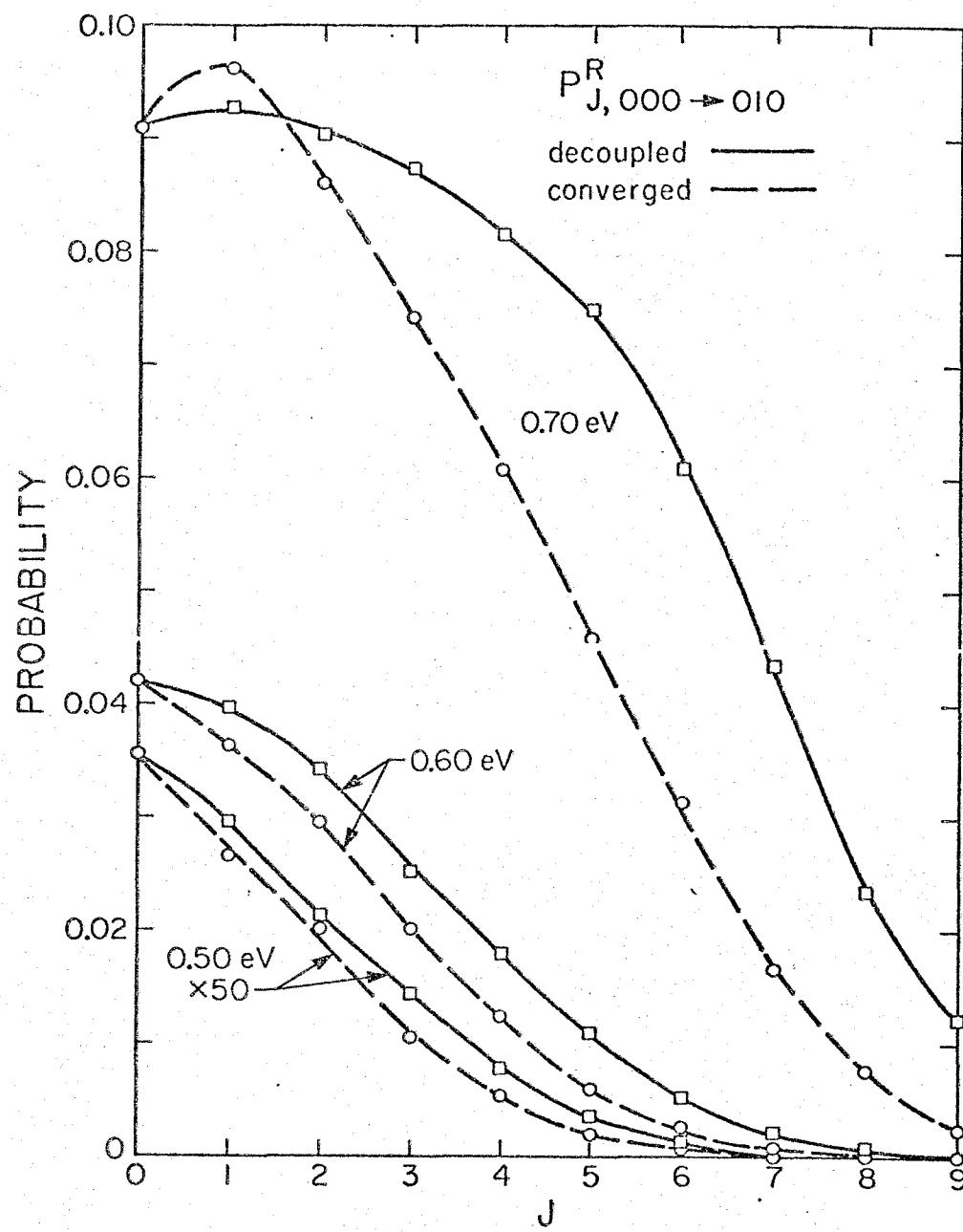
Figure 34
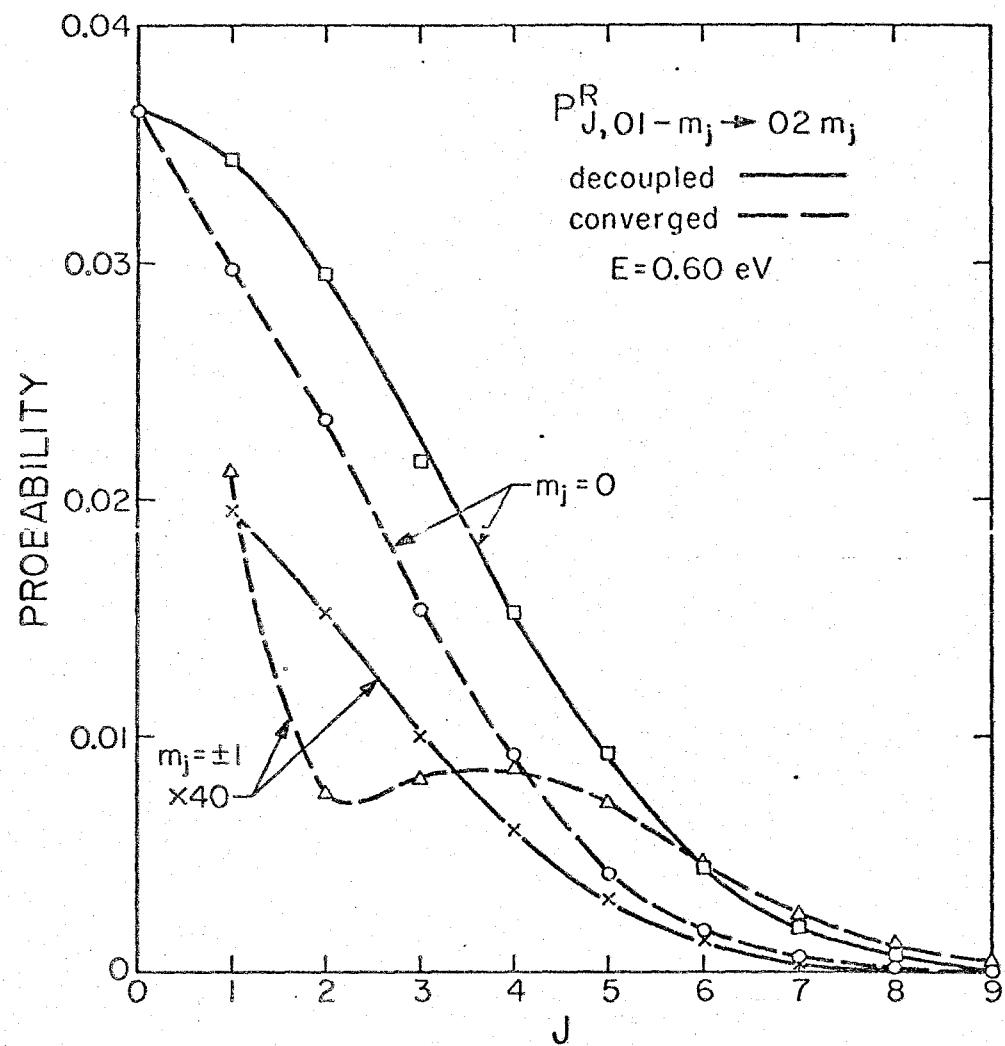
Figure 35
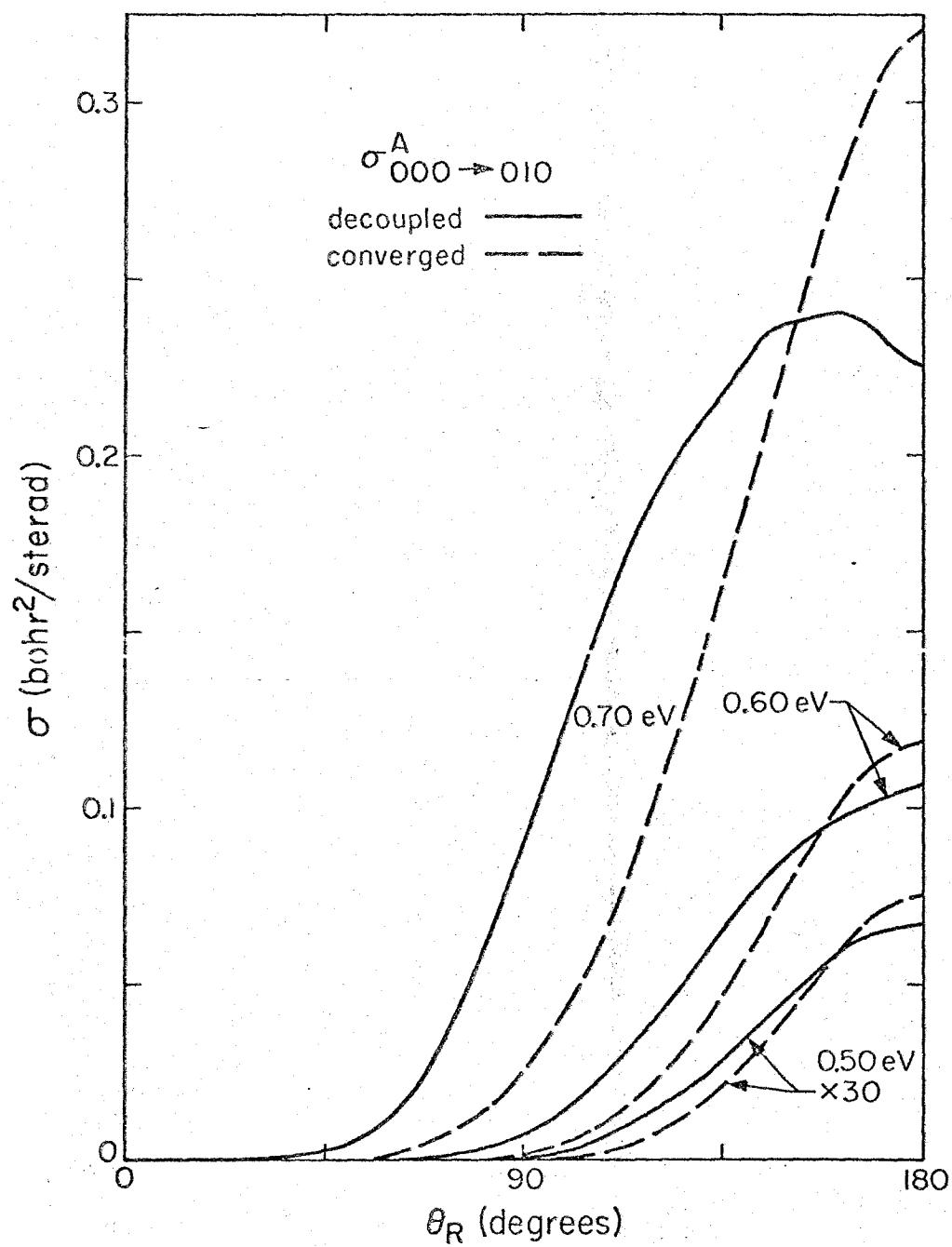
Figure 36
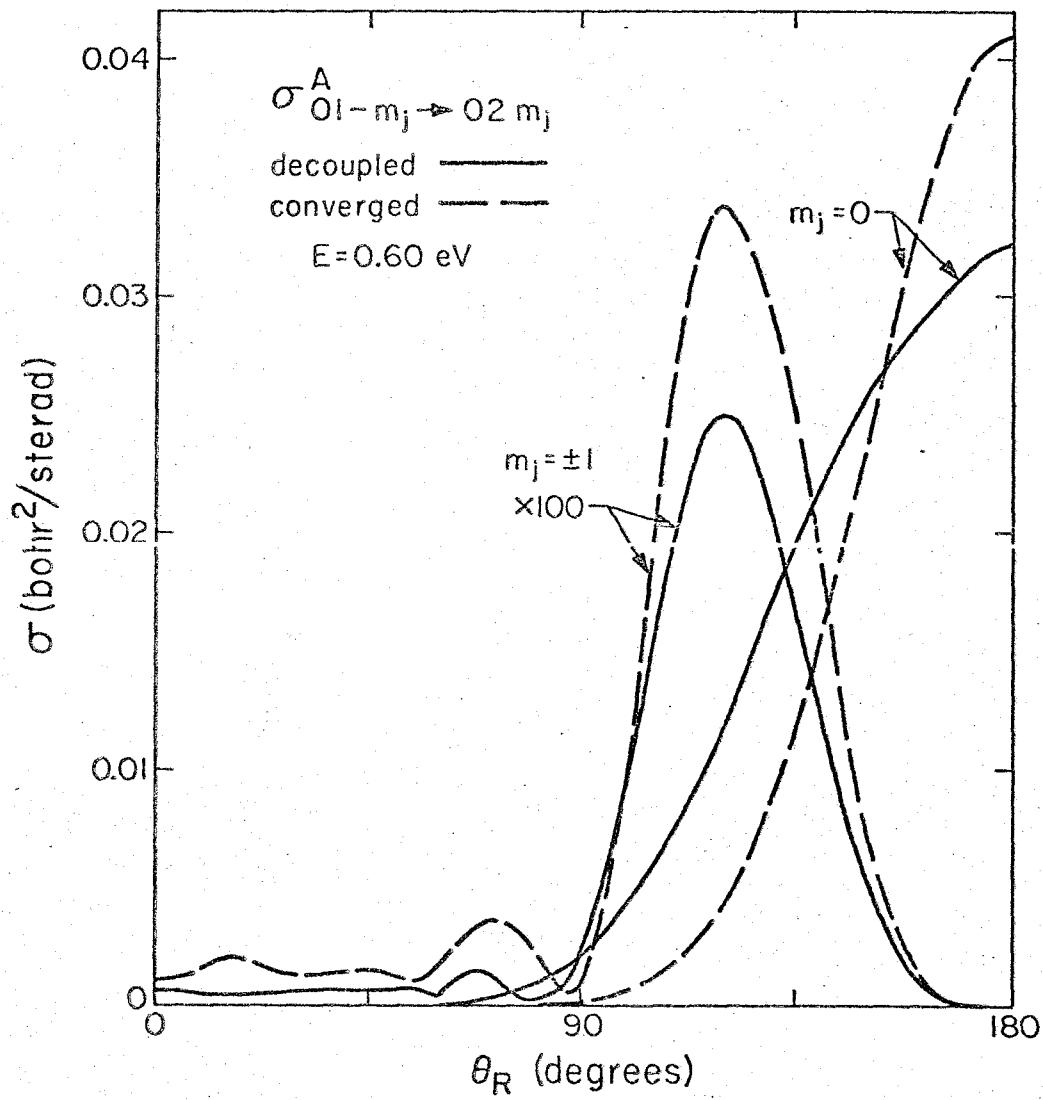
Figure 37
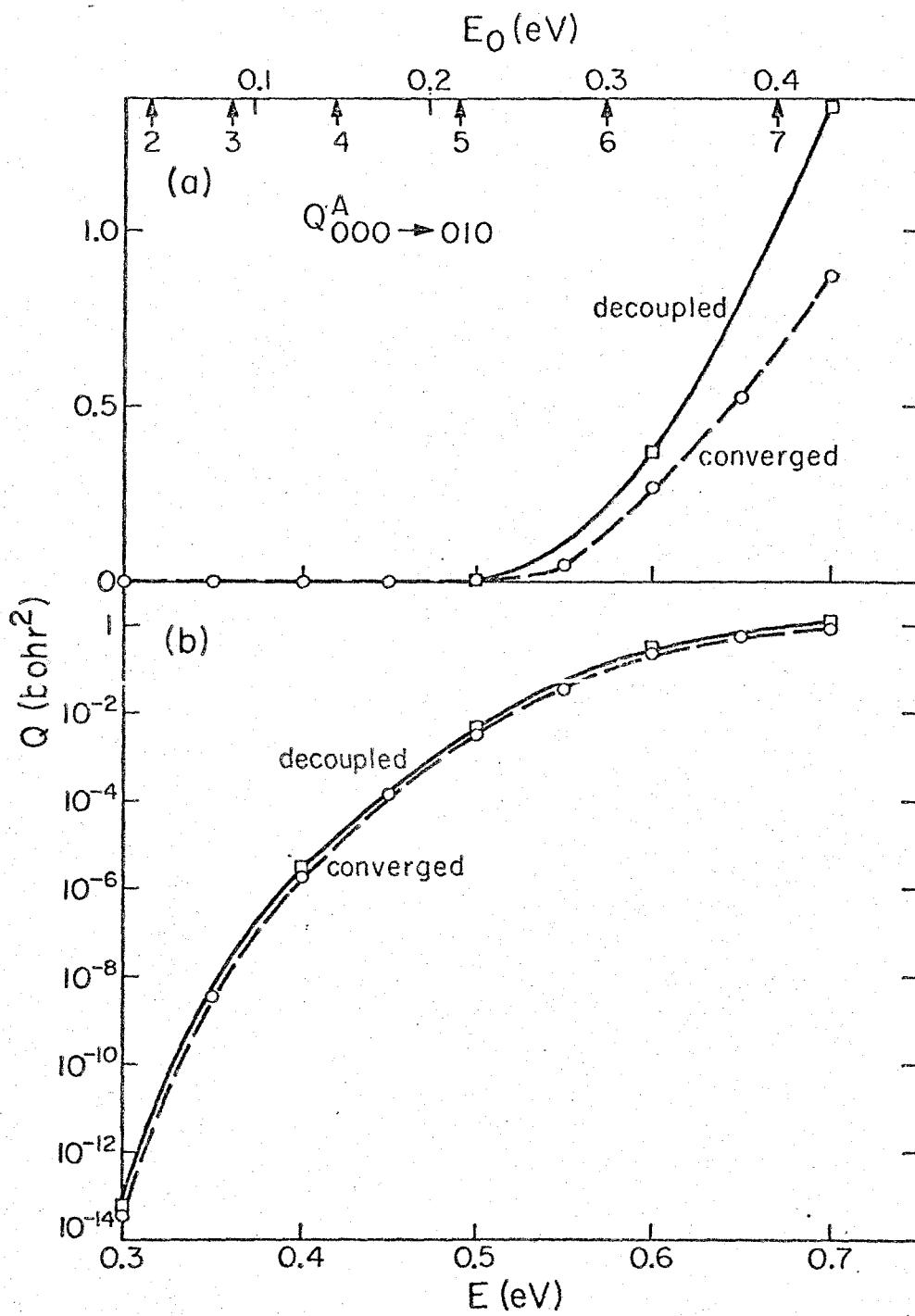
Figure 38
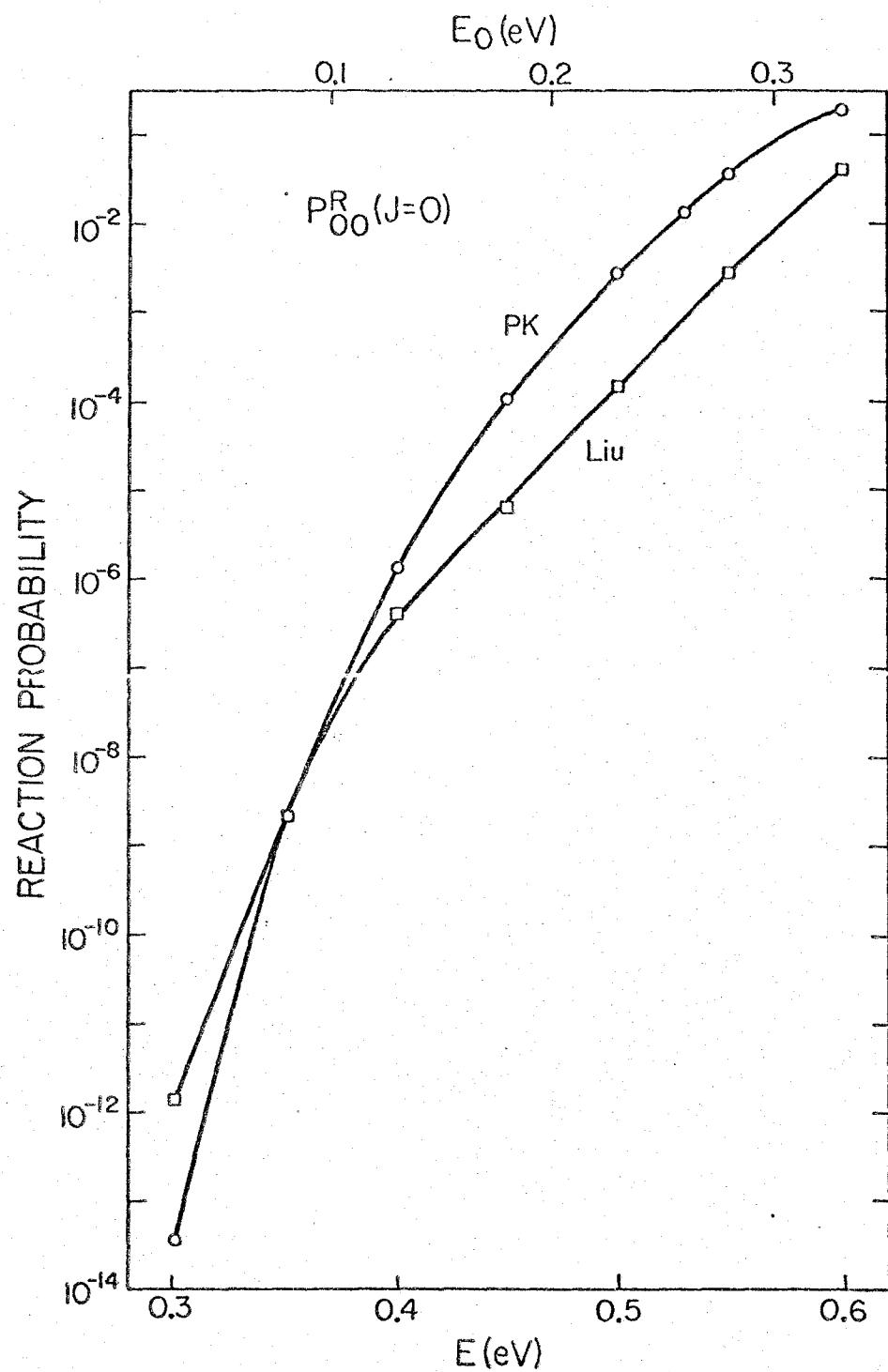
Figure 39
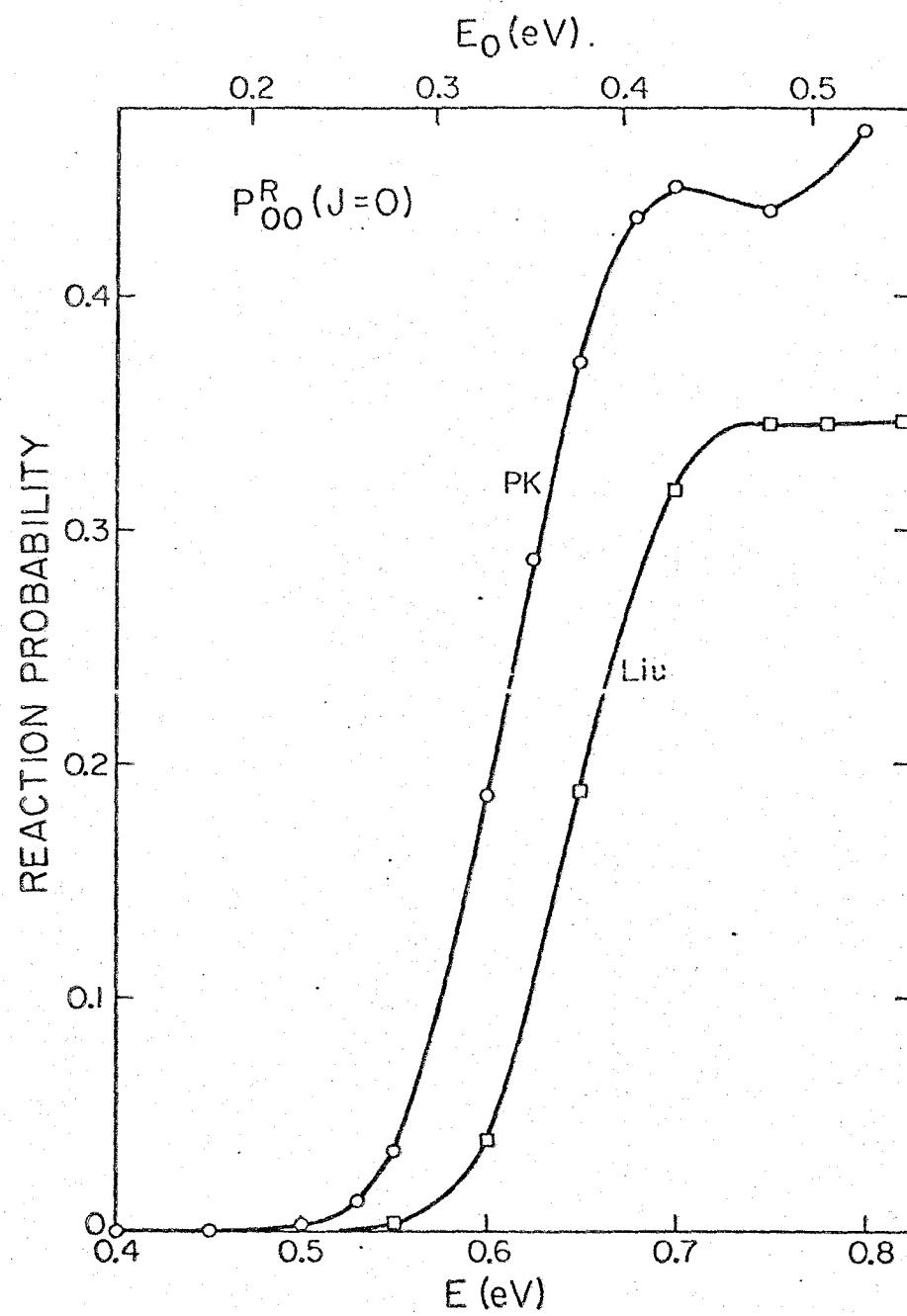
Figure 40
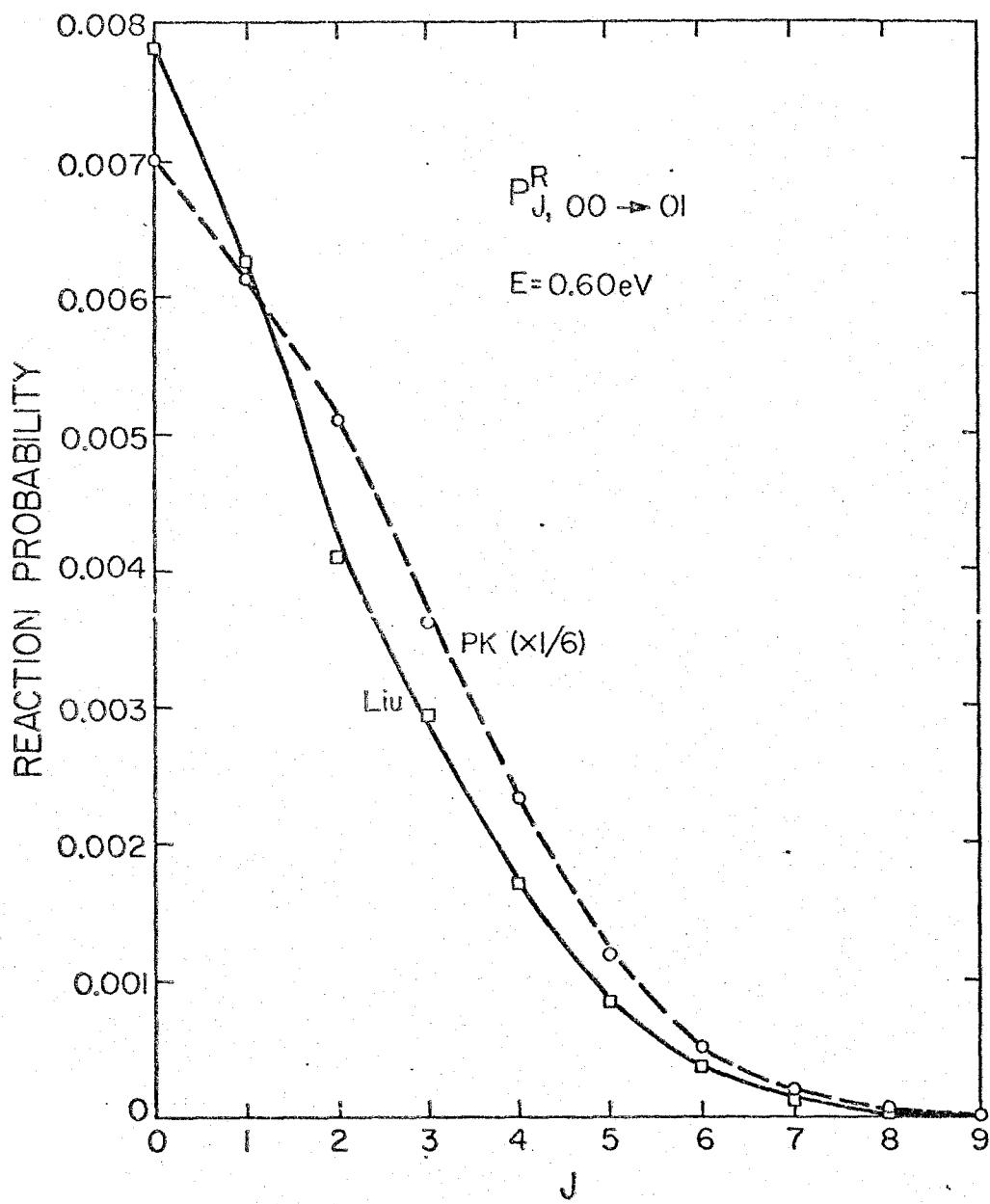
Figure 41
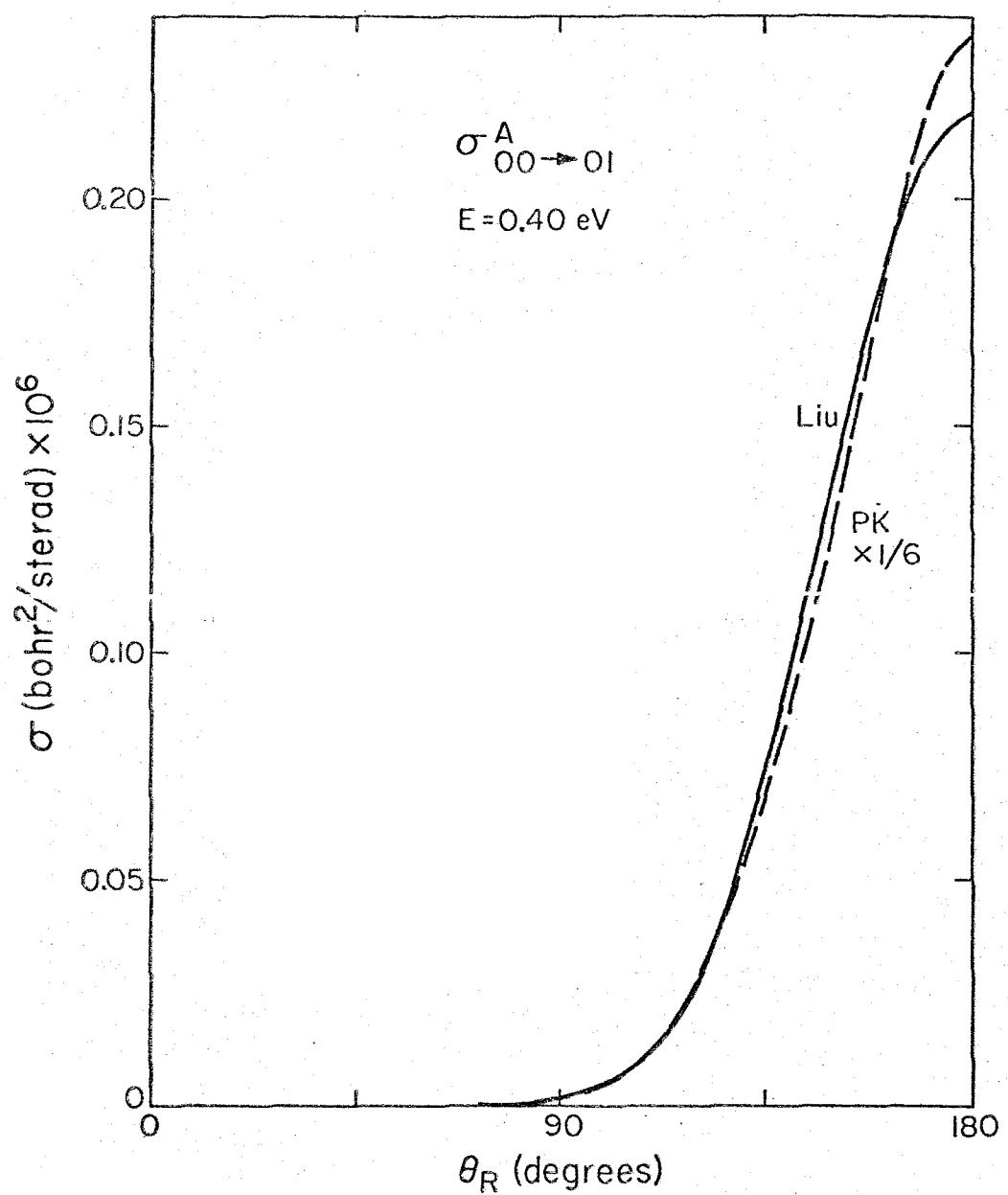
Figure 42
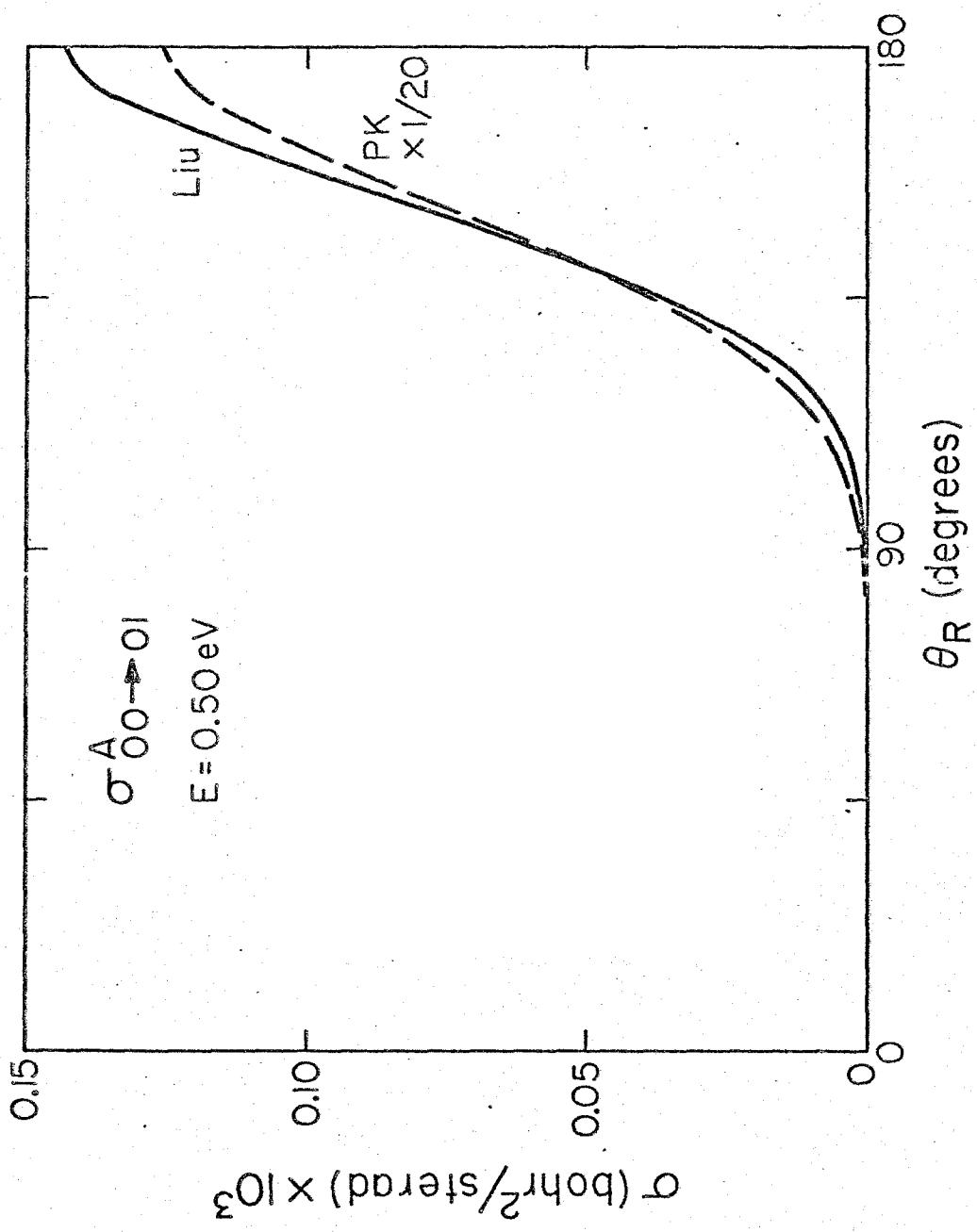
Figure 43
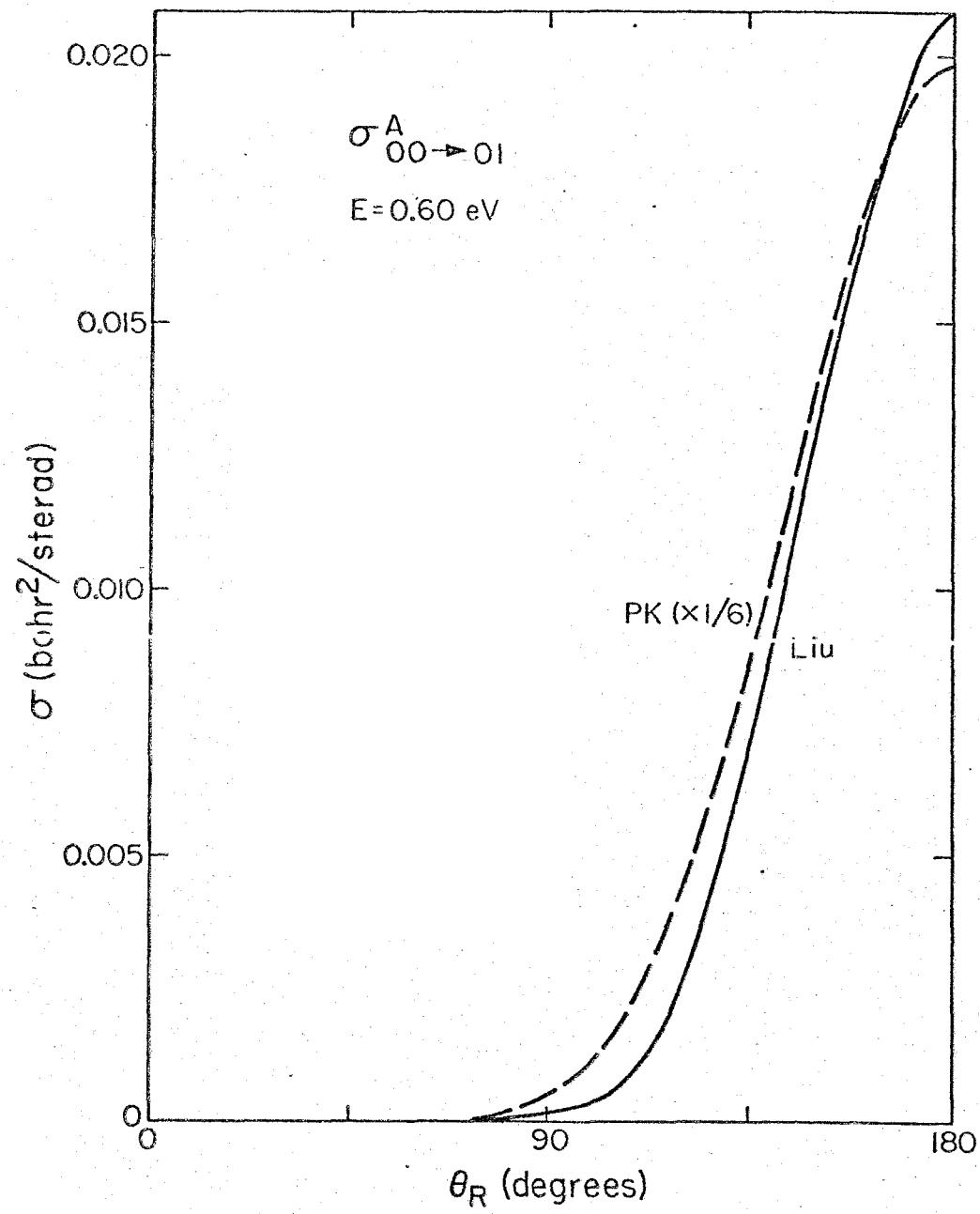
Figure 44
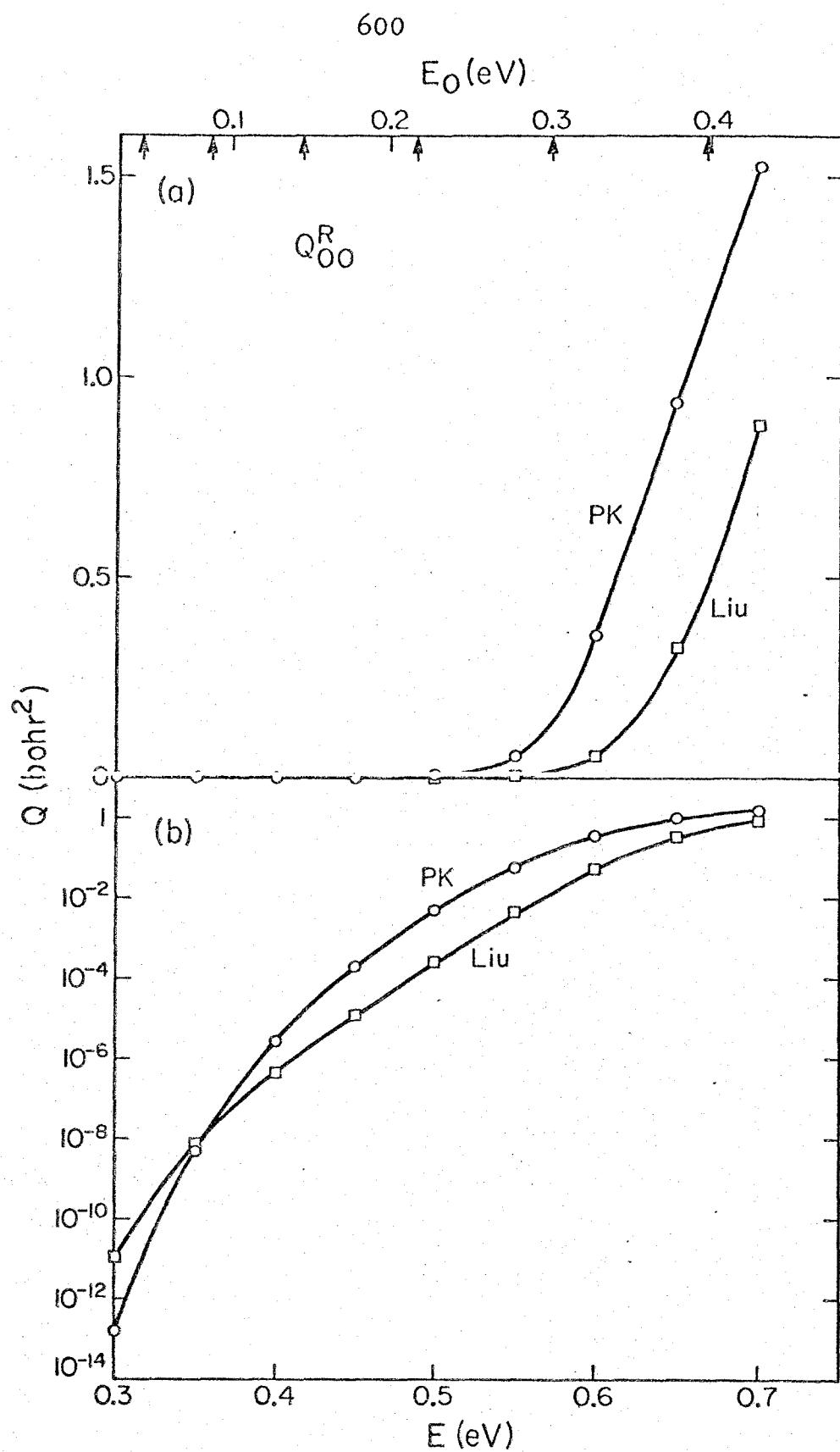
Figure 45
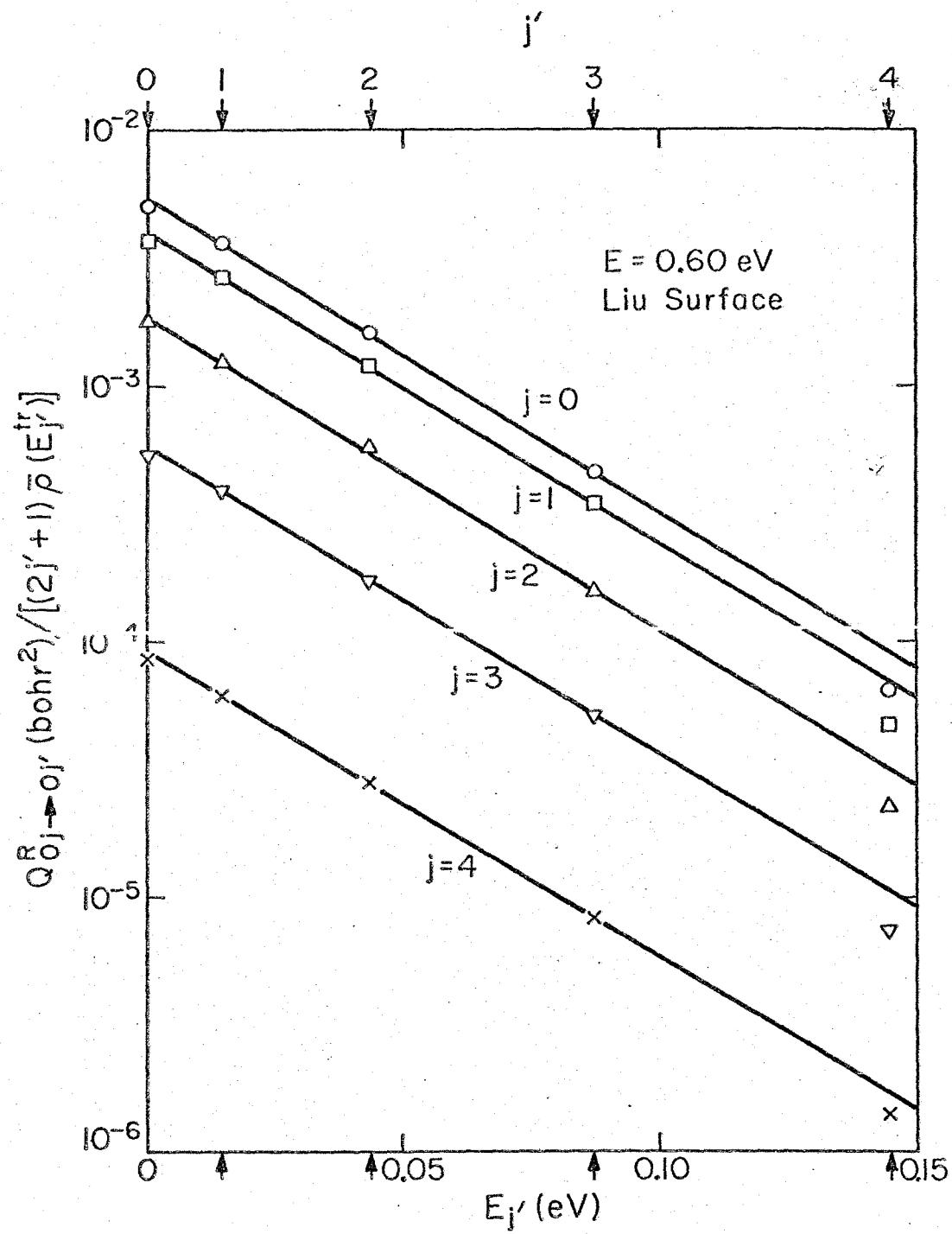
Figure 46

8. THE ROLE OF DIRECT AND RESONANT (COMPOUND STATE)

PROCESSES AND OF THEIR INTERFERENCES IN THE QUANTUM

DYNAMICS OF THE COLLINEAR $H + H_2$ EXCHANGE REACTION[*]

[*] This paper appeared in the Journal of Chemical Physics 59, 964 (1973).

THE ROLE OF DIRECT AND RESONANT (COMPOUND STATE) PROCESSES AND OF THEIR INTERFERENCES IN THE QUANTUM DYNAMICS OF THE COLLINEAR H + H₂ EXCHANGE REACTION[*]

George C. Schatz[†] and Aron Kuppermann

Arthur Amos Noyes Laboratory of Chemical Physics,[‡]

California Institute of Technology, Pasadena, California 91109

(Received   )

The question of the relative importance of compound state (i. e. activated complex) and direct reaction mechanisms has been of central importance for the dynamical foundations of chemical kinetics.[1,2] The studies here reported indicate that in the quantum dynamics of the historically important collinear H + H₂ exchange reaction not only do both such mechanisms contribute but also that their interference plays a central role in determining the pronounced quantum oscillations of the reaction probability as a function of energy.[3] This accounts not only for the absence of such oscillations in quasi-classical calculations,[4] but also for the inability of the present semi-classical formalism[5] to produce them.[6]

We have used the close-coupling propagation method of Kuppermann[7] to obtain accurate values for the elements of the scattering matrix $\underset{\approx}{S}$ as a function of the total energy E for the collinear collision H + H₂, using the same surface as previously.[3] From these elements, we calculated the reaction probabilities $P_{ij}^R(E)$, phases $\delta_{ij}^R(E)$ and time delays $\tau_{ij}^R(E) = \hbar\, d\delta_{ij}^R(E)\,/\,dE$ corresponding to the vibrational states i and j of the reagent and product H₂, respectively.

Fig. 1 shows $P_{00}^R(E)$, $\delta_{00}^R(E)$ and $\tau_{00}^R(E)$ in the energy ranges

0.80 eV to 1.00 eV and 1.20 eV to 1.35 eV. $\delta_{00}^R(E)$ and $\tau_{00}^R(E)$ are reasonably

smooth monotonic functions except near E = 0.90 eV and 1.276 eV.[8] In the

regions of relatively smooth behavior, the direct processes dominate the

reaction mechanism. The more rapid variations in $\delta_{00}^R(E)$ and $\tau_{00}^R(E)$

near 0.90 eV and 1.276 eV result from the presence of internal excitation

(Feshbach) resonances[9] at these energies.[10,11] The resonant component

of the scattering matrix element S_{00}^R has essentially a Breit-Wigner energy

dependence[12] while the direct component is characterized, in our case, by

a slowly varying amplitude and a monotonically decreasing phase.[13] We find

that these direct and resonant components have amplitudes within an order

of magnitude or less of one another at the resonance energies and that their

interferences determine the overall shapes of the curves in Fig. 1. The

widths of the resonances at 0.90 eV and 1.276 eV are about 0.05 eV and

0.008 eV respectively. An additional resonance of intermediate width has

been found at E = 1.67 eV.[14] From the resonant contribution to S_{00}^R, we

have computed the corresponding resonance state delay times $(\tau_{00}^R)_{res}$ and

displayed them as the solid curves of Fig. 1c. The maximum delay time at

the 1.276 eV resonance is about an order of magnitude greater than the

vibrational period of 1.66×10^{-14} sec for the symmetric stretch of H_3 at

the saddle point, indicating a long-lived state.

The interference effects are most clearly revealed by the Argand

plot[15] of Im S_{00}^R versus Re S_{00}^R with E as a parameter, as shown in Fig. 2.

Near 1.276 eV, a characteristic counter-clockwise resonance circle[15]

is traced out while elsewhere the plot tends to circle the origin clockwise

as E increases. The resonance at 0.90 eV is too broad to show a well-

formed resonance circle but its effect on the Argand diagram is quite apparent. Despite this broadness, the interference effects between the resonant and direct interactions at each of the resonances result in the very significant oscillations in the reaction probability plot (Fig. 1a) and are to a large extent responsible for the differences between these exact quantum calculations and the corresponding quasi-classical and semi-classical results.

We are presently investigating the importance of such resonances and interferences for other reactions, such as $F + H_2 \rightarrow FH + H$.[16]

FOOTNOTES

* Research supported in part by the U.S. Atomic Energy Commission, Report Code Number CALT-767P4-115.

† National Science Foundation predoctoral fellow. Work performed in partial fulfillment of the requirements for the Ph. D. in Chemistry at the California Institute of Technology.

‡ Contribution Number 4679.

1. S. Glasstone, K. Laidler and H. Eyring, The Theory of Rate Processes, McGraw-Hill (New York, 1941), Chapters 3,4.

2. M. Karplus, R. N. Porter and R. D. Sharma, J. Chem. Phys. 43, 3259 (1965).

3. (a) D.G. Truhlar and Aron Kuppermann, J. Chem. Phys. 52, 3841 (1970); (b) ibid., 56, 2232 (1972).

4. J. M. Bowman and Aron Kuppermann, Chem. Phys. Lett. 12, 1 (1971).

5. W. H. Miller, J. Chem. Phys. 53, 1949 (1970); 53, 3578 (1970); 54, 5386 (1971).

6. J. M. Bowman and Aron Kuppermann, Chem. Phys. Lett., in press.

7. Aron Kuppermann, Potential Energy Surfaces in Chemistry, (ed. W. Lester), University of California at Santa Cruz, August 1970, p. 121-129; Electronic and Atomic Collisions, VIIth International Conference on the Physics of Electronic and Atomic Collisions, Abstracts of Papers (North Holland, 1971), p. 3.

8. The results presented near 1.276 eV in ref. 3b (the dashed portions of the curves in their Figs. 3-6, 11-13) were inaccurate because an insufficient number of closed channels was used, whereas the present results are fully converged.

9. H. Feshbach, Ann. Phys. (N.Y.) $\underset{\sim}{5}$, 357 (1958); ibid. $\underset{\sim}{19}$, 287 (1962).

10. G. C. Schatz and Aron Kuppermann, VIII International Conference on the Physics of Electronic and Atomic Collisions (Belgrade, July (1973).

11. Related resonances were studied by R. D. Levine and S.-F. Wu, Chem. Phys. Lett. $\underset{\sim}{11}$, 557 (1971); S.-F. Wu and R. D. Levine, Mol. Phys. $\underset{\sim}{22}$, 881 (1971).

12. G. Breit and E. Wigner, Phys. Rev. $\underset{\sim}{49}$, 519 (1936).

13. The partitioning of the scattering matrix into resonant and direct components is discussed by Feshbach.[9]

14. G. C. Schatz and Aron Kuppermann, unpublished results.

15. R. K. Adair, Phys. Res. $\underset{\sim}{113}$, 338 (1959); R. H. Dalitz, Ann. Rev. Nucl. Sci. $\underset{\sim}{13}$, 346 (1964); J. Macek and P. G. Burke, Proc. Phys. Soc. $\underset{\sim}{92}$, 351 (1967); R. G. Moorhouse, Ann. Rev. Nucl. Sci. $\underset{\sim}{19}$, 301 (1969); R. D. Levine, M. Shapiro and B. R. Johnson, J. Chem. Phys. $\underset{\sim}{52}$, 1755 (1970).

16. G. C. Schatz, J. M. Bowman and Aron Kuppermann, J. Chem. Phys. $\underset{\sim}{58}$, 000 (1973).

FIGURE CAPTIONS

Fig. 1   Reaction probability P_{00}^R, phase δ_{00}^R of the scattering matrix element, time delay τ_{00}^R and resonant component of the time delay $(\tau_{00}^R)_{res}$ for the collinear $H + H_2$ reaction as a function of the total energy E and the relative translational energy E_0. The arrow in the abscissa indicates the opening of the $j = 2$ vibrational state of H_2 (at 1.280 eV). For display purposes, the phases in the 1.20 eV to 1.35 eV range have been increased by 2π with respect to those in the 0.80 eV to 1.00 eV range.

Fig. 2   Argand diagram of Im S_{00}^R versus Re S_{00}^R with the energy E as a parameter. The crosses are placed at intervals of 0.01 eV. The squares near the 1.276 eV resonance are at 0.001 eV intervals and indicate that the resonance component of the phase is increasing rapidly near this energy (although the overall phase varies in a manner indicated in Fig. 1b). The dashed circle calls attention to the existence of a resonance circle in the energy region near 1.276 eV.
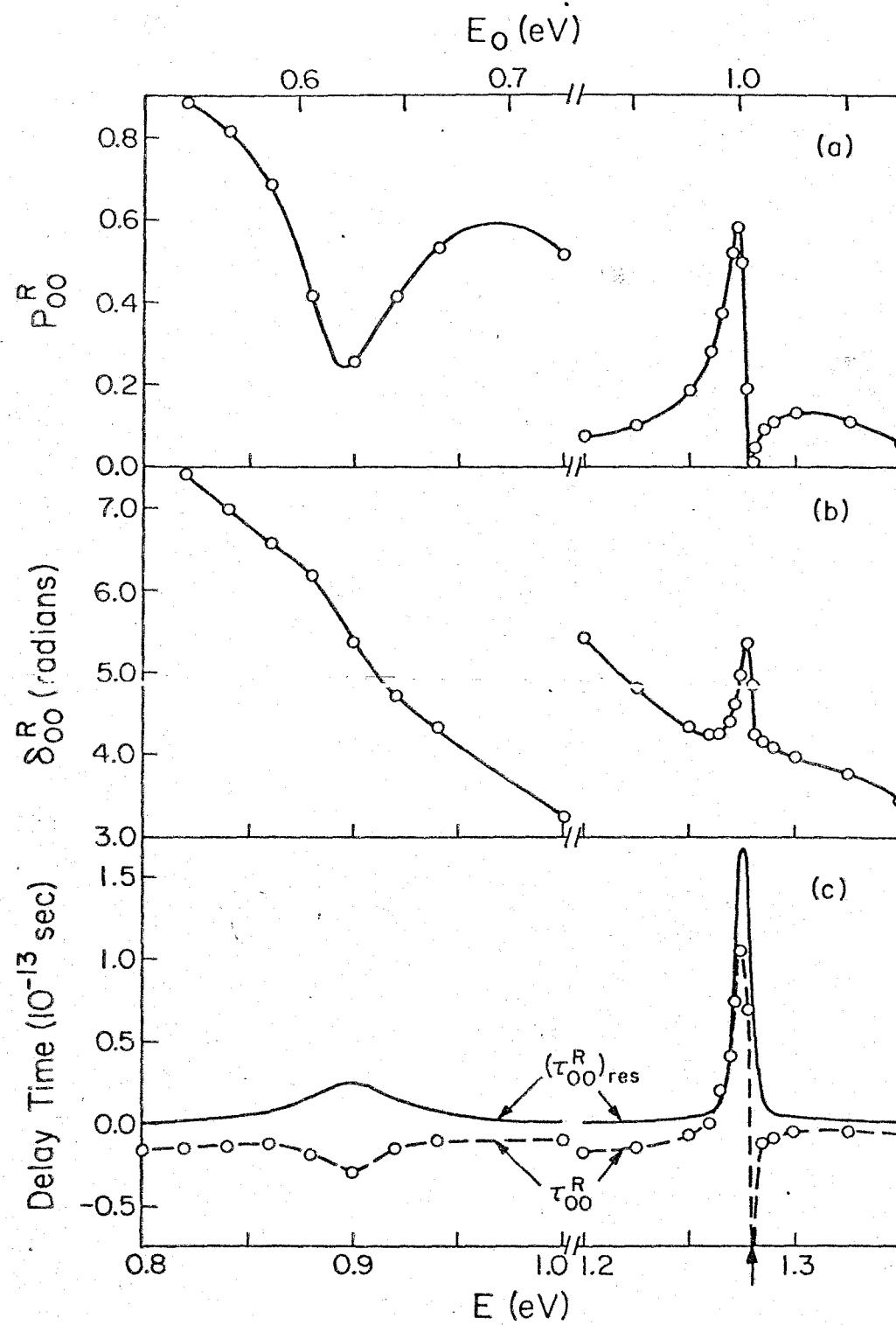
Figure 1
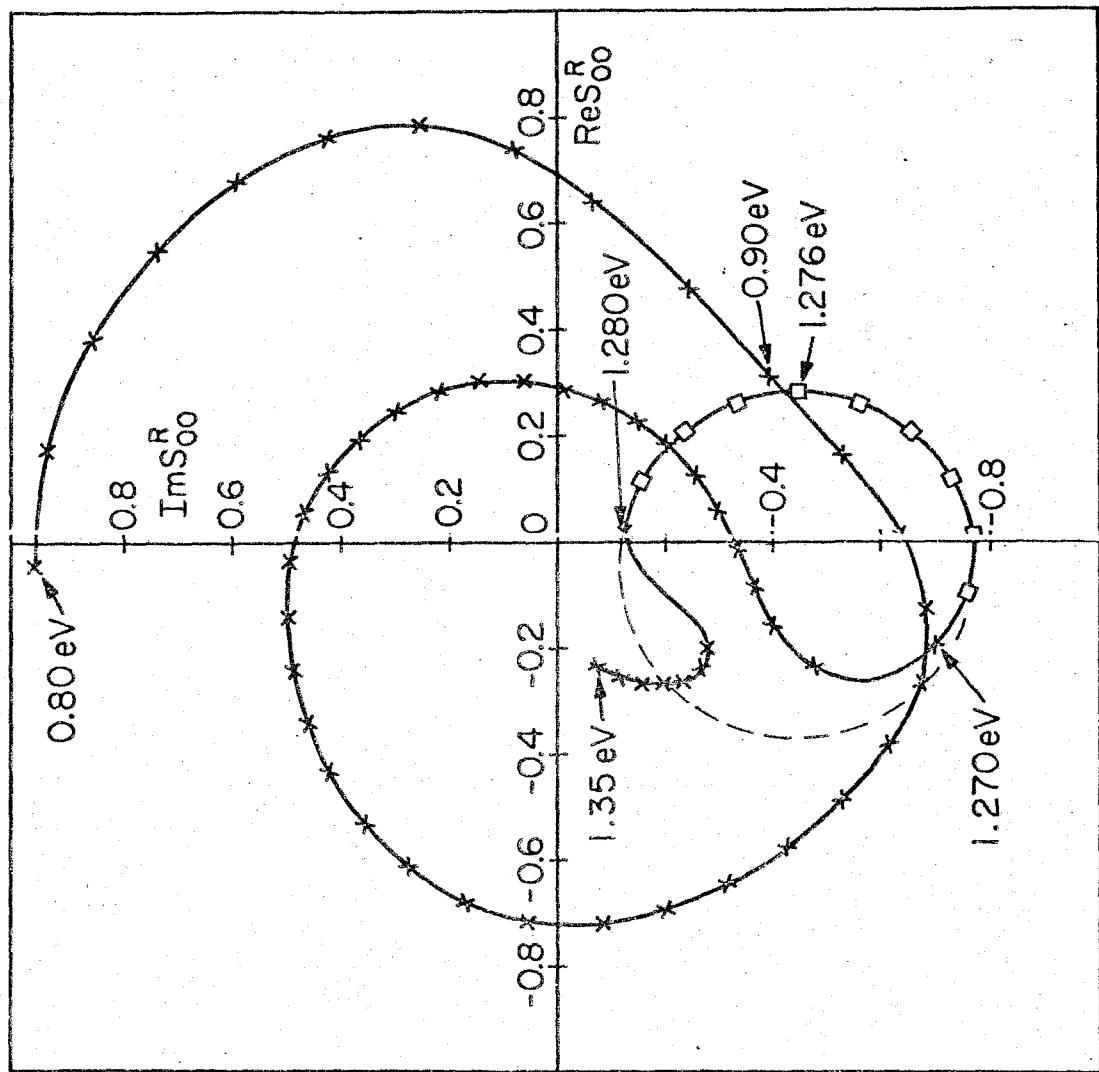
Figure 2

9. AN ANALYSIS OF RESONANT AND DIRECT PROCESSES IN
    CONVERGED COLLINEAR CALCULATIONS ON ATOM DIATOM
    CHEMICAL REACTIONS

An analysis of resonant and direct processes in collinear atom diatom chemical reactions [*]

George C. Schatz[†] and Aron Kuppermann

Arthur Amos Noyes Laboratory of Chemical Physics,

Division of Chemistry and Chemical Engineering, [‡]

California Institute of Technology, Pasadena, California 91125

The importance of resonant and direct processes is examined in two collinear atom diatom chemical reactions. The reactions considered are the $H + H_2$ exchange reaction (on two different potential surfaces) and the $H + FH \rightarrow HF + H$ reaction. Information examined includes phases and amplitudes of the scattering matrix, eigenphase shifts, time delays, the lifetime matrix and Argand diagrams. For the resonances observed in $H + H_2$, competition between resonant and direct processes is important, making it difficult to achieve a separation and parametrization of these two mechanisms. For $H + FH$, by using certain symmetry properties inherent in the system, and examining eigenphase shifts, a complete separation can, however, be achieved, and the resonance and direct processes are examined in detail. Still lacking is a complete physical picture of the resonant state (which is only poorly described by a vibrationally adiabatic analysis).

1. INTRODUCTION

A very useful concept in scattering theory has been the classification of collisions as proceeding via direct or resonant (shape or Feshbach) mechanisms. The literature on the subject is extensive[1-6] as is the diversity of physical applications -- ranging from collisions of elementary particles[7] (at GeV collision energies), to collisions between nuclei[8] (MeV energies), to electron molecule scattering[9] (several eV) and heavy particle scattering (a few meV to several eV). In the field of atomic and molecular physics, such diverse processes as predissociation,[10] autoionization[11] and uni-molecular chemical reactions[12] are all examples of scattering processes which may be classified as predominantly resonant. At the same time, many kinds of collision processes between atoms, molecules and electrons are predominantly direct.[13]

Our understanding of direct and resonant processes in atom diatomic molecule chemical reactions is based largely on the results of molecular beam experiments.[13,14] In these experiments, whenever the lifetime of the activated complex is appreciably longer than its average rotational period, the product angular distribution shows backward forward symmetry and this identifies the reaction as proceding by a resonant mechanism. Direct reactions, on the other hand, do not show this forward backward symmetry. This is, however, usually a course grained experiment, for velocity and state selection of reagents and products is never more than partially achieved, and furthermore, resonances with a shorter lifetime than the rotational period of the transition state are not easily discerned. An alternative

procedure for characterizing direct and resonant processes in chemical reactions is to examine the results of theoretical calculations. Unfortunately, most theoretical reactive scattering calculations use approximate dynamical techniques which either preclude resonant processes (such as many applications of the distorted wave method[15]), or include them with great difficulty (semi-classical methods[16,17]). The quasi-classical method,[18] which does in principle include both direct and resonant mechanisms, does not include their interference. Alternative procedures which concentrate only on resonant processes (analogous to the Hartree-Fock model in electron molecule Feshbach resonances[9]) have yet to be developed for systems with unbound transition states. In addition to these important problems with dynamical methods for examining direct and resonant processes in chemical reactions, the electronically adiabatic potential energy surfaces must be accurately known in order to reliably make any predictions on a specific system.

In this paper, we use the results of converged quantum mechnical calculations on several atom diatom systems to examine the importance of resonant and direct processes in chemical reactions. In all calculations, we assume the three atoms to be collinear during the collision. For the types of direct and resonant mechanisms we are interested in here, this assumption should not crucially affect the conclusions to be made (as has recently been shown elsewhere[19]). A preliminary communication of this work has been published previously.[20] This paper is largely a phenomenological study in that we will examine exact collinear results and attempt to see what information can be

extracted from them concerning the dynamical processes involved. The analysis will primarily concentrate on the information contained in the elements of the scattering matrix $\underset{\approx}{S}$. Besides the amplitudes and phases thereof, we will also examine such quantities as time delays, eigenphase shifts, and the lifetime matrix, all of which are derivable from $\underset{\approx}{S}$. To a certain extent, we shall concentrate on the separation of resonant and direct processes, but it must be remembered that this separation is not unique, and in most cases to be described below, is not particularly obvious either.

In Section 2 we will introduce the theoretical tools for examining resonances, and apply them to a simple but relevant analytically soluble example. The results of collinear calculations are considered in Section 3. Three separate calculations will be examined: the $H + H_2$ exchange reaction (using a scaled SSMK surface[21-23]), the $H + FH \rightarrow HF + H$ reaction,[24] and the $H + H_2$ reaction (using the Porter-Karplus potential surface[25]). A summary of the results and some generalizations which may be obtained from them are included in Section 4.

2. THEORY

In this section, we introduce the important theoretical quantities involved in analyzing direct and resonant mechanisms. To do this, we develop the simple example of the one dimensional symmetric square well. As we shall see, this one mathematical dimensional (1MD) model of a reactive system is similar in many ways to the 2MD collinear chemical reactions to be examined later.

Let the depth of the well be $-V_0$ $(V_0 > 0)$, the collision energy be E_0, and the width be 2a. If we assume that we initially have a wave of unit incident flux for $x < -a$, then the asymptotic form of the wave function for this problem is

$$\psi_k = Te^{ikx} \qquad\qquad x > a$$
$$\psi_k = e^{ikx} + Re^{-ikx} \qquad x < -a \qquad\qquad (2.1)$$

where k is the wave number for $x < -a$ and $x > +a$. T and R are the reflection and transmission amplitudes, and, the scattering matrix for this problem is

$$\underset{\approx}{S} = \begin{pmatrix} R & T \\ \\ T & R \end{pmatrix} \qquad\qquad (2.2)$$

The exact expressions for R and T are[26]

$$R = \frac{-\frac{1}{2}i\eta e^{-2ika}\sin 2k'a}{\cos 2k'a - \frac{1}{2}i\epsilon \sin 2k'a} \qquad\qquad (2.3)$$

$$T = \frac{e^{-2ika}}{\cos 2k'a - \frac{1}{2}i\epsilon \sin 2k'a} \qquad\qquad (2.4)$$

$$\eta = k/k' - k'/k$$
$$\epsilon = k/k' + k'/k$$

where k' is the wave number inside the well.

We now introduce the concept of a time delay for this example. As is shown in many standard texts[26,27], the time independent solutions (Eqs. 2.1) may be transformed to time dependent solutions by forming the wave packet

$$\psi(x,t) = \int f(k'') \, \psi_{k''}(x) \, e^{-i\omega(k'')t} dk'' \qquad (2.5)$$

where $f(k'')$ determines the width of the packet and has a peak at $k'' = k$. If we substitute the asymptotic forms of Eqs. 2.1 into Eq. 2.5 and use a stationary phase argument, we can determine an equation for the motion of the center of the wave packet. For the incident wave, we find

$$x = vt \qquad x < -a$$

where v is the asymptotic group velocity. For the reflected wave

$$x = -v(t - \hbar \frac{d\phi_R}{dE_0}) \qquad x < -a \qquad (2.6)$$

and, for the transmitted wave,

$$x = v(t - \hbar \frac{d\phi_T}{dE_0}) \qquad x > a \qquad (2.7)$$

where ϕ_R and ϕ_T are the phases of R and T (in Eqs. 2.3 and 2.4) respectively. For the transmitted wave packet, the equation of motion in the absence of a barrier would have been $x = vt$, so we see that the second term in Eq. 2.7 is proportional to the time delay for the motion of the wave packet in the potential $-V_0$. By the same reasoning, the time delay for the reflected wave in Eq. 2.6 also represents the time spent near the scattering center in excess of the "unperturbed" time of passage, which in this case is the time required to travel to the origin with $V_0 = 0$, be reflected at the origin by an infinite barrier, and continue back to $x = -\infty$ with the velocity v. In both the reflected and transmitted waves, we obtain the general definition of time delay, which may be written as

$$\tau_{ij} = \hbar \frac{d\phi_{ij}}{dE_0} \qquad (2.8)$$

where ϕ_{ij} is the phase of the element of $\underset{\approx}{S}$ associated with the transition $i \to j$. For the square well, Eqs. 2.3 and 2.4 provide

$$\phi_T = \phi_R + (n + \tfrac{1}{2})\pi \qquad n = 0, \pm 1, \pm 2, \ldots$$

$$= -2ka + \tan^{-1} (\tfrac{1}{2}\epsilon \tan 2k'a) \qquad (2.9)$$

and

$$\tau_T = \tau_R = -2a/v + \frac{a|T|^2}{v} \left(\frac{2E_0 + V_0}{E_0 + V_0}\right) - \frac{|T|^2 V_0^2 \sin 4k'a}{4vk'(E_0 + V_0)E_0} \qquad (2.10)$$

where the transmission probability $|T|^2$ is

$$|T|^2 = (\cos^2 2k'a + \tfrac{1}{4}\epsilon^2 \sin^2 2k'a)^{-1} \qquad (2.11)$$

Before we examine the physical meaning of the phases ϕ and time delays τ let us first introduce the eigenphase shifts and lifetime matrix for this problem.

The eigenphase shifts are found by diagonalizing $\underset{\approx}{S}$ in Eq. 2.2. Since the S matrix is unitary, its eigenvalues must have unit modulus and we shall write these eigenvalues in the form $\exp(2i\delta)$ where δ is an eigenphase shift. For the square well example, the results of the diagonalization procedure are

$$\underset{\approx}{S} = \underset{\approx}{\tilde{U}} \exp 2i\underset{\approx}{\Delta}\, \underset{\approx}{U} \qquad (2.12)$$

where the diagonal matrix $\underset{\approx}{\Delta}$ is

$$\underset{\approx}{\Delta} = \begin{pmatrix} \delta_S & 0 \\ 0 & \delta_A \end{pmatrix} \qquad (2.13)$$

and the matrix $\underset{\approx}{U}$ is

$$\underset{\approx}{U} = \begin{pmatrix} \dfrac{1}{\sqrt{2}} & \dfrac{1}{\sqrt{2}} \\[2ex] \dfrac{1}{\sqrt{2}} & \dfrac{-1}{\sqrt{2}} \end{pmatrix} \tag{2.14}$$

$\underset{\approx}{U}$ is orthogonal since $\underset{\approx}{S}$ is unitary symmetric. The labels S and A on the eigenphase shifts δ_S and δ_A stand for symmetric and antisymmetric respectively, referring to the fact that the linear combinations of the two scattering solutions (Eqs. 2.1 and its reflection through the origin x = 0) which diagonalize $\underset{\approx}{S}$ are symmetric and antisymmetric respectively about x = 0. This is evident by noting that the first column of $\underset{\approx}{U}$ results in the addition of these two scattering solutions while the second leads to their subtraction. By solving Eq. 2.12 for the eigenphase shifts δ_S and δ_A in terms of R and T (Eq. 2.2), then substituting the explicit results in Eqs. 2.3 and 2.4, we find

$$\delta_A = -ka - \tfrac{1}{2}\tan^{-1}(\tfrac{1}{2}\eta \sin 2k'a) + \tfrac{1}{2}\tan^{-1}(\tfrac{1}{2}\epsilon \tan 2k'a) \tag{2.15}$$

$$\delta_S = -ka + \tfrac{1}{2}\tan^{-1}(\tfrac{1}{2}\eta \sin 2k'a) + \tfrac{1}{2}\tan^{-1}(\tfrac{1}{2}\epsilon \tan 2k'a) + \pi/2 \tag{2.16}$$

The phase ϕ_T (and hence ϕ_R) may be related to δ_A and δ_S via

$$\phi_T = \delta_S + \delta_A - \pi/2 \tag{2.17}$$

Note that phases are modulo 2π while eigenphase shifts are modulo π.

The lifetime matrix $\underset{\approx}{Q}$, as defined by F. Smith[6], is related to $\underset{\approx}{S}$ by

$$\underset{\sim\sim}{Q} = i\hbar \underset{\sim\sim}{S} \frac{d\underset{\sim\sim}{S}^{\dagger}}{dE} \qquad (2.18)$$

$\underset{\sim\sim}{Q}$ is related to the excess in the probability density of the time independent wave function over the probability density of the corresponding "unperturbed" wave function integrated over all space. Smith has demonstrated that $\underset{\sim\sim}{Q}$ is hermitian and that $\underset{\sim\sim}{Q}$ and $\underset{\sim}{\tau}$ (the matrix of time delays) are related by

$$Q_{ii} = \sum_{j} S_{ij}^{*} S_{ij} \tau_{ij} \qquad (2.19)$$

This implies that Q_{ii} is the average time delay experienced in a collision where the system is initially in state i. For the square well example, Eqs. 2.2 and 2.19 lead to $Q_{ii} = \tau_R = \tau_T$, so both the lifetime matrix and time delay matrix provide the same information. Also of interest are the eigenvalues of $\underset{\sim\sim}{Q}$, which Smith has related to the lifetimes of metastable states. One can easily show that $\underset{\sim\sim}{Q}$ for the square well problem is diagonalized by the matrix $\underset{\sim}{U}$ of Eq. 2.14 which also diagonalizes $\underset{\sim}{S}$. (This is not generally true.) Its eigenvalues q_S and q_A are simply

$$q_S = 2\hbar \frac{d\delta_S}{dE_0} \qquad (2.20)$$

$$q_A = 2\hbar \frac{d\delta_A}{dE_0} \qquad (2.21)$$

where δ_S and δ_A are given by Eq. 2.15 and 2.16.

Now consider a specific application of the formulas of this section. Suppose that the quantity $\beta = (2mV_0 a^2/\hbar^2)^{\frac{1}{2}}$ has the value 315 and consider the range of E_0/V_0 between 0 and 0.009. In Fig. 1 we plot the resulting transmission probability $|T|^2$ (Eq. 2.11) as a function of

E_0/V_0. The figure shows a typical resonance profile with a peak in $|T|^2$ at $E_0/V_0 = 0.00464$. This resonance energy corresponds to the infinite square well bound state expression $2k'a = n\pi$ where $n = 201$. (There are 200 bound states in the well.) This is a typical example of a shape resonance, but note that $|T|^2$ does not decrease to zero for energies E_0/V_0 much greater than the resonance energy. This is because the direct processes are also contributing to $|T|^2$. As E_0/V_0 increases, the resonance contributions become less and less significant while the direct contributions increase and eventually dominate completely. This is manifested by the fact that $|T|^2$ rises to a constant value of unity independent of E_0 for large enough E_0/V_0. The phase ϕ_T of Eq. 2.9 is plotted in Fig. 2 as a function of E_0/V_0. We see that ϕ_T is a monotonically decreasing function of E_0/V_0 even at the resonance energy. A small inflection is, however, noted there, and an examination of Eq. 2.9 indicates that the second term in that equation is responsible for it. Indeed, if that second term alone is plotted (Fig. 2), we obtain a function which increases rapidly by π at the resonance energy. The first term in Eq. 2.9 is the direct contribution to ϕ_T and is a monotonically decreasing function of E_0/V_0. (See dashed curve in Fig. 2.) This direct phase is equal to that obtained for reflection off a hard sphere of radius a (the limit $V_0 \rightarrow \infty$ for ϕ_R in Eq. 2.9) and will be called the hard sphere phase below. This example illustrates that even though the resonant component of ϕ_T increases by π at the resonance energy, the direct component can easily obscure this. We should also note that for a general many channel problem, the phase of S_{ij} is not in general simply the sum of resonant and direct contributions,

and therefore is not easily separated into two parts as was done in Fig. 2.

If we examine the eigenphase shift δ_S, we find an energy dependence similar to ϕ_T in Fig. 2. δ_A, on the other hand, shows no inflection near the resonance energy because the second and third terms in Eqs. 2.15 cancel when $2k'a \simeq n\pi$ for odd n. This example illustrates the even-odd character of the quasi-bound resonance state. For odd n, the resonance state will be symmetric with respect to reflection through $x = 0$ and hence will not couple to the antisymmetric eigensolution, although it will couple to the symmetric one. For even n, the resonance state is antisymmetric and the opposite coupling occurs. This property of δ_S and δ_A can be useful in this example, because the difference $\delta_S - \delta_A$ will characterize only resonance contributions, thus enabling us to approximately separate out resonant and direct contributions. We shall see how this can be useful in Section 3. For the general multichannel problem, the sum of the eigenphase shifts should increase by π[1] at a resonance (in the absence of direct contributions). Inspection of Eqs. 2.15, 2.16 and Fig. 2 shows that this is trivially the case here, but this fact would be difficult to prove without a procedure for separating off the direct contributions.

We conclude this section by examining the time delays for the example of Figs. 1 and 2. The direct component of τ corresponds to the first term in Eq. 2.10 (-2a/v). Its negative sign means that the "time of passage" through the scattering center is shorter than the time of passage in the absence of a potential. Indeed, since this unperturbed time of passage is precisely 2a/v, we see that the direct

mechanism corresponds to scattering in which the incident particle spends essentially zero time within the boundaries of the well. This is the expected result for reflection from a hard sphere ($V_0 \rightarrow -\infty$), and the value of this direct time delay is, in fact, the smallest time delay allowed by causality. This was first shown by Wigner.[28] The resonant contribution to τ_T in Eq. 2.10 is positive and sharply peaked near the resonance energy. (It is just the slope of the $\phi_T + 2ka$ curve in Fig. 2.) The sum of resonant plus direct contributions to τ_T is always negative (since the slope of ϕ_T in Fig. 2 is always negative) in spite of the sharp resonance, thus indicating that caution must be used in attempting to correlate the absence of resonances with the absence of positive time delays.

We should also mention that the ϕ_T, τ and $|T|^2$ can be easily parametrized in terms of a resonance energy E_r and half width Γ by setting (for $\epsilon \gg 2$)

$$E_r = \frac{\hbar^2 n^2 \pi^2}{8ma^2} - V_0 \tag{2.22}$$

$$\Gamma = \frac{8}{n\pi} \sqrt{E_r(E_r + V_0)} \tag{2.23}$$

and expanding all quantities in Eqs. 2.9 - 2.11 in powers of $E_0 - E_r$. We find

$$\phi_T = -2ka - \frac{\pi}{2} + \tan^{-1}\left(\frac{\Gamma/2}{E_r - E_0}\right) \tag{2.24}$$

$$\tau_T = -\frac{2a}{v} + \frac{\hbar\Gamma/2}{(\Gamma/2)^2 + (E_r - E_0)^2} \tag{2.25}$$

and

$$|T|^2 = (1 + (\frac{2(E_r - E_0)}{\Gamma})^2)^{-1} \qquad (2.26)$$

The resonant components of these equations have the usual Lorentzian form with a maximum time delay $\tau_T(E_r) = 2\hbar/\Gamma$. Although the resonant interactions considered in this section have been shape resonances, much of the discussion is also true about Feshbach (internal excitation) resonances. In particular, the above parametrization (Eqs. 2.24 - 2.26) can be generalized to many channel problems in a straightforward manner (Ref. 4).

3. APPLICATION TO COLLINEAR REACTIVE ATOM DIATOM SCATTERING

We now consider an application of the concepts developed in Section 2 to the results of accurate quantum mechanical calculations on collinear atom diatom reactive systems. In all cases, a close coupling method described elsewhere[17,29] was used to obtain scattering matrices for the reactions and energies desired. All transition probabilities and phases considered are accurate to 1% or better, but time delays and lifetime matrices are subject to much larger uncertainties (perhaps 5 - 10%) due to the necessity of interpolating between energies to obtain the required energy derivatives (Eqs. 2.8 and 2.18).

We first consider the collinear $H + H_2$ reaction on a scaled SSMK potential surface.[21-22] The reaction probabilities for this system have been extensively analyzed by Truhlar and Kuppermann.[23] The results of the close coupling calculations in the form of phases ϕ_{ij} as a function of the total energy E (E = E_0 + 0.273 eV for $H + H_2$) are presented in Figs. 3 - 7. The notation is analogous to Ref. 23 with R

symbolizing reactive transitions and V nonreactive ones. All (distinct) possible initial and final vibrational quantum numbers i and j between 0 and 2 are considered in the figures. Appropriate multiples of 2π have been added so as to make the plots continuous (at least where they should be continuous). From these plots one can make the following observations:

(a) The most obvious behavior of the phases is that they are all monotonically decreasing functions of energy except at a few energies. This is very much like the phase ϕ_T in Fig. 2 for the square well problem. We shall assign this monotonic energy dependence of the phases as arising from the direct interactions.

(b) There is a discontinuity of π in the ϕ_{00}^V plot near E = 0.60 eV. This discontinuity actually exists and is related to (but not the same as) the rapid change of the square well phase by π when a transmission resonance occurs. We shall elaborate upon this below.

(c) Most of the phase plots (Figs. 3 - 5) show a small but rapid change in the derivative of the phase near E = 0.90 eV. This fluctuation is more easily seen in the time delay plots (Figs. 6 - 7). In addition, the reaction probabilities for the $0 \rightarrow 0$ transitions, plotted in Fig. 10, show a sudden change near 0.90 eV. These observations -- a rapid change in time delay and in reaction probability as a function of energy near 0.90 eV--are indicative that a resonance is occurring near that energy. However, the direct processes are also present and what we are actually looking at in the figures are contributions from amplitudes for both of these processes. Since each mechanism has its own phase, the S matrix phases, time delays and probabilities

show the effects of interferences between these mechanisms. The resonance responsible for the fluctuations at 0.90 eV appears to be quite broad (width of around 0.03 eV) and is not easily characterized because the amplitude for the direct processes tends to wash out the resonant behavior. No simple decomposition of resonant and direct processes is obvious here, although a partial decomposition is possible as will be described for a related $H + H_2$ resonance below. It is also not easy to classify the resonance as cleanly shape or Feshbach in nature, although it seems logical (from arguments given below) that this and most other resonances analyzed in this paper are Feshbach resonances.

(d) The phases plotted in Figs. 3 - 5 show an extremely rapid fluctuation near $E = 1.276$ eV. Simultaneously, the reaction probabilities (Fig. 10) undergo very rapid fluctuations. This again is indicative of a resonance but this time it is quite narrow (0.008 eV) and the effects of phase interferences with the direct interactions are much more easily discerned. This resonance and that at 0.90 eV were examined in Ref. 20, and will be further examined below.

(e) Finally, we note that the phases for different transitions often seem to be related to each other in certain ways. Some of these relations are consequences of unitarity and other properties of $\underset{\approx}{S}$. For energies below 0.793 eV, only the ground state of H_2 is open and the $\underset{\approx}{S}$ matrix is 2 x 2. Unitarity and symmetry of $\underset{\sim}{S}$ as well as additional symmetries which occur specifically for $H + H_2$ and similar reactions require that (analogous to Eq. 2.9)

$$\phi_{00}^{R} = \phi_{00}^{V} + (n + \tfrac{1}{2})\pi \qquad n = 0, \pm 1, \pm 2, \ldots \qquad (3.1)$$

so that

$$\tau_{00}^{R} = \tau_{00}^{V} \qquad (3.2)$$

In addition,

$$\phi_{00}^{V} (E_0 = 0) = n\pi \qquad (3.3)$$

$$\phi_{00}^{R} (E_0 = 0) = (n + \tfrac{1}{2})\pi \qquad (3.4)$$

where n should be determined by Levinson's theorem[1] although we have not tested this yet. For energies above 0.793 eV, more channels are open and Eq. 3.1 ceases to hold. The following relation does, however, result from the unitarity of $\underset{\approx}{S}$, at least at the threshold for opening of the first excited vibrational state of H_2

$$\phi_{11}^{R} = \phi_{11}^{V} + (n + \tfrac{1}{2})\pi \qquad (3.5)$$

One additional relation also seems to be obeyed near this threshold

$$\phi_{01}^{R} = \phi_{01}^{V} + 2n\pi \qquad (3.6)$$

but this is not a consequence of unitarity unless we make the additional assumption that $\left| S_{01}^{R} \right|^{2} = \left| S_{01}^{V} \right|^{2}$. This latter relation seems to hold quite well just above the threshold for opening of the first excited state of H_2 although the reason for this is unknown.

Some additional information which we have obtained is in the form of the eigenvalues of $\underset{\approx}{Q}$ at certain energies. These are listed in Table I. They cannot be correlated with specific channels and thus

are listed by magnitude. Note that near E = 1.276 eV, one of the
eigenvalues becomes quite large and positive. This apparently
results from the resonance at that energy, but unfortunately, the full
energy dependence of this eigenvalue is lost because the opening of
an additional vibrational state at E = 1.28 eV changes $\underset{\sim}{Q}$ from 4 x 4 to
6 x 6 and this changes the eigenvalue spectrum considerably.

We shall now discuss the direct contributions to the time delays.
Figs. 8 - 9 show that the time delays tend to behave qualitatively
like

$$\tau_{ij}^{R} = \tau_{ij}^{V} \ \alpha - (E - \epsilon_i)^{-\frac{1}{2}} = (-E_i^{-\frac{1}{2}}) \tag{3.7}$$

just above the threshold for opening of vibrational state i. (Note $i \geq j$
and ϵ_i is the vibrational energy of state i.) This is similar to the hard
sphere time delays observed with the square well (Section 2). We can
understand the reason for this similarity by observing that when these
direct processes occur, the system spends very little time in the inter-
action region and thus the time delays as a function of energy will be
sensitive primarily to the distance at which the atom and molecule begin
to interact strongly and less sensitive to the detailed shape of the
potential energy surface. As a result, the scattering region behaves
much like a hard sphere at least in the time delay behavior with τ pro-
portional to the inverse of the velocity. In addition, for a reaction
such as H + H_2, there should be little difference in the direct mechanism
time delays between a reactive and a nonreactive transition with the
same initial and final states. We see in Figs. 8 - 9 that this is approxi-
mately the case. Finally, the time delays often seem to be additive

according to the relation (which should be the same for both reactive and nonreactive transitions when direct processes are dominant):

$$\tau_{01} \sim \tfrac{1}{2}(\tau_{00} + \tau_{11}) \qquad (3.8)$$

This suggests that we can think of the direct processes as occurring in separable segments: an incoming time delay in the incident channel, an instantaneous transition to the exit channel followed by an outgoing time delay in that channel. The separability of these segments implies that we can add the incoming and outgoing time delays of any two channels to get the overall time delay for the transition between these two channels. Deviations from the additivity property of time delays indicate that transitions to intermediate channels are becoming important in the scattering process.

As mentioned in (b) above, the nonreactive phase ϕ_{00}^{V} undergoes an apparently discontinuous change by π near $E = 0.60$ eV. This must be a discontinuity rather than a rapid change because ϕ_{00}^{R} does not change by π in this region of energy and Eq. 3.1 implies that ϕ_{00}^{V} can change by π while δ_{00}^{R} does not only if n changes by ± 1 and this would occur discontinuously. The explanation of the discontinuity is most easily understood by reference to Fig. 11 which contains a plot of $\mathrm{Im}(S_{00}^{V})$ versus $\mathrm{Re}(S_{00}^{V})$ and similarly for S_{00}^{R}. We see that near $E = 0.60$ eV, S_{00}^{V} goes exactly through the origin. This results in a reaction probability of unity and we see this in Fig. 10. The change by π in the phase is now easily seen to result from a change in the sign of S_{00}^{V} as it goes through the origin. The physical meaning of this phenomenon is that when $S_{00}^{V} = 0$, there is no reflected wave.

As a consequence, a time delay for this channel has no meaning. Exactly the same phenomenon occurs with the reflection probability in the square well transmission resonances of Section 2. By analogy, we will label this discontinuity in the phase for $H + H_2$ as resulting from a transmission resonance (as distinct from the Feshbach resonances at 0.90 eV and 1.276 eV as discussed below). Our assignment of this behavior as resulting from a resonance is somewhat speculative, since the probability in Fig. 10 shows little resemblance to that in Fig. 1. In addition, there is little change in the time delay as a function of energy over what would be obtained from the direct contribution. An alternative description of this phenomena could be developed in terms of threshold effects and it appears that a clear cut distinction between the resonant and threshold designations will require additional information.

The resonances at 0.90 eV and 1.276 eV are apparently much different in nature from that observed at 0.60 eV. Near 0.90 and 1.276 eV, we can explain the energy dependence of the observed phases (Figs. 3 - 5) and reaction probabilities (Fig. 10) as resulting from the interference of the direct processes with resonant processes which occur because of the existence of a metastable vibrational state of the H_3 system. Such discreet states embedded in the continuum have been seen in nonreactive molecular scattering[30] and related resonances for the same $H + H_2$ reaction but a different potential surface, were examined in Ref. 31. To justify the statement that these resonances are Feshbach rather than shape resonances, we need to develop a model which isolates single channel or vibrationally adiabatic processes

from those which are not. Such vibrationally adiabatic models have been developed and tested elsewhere.[31,32] If we expand the exact scattering wave function in terms of symmetric stretch H_3 eigenfunctions (the numerically determined transition state vibrational functions), we obtain a set of expansion coefficients at each energy, the squares of which are shown in Table II for energies near the 1.276 eV resonance. The expansion coefficients indicate the relative importance of the different vibrationally adiabatic states at the transition state, remembering that asymptotically, $|a_{00}|^2 = 1$ and $|a_{0j}|^2 = 0$ for $j \neq 0$. At energies well above and well below resonance (i.e., 1.260 eV and 1.290 eV), the reaction is primarily direct, but the coefficients indicate that it is strongly nonadiabatic (within the zero curvature adiabatic framework chosen). Roughly the same $|a_{0j}|^2$ are obtained at 1.260 eV and at 1.290 eV indicating that the rate of change of the direct components to these coefficients is small. As the energy approaches 1.276 eV from either above or below, we see in Table II that rapid changes in the $|a_{0j}|^2$ occur, with the largest being $|a_{02}|^2$ and $|a_{03}|^2$. Since the $i = 2$ and 3 states of H_2 are closed over much of the energy range, we see that the resonance is responsible for significant changes in the coefficients for these nonadiabatic virtual states. This is the expected behavior of a Feshbach resonance. The description is quite crude, however, for the resonance is not associated exclusively with any one particular virtual state, and a clean separation of adiabatic and nonadiabatic effects, or of resonant and direct effects is not possible. The resonance at 0.90 eV seems to be associated with excitations to the second vibrational state of H_3 (from the same vibrationally

adiabatic analysis).[32] Although this state is open at 0.90 eV, we still consider the resonance to be of the Feshbach type, since it results in excitations between adiabatic vibrational states. Open channel Feshbach resonances related to this one have been considered by Taylor et al.[34] In contrast to the nonadiabatic behavior near 0.90 eV and 1.276 eV, a similar analysis at 0.60 eV[33] indicates almost perfectly adiabatic behavior implying that if a resonance occurs at all at this energy, it must be a shape or transmission resonance, and not a Feshbach resonance.

Now we consider the H + FH $\rightarrow$ HF + H reaction. Reaction probabilities for this and related systems have been described elsewhere[24] as has the LEPS potential surface. For this reaction, it was found that a sharp resonant-like oscillation in the transition probabilities was obtained near $E_0(HF) \simeq 0.412$ eV. Fig. 12 shows these probabilities. Two properties of this reaction make it exceptionally easy to analyze this resonance. First, the amplitude for the direct processes remains essentially constant over the range of energies in which the resonance makes a significant contribution. This is manifested by the symmetry of the curves in Fig. 12 about $E_0 = 0.412$ eV. Second, only one vibrational state is open in each arrangement channel at the resonance energy so the symmetry properties of the scattering matrix are identical to those previously examined for the square well problem in Section 2. In that square well analysis, we found that the eigenphase shifts δ_S and δ_A could be useful in understanding resonances, since any given resonance would influence either the symmetric or antisymmetric eigensolutions but not both. In Fig. 13 we plot these two eigenphase

shifts for H + FH. As with the square well example, δ_A is monotonic over the energy range considered. δ_S increases near the resonance energy, indicating that the resonance wave function must be symmetric with respect to interchange of the two hydrogen atoms in the HFH complex. The difference between δ_S and δ_A (also plotted in Fig. 13) increases rapidly by π, in agreement with our expectations that this difference should correspond to the resonance component of the eigenphase shifts. A surprisingly accurate parametrization of $\delta_S - \delta_A$ may be obtained by fitting it to the formula

$$\delta_S - \delta_A = -\frac{\pi}{2} + \tan^{-1}\left(\frac{\Gamma}{2(E_r - E_0)}\right) \tag{3.9}$$

which may be obtained from arguments similar to those leading to Eqs. 2.24 and 2.26. In Fig. 14 we plot $\tan(\delta_S - \delta_A)$ versus E_0 for H + FH. If Eq. 3.9 is accurate, the resultant curve should be a straight line of slope $2/\Gamma$ and intercept $2E_r/\Gamma$. The straight line drawn in the figure connects all of the calculated points very accurately except those far away from resonance. From the slope and intercept of the straight line, we find $E_r = 0.412$ eV and $\Gamma = 0.0207$ eV. These parameters may then be used to calculate P_{00}^R and P_{00}^V using formulas analogous to Eq. 2.25. These formulas were used in Fig. 12 to connect the calculated points and it is obvious that the fit is excellent. A more stringent test of the validity of the parametrization of Eq. 3.9 is afforded by examining the Argand diagrams of S_{00}^R and S_{00}^V analogous to Fig. 11. To do this, we need also to parametrize the direct contribution to the eigenphase shifts. For simplicity we have assumed a linear energy dependence. An examination of δ_A in Fig. 13 (which should reflect

primarily the direct mechanism) indicates that this assumption is quite accurate. The resulting Argand diagrams are plotted in Fig. 15 where we again see good correspondence between calculated and fitted curves, except at energies far removed from resonance. The general behavior of the S_{00}^R and S_{00}^V curves is to circle the origin clockwise as E_0 increases, except near the resonance energy, where a sudden counterclockwise circle not about the origin occurs. These counterclockwise circles have been previously used in analyzing resonances[7,20,30] and are often quite useful in identifying their existence provided that the direct scattering matrix contributions are not strongly energy dependent. With both δ_S and δ_A parametrized in a simple way, we may now easily calculate the time delay and lifetime matrices. For example, the τ_{00}^V time delay is simply

$$\tau_{00}^V = 2\hbar\frac{d\delta_A}{dE} + \frac{\hbar\Gamma/2}{(E_r - E_0)^2 + \Gamma^2/4} \qquad (3.10)$$

and for a linear δ_A, τ_{00}^V is simply the sum of a constant direct contribution plus a sharply peak resonant one. The maximum value of τ_{00}^V is 4.3×10^{-14} sec, which is about twice the unperturbed time of passage.

Now we consider the same eigenphase shift analysis for an analogous resonance in collinear $H + H_2$. This time we use accurate results for the Porter-Karplus potential surface[25] in the vicinity of the first internal excitation resonance which occurs at $E = 0.875$ eV. Figure 16 shows some of the pertinent reaction probabilities. These have been given previously by Diestler.[35] This resonance occurs above the threshold for the first excited vibrational state of H_2, so the scattering matrix is 4 x 4. In this case, the diagonalization of $\underset{\approx}{S}$ requires

an energy dependent matrix $\underset{\approx}{U}$ and leads to the eigenphase shifts

plotted in Fig. 17. There are now two symmetric eigenphase shifts

δ_{S_1} and δ_{S_2} and two antisymmetric ones δ_{A_1} and δ_{A_2}. The anti-

symmetric ones vary monotonically near the resonance energy while

the symmetric eigenphase shifts increase there. Unfortunately,

δ_{A_1} and δ_{A_2} no longer cleanly represent the direct contributions, and

the difference $\delta_{S_1} + \delta_{S_2} - \delta_{A_1} - \delta_{A_2}$ does not increase by π (see

Fig. 17). Also, a parametrization analogous to Eq. 3.9 is not very

accurate as is evident from Fig. 18, where the resulting curve is

linear only for an energy range of 0.02 eV. Thus unlike the H + FH

reaction, eigenphase shifts are less useful for characterizing the

resonant and direct interactions for $H + H_2$. A primary reason for

this is the strong energy dependence of the transformation matrix $\underset{\approx}{U}$

for this system.[33] If $\underset{\approx}{U}$ were energy independent (as was required by

symmetry for H + FH), the eigenphase shifts would provide all of the

energy dependent formation necessary to characterize the scattering

matrix. This is not true for $H + H_2$, and a description of $\underset{\approx}{U}$ will also be

required to complete the characterization of $\underset{\approx}{S}$. We conclude this

section by presenting an Argand diagram of S_{00}^R and S_{01}^R for $H + H_2$,

plotted in Fig. 19. S_{00}^R of that figure is very similar to S_{00}^R (H + FH)

of Fig. 15 and we can consequently see the strong analogy between the

two resonances in these two reactions. S_{01}^R shows a more poorly

developed resonance circle because of the stronger influence of the

direct interactions in $H + H_2$ (as is obvious by comparison of Figs. 10

and 16).

4. SUMMARY

We will now summarize the various tools we have used for examining direct and resonant processes in chemical reactions. The scattering matrix itself provides us directly with the transition probabilities and phases. The probabilities are very sensitive to resonances as was apparent in Figs. 10, 12 and 16, although the interference between resonant and direct processes makes it difficult to parametrize these resonances on the basis of probability information only. The phases of $\underset{\approx}{S}$ (Figs. 3 - 7) are usually dominated by the monotonically decreasing contributions of the direct processes. The influence of resonances on these phases is apparent in the figures but not easily separated from the direct contributions. This separation problem is also usually true of the eigenphase shifts (Figs. 13 and 17), but by using the symmetry properties of the eigensolutions present in the reactions considered, a partial separation is possible. The time delays provide indications of the existence of resonances, but their physical interpretation is hampered by interferences between direct and resonant mechanisms. When both of these mechanisms are important in a reaction, the scattering matrix element S_{ij} contains contributions from both of them. This leads to a time delay τ_{ij} (Eq. 2.8) which is not in general simply a sum of resonant plus direct contributions (as it was in Eq. 2.10) but rather it shows the effects of interferences between the two. This makes it impossible to extract resonant lifetimes directly from the τ_{ij}'s without some type of parametrization procedure similar to that used for the H + FH reaction. The eigenvalues of $\underset{\approx}{Q}$ seem to be of lesser usefulness for the problems we are considering,

because the opening of new channels brings about considerable changes in the nature of these eigenvalues. Argand diagrams are useful for identifying resonances and for testing parametrizations, since all of the information contained in each element of $\underset{\approx}{S}$ is displayed in a single curve.

With the aid of the above tools for characterizing reactions, we have found that both direct and resonant mechanisms play important roles in the chemical reactions considered. The resonances are usually weak and seem to be associated with virtual excitations in the transition state region. There remains, however, a large number of unanswered questions. For example, an adiabatic analysis of the 1.276 eV Feshbach resonance in $H + H_2$ indicated that it strongly perturbs both the $j = 2$ and 3 levels of the transition state. This implies that the true resonance state is a mixture of these and other levels. How can we separate out this resonance state? Equivalently, we can ask, is there an approximate partitioning of the Hamiltonian which allows us to isolate the discreet resonance state from the continuum? Another unresolved question is the separation of resonant effects from threshold phenomena. This problem occurs for example at 0.60 eV in $H + H_2$ (SSMK surface), where an analysis of probabilities and time delays could not provide a conclusive description in terms of resonance or threshold phenomena. It is apparent that for the strongly coupled reactive problems we are interested in, a clean separation of resonance and direct effects will be difficult at best. Nevertheless, the development of approximate models for doing this is important, for such models might be more easily applied to three dimensional reactions

than are exact calculations[19], and hence would be of use in predicting

and interpreting the results of experiments.

TABLE I. Eigenvalues of the collision lifetime matrix $\underset{\sim}{Q}$.

E(eV)	Eigenvalues $\times 10^{13}$ (sec)					
1.1005	-0.279	-0.244	-0.131	-0.127		
1.1505	-0.255	-0.216	-0.125	-0.116		
1.2005	-0.234	-0.192	-0.121	-0.099		
1.2255	-0.225	-0.180	-0.119	-0.076		
1.2505	-0.192	-0.152	-0.103	+0.017		
1.2605	-0.211	-0.169	-0.115	+0.193		
1.26525	-0.208	-0.176	-0.114	+0.571		
1.27025	-0.203	-0.168	-0.112	+1.117		
1.2726	-0.199	-0.168	-0.110	+1.837		
1.2751	-0.192	-0.167	-0.106	+2.769		
1.2776	-0.166	-0.152	-0.044	+2.859		
1.2799	-0.164	-0.144	-0.076	+3.389		
1.2781	-8.726	-6.786	-0.890	-0.529	-0.161	-0.137
1.28525	-3.209	-2.934	-0.773	-0.266	-0.161	-0.126
1.29025	-2.331	-1.862	-0.649	-0.237	-0.160	-0.121

TABLE II. Normalized[*] vibrationally adiabatic projection coefficients for the v = 0 scattering solution of H + H_2.

E(eV)	$\|a_{00}\|^2$	$\|a_{01}\|^2$	$\|a_{02}\|^2$	$\|a_{03}\|^2$	$\|a_{04}\|^2$
1.260	0.100	0.205	0.324	0.342	0.027
1.265	0.100	0.184	0.423	0.256	0.031
1.270	0.015	0.241	0.090	0.586	0.065
1.275	0.014	0.163	0.038	0.682	0.100
1.2775	0.079	0.067	0.171	0.572	0.103
1.280	0.202	0.002	0.499	0.227	0.061
1.285	0.118	0.079	0.435	0.334	0.030
1.290	0.096	0.104	0.385	0.385	0.027

[*] Normalized so that $\sum_j \|a_{ij}\|^2 = 1$. Not all $\|a_{0j}\|^2$ have been tabulated.

[1] R. G. Newton, Scattering Theory of Waves and Particles, McGraw-Hill, New York, 1966.

[2] M. L. Goldberger and K. M. Watson, Collision Theory, John Wiley and Sons, New York, 1964, Chap. 8.

[3] L. S. Rodberg and R. M. Thaler, Introduction to the Quantum Theory of Scattering, Academic Press, New York, 1967, p. 379.

[4] U. Fano, Phys. Rev. 124, 1866 (1961).

[5] H. Feshbach, Ann. Phys. (N. Y.) 5, 357 (1958); ibid., 19, 287 (1962).

[6] F. T. Smith, Phys. Rev. 118, 349 (1960).

[7] For example, R. K. Adair, Phys. Rev. 113, 338 (1959); R. G. Moorhouse, An. Rev. Nucl. Sci. 19, 301 (1969).

[8] For example, J. M. Blatt and V. F. Weisskopf, Theoretical Nuclear Physics, John Wiley and Sons, New York, 1952, Chap. 9.

[9] For example, P. G. Burke, Adv. At. Mol. Phys. 4, 173 (1968).

[10] R. J. LeRoy and R. B. Bernstein, J. Chem. Phys. 54, 5114 (1971).

[11] See, for example, W. D. Price, Adv. At. Mol. Phys. 10, 131 (1974); and J. A. Samson, ibid., 2, 177 (1966).

[12] Wendell Forst, Theory of Unimolecular Reactions, Academic Press, New York, 1973, p. 5.

[13] T. T. Warnock, R. B. Bernstein and A. E. Grosser, J. Chem. Phys. 46, 1685 (1967); see also D. R. Herschbach, Molecular Beams, Ed. John Ross, Wiley Interscience, New York, 1966, p. 319.

[14] D. O. Harn and J. L. Kinsey, J. Am. Chem. Soc. 48, 939 (1968); W. B. Miller, S. A. Safron and D. R. Herschbach, Disc. Far. Soc. 44, 108 (1968).

[15] K. T. Tang and M. Karplus, Phys. Rev. A4, 1844 (1971).

[16] J. M. Bowman and A. Kuppermann, J. Chem. Phys. 59, 6524 (1973); J. R. Stine and R. A. Marcus, Chem. Phys. Lett. 29, 575 (1974).

[17] G. C. Schatz, J. M. Bowman and A. Kuppermann, J. Chem. Phys. 63, 674 (1975); ibid., 63, 685 (1975).

[18] M. Karplus, R. N. Porter and R. D. Sharma, J. Chem. Phys. 43, 3259 (1965); J. M. Bowman and A. Kuppermann, Chem. Phys. Lett. 12, 1 (1972).

[19] G. C. Schatz and A. Kuppermann, Phys. Rev. Lett., submitted.

[20] G. C. Schatz and A. Kuppermann, J. Chem. Phys. 59, 964 (1973).

[21] I. Shavitt, R. M. Stevens, F. L. Minn and M. Karplus, J. Chem. Phys. 48, 2700 (1968).

[22] The numerical results of Ref. 20 were fitted to a Wall-Porter [F. Wall and R. Porter, J. Chem. Phys. 36, 3256 (1962)] parametrized surface for the purpose of this calculation. See Ref. 23.

[23] D. G. Truhlar and A. Kuppermann, J. Chem. Phys. 52, 3841 (1970); ibid., 56, 2232 (1972).

[24] G. C. Schatz, Ph. D. thesis, California Institute of Technology (unpublished), 1975.

[25]R. N. Porter and M. Karplus, J. Chem. Phys. $\underline{40}$, 1105 (1964).

[26]E. Merzbacher, Quantum Mechanics (2nd. Ed.), John Wiley and Sons, New York, 1970, Chap. 6.

[27]A. Messiah, Quantum Mechanics (Vol. I), trans. G. M. Temmer, North Holland, Amsterdam, 1965, Chap. 10.

[28]E. P. Wigner, Phys. Rev. $\underline{98}$, 145 (1955).

[29]A. Kuppermann, Potential Energy Surfaces in Chemistry (ed., W. Lester), University of California at Santa Cruz, August, 1970, p. 121 - 129; Electronic and Atomic Collisions, VIIth International Conference on the Physics of Electronic and Atomic Collisions, Abstracts of Papers (North Holland, 1971), p. 3.

[30]R. D. Levine, M. Shapiro and B. R. Johnson, J. Chem. Phys. $\underline{52}$, 1755 (1970); D. A. Micha, Phys. Rev. $\underline{162}$, 88 (1967); R. D. Levine, B. R. Johnson, J. T. Muckerman, and R. B. Bernstein, J. Chem. Phys. $\underline{49}$, 56 (1968).

[31]R. D. Levine and S. F. Wu, Chem. Phys. Lett. $\underline{11}$, 557 (1971); S. F. Wu and R. D. Levine, Mol. Phys. $\underline{22}$, 881 (1971).

[32]J. M. Bowman, A. Kuppermann, J. T. Adams and D. G. Truhlar, Chem. Phys. Lett. $\underline{20}$, 229 (1973); J. M. Bowman, Ph. D. thesis, California Institute of Technology (unpublished), 1974.

[33]G. C. Schatz, unpublished results.

[34]H. S. Taylor, G. V. Mazaroff and A. Golebiewski, J. Chem. Phys. $\underline{45}$, 2872 (1966).

[35]D. J. Diestler, J. Chem. Phys. $\underline{54}$, 4547 (1971).

FIG. 1. Transmission probability $|T|^2$ for a symmetric square well having $\beta = 315$ as a function of E_0/V_0.

FIG. 2. Phase ϕ_T of the transmission amplitude T as a function of E_0/V_0 for the $\beta = 315$ square well. Also plotted is the direct phase $(-2ka)$ and the resonant phase $\phi_T + 2ka$ as explained in the text.

FIG. 3. Phases ϕ_{00}^R and ϕ_{00}^V for H + H$_2$ (SSMK surface) as a function of the total energy E. Arrows in abscissa at 0.793 eV and 1.28 eV indicate the value of E at which the $i = 1$ and 2 vibrational states of H$_2$ become energetically accessible. Inset shows the 1.25 eV to 1.30 eV energy range in greater detail.

FIG. 4. Phases ϕ_{01}^R and ϕ_{01}^V for H + H$_2$ analogous to Fig. 3.

FIG. 5. Phases ϕ_{11}^R and ϕ_{11}^V for H + H$_2$ analogous to Fig. 3.

FIG. 6. Phases ϕ_{02}^R, ϕ_{02}^V, ϕ_{12}^R and ϕ_{12}^V for H + H$_2$ analogous to Fig. 3.

FIG. 7. Phases ϕ_{22}^R and ϕ_{22}^V for H + H$_2$ analogous to Fig. 3.

FIG. 8. Time delays τ_{00}^R, τ_{00}^V and τ_{01}^V for H + H$_2$ as a function of the total energy E. The time delays near 1.276 eV are omitted because the strong interference between resonance and direct interactions at that energy leads to rapidly oscillating time delays which are difficult to calculate. (In addition, unless a separation of direct and resonant effects can be accomplished, the time delays are not necessarily physically meaningful. See Section 4.)

FIG. 9. Time delays τ_{01}^{R}, τ_{11}^{R} and τ_{11}^{V} analogous to Fig. 8.

FIG. 10. Reaction probabilities P_{00}^{R} and P_{00}^{V} for $H + H_2$ (SSMK surface) as a function of the total energy E.

FIG. 11. Argand diagram of S_{00}^{R} (outside curve) and S_{00}^{V} (curve going through the origin) for $H + H_2$ in the 0.50 to 0.70 eV energy range. Numbers next to the circles indicate the energy at which that element of $\underset{\approx}{S}$ was calculated.

FIG. 12. Reaction probabilities P_{00}^{R} (circles) and P_{00}^{V} (squares) for $H + FH$ as a function of the reagent translational energy E_0 in the vicinity of the 0.412 eV resonance. Solid and dashed curves were calculated by formulas described in the text.

FIG. 13. Eigenphase shifts δ_S and δ_A and their difference $\delta_S - \delta_A$ for $H + FH$ as a function of E_0.

FIG. 14. Tan $(\delta_S - \delta_A)$ as a function of E_0 for $H + FH$. A straight line has been drawn through the calculated points.

FIG. 15. Argand diagram of S_{00}^{R} (squares) and S_{00}^{V} (circles) for $H + FH$ for a range of E_0 between 0.307 eV and 0.484 eV. Solid and dashed curve are calculated from formulas described in the text.

FIG. 16. Reaction probabilities P_{00}^{R}, P_{01}^{R} and P_{11}^{R} for $H + H_2$ (Porter-Karplus surface) as a function of E.

FIG. 17. Eigenphase shifts δ_{S_1}, δ_{S_2}, δ_{A_1}, δ_{A_2} and the quantity $\delta_{S_1} + \delta_{S_2} - \delta_{A_1} - \delta_{A_2}$ for H + H$_2$ (Porter-Karplus) versus E.

FIG. 18. Tan $(\delta_{S_1} + \delta_{S_2} - \delta_{A_1} - \delta_{A_2})$ versus E for H + H$_2$ (Porter-Karplus). A straight line has been drawn through the points.

FIG. 19. Argand diagram of S_{00}^R (circles) and S_{01}^R (squares) for H + H$_2$ (Porter-Karplus) for E between 0.816 eV and 0.925 eV. Calculated points are at the same energies as those in Fig. 16.
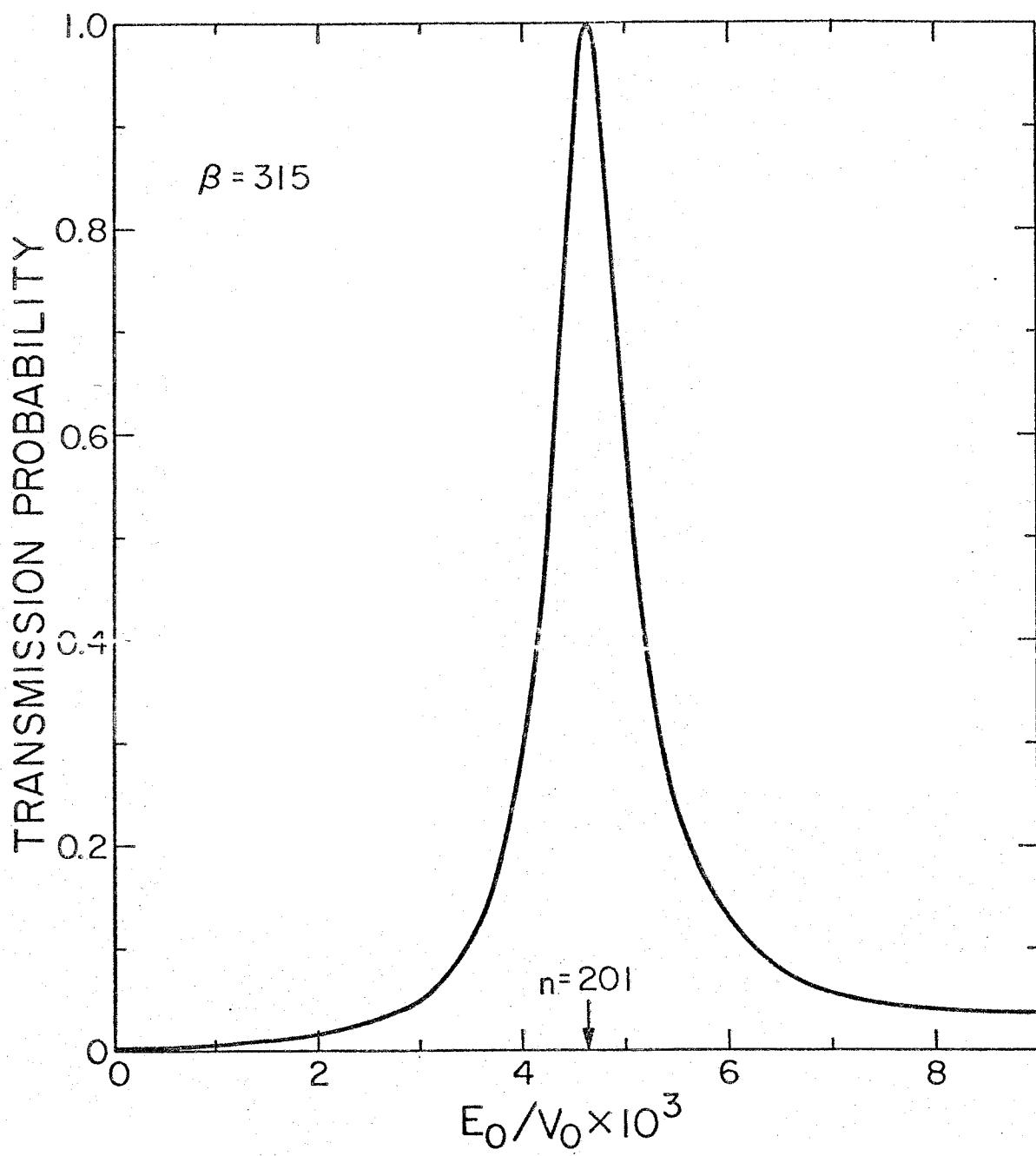
Figure 1
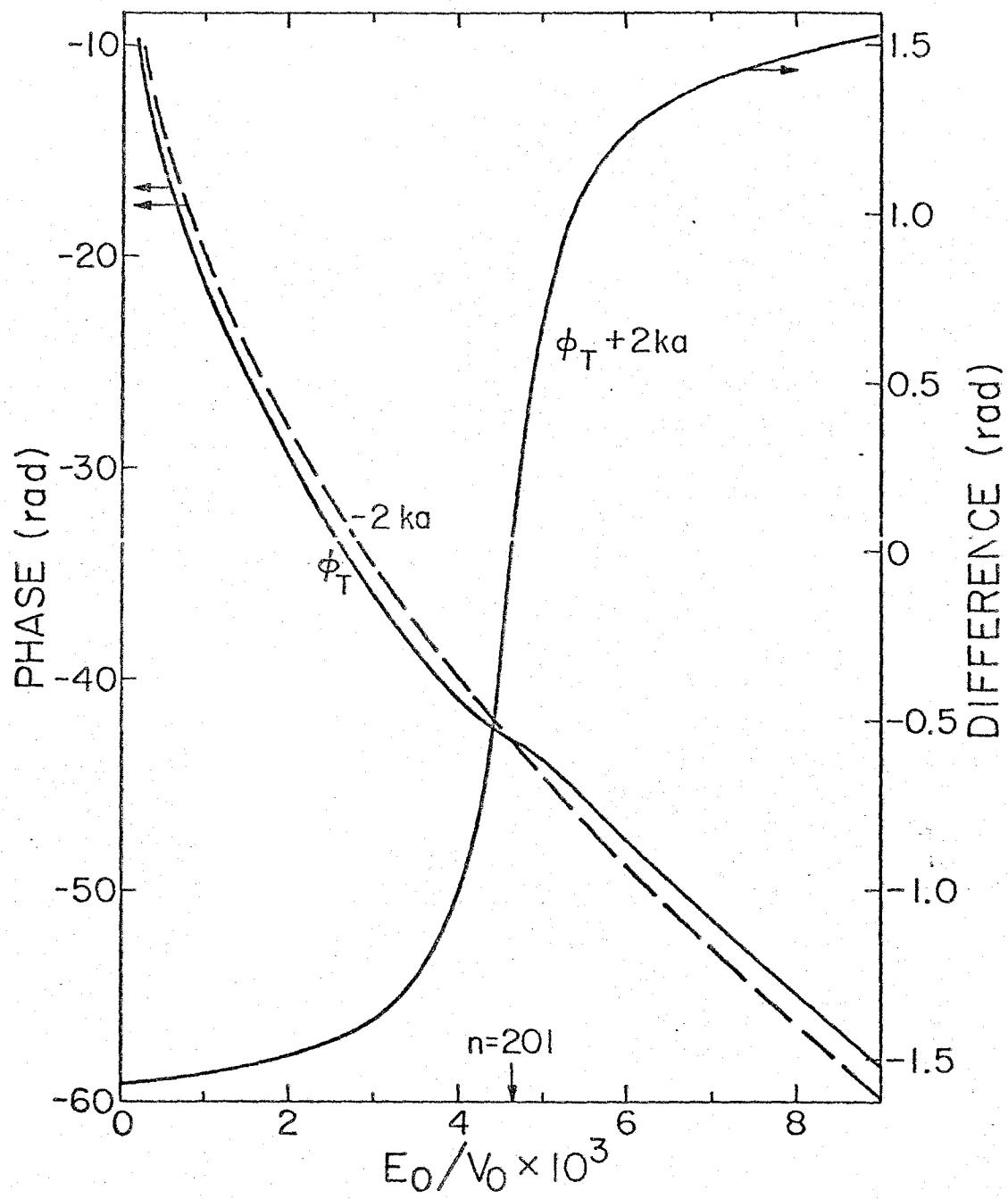
Figure 2
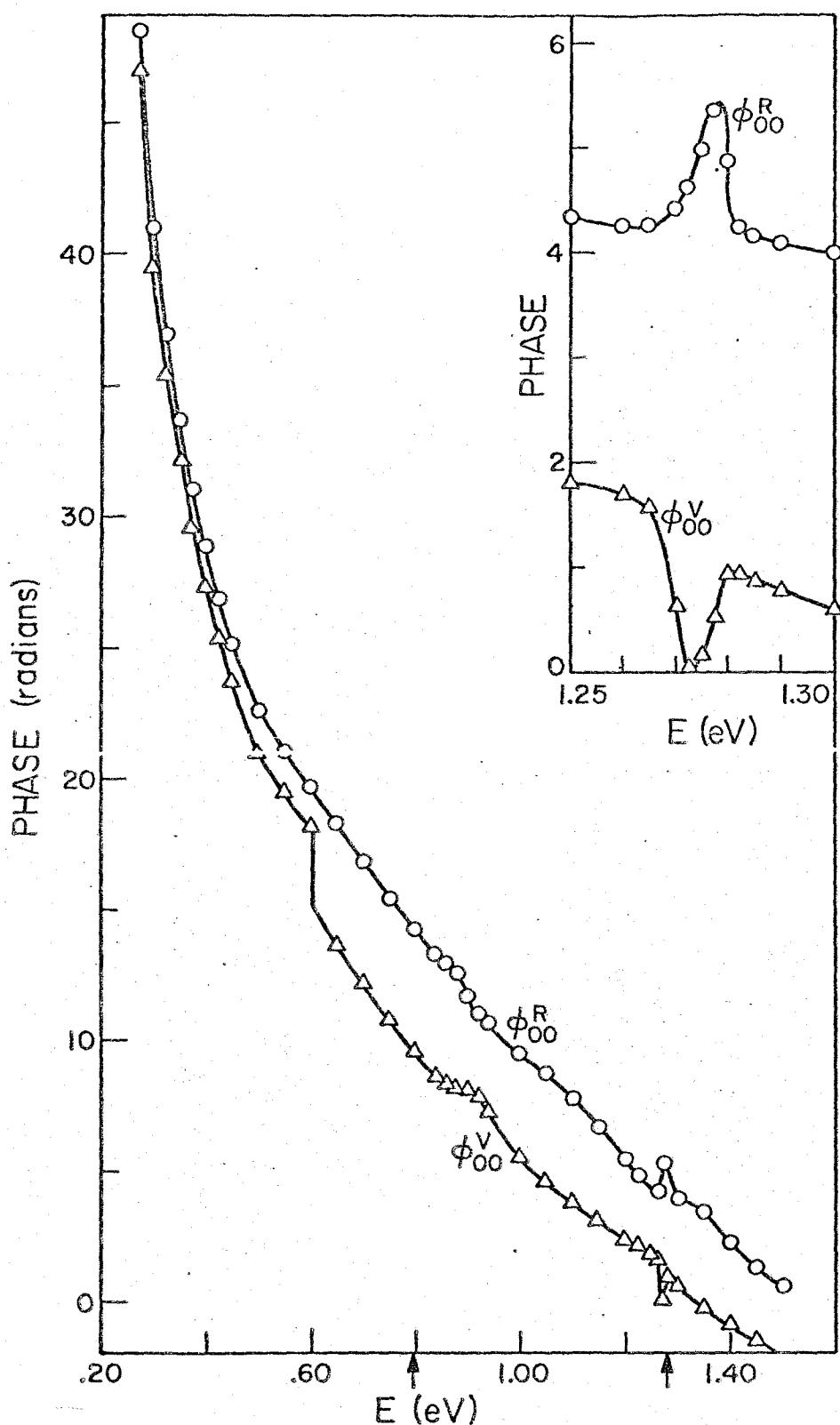
Figure 3
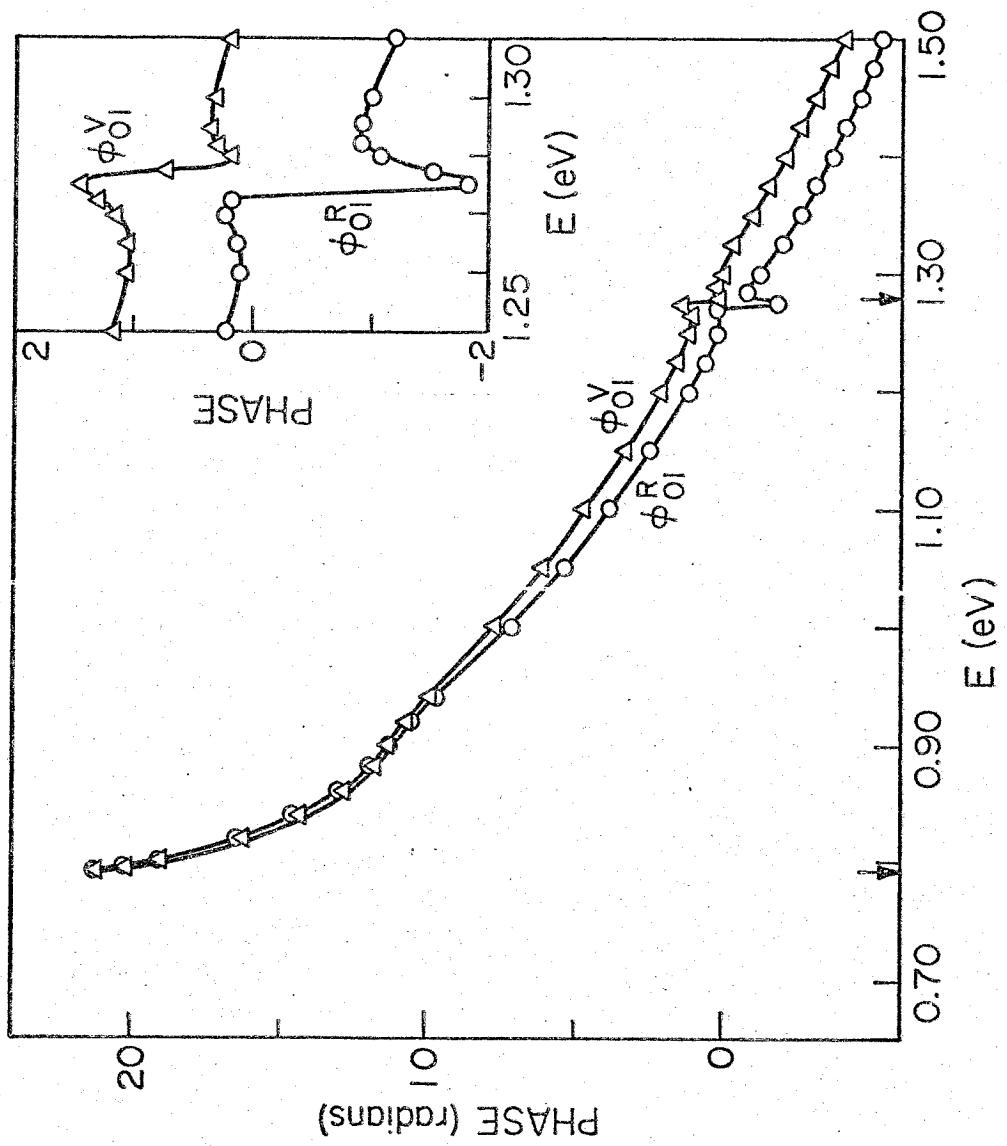
Figure 4
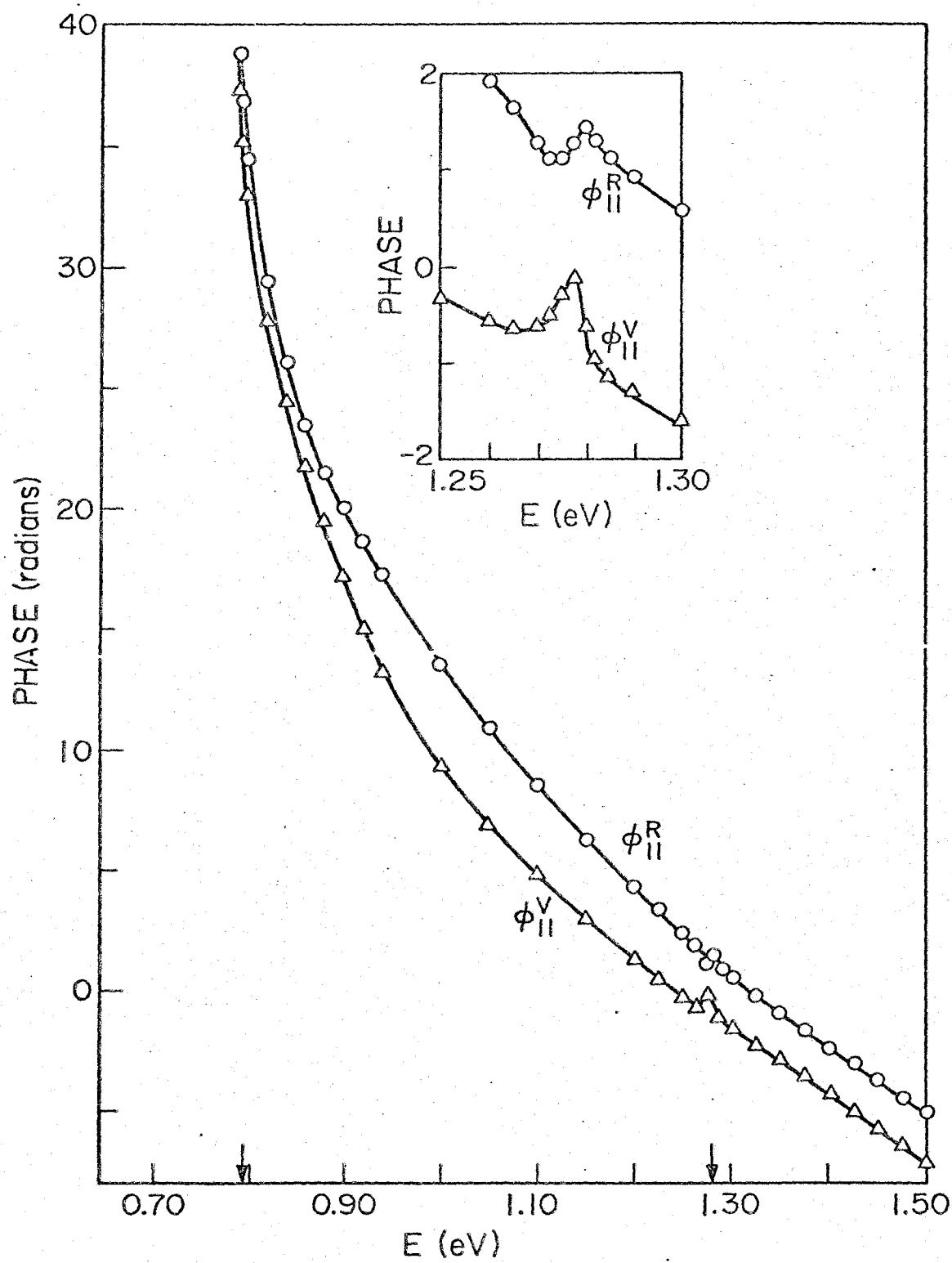
Figure 5
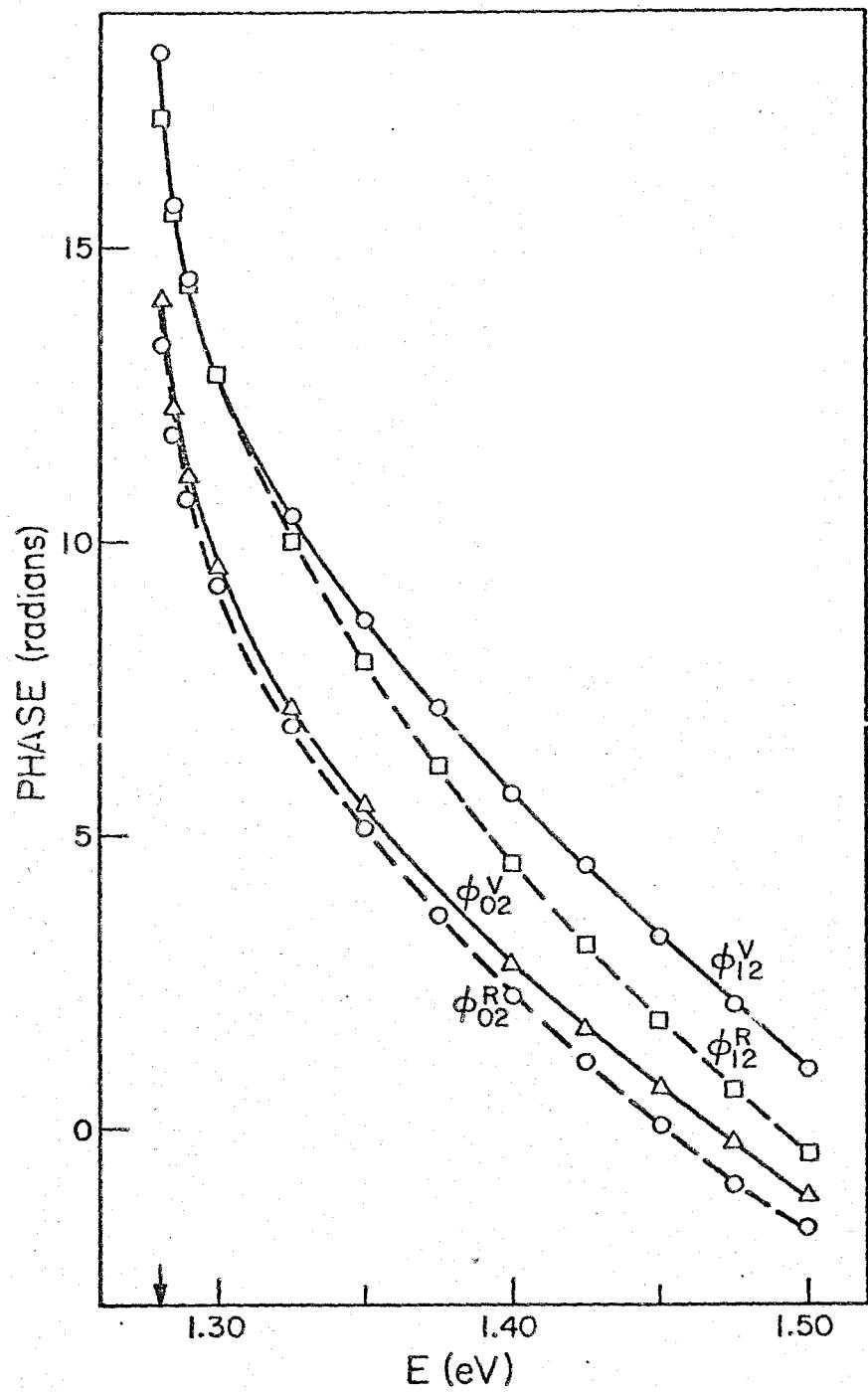
Figure 6
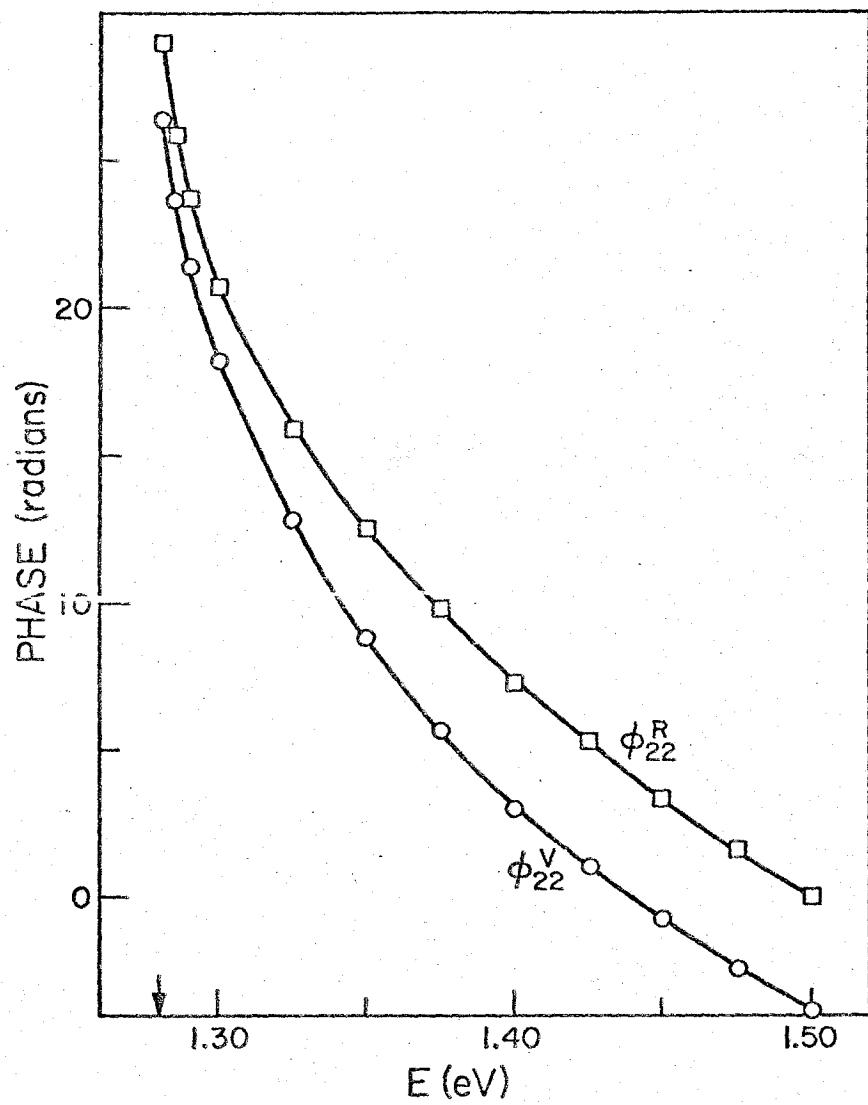
Figure 7
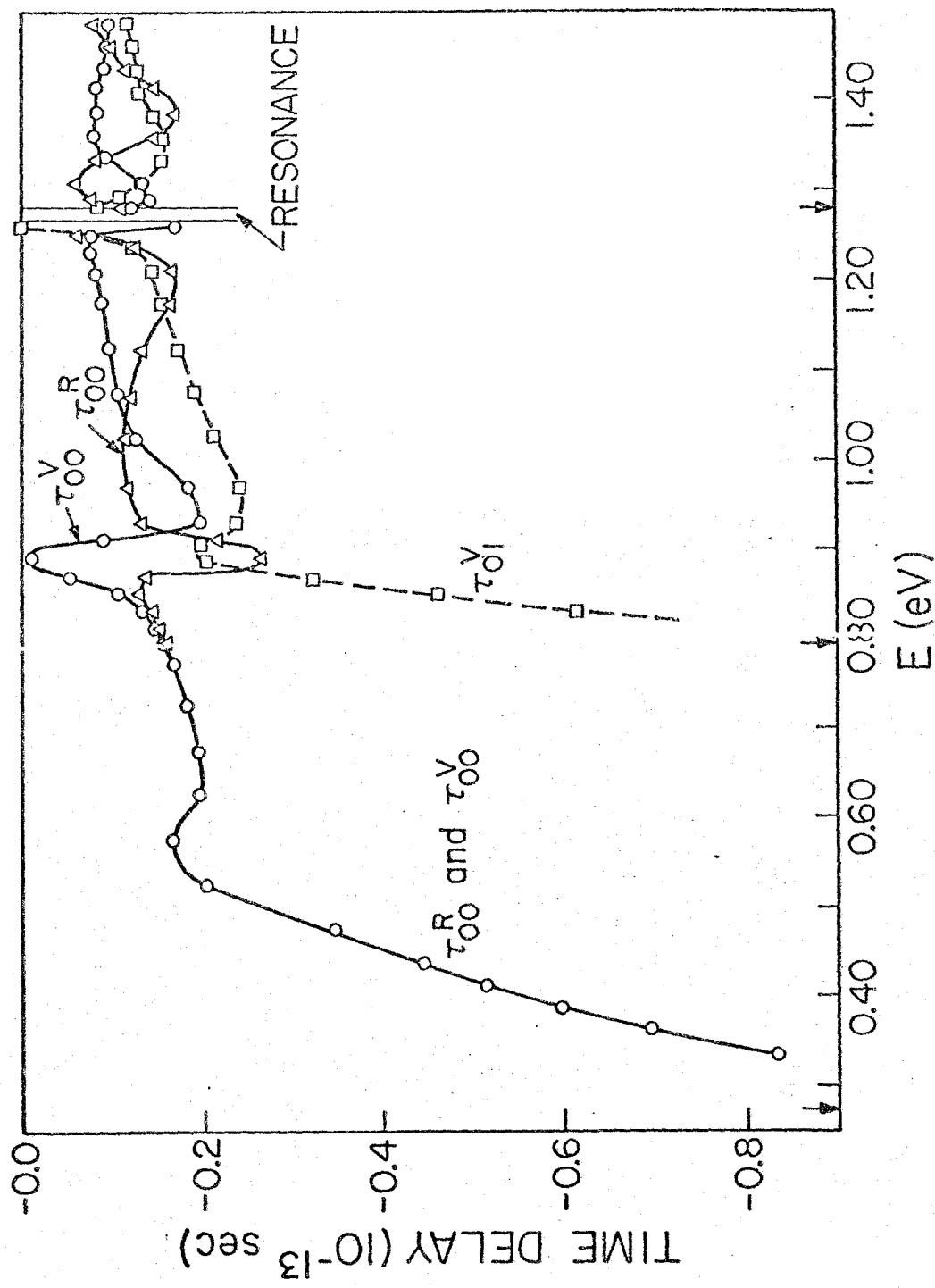
Figure 8
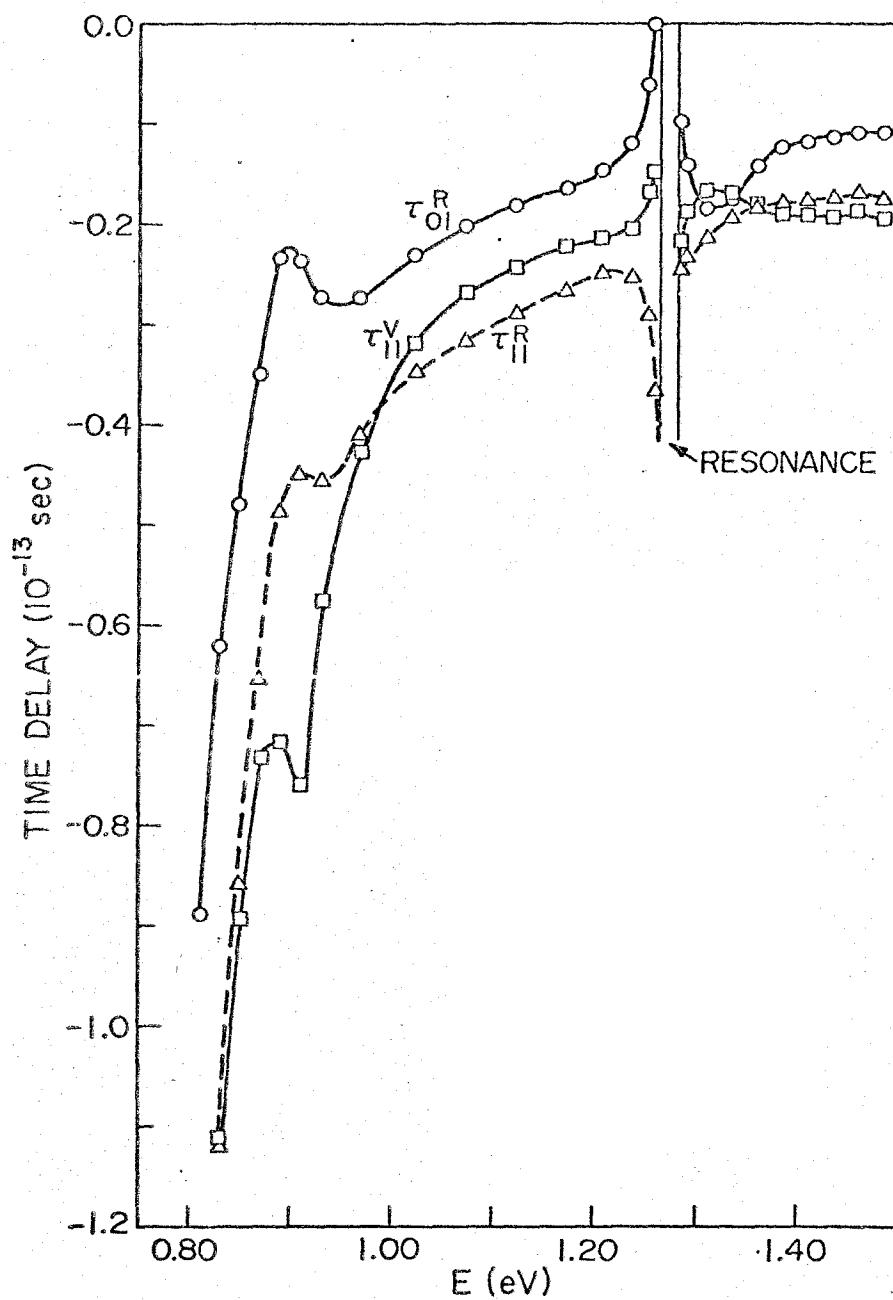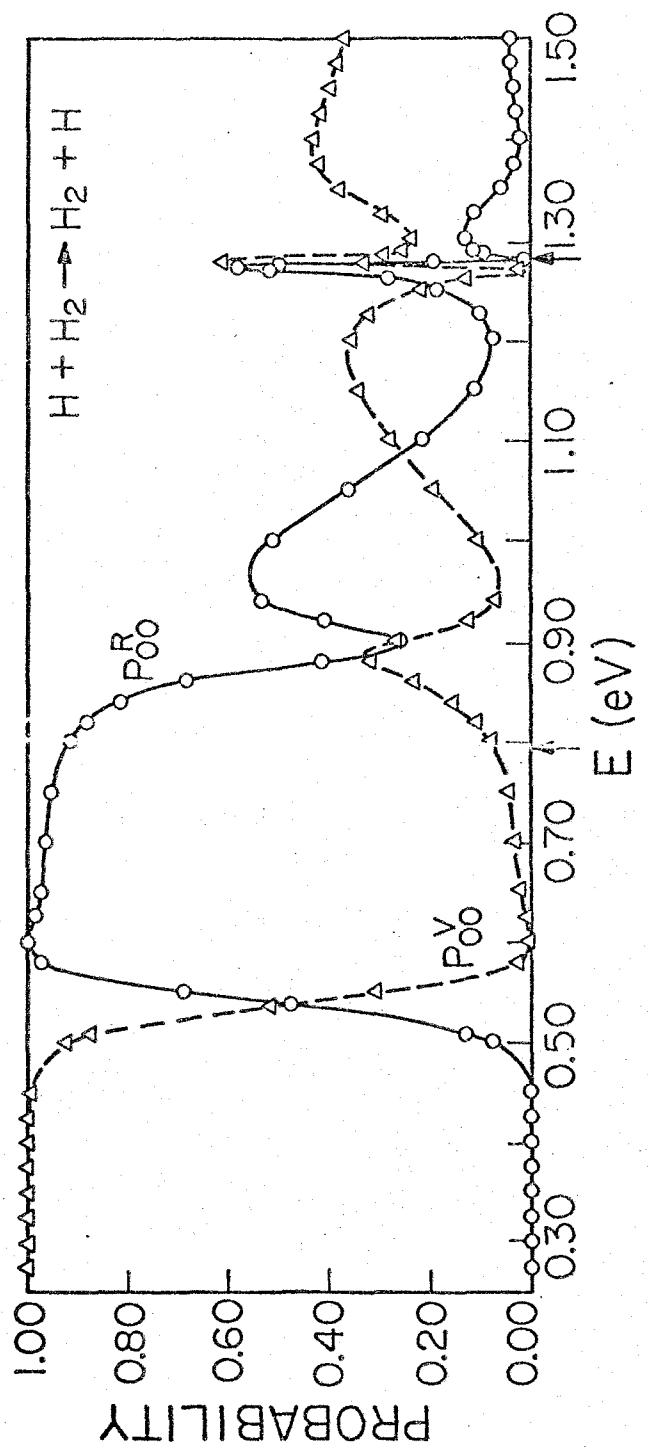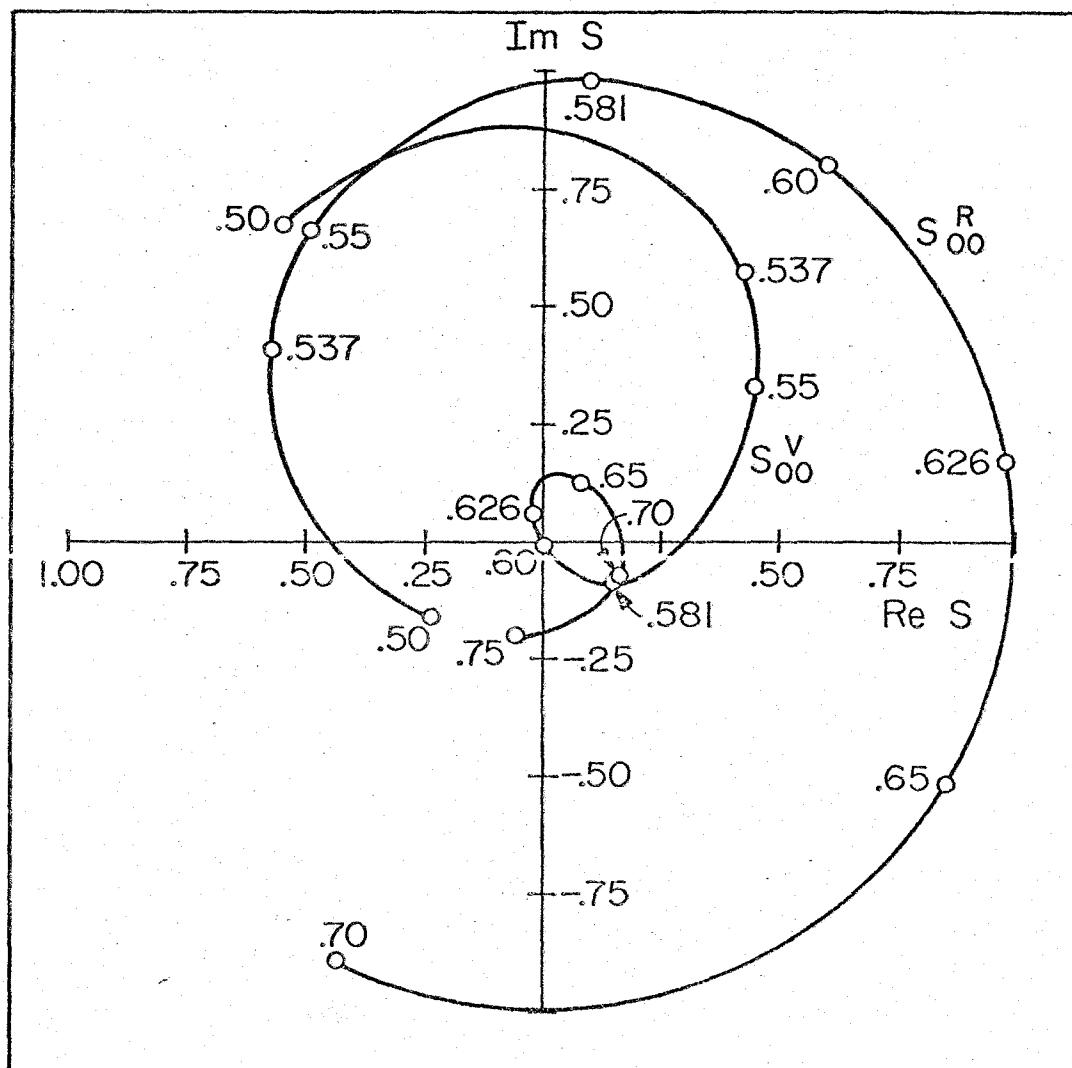
Figure 9
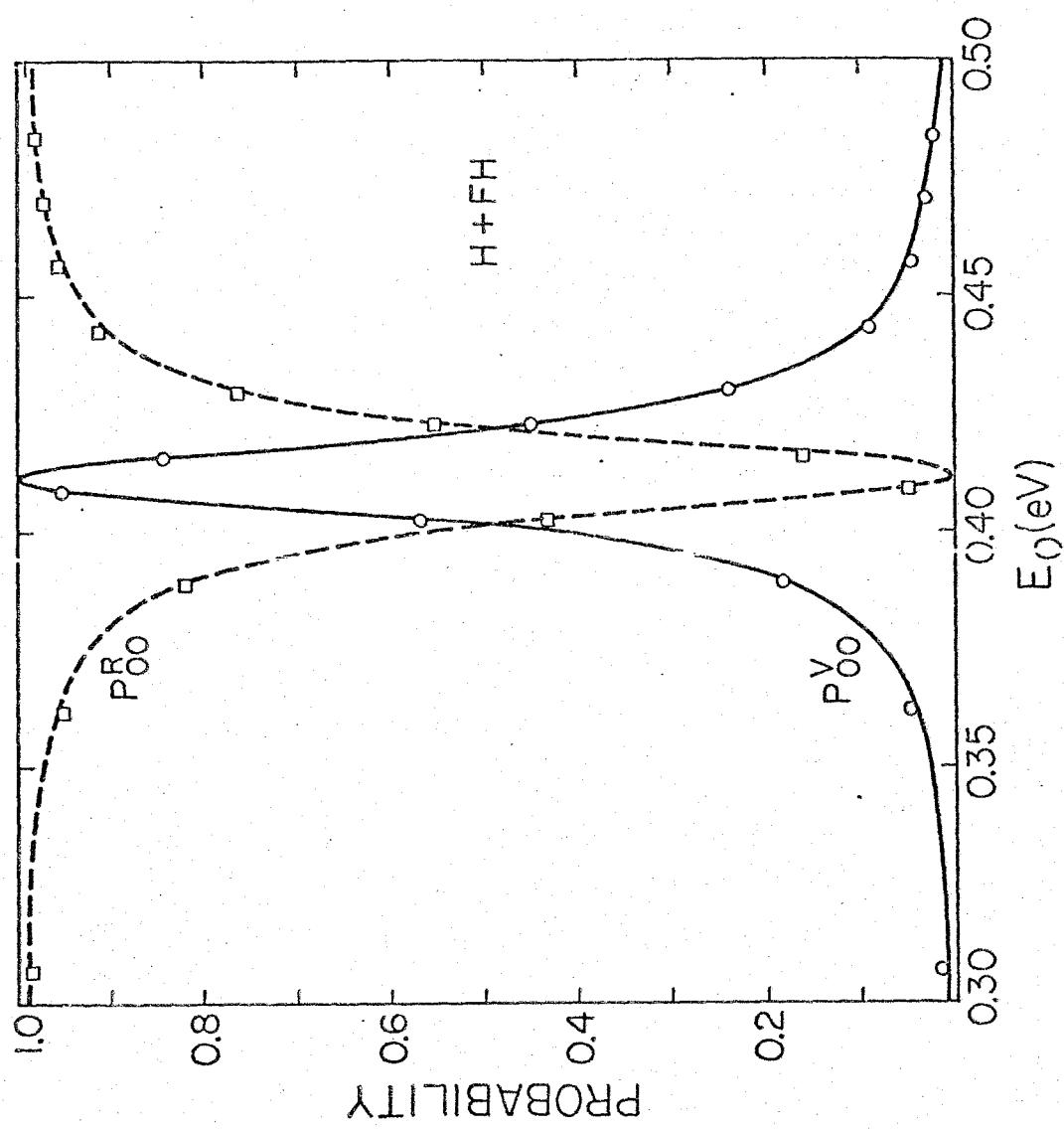
Figure 10
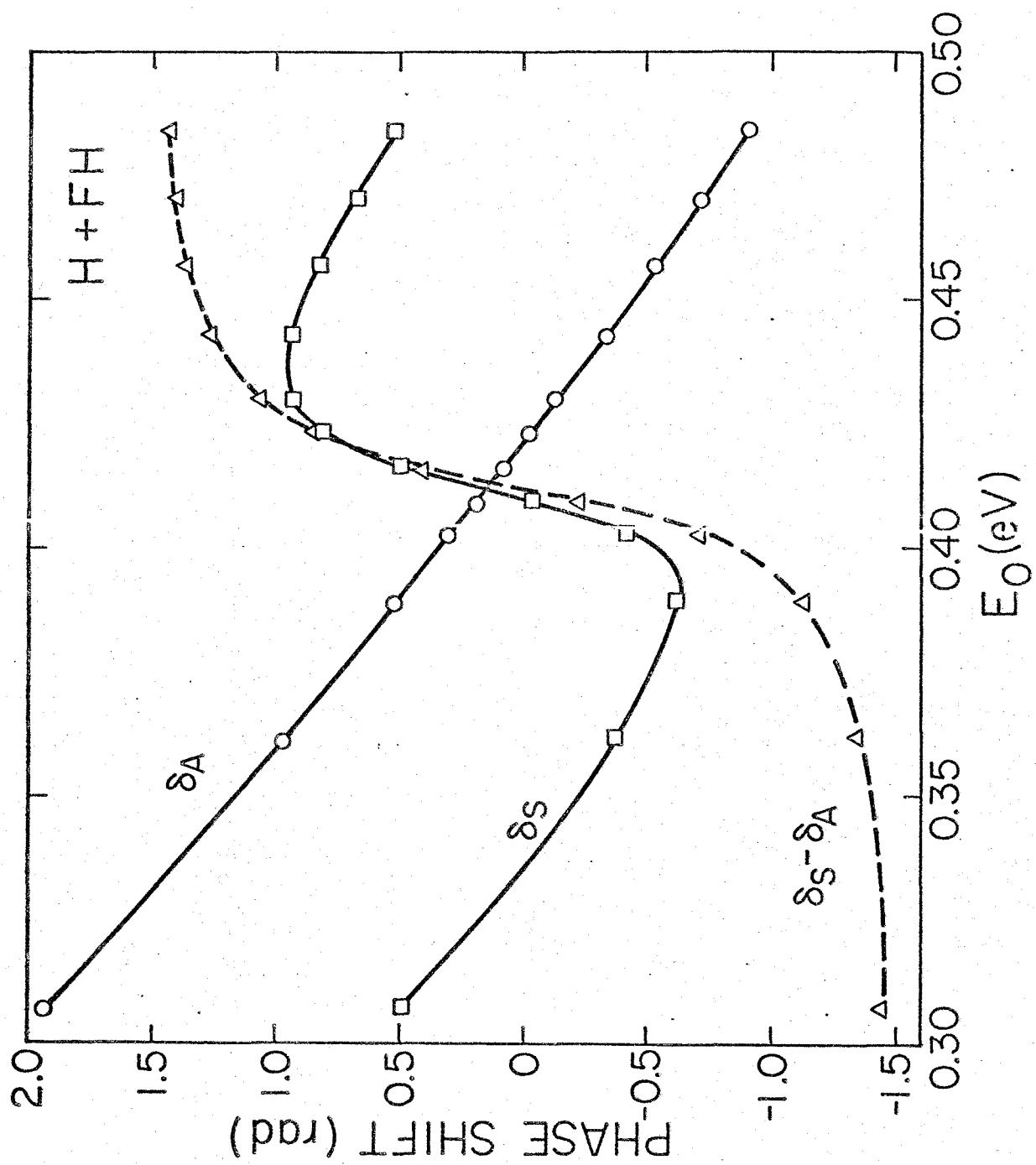
Figure 11
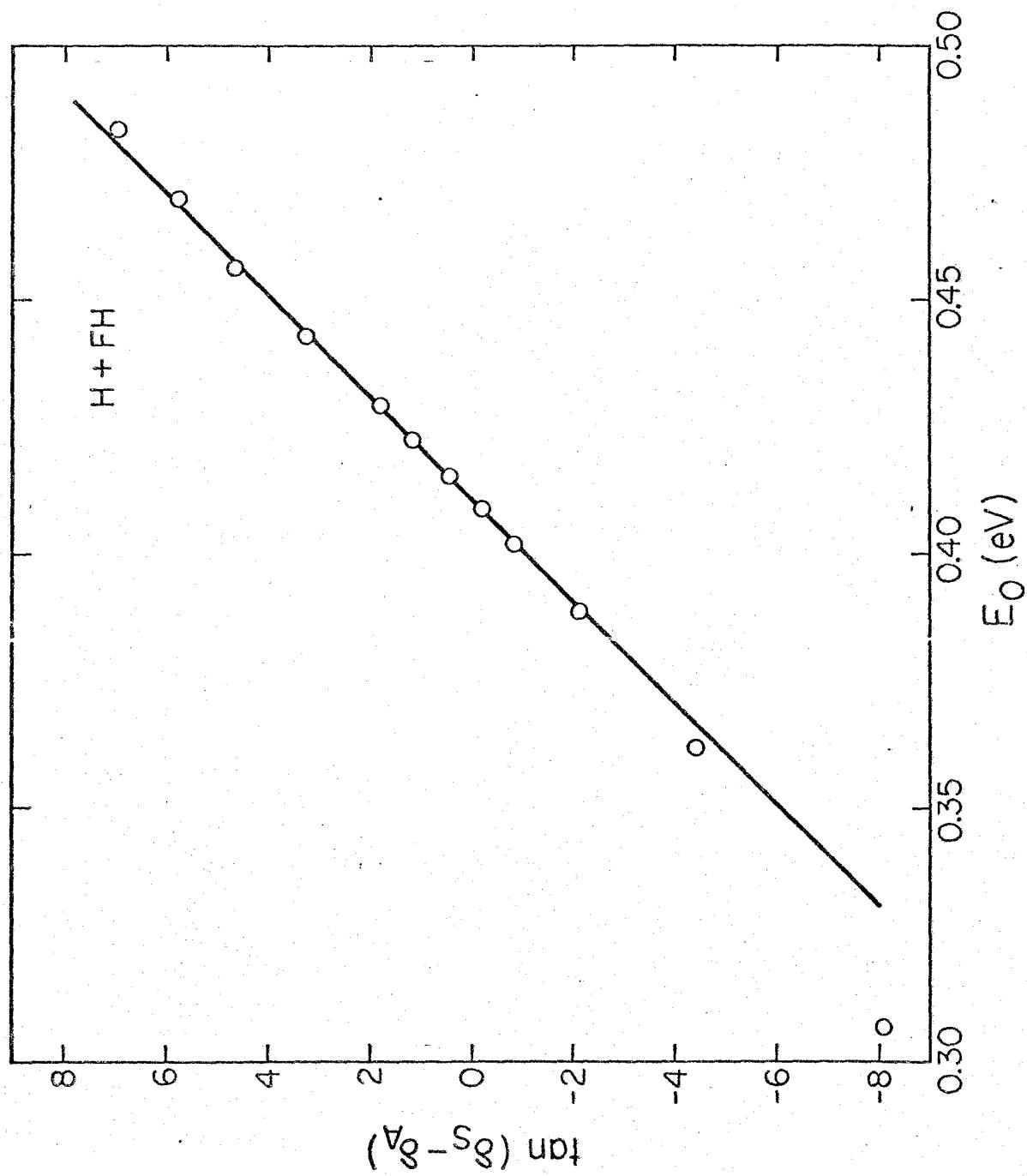
Figure 12
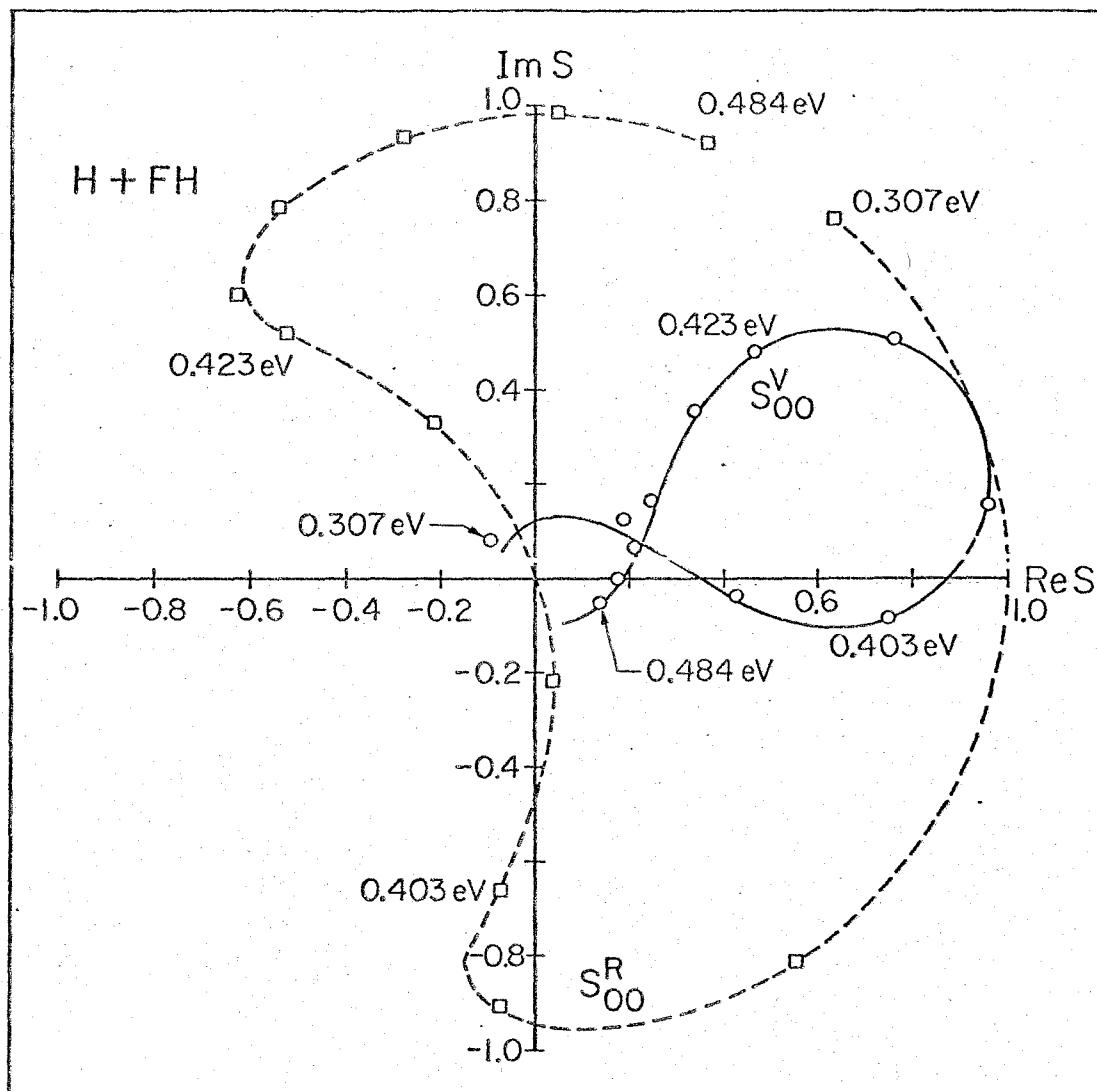
Figure 13
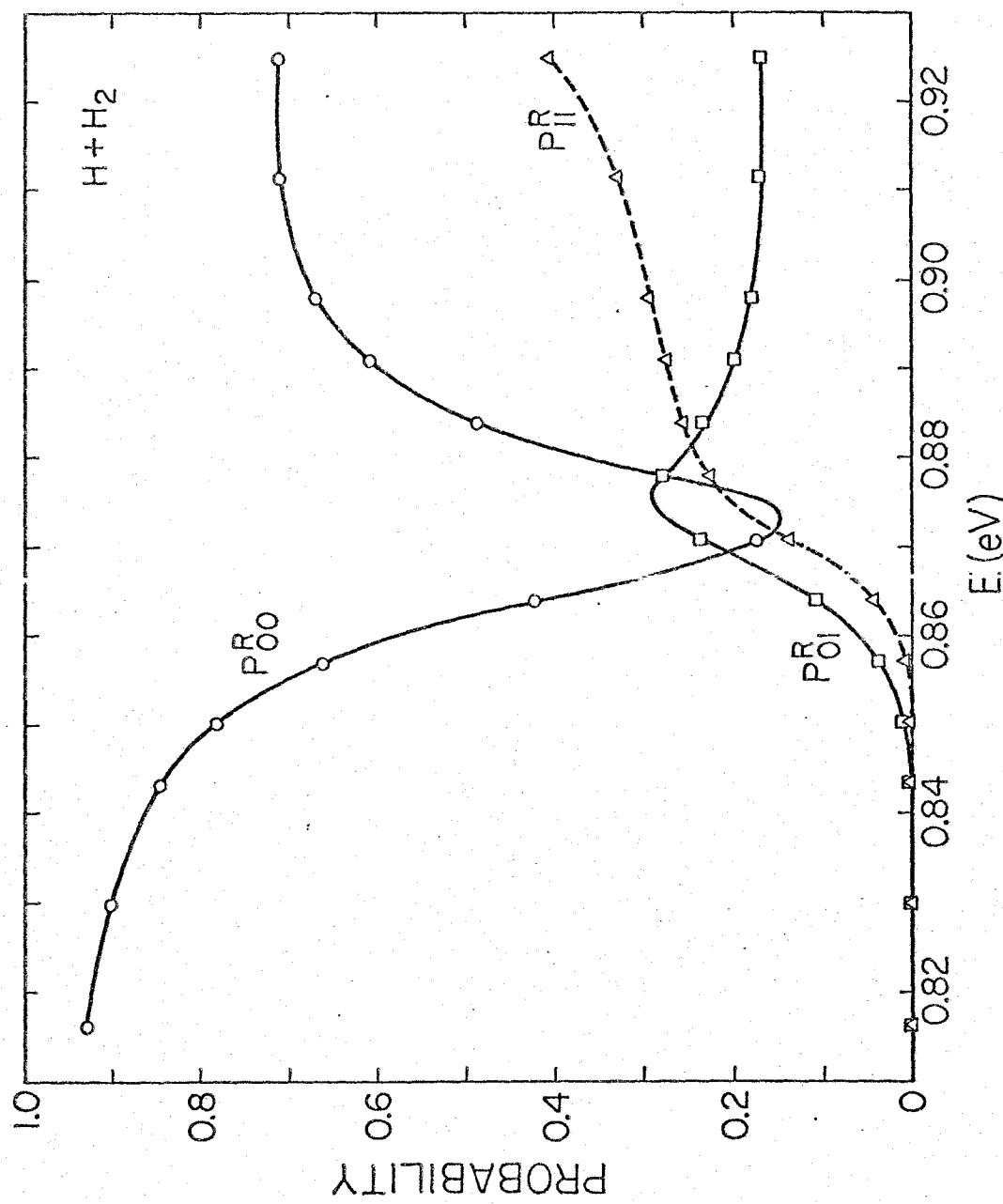
Figure 14
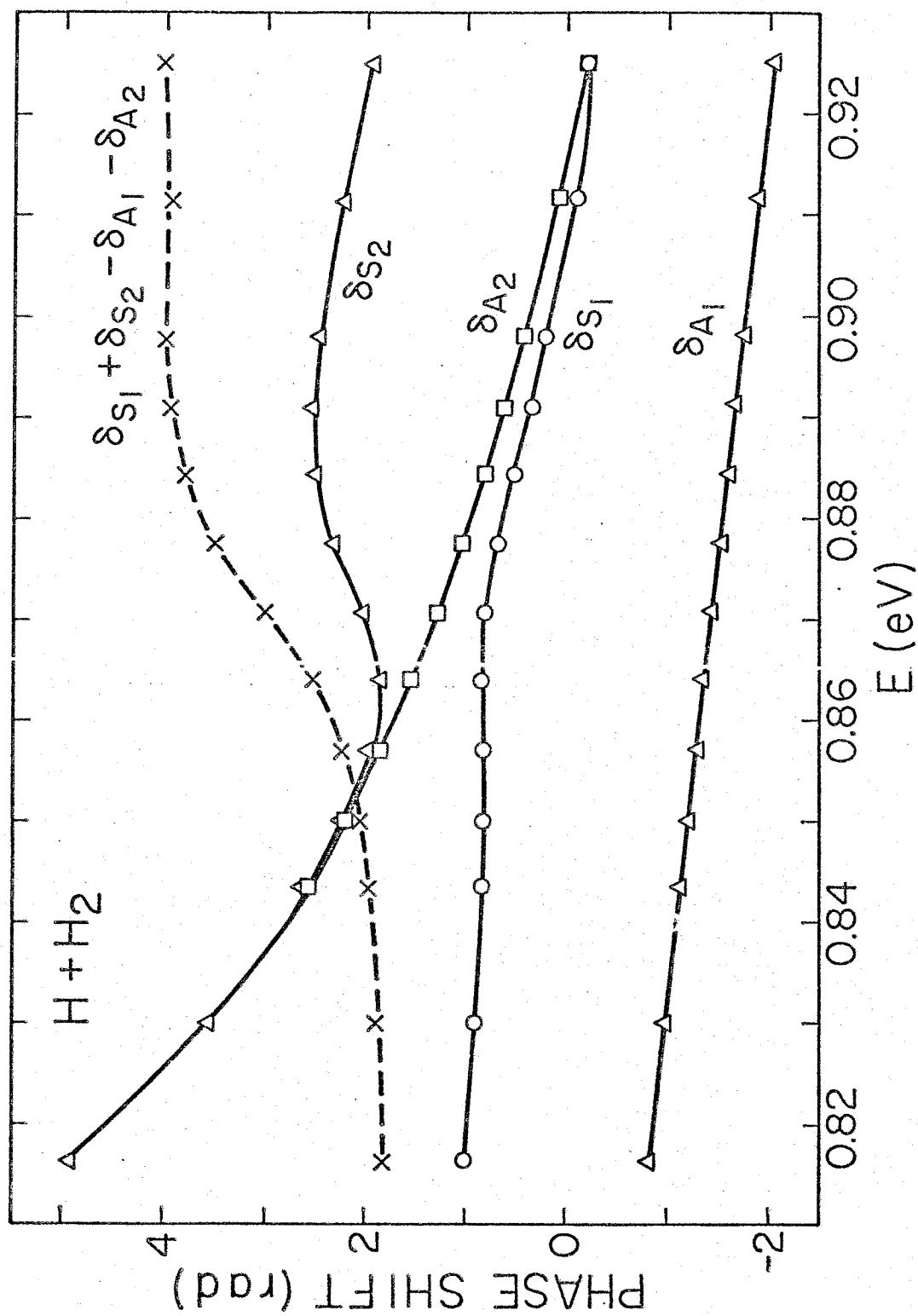
Figure 15
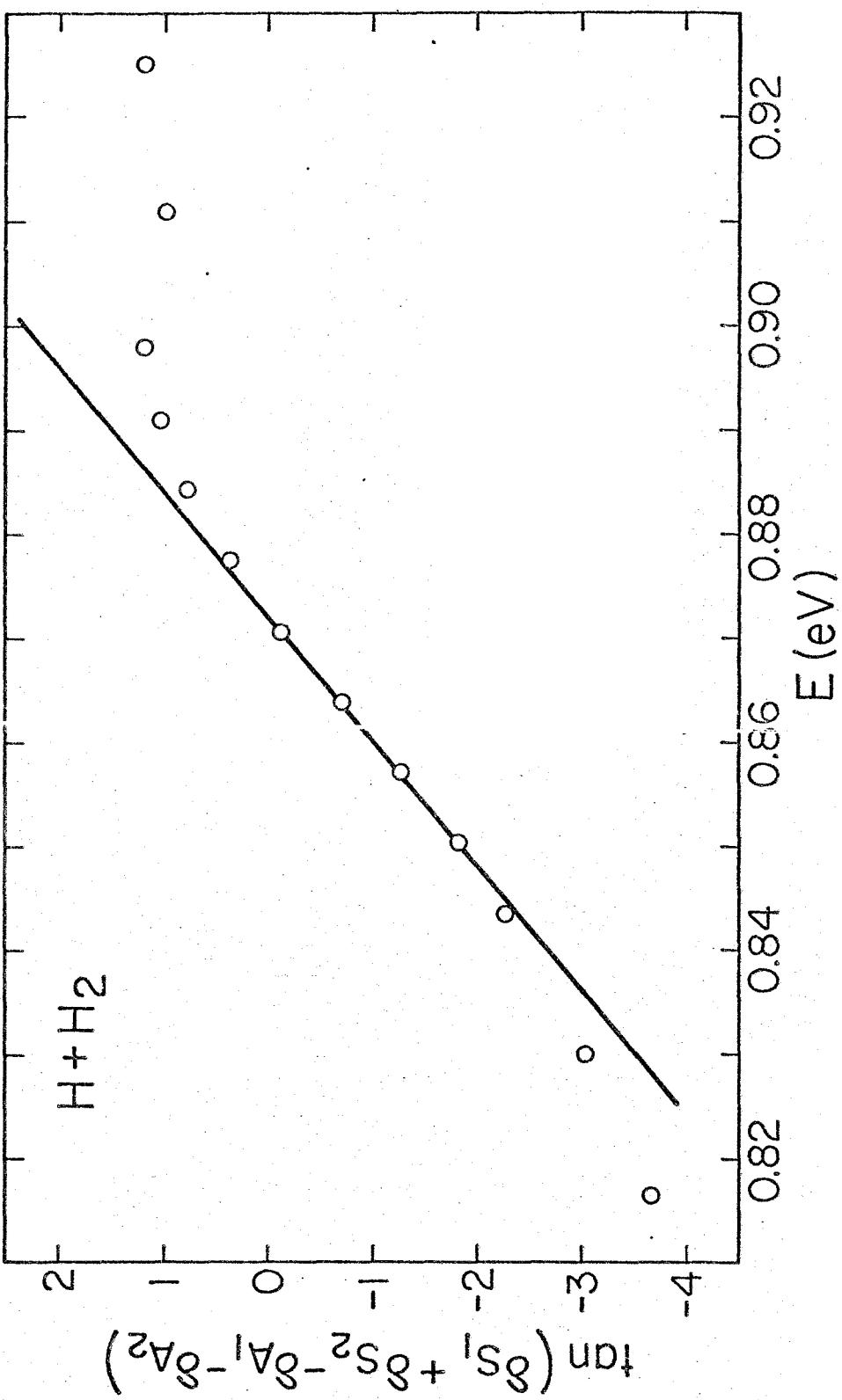
Figure 16
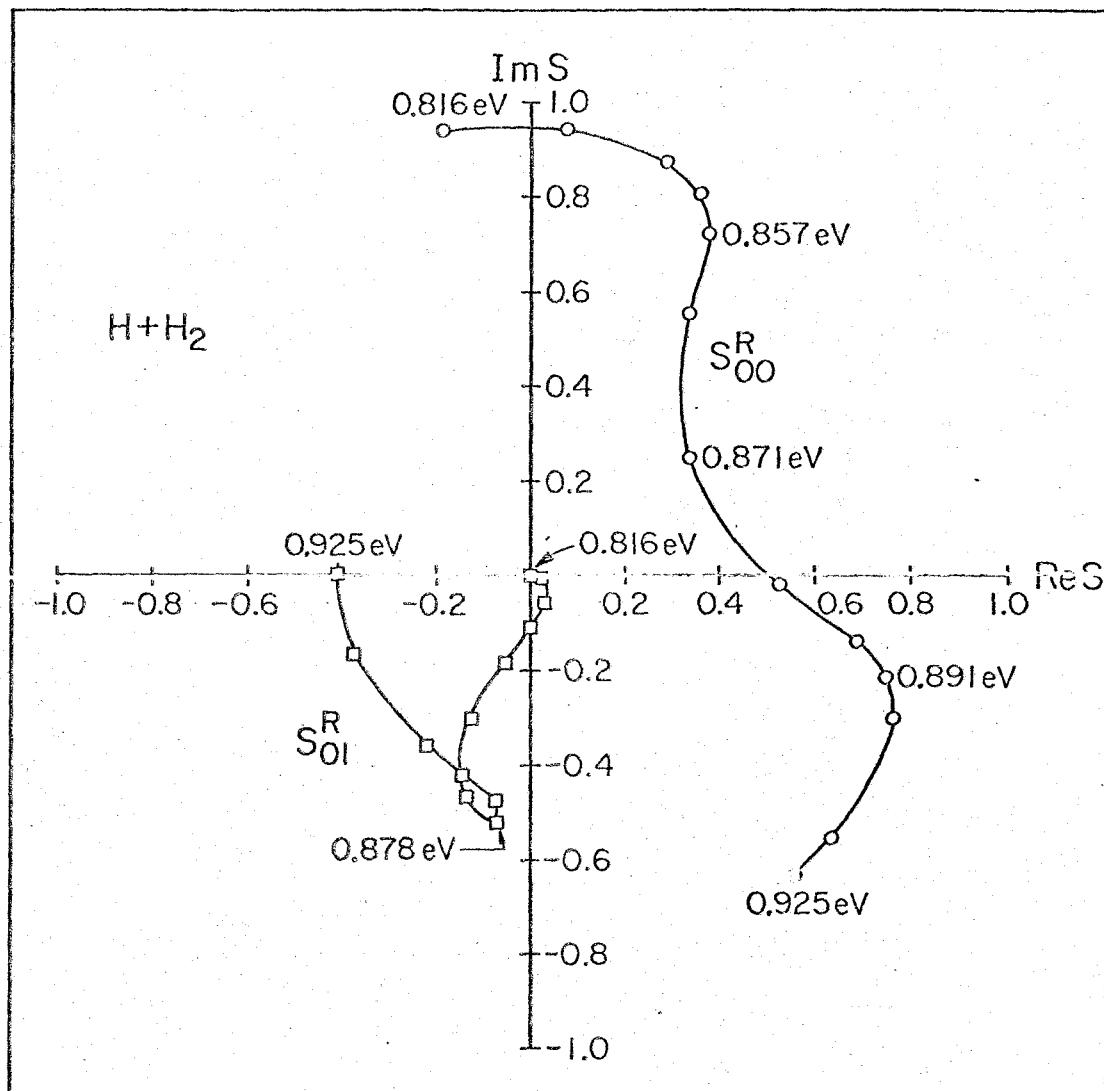
Figure 17

Figure 18

Figure 19

10. DYNAMICAL RESONANCES IN COLLINEAR, COPLANAR, AND THREE-DIMENSIONAL QUANTUM MECHANICAL REACTIVE SCATTERING

Dynamical resonances in collinear, coplanar, and three-dimensional quantum mechanical reactive scattering[*]

George C. Schatz[†] and Aron Kuppermann

Arthur Amos Noyes Laboratory of Chemical Physics,[‡]

California Institute of Technology, Pasadena, California 91125

(Received

Abstract

Results of 1D, 2D, and 3D calculations on the $H + H_2$ exchange reaction are presented which provide the first evidence for dynamical internal excitation (Feshbach) resonances in chemical reactions using noncollinear calculations. The change of the resonance energy and width with collision dimensionality and with total angular momentum is analyzed and predictions concerning its effect on cross sections for certain transitions are made.

Internal excitation resonances have been observed in a large number of diverse collision phenomena including π-p scattering,[1] electron-atom and electron-molecule scattering[2] and (theoretically) rotationally inelastic atom molecule scattering,[3] but they have yet to be detected in atom-diatom reactive scattering experiments. Their theoretical existence has previously been established theoretically only in collinear models of these simple chemical reactions.[4-8] The results of these collinear calculations indicate that they are responsible for oscillations in the reaction probabilities near the resonance energies due to their interference[8] with the direct mechanisms. However, because of angle and partial wave averaging, it was not known whether such resonances would exist in the 3-D world. We present here the results of accurate quantum mechanical calculations for one-, two-, and three-dimensional collisions for the historically important $H + H_2$ exchange reaction which provide the first evidence for dynamical resonances in chemical reactions for noncollinear systems. An understanding of the relation between the characteristics of such resonances and the nature of the potential surfaces which give rise to them may prove a sensitive probe in the experimental characterization of these surfaces and in the development and testing of approximate reaction-dynamic theories.

The methods used for solving the Schrödinger equation for the collinear, coplanar, and three-dimensional $H + H_2$ collisions are the same as those we developed and used previously.[8-11] In order to obtain accurate results in the 2-D and 3-D calculations at the relatively high energies at which the resonances were found, quite large vibration-rotation basis sets were required, involving five or six vibrations and rotational quantum numbers $j = 0 - 6$ to $j = 0 - 9$ for each vibration for a total of 60 coplanar channels (for all values of total angular momentum quantum number J), and 40 to 90 (J = 0, 1) three-dimensional channels. For most of these noncollinear calculations, tests of conservation of flux, microscopic reversibility and invariance with respect to number and choice of expansion functions indicated convergence of 5 to 10% although a few poorer results (20%) were included. The collinear results, for which ten vibrational basis functions were used, are accurate to 0.5% or better. The Porter-Karplus[12] potential energy surface was used for all calculations.

The resulting collinear, [13] coplanar, and three-dimensional reaction probabilities P^R, defined in the figure caption, are plotted as a function of the total energy E in Fig. 1. It can be seen that ————————————————————| all vibrationally elastic probabilities in Fig. 1a show a similar behavior, rising from an effective threshold energy E_{th} (the value of E for which $P^R = 0.01$) to a relatively flat plateau, and dipping later to a minimum at an energy E_r. The values of E_{th} are 0.420 eV, 0.470 eV, and 0.525 eV and of E_r are 0.873 eV, 0.922 eV, and 0.975 eV for the 1-D, 2-D, and 3-D systems, respectively. The vibrationally inelastic P^R of Fig. 1b are also analogous to one-another and display maxima at the same energies E_r for which the vibrationally elastic ones show minima. Since the dip in the 1-D $P^R_{0 \to 0}$ curve has been shown, by a time-delay analysis,[8] to be due to a Feshbach resonance, we conclude that the analogous feature for the 2-D and 3-D systems is also due to such a resonance.

Therefore, the 1-D, 2-D, and 3-D reactions have resonances centered at the values of E_r given above, with approximate widths of 0.022 eV, 0.045 eV, and 0.035 eV, respectively.

The change in resonance energy with dimensionality is almost identical to the corresponding change in the effective threshold energies and is in the 0.050 eV to 0.055 eV range for both the 1-D to 2-D and 2-D to 3-D shifts. These shifts agree with previous estimates[14] of the additional zero-point "bending" energy which must be put into the triatomic motions of the coplanar and three-dimensional transition states. This indicates that these resonances are influenced by the potential energy surface in the strong interaction region. Coplanar calculations indicate that the resonance has a significant effect only on the $J = 0 - 7$ partial waves (which appears to coincide with the range of J for which $P_{00 \to 1}^R$ (2-D) is significant), whereas non-negligible reaction probabilities $P_{00 \to 0}^R$ (2-D) are found for the wider J range $0 - 17$. No significant change of either resonance energy or width with the quantum number J was detected for the 2-D system.[15] This very important result is probably due to the dominant character of potential (rather than angular momentum) coupling in the region of strong interaction, and permits us to predict that the partial wave sum present in the expressions for the reaction cross sections will not seriously attenuate the effects of the individual partial wave resonances. From the width of the 3-D resonance we estimate a lifetime of 3.8×10^{-14} sec (corresponding approximately to 2-3 transition state symmetric stretch vibrations), about 2/3 of the 1-D lifetime.

As a result of the preceding considerations, the following qualitative predictions concerning the effect of the resonance on the reaction cross sections can be made: (a) The energy dependence of the vibrationally elastic integral reaction cross sections should show only a small dip at the resonance energy,

similar in appearance to the J = 0 reaction probabilities in Fig. 1a, but probably of smaller amplitude. (b) The vibrationally inelastic reaction cross sections should be dominated by the effects of this resonance even when averaged and summed over a distribution of rotational levels within the reagent and product vibrational manifolds, respectively. (c) The differential reaction cross sections at the resonance energies should show significant oscillations as a function of scattering angle, in contrast with the smooth behavior[11] displayed away from resonance.

We conclude, in summary, that resonances do indeed exist in noncollinear H + H_2 and can cause non-negligible quantum interference oscillations on observable reaction cross sections. Such resonances are bound to exist in other reactions also, as they have already been detected in collinear calculations for F + H_2 (D_2, HD)[16] and Cℓ + H_2.[17] Since classical trajectory methods do not include these interference effects, nor do most semiclassical[16,18] and approximate quantum methods,[19] a theoretical 3-D treatment of resonances for most other chemical reactions will require the development of better approximate techniques, and the results presented here should be valuable in this endeavor. In addition, accurate quantum mechanical results (be they 1-D, 2-D, or 3-D) can serve as a useful predictive guide in the experimental search for dynamical resonances, and it is hoped that the present paper will stimulate such a search.

REFERENCES

1. (a) R. Cool, O. Picconi, and D. Clark, Phys. Rev. 103, 1082 (1956);

    (b) R. K. Adair, Phys. Rev. 113, 338 (1959); (c) R. G. Moorhouse,

    Ann. Rev. Nucl. Sci. 19, 301 (1969).

2. (a) G. J. Schultz, Phys. Rev. Lett. 10, 104 (1963); (b) P. G. Burke,

    Adv. At. Mol. Phys. 4, 173 (1968) and references therein.

3. (a) D. A. Micha, Phys. Rev. 162, 88 (1967); (b) R. D. Levine,

    B. R. Johnson, J. T. Muckerman, and R. B. Bernstein, J. Chem.

    Phys. 49, 56 (1968).

4. (a) D. G. Truhlar and A. Kuppermann, J. Chem. Phys. 52, 3841

    (1970); (b) ibid. 56, 2232 (1972).

5. (a) R. D. Levine and S.-F. Wu, Chem. Phys. Lett. 11, 557 (1971);

    (b) S. F. Wu and R. D. Levine, Mol. Phys. 22, 881 (1971).

6. (a) D. J. Diestler, J. Chem. Phys. 54, 4547 (1971); (b) D. J. Diestler,

    D. G. Truhlar, and A. Kuppermann, Chem. Phys. Lett. 13, 1 (1972).

7. B. R. Johnson, Chem. Phys. Lett. 13, 172 (1972).

8. G. C. Schatz and A. Kuppermann, J. Chem. Phys. 59, 964 (1973).

9. A. Kuppermann, Potential Energy Surfaces in Chemistry, W. Lester,

    Ed. (University of California at Santa Cruz, 1970), pp. 121-129;

    Electronic and Atomic Collisions, VII International Conference on the

    Physics of Electronic and Atomic Collisions, Abstracts of Papers

    (North-Holland Publishing Company, Amsterdam, 1971), p. 3.

10. A. Kuppermann, G. C. Schatz, and M. Baer, J. Chem. Phys. 61,

    4362 (1974).

11. A. Kuppermann and G. C. Schatz, J. Chem. Phys. 62, 2502 (1975).

12. R. N. Porter and M. Karplus, J. Chem. Phys. 40, 1105 (1964).

13. These results are essentially identical to those of Ref. 3a.

14. A. B. Elkowitz and R. E. Wyatt, J. Chem. Phys., 62, 3683 (1975).

15. Accurate 3-D calculations for J > 0 in the neighborhood of the resonance are very difficult to perform because of the large number of basis functions required in the close-coupling expansion. We do however have some preliminary 3-D J > 0 results which are in agreement with the italicized statement about the 2-D system.

16. G. C. Schatz, J. M. Bowman, and A. Kuppermann, J. Chem. Phys., in press.

17. M. Baer, Mol. Phys. 27, 1429 (1974).

18. J. M. Bowman and A. Kuppermann, J. Chem. Phys. 59, 6524 (1973); for a counter-example, see J. R. Stine and R. A. Marcus, Chem. Phys. Lett. 29, 575 (1974).

19. For example, the distorted wave method [K. T. Tang and M. Karplus, Phys. Rev. A 4, 1844 (1971)] and the one vibrational basis function method [G. Wolken and M. Karplus, J. Chem. Phys. 60, 351 (1974)].

FIGURE CAPTION

Figure 1:

Collinear (1-D), coplanar (2-D), and three-dimensional (3-D) reaction probabilities for the H + H_2 exchange reaction as a function of the total energy E and relative translational energy E_0. $P_{0 \to 0}^R$ and $P_{0 \to 1}^R$ are the collinear reaction probabilities from v = 0 of the reagent H_2 to v' = 0 and v' = 1, respectively, of the product H_2. $P_{00 \to 0}^R$ and $P_{00 \to 1}^R$ are the 2-D or 3-D (as specified) reaction probabilities for the total angular momentum J = 0 partial wave from v = 0, j = 0 of the reagent H_2 to v' = 0 and v' = 1, respectively, of the product H_2 summed over all product rotational states within a given vibrational manifold. Panel (a) curves are used to denote vibrationally elastic reaction probabilities while panel (b) denote vibrationally inelastic ones. The points actually computed are indicated on the curves by geometrical symbols. Arrow in abscissa indicates the energy at which the v = 1 state of H_2 becomes accessible.
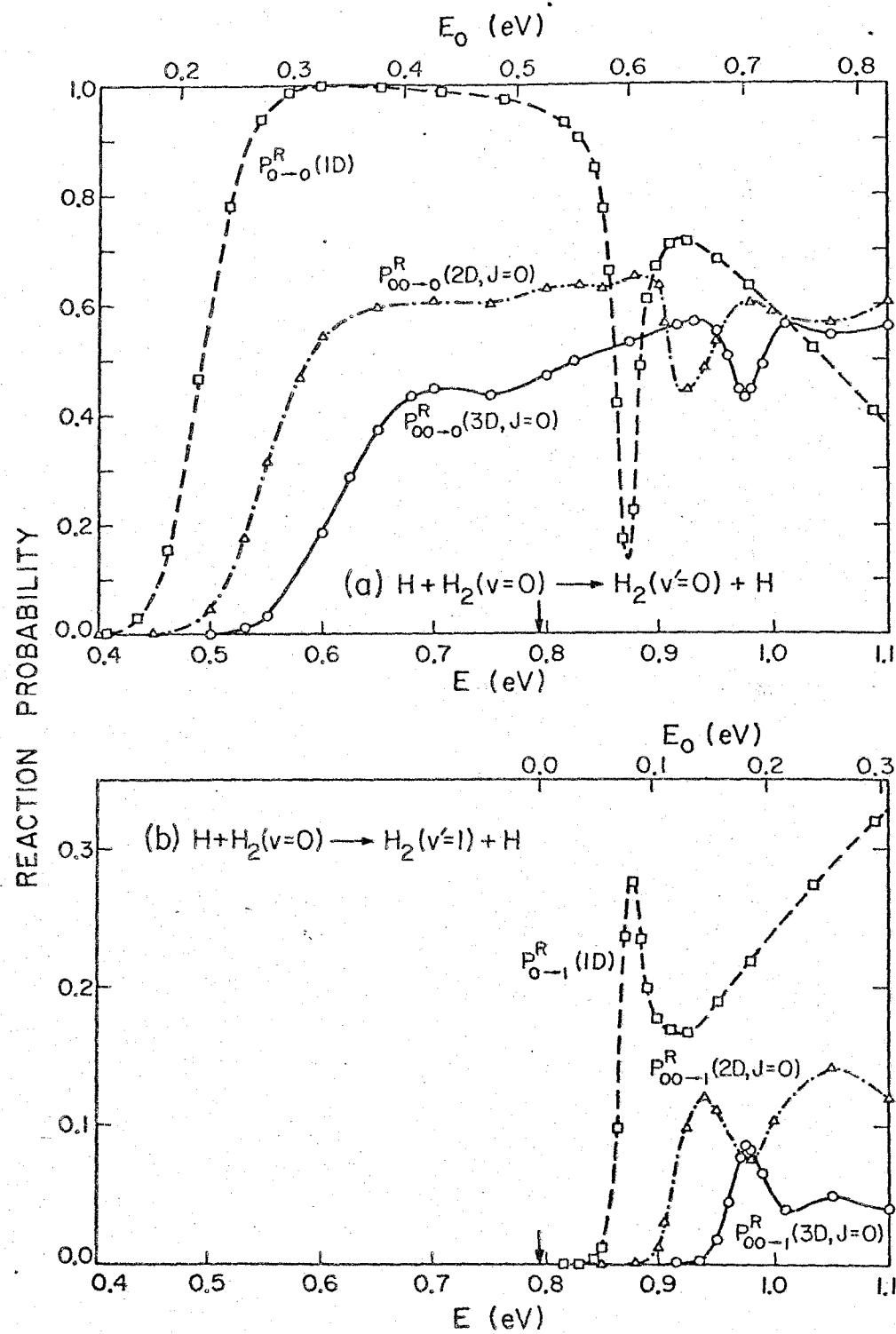
Figure 1

PROPOSITION I

Abstract

A method for applying sudden (or strong coupling) approximations to reactive collisions is proposed. The method seeks to uncouple or partially uncouple the rotational and/or vibrational degrees of freedom by exactly diagonalizing the Schrödinger equation in the regions of strongest potential coupling. For many applications, this region is the transition state of the reaction, and if one simultaneously performs the arrangement channel transformations at that point, a completely diagonalized arrangement channel transformation is achieved. Recoupling is then accomplished in the evaluation of the scattering matrix. The method is, however, more general and may be applied in situations where computational convenience requires different uncoupling transformations in different arrangement channels. Because the number of coupled channels is substantially reduced by this method, a reduction in computation time by several orders of magnitude is possible, so we may apply it to a wide variety of atom-diatom and diatom-diatom systems including many for which more accurate procedures are currently impossible.

In several recent papers[1-3], sudden (or strong coupling) approximations have been used quite successfully in nonreactive atom-diatom rotational excitation problems. In these systems, the potential coupling is strong in comparison with differences in energy between rotational levels, and is responsible for significant probabilities for large Δj transitions. This is an ideal situation for using rotational sudden approximations, in which these differences are neglected in order to uncouple the coupled Schrödinger equations describing the collision. In many respects, the situation for reactive scattering should be even more suited to the use of sudden approximations. This is because the potential coupling is usually more significant for reactive encounters, where there is often a severe steric restriction on reactive geometries. The results of accurate 3D calculations[4,5] on the $H + H_2$ reaction support this contention in two respects. First, the distribution of product rotational states is temperature-like (with the same temperature parameter for all initial rotational states) even though the reaction mechanism is predominantly direct.[6] This indicates a lack of correlation between the product rotational distributions and the initial state involved. Such an effect is very likely a consequence of the strong coupling. Second, the neglect of angular momentum coupling in comparison with potential coupling (the tumbling decoupling approximation) proves to be reasonably accurate for reactive collisions even when it is not accurate for inelastic nonreactive ones. In light of these observations, we believe that sudden approximations (if properly used) should prove to be accurate approximate techniques for reactive systems. The primary advantage of this method is the significant decrease in computational effort possible. The precise

amount of reduction in time depends on the degree of uncoupling desired, but for the usual situation in which rotations and projections are uncoupled while vibrations are not (as described below), the number of coupled channels needed for convergence at 0.50 eV for H + H_2[4] changes from 100 to 4 or 5. For rotationally inelastic scattering, reductions in computation time by a factor of 9,000 have been reported for the Ar + TlF and Ar + N_2 systems.[1] In addition, the procedure may be generalized to more complicated reactions, such as H_2 + H_2, which are not currently feasible with more accurate quantum methods.

Let us now describe the general approach to sudden approximations for reactive atom diatom systems. The fully coupled body fixed Schrödinger equation for each partial wave J in each arrangement channel region is (See Ref. 5 for definitions of terms)

$$\frac{d^2 g_{J}^{\lambda}}{dR_{\lambda}^2} + (K_{\lambda}^2 - U_{cJ} - U_{p}) g_{J}^{\lambda} = 0 \tag{I.1}$$

where the full wave function Ψ_{JM} has been expanded as

$$\Psi_{JM}(r_{\lambda}, R_{\lambda}) = \sum_{v_{\lambda} j_{\lambda} \Omega_{\lambda}} D_{M\Omega_{\lambda}}^{J}(\phi_{\lambda}, \theta_{\lambda}, 0) Y_{j_{\lambda}\Omega_{\lambda}}(\gamma_{\lambda}, \psi_{\lambda}) \frac{\phi_{v_{\lambda} j_{\lambda}}}{r_{\lambda} R_{\lambda}} g_{Jv_{\lambda} j_{\lambda} \Omega_{\lambda}}^{\lambda}(R_{\lambda}) \tag{I.2}$$

and

$$(K_{\lambda}^2)_{t_{\lambda}}^{t_{\lambda}'} = \delta_{t_{\lambda}}^{t_{\lambda}'} k_{v_{\lambda} j_{\lambda}}^{\lambda} \tag{I.3}$$

$$(\underset{\approx}{U}_{cJ})_{t_\lambda}^{t_\lambda'} = \frac{\delta_{v_\lambda j_\lambda}^{v_\lambda' j_\lambda'}}{R_\lambda^2} \left\{ \delta_{\Omega_\lambda \Omega_\lambda'} [J(J+1) - 2\Omega_\lambda^2 + j_\lambda(j_\lambda+1)] \right.$$

<div align="right">(I.4)</div>

$$-\xi_+(J,\Omega_\lambda)\xi_+(j_\lambda,\Omega_\lambda)\delta_{\Omega_\lambda+1,\Omega_\lambda'} - \xi_-(J,\Omega_\lambda)\xi_-(j_\lambda,\Omega_\lambda)\delta_{\Omega_\lambda-1,\Omega_\lambda'}$$

$$\xi_\pm(J,\Omega_\lambda) = (J(J+1) - \Omega_\lambda(\Omega_\lambda \pm 1))^{\frac{1}{2}} \qquad \text{(I.5)}$$

and

$$(\underset{\approx}{U}_p)_{t_\lambda}^{t_\lambda'} = -\frac{2\mu}{\hbar^2}\, \delta_{\Omega_\lambda \Omega_\lambda'}\, \langle v_\lambda j_\lambda \Omega_\lambda | V(r_\lambda, R_\lambda, \gamma_\lambda) - v_\lambda(r_\lambda) | v_\lambda' j_\lambda' \Omega_\lambda \rangle \qquad \text{(I.6)}$$

The abbreviation t_λ has been used for $(v_\lambda j_\lambda \Omega_\lambda)$. The vibration rotation functions $\phi_{v_\lambda j_\lambda}(r_\lambda) Y_{j_\lambda \Omega_\lambda}(\gamma_\lambda, \psi_\lambda)$ are eigenfunctions of the asymptotic reference potential $v_\lambda(r_\lambda)$ and should be used in evaluating Eq. I.5. It is important to note that $\underset{\approx}{K}_\lambda^2$ is a diagonal wave number matrix, $\underset{\approx}{U}_{cJ}$ is a tridiagonal (in the tumbling quantum number Ω_λ) centrifugal coupling matrix and $\underset{\approx}{U}_p$ is the potential matrix (which is diagonal in Ω_λ). In solving Eq. I.1, one must generally reexpand Ψ_{JM} in terms of a locally adiabatic vibration rotation basis in order to obtain an efficient representation of the wave function in the interaction region.[5,7] To solve the reactive problem exactly, we must propagate Eq. I.1 through each of the three arrangement channel regions (for a two path reaction) and then match the wave functions at the mutual boundaries of these regions. The z axis of quantization may be changed smoothly during the propagation[7] or abruptly at the matching boundary.[5]

To make a sudden approximation, we must assume that the off diagonal elements of $\underset{\approx}{U}_p$ are large compared to the differences in wave numbers, and in comparison to centrifugal coupling for R_λ where the interactions are strong and transitions are occurring. This may be done

on three different levels of approximation as follows: Case I - The approximation is assumed for all degrees of freedom--vibrations, rotations and projections, and all are uncoupled; Case II - Only rotations and projections are uncoupled; Case III - Only projections are uncoupled. At collision energies of 1 eV or less, Case I will not be an accurate approximation because the vibrational spacings are generally large. Cases II and III should be quite accurate however, for the rotational spacings are small for the low j_λ's which are important in reactive collisions, and the j_λ dependence of the centrifugal terms is usually much less important than potential coupling. Case III is very similar to the tumbling decoupling approximations which have been discussed elsewhere.[5] We shall continue our discussion with Case II. Modifications necessary for Cases I and III will be stated explicitly where they are not obvious. If the differences between wave numbers within each vibrational manifold are negligible, then we can set all wave numbers $k_{v_\lambda j_\lambda}$ equal to $k_{v_\lambda \bar{j}_\lambda}$ where $\bar{j}_\lambda$ may be chosen as the initial state wave number, although other choices are possible.[3] We then neglect the off diagonal elements of $\underset{\approx}{U}_{cJ}$, and set j_λ and Ω_λ in the diagonal part of that matrix (Eq. I.4) equal to $\bar{j}_\lambda$ and $\bar{\Omega}_\lambda$. This makes $\underset{\approx}{U}_{cJ}$ a multiple of the identity matrix. The final step in the approximation involves the transformation to a "diagonalized representation" with the aid of a constant unitary matrix $\underset{\approx}{M}_\lambda$ to be defined below. We set

$$g_{\underset{\approx}{\sim}J}^\lambda = \underset{\approx}{\tilde{M}}_\lambda \, \underset{\approx}{h}_{J}^\lambda \, \underset{\approx}{M}_\lambda \tag{I.6}$$

$$\overline{\underset{\approx}{U}}_p = \underset{\approx}{M}_\lambda \, \underset{\approx}{U}_p \, \underset{\approx}{\tilde{M}}_\lambda \tag{I.7}$$

and substitute into Eq. I.1 (as modified by the above approximations),

obtaining

$$\frac{d^2 h_{\approx J}^\lambda}{dR_\lambda^2} + (M_{\approx\lambda} K_{\approx\lambda}^2 \tilde{M}_{\approx\lambda} - M_{\approx\lambda} U_{\approx cJ} M_{\approx\lambda} - \bar{U}_{\approx p}) h_{\approx J}^\lambda = 0 \qquad (I.8)$$

In order to retain the proper asymptotic solutions,[1] we must (for case II) choose $M_{\approx\lambda}$ to be diagonal in v_λ so that it commutes with $K_{\approx\lambda}^2$. $M_{\approx\lambda}$ will also commute with $U_{\approx cJ}$ since we have simplified it to be proportional to the identity matrix. Finally, our choice of $M_{\approx\lambda}$ given below will be such that we should be able to neglect the elements of $\bar{U}_{\approx p}$ which are off diagonal in j_λ and Ω_λ. We are finally left with a set of equations for each $j_\lambda, \Omega_\lambda$ which are coupled only in v_λ and may be solved by standard collinear reactive methods.[9]

$M_{\approx\lambda}$ is chosen so as to diagonalize the Hamiltonian along a suitably chosen surface in the strong interaction region. Our intent in doing so is to treat the potential coupling exactly in the region where that coupling is most important. Precisely where that region is cannot be determined in general without an adiabatic analysis of the full scattering solution, but for reactive systems with an activation energy having a restricted range of allowed transition state (or saddle point) geometries, a very logical choice for this region is the transition state. Some support for this statement may be seen in a vibrationally adiabatic analysis of the $H + H_2$ collinear scattering wave function.[11] In that case, the most strongly nonadiabatic behavior was found near the transition state. We would expect that a rotationally adiabatic analysis of 3D results would give similar conclusions. Accordingly, we choose a surface perpendicular to the reaction coordinate which passes through the transition state, and diagonalize the Hamiltonian there. The rows

of the matrix $\underset{\approx\lambda}{M}$ are composed of the projections of the surface eigenfunctions on the asymptotic vibration rotation states. In an application of Case II, we must determine the vibrational eigenfunctions appropriate to the most stable geometry at the transition state before diagonalizing the rotational potential (obtained by averaging the full transition state potential separately over each vibrational eigenfunction). This procedure leads to a matrix $\underset{\approx\lambda}{M}$ which is diagonal in the vibrational quantum number v_λ. For a two path reaction, there will generally be a transition state for reaction to either of the two product arrangement channels. Both of these transition states must simultaneously be considered in the diagonalization of the interaction potential. With some cleverness, the surface functions of any transition state geometry can be determined and their projections on the asymptotic solutions calculated. In all cases, a normal mode analysis of the transition state can be performed and a harmonic approximation set of surface eigenfunctions obtained. If it is desirable to switch to locally adiabatic vibrational functions during the propagation, we can construct an $\underset{\approx\lambda}{M}$ for these adiabatic functions by simply taking their overlap with the transition state surface functions. Note that we are free to diagonalize either the full Hamiltonian at the transition state, or the approximate one obtained after simplifying $\underset{\approx\lambda}{K}^2$ and $\underset{\approx cJ}{U}$ as described above.

With the Schrödinger equation partially (Cases II and III) or fully (Case I) uncoupled, we now integrate the resulting differential equations in each arrangement channel region λ. At the completion of these integrations, the different arrangement channel solutions may be smoothly matched to one another in one of the following two ways.

First, if the same transition state surfaces and surface eigenfunctions are used in defining the $\underset{\approx}{M}_\lambda$ matrices for all arrangement channels, then the uncoupled solutions may be matched directly. Indeed, if the transition state surfaces and matching surfaces are identical, if locally adiabatic vibrational functions are used for the propagation (Case II), and if a floating z axis of quantization is used[7], then the matching simply amounts to a reorganization of solutions and may be done analytically. Second, if different transition state surface eigenfunctions are chosen in different arrangement channels, then the matching must be done with the fully coupled $\underset{\approx}{g}_J^\lambda$ solutions which may be calculated from Eq. I.6. In this second case, the procedure for obtaining the scattering matrix, and hence cross sections is identical to the exact procedure[5] for all steps following the conversion of the matched and asymptotic uncoupled $\underset{\approx}{h}_J^\lambda$ solutions to the coupled $\underset{\approx}{g}_J^\lambda$ solutions. A somewhat more efficient computational procedure seems to be the first matching method, since in that case, a recoupling of the uncoupled solutions may be postponed until the final scattering matrix is calculated, and this last step involves the simple evaluation of:

$$\underset{\approx}{S}_J^{\nu\lambda} = \underset{\approx}{\tilde{M}}_\nu \; \underset{\approx}{\overline{S}}_J^{\nu\lambda} \; \underset{\approx}{M}_\lambda \tag{I.9}$$

where $\underset{\approx}{\overline{S}}_J^{\nu\lambda}$ is the uncoupled subblock of the scattering matrix between arrangement channels ν and λ $(\lambda, \nu = \alpha, \beta, \gamma)$, $\underset{\approx}{S}_J^{\nu\lambda}$ is the coupled one, and $\underset{\approx}{M}_\lambda$ and $\underset{\approx}{M}_\nu$ are the appropriate transformation matrices in channels λ and ν, respectively. We should point out here that this approximation may be applied to a variety of reactive systems which are essentially

impossible to treat at present by accurate methods. These include atom-diatom reactions which have a saddle point geometry in which the diatom internuclear vector is perpendicular to the vector between the atom and the center of mass of the diatom. One reaction path atom-diatom reactions are easily treated, and the comparison between the results of such an application and that of a two path reaction should be important in distinguishing the differences in rotational distributions. Finally, this approximation should also be able to treat diatom-diatom reactions such as $H_2 + H_2$. The major obstacle to accurately treating this system, namely the large number of coupled channels involved, is eliminated by this procedure, and the only remaining problem is the development of locally adiabatic coordinates which provide a framework in which a noncoupling arrangement channel matching can be accomplished. If this can be done, then the problem can be solved a single channel at a time up to the point of calculating the full scattering matrix which requires the evaluation of Eq. I.9.

References

1. R. T. Pack, J. Chem. Phys. $\underset{\sim}{60}$, 633 (1974).

2. D. Secrest, J. Chem. Phys. $\underset{\sim}{62}$, 710 (1975).

3. T. P. Tsien, G. A. Parker and R. T. Pack, J. Chem. Phys. $\underset{\sim}{59}$, 5373 (1973); T. P. Tsien and R. T. Pack, Chem. Phys. Lett. $\underset{\sim}{6}$, 54, 400 (1970); ibid., $\underset{\sim}{8}$, 579 (1971); R. T. Pack, Chem. Phys. Lett. $\underset{\sim}{14}$, 393 (1972).

4. A. Kuppermann and G. C. Schatz, J. Chem. Phys. $\underset{\sim}{62}$, 2502 (1975).

5. G. C. Schatz and A. Kuppermann, J. Chem. Phys., in preparation. See also Ref. 8.

6. M. Karplus, R. N. Porter and R. D. Sharma, J. Chem. Phys. $\underset{\sim}{43}$, 3259 (1965).

7. R. E. Wyatt, J. Chem. Phys. $\underset{\sim}{56}$, 390 (1972); A. B. Elkowitz and R. E. Wyatt, J. Chem. Phys. $\underset{\sim}{63}$, 702 (1975).

8. G. C. Schatz, Ph. D. thesis, California Institute of Technology, unpublished, 1975.

9. See, for example, D. G. Truhlar and A. Kuppermann, J. Chem. Phys. $\underset{\sim}{56}$, 2232 (1972), and references therein.

PROPOSITION II

Abstract

A method for using pseudo-diffraction functions in close coupling expansions for atom surface elastic scattering is proposed and its application to the study of the diffraction of He off tungsten and tungsten carbide surfaces is suggested. The main advantage of pseudo-diffraction states is that this basis allows for a more efficient representation of the local behavior of the wave function parallel to the surface. As such, it should enable a reduction in the number of diffraction channels needed and it should allow for the treatment of highly anisotropic crystal surfaces, including chemically reactive ones and those where diffusion is important. The application to He + tungsten (112) and He + tungsten carbide (W(110)R(3x5)) surfaces is proposed as a means for elucidating the factors which cause these two systems to exhibit diffraction when other tungsten and tungsten carbide surfaces do not. Certain questions concerning the remarkable coherence of the diffracted beam in the He + tungsten carbide experiments will also be considered.

In recent years, experimental advancements in beam surface
scattering techniques have rendered diffraction scattering a sensitive
probe of the atom surface interaction potential.[1] To theoretically
describe these collision processes, quantum[2-4], semiclassical[5] and
classical[6] techniques appropriate to the atom surface problem have
been developed. The quantum methods usually involve a close coupling
expansion in terms of the "unperturbed" diffraction states (as will be
defined below). This is adequate in situations where the surface
anisotropy is weak so the number of states coupled is small. It is well
established[2], however, that the coupling is often quite strong, and
the use of close coupling expansions requires a large number ($>$ 30)
of open and closed channels for convergence of the probabilities for
diffractive and specular scattering. By analogy with atom molecule
inelastic and reactive scattering, we propose to use locally "adiabatic"
pseudo-diffraction states for these close coupling expansions. This
procedure has been quite useful in reducing the number of required
closed channels in atom molecule scattering[7] and we expect that the
same will be true in atom surface scattering since the physical pheno-
menon is very analogous. By using pseudo-states in surface scattering,
we may also be able to examine surface reactions, chemisorption, and
diffusion processes well. We shall describe below a method for
numerically obtaining these states and will include a simple example
to illustrate the procedure. In the second part of this proposition,
we consider the application of this close coupling method to He + tungsten
and He + tungsten carbide diffraction. These two systems have been
well characterized experimentally[8-9] and many features of the diffraction

patterns differ substantially from those in the well-studied He + LiF[10] system. An understanding of these differences in terms of the nature of the interaction potential involved should be useful in characterizing the structures of the surfaces.

We consider the elastic collision of an atom with a solid crystalline surface. The atoms in the crystal are not allowed to exchange energy with the incident particle and hence their sole purpose is to define the interaction potential $V(\underset{\sim}{r})$. $\underset{\sim}{r} = (x, y, z)$ specifies the coordinates of the incident atom with the z direction normal to the surface and directed away from the crystal. Inclusion of dissipative processes[11] or molecule plus surface collisions[12] has been treated elsewhere and is done in an analogous way in the present method.

The Schrödinger equation is

$$\left(- \frac{\hbar^2}{2\mu} \nabla_{\underset{\sim}{r}}^2 + V(\underset{\sim}{r})\right) \Psi(\underset{\sim}{r}) = \frac{\hbar^2 k^2}{2\mu} \Psi(\underset{\sim}{r}) \qquad (\text{II.1})$$

The full wave vector $\underset{\sim}{k}$ is divided into a z component k_z and an x, y vector $\underset{\sim}{K}$. These components are determined by the direction of the incident wave. In elastic scattering, the incident wave number $\underset{\sim}{k} = (k_z, \underset{\sim}{K})$ is changed (upon interaction between atom and crystal) to $\underset{\sim}{k}'_{mn} = (k_z^{mn}, \underset{\sim}{K} + \underset{\sim}{G}_{mn})$ where $\underset{\sim}{G}_{mn}$ is a reciprocal lattice vector and $k_z^{mn} = (k^2 - (\underset{\sim}{K} + \underset{\sim}{G}_{mn})^2)^{\frac{1}{2}}$. For nonzero $\underset{\sim}{G}_{mn}$, we say that diffraction has occurred, and our scattering problem consists of finding the probabilities of diffraction into states having different indices m and n. The diffraction "states" are given by $\exp i(\underset{\sim}{K} + \underset{\sim}{G}_{mn}) \cdot \underset{\sim}{R}$ with $\underset{\sim}{R} = (x, y)$. Rather than expand $\Psi(\underset{\sim}{r})$ in terms of $\exp i(\underset{\sim}{K} + \underset{\sim}{G}_{mn}) \cdot \underset{\sim}{R}$ for all z (as has always been done previously[2-4]), we expand it instead in terms

of locally adiabatic pseudo-diffraction states $F_{mn}(x,y;z_i)$ as follows:

$$\Psi(x,y,z) = \sum_{m,n} F_{mn}(x,y;z_i)\psi_{mn}(z;z_i) \tag{II.2}$$

$F_{mn}(x,y;z_i)$ solves a two dimensional Schrödinger equation for the x,y motions of the atom for a given z_i, and is to be used as the basis for expansion in a region of z (region i) which contains z_i. The Schrödinger equation for $F_{mn}(x,y;z)$ is

$$\left\{ -\frac{\hbar^2}{2\mu}\left(\frac{\partial^2}{\partial x^2} + \frac{\partial^2}{\partial y^2}\right) + V(x,y;z_i)\right\} F_{mn}(x,y;z_i)$$

$$= \frac{\hbar^2 q_{mn}^2}{2\mu} F_{mn}(x,y;z_i) \tag{II.3}$$

where $V(x,y;z_i)$ can either be the exact potential function $V(x,y,z)$ evaluated at z_i, or it can be some other conveniently chosen reference potential. Upon substitution of Eq. II.2 into Eq. II.1, using Eq. II.3 to simplify, then multiplying by $F_{mn}^{*}(x,y;z_i)$ and integrating over a unit cell (the F_{mn}'s are orthonormal), we obtain

$$\left(\frac{d^2}{dz^2} + d_{mn}^2\right)\psi_{mn}(z;z_i) = \sum_{m',n'} U_{mn,m'n'}(z;z_i)\psi_{m'n'}(z;z_i) \tag{II.4}$$

where

$$d_{mn}^2 = k^2 - q_{mn}^2 \tag{II.5}$$

$$U_{mn,m'n'}(z;z_i) = \frac{2\mu}{\hbar^2} \iint F_{mn}^{*}(x,y;z_i)[V(x,y,z) - V(x,y;z_i)]$$

$$\tag{II.6}$$

$$\times F_{mn}(x,y;z_i)dx\,dy$$

Eq. II.4 may be propagated through region i by standard integration procedures.[13] By partitioning the total range of integration into several regions $i = 0, \dots, n$ in which different pseudo-functions are

chosen for propagation in each region, we may generate complete solutions to Eq. II.1 in all regions of physical interest. The functions ψ_{mn} in regions i and i + 1 may be related at the boundary z_b^i of these two regions by

$$\psi_{mn}(z_b^i; z_{i+1}) = \sum_{m'n'} s_{mn,m'n'}(z_{i+1}, z_i)\psi_{m'n'}(z_b^i; z_i) \qquad (II.7)$$

where

$$s_{mn,m'n'} = \iint F_{mn}^*(x, y; z_{i+1}) F_{m'n'}(x, y; z_i)\, dx\, dy \qquad (II.8)$$

By choosing region n to coincide with the asymptotic region, we obtain the required solutions for calculating the scattering matrix $S_{mn,m'n'}$. The asymptotic analysis is identical to that described elsewhere.[2]

The solution of Eq. II.3 requires a somewhat different procedure than is used for the analogous atom molecule problems.[7] $|F_{mn}|^2$ must be a periodic function, so F_{mn} can change by at most a phase upon translation by a lattice vector. In order to properly satisfy the asymptotic boundary conditions, we must set (see Ref. 14)

$$F_{mn}(x, y; z_i) = e^{i\underset{\sim}{K}\cdot\underset{\sim}{R}}\varphi_{mn}(x, y; z_i) \qquad (II.9)$$

and impose the condition that φ_{mn} be periodic in the lattice spacing. By substituting Eq. II.9 into Eq. II.3 we find that φ_{mn} must satisfy

$$\left\{\nabla_{\underset{\sim}{R}}^2 + 2i\underset{\sim}{K}\cdot\nabla_{\underset{\sim}{R}} + (q_{mn}^2 - K^2) - \frac{2\mu}{\hbar^2} V(x, y; z_i)\right\} \varphi_{mn} = 0 \qquad (II.10)$$

where $\nabla_{\underset{\sim}{R}}$ is the appropriate two dimensional gradient operator. One way to solve Eq. II.10 is to use finite difference procedures.[15] As an example of this, we examine the somewhat simpler case that arises

when motion is restricted to the x, z plane only. In that case, Eq. II.10 becomes

$$\{\frac{d^2}{dx^2} + 2iK_x \frac{d}{dx} + (q_m^2 - K_x^2) - \frac{2\mu}{\hbar^2} V(x;z_i)\} \varphi_m = 0 \qquad (II.11)$$

Evaluating Eq. II.11 by finite difference on a grid of points x_j ($j = 0, \ldots, N$) which span the one dimensional unit cell, we obtain the following set of algebraic equations for the $\varphi_m(x_j;z_i)$:

$$\varphi_m(x_{j+1};z_i)(1 + i K_x \Delta x) + \varphi_m(x_j;z_i)(-2 + \Delta x^2 (q_m^2 - K_x^2) + V(x_j;z_i))$$

$$(II.12)$$

$$+ \varphi_m(x_{j-1};z_i)(1 - i K_x \Delta x) = 0$$

where Δx is the grid spacing. If $\varphi_m(x)$ and $\varphi'_m(x)$ are to be periodic in the lattice spacing, then $\varphi_m(x_0) = \varphi_m(x_N)$ and $\varphi_m(x_{-1}) = \varphi_m(x_{N-1})$ are the required boundary conditions for Eqs. II.12. If these are incorporated into the above equations, we obtain a set of N homogeneous linear equations for the $\varphi_m(x_j;z_i)$ which may be solved by standard eigenvalue-eigenvector methods.[15] Note that the matrix of coefficients obtained from Eq. II.11 is hermitian.

As an example of this finite difference procedure, we consider the asymptotic case $z_i = \infty$ where $V(x_j;z_i) = 0$. In this situation, the secular equation obtained from the diagonalization of the matrix of coefficients can be solved exactly, and we obtain the following expression for the eigenvalues q_m:

$$q_m^2 = K_x^2 + \frac{2K_x}{\Delta x} \sin \frac{2\pi m \Delta x}{a} + \frac{2(1 - \cos \frac{2\pi m \Delta x}{a})}{\Delta x^2}$$

$$(II.13)$$

$$m = 0, \pm 1, \pm 2, \ldots$$

with

$$\varphi_m(x_j; z_i) = \exp i \frac{2\pi m}{a} x_j \qquad (\text{II}.14)$$

where a is the lattice spacing. Taking the limit $\Delta x \to 0$, we find $q_m = K_x + 2\pi m/a$ which is precisely the asymptotic solution since $2\pi m/a$ is the one dimensional reciprocal lattice vector.

The main advantage of this procedure is the reduction in number of closed ($d_{mn}^2 < 0$) diffraction states that are required for convergence of the probabilities ($|S_{mn, m'n'}|^2$) due to a smaller coupling in the $U_{mn, m'n'}$ in Eq. II.6. In addition, since the $\varphi_{mn}(x, y; z_i)$ adjust locally to the shape of the potential, it should be possible to treat highly anisotropic potentials such as those that lead to chemical reaction, chemisorption and diffusion. Indeed, one can imagine situations where attractive wells in the crystal lattice might be so "deep" and well separated from each other that a decoupling of the surface states is possible at some point in the propagation followed by separate integrations "down" each well.

A very useful application of the method presented above would be to the diffraction of He off tungsten (112)[9] and tungsten carbide [W(110)R(3x5)].[8] The first of these two surfaces is the only known pure metal which exhibits diffraction. The surface is characterized by a series of parallel ridges, which will diffract the incident beam if it is perpendicular to the ridges, but not if it is parallel.[9] An obvious application of the close coupling method would be to use the asymptotic diffraction states for expanding the relatively smooth potential along the ridges and pseudo-states to describe the rough

potential perpendicular to them. A primary question to be examined in this theoretical study is the relative importance of thermal effects in broadening and washing out diffraction peaks. This can be examined by first ignoring and then including dissipation in the calculation; using, for example, the discreet function expansion procedure of Wolken[11] to handle the phonon modes.

In the example of helium diffraction from tungsten carbide,[8] the tungsten 110 surface is smooth and it appears that the 3x5 carbide lattice is primarily responsible for the diffraction. A model of the structure of the surface has been proposed by Weinberg and Merrill[8] and we should be able to test this model provided that adequate estimates of the potential parameters can be made.[16] One interesting feature of the experimental results[8] which requires examination is the remarkable coherence of the diffracted beam. This phenomenon leads to sharp peaks in the diffraction line profiles and contrasts strongly with the relatively broad peaks observed in He + LiF scattering. Also of interest in our theoretical analysis will be the He + tungsten carbide (110)R(1x1) system. Unlike the (3x5) counterpart, this surface does not show diffraction peaks in the scattered angular distributions. A comparison of results from these two carbide surfaces should provide a sensitive test of the assumed surface structure, and of the interaction potential.

References

1. For an experimental review, see: J. N. Smith, Surf. Sci. 34, 613 (1973).

2. G. Wolken, J. Chem. Phys. 58, 3047 (1973); ibid., 61, 456 (1974).

3. F. O. Goodman and W. Tan, J. Chem. Phys. 59, 1805 (1973); N. Cabrera, V. Celli, F. O. Goodman, R. Manson, Surf. Sci. 19, 67 (1970).

4. A. Tsuchida, Surf. Sci. 14, 375 (1969).

5. J. D. Doll, Chem. Phys. 3, 257 (1974); J. Chem. Phys. 61, 954 (1974).

6. J. D. McClure, J. Chem. Phys. 57, 2810 (1972).

7. See, for example, A. Kuppermann, G. C. Schatz and M. Baer, Mol. Phys., in preparation; also, G. C. Schatz, Ph. D. thesis, California Institute of Technology, (unpublished), 1975.

8. W. H. Weinberg and R. P. Merrill, Phys. Rev. Lett. 25, 1198 (1970); W. H. Weinberg and R. P. Merrill, J. Chem. Phys. 56, 2893 (1972).

9. D. V. Tendulkan and R. E. Strickney, Surf. Sci. 27, 517 (1971).

10. (a) J. C. Crews, J. Chem. Phys. 37, 2004 (1962); (b) B. R. Williams, J. Chem. Phys. 55, 3220 (1971); (c) D. R. O'Keefe, J. N. Smith, R. L. Palmer, and H. Saltsburg, J. Chem. Phys. 52, 4447 (1970).

11. G. Wolken, J. Chem. Phys. 60, 2210 (1974).

12. G. Wolken, Chem. Phys. Lett. 21, 373 (1973); J. Chem. Phys. 59, 1159 (1973).

13. R. Gordon, J. Chem. Phys. 51, 14 (1969).

14. L. D. Landau and E. M. Lifshitz, <u>Statistical Physics</u> (trans. J. B. Sykes and M. J. Kearsley), Addison Wesley, (Reading, Mass.), 1970, p. 203.

15. See, for example, D. Truhlar, Ph. D. thesis, California Institute of Technology, (unpublished), 1970, p. 266.

16. For a description of semi-empirical methods for describing the interaction potentials, see E. C. Beder, Ad. At. Mol. Phys. $\underset{\sim}{3}$, 205 (1967).

PROPOSITION III

Abstract

An experimental study of electronic energy transfer in collisions between metastable mercury (Hg $6\,^3P_{2,0}$) and the 001 surface of LiF is proposed. Using a previously developed electron impact excitation method to specifically excite Hg to the $^3P_{2,0}$ states, the transfer from these states to the $^3P_1$ state (as a result of collisions with the LiF surface) is detected by observing the resulting 2537 Å ($^3P_1 \rightarrow {}^1S_0$) emission line. The (electronically) elastically scattered $^3P_{2,0}$ states may also be detected, so that transition probabilities between a number of electronic channels may be ascertained. Additional experiments using ground state Hg are also suggested for the purpose of characterizing the Hg - LiF interaction potential.

Energy transfer in collisions between electronically excited atoms and crystal surfaces is a very poorly understood process both theoretically and experimentally. Nevertheless, it is very important, for the quenching of excited atoms at surfaces is often a primary mechanism for their deactivation[1]. In addition, surface ionization in collisions between metastables and metals is an often used (and not well characterized) procedure for detecting these metastables.[2] A theoretical description of the electronically excited states of the atom-surface system has largely been confined to models[3]. No realistic attempt to calculate the probabilities for electronic energy transfer in collisions of atoms or molecules with any kind of surface has been made. Indeed, the only qualitative theories in existence[4] are based largely on general principles such as energy conservation, and provide little mechanistic understanding of the processes involved. Most experimental studies on collisions between electronically excited species and surfaces have used metastable rare gas atoms along with metallic (Pt, Ag, W) or covalent (Si, Ge) targets.[5] In these cases, the work functions of the crystals are smaller than the excitation energies of the rare gas atoms so a primary result of the collision is ejection of electrons, and it is these electrons that are normally detected. Similar considerations apply to experiments involving metastable mercury ($6^3P_{2,0}$) colliding with metallic surfaces.[6] In the most sophisticated of these surface ionization experiments,[5] the yield γ_M of electrons per metastable collision has been determined. In a recent experiment[7] the electronically <u>elastic</u> scattering of metastable

He, Ar, Ne, N_2, and H_2 off Ge (covered with O_2) was examined so that the probability of excited state survival could be evaluated. By measuring time of flight distributions of metastables in the direct and scattered beams, it was determined that slower metastables were being preferentially de-excited.[7]

It is apparent from these examples that more quantitative and detailed experiments are desirable if the energy transfer process is to be accurately characterized. In this proposition, we consider the beam surface experimental study of the deactivation of Hg ($6\,^3P_{2,0}$) by LiF (001). The Hg($6\,^3P_{2,1,0}$) states have excitation energies of 5.460 eV, 4.887 eV and 4.667 eV,[8] respectively, but only the $J = 0$ and 2 states are metastable (with natural lifetimes $> 10^{-3}$ sec). This allows us to monitor the $^3P_{2,0} \rightarrow {}^3P_1$ energy transfer process by observing the 2537 Å ($^3P_1 \rightarrow {}^1S_0$) emission which should occur shortly (10^{-7} sec) after the collision takes place. That this is feasible was recently demonstrated by Krause et al.[8] in a crossed beam study of the de-excitation of Hg ($^3P_2$) by H_2, D_2, N_2, NO and CH_4. In that experiment, the collision energy was kept below 0.20 eV so that the excitation channel $^3P_0 \rightarrow {}^3P_1$ was closed and the $^3P_2 \rightarrow {}^3P_1, E \rightarrow V$ de-excitation cross section was measured directly. A potential defect in using this detection procedure in Hg + LiF collisions is that it will probably not be possible to avoid the $^3P_0 \rightarrow {}^3P_1$ excitation process if the Hg - LiF interaction potential is attractive by more than 0.20 eV. In any circumstance, we shall be measuring the efficiency of transfer between electronic energy of the incident atom and phonon modes of the crystal. A comparison of these results with those of the

above mentioned crossed beam studies,[8] and with the probabilities

for transitions between other channels in the system (see below)

should provide us a detailed understanding of energy transfer in atom

surface collisions not previously available. Two other measurements

which we can also make on the Hg + LiF system are (a) an analysis

of the electronically elastic $^3P_{2,0} \rightarrow {}^3P_{2,0}$ probabilities (via a surface

ionization detector), and (b) (in a separate experiment) the characteri-

zation of scattering of ground state $(^1S_0)$ Hg from LiF (using, for

example, mass spectrometric detection). The latter experiment,

in conjunction with a classical theoretical study should enable an

estimation of the Hg $(^1S_0)$ - LiF interaction potential. One possible

experimental difficulty which might be anticipated is the strong adsorp-

tion of Hg on the LiF surface. Hg $(^1S_0)$ + LiF(001) scattering was

investigated over 40 years ago by several groups[9,10] and it appears

that the scattering mechanism is predominantly direct (as judged by

the absence of a strong $\cos\theta$ component in the angular distribution).

The suggestion made above that Hg $(^1S_0)$ + LiF should be examined

in the proposed experiment is in part for the purpose of reconfirming

these ground state experiments.

We now consider details of the Hg $(^3P_{2,0})$ + LiF(001) experiment.

A metastable Hg source has been described in Ref. 8, and can be

used with slight modification in the present experiment. Included

in this source is an electron impact exciter similar to that used by

McDermott and Lichten.[11] This method of excitation is known[8] to

produce principally the $6^3P_{2,0}$ metastable states of Hg (with all other

excited states decaying before the beam reaches the scattering region).

Decay of the $^3P_{2,0}$ states should be negligible in the experiment if the total length of the beam path is not much longer than 10 cm. Following excitation, collimation and modulation,[12] the beam is impacted on the 001 surface of LiF. Techniques for preparation and use of LiF crystals are well described elsewhere.[13] The crystal should be enclosed in an ultrahigh vacuum scattering chamber with base pressure (with beam off) of close to 10^{-10} torr[13] in order to avoid rapid build up of adsorbed impurities. The number densities of Hg atoms used in the crossed beam experiment of Ref. 8 are similar to those required in gas surface beam experiments[7,12,13], so the two kinds of experiments can be integrated with one another without significant redesign. The $^3P_1 \rightarrow {}^1S_0$ photons will be emitted before the Hg ($^3P_1$) can leave the scattering region so the photon detector should be directed towards it. It will probably be desirable to use gratings or interference filters in examining the 2537 Å radiation since it is possible that the $^3P_{2,0} \rightarrow {}^1S_0$ emission (2271 Å and 2657 Å) will be induced on the LiF surface if the Hg is strongly adsorbed there. Techniques for detecting and velocity analyzing the scattered $^3P_{2,0}$ and $^1S_0$ Hg atoms are similar to those used elsewhere.[7,9,13]

References

1. As an example for the case of N $(^2P; \, ^2D)$, see S. N. Foner and R. L. Hudson, J. Chem. Phys. $\underset{\sim}{37}$, 1662 (1962).

2. R. D. Rundel and R. F. Stebbings, in <u>Case Studies in Atomic Collision Physics</u> (Vol. 2), E. W. McDaniel and M. R. C. McDowell, North Holland, Amsterdam, 1972, Chap. 8.

3. C. B. Duke, Ann. Rev. Mat. Sci. $\underset{\sim}{1}$, 165 (1971).

4. (a) H. D. Hagstrum, Phys. Rev. $\underset{\sim}{104}$, 317 (1956); (b) M. Kaminsky, <u>Atomic and Ionic Impact Phenomena on Metal Surfaces</u>, Academic Press, New York, 1965, Chap. 12 and 13.

5. M. E. Oliphant, Proc. Roy. Soc. (London) $\underset{\sim}{A124}$, 228 (1929); R. F. Stebbings, Proc. Roy. Soc. (London), $\underset{\sim}{A241}$, 270 (1957); R. N. Varney, Phys. Rev. $\underset{\sim}{175}$, 98 (1968); D. A. MacLennen and T. A. Delchar, J. Chem. Phys. $\underset{\sim}{50}$, 1772 (1969); F. B. Dunning and A. C. H. Smith, J. Phys. $\underset{\sim}{B4}$, 1683, 1696 (1971).

6. H. W. Webb, Phys. Rev. $\underset{\sim}{24}$, 113 (1924); A. Buehl, Helv. Phys. Acta. $\underset{\sim}{6}$, 231 (1933); S. Sonkin, Phys. Rev. $\underset{\sim}{43}$, 788 (1933).

7. J. H. Craig, J. R. Dickinson, J. Vac. Sci. Tech. $\underset{\sim}{10}$, 319 (1973).

8. H. F. Krause, S. Datz and S. G. Johnson, J. Chem. Phys. $\underset{\sim}{58}$, 367 (1973).

9. H. A. Zahl and A. Ellett, Phys. Rev. $\underset{\sim}{38}$, 977 (1931); B. Josephy, Z. Physik $\underset{\sim}{80}$, 755 (1933); see also the review article by R. E. Stickney, Ad. At. Mol. Phys. $\underset{\sim}{3}$, 143 (1967).

10. R. R. Hancox, Phys. Rev. $\underset{\sim}{42}$, 864 (1932).

11. M. N. McDermott and W. L. Lichten, Phys. Rev. $\underset{\sim}{119}$, 134 (1960).

12. S. L. Bernasek and G. A. Somerjai, J. Chem. Phys. $\underset{\sim}{62}$, 3149 (1975).

13. See, for example, a review by J. P. Toennies, Appl. Phys. 3, 91 (1974).

PROPOSITION IV

Abstract

A study of the properties of fluctuations (in temperature and concentration) around the nonequilibirium steady states of illuminated chemically reactive systems is proposed. Included in the analysis will be an examination of transition probabilities between multiple steady states, deviations from the Einstein formula for fluctuations, correlations between temperature and concentration fluctuations, and fluctuations near unstable steady states. A Markovian stochastic approximation method for obtaining the joint temperature (or energy)-concentration probability density is suggested along with simplifying models of the energy transfer processes so as to enable an approximate analytical study of the resulting master equation.

The behavior of fluctuations around equilibrium states of of physical systems has been extensively studied by many different approaches,[1,2] and may be summarized (for small fluctuations) by the well-known Einstein equation[3]

$$P(\Delta x) \sim \exp [\Delta S(x)/k] \qquad (IV.1)$$

(Here $P(\Delta x)$ is the probability for a fluctuation Δx in the thermodynamic variable x and $\Delta S(x)$ is the entropy change associated with that fluctuation.) Fluctuations about steady states in nonequilibrium systems (such as chemically reacting systems) are not as well understood, especially when the systems are nonlinearly coupled. An understanding of fluctuations in these situations is, however, fundamental to the characterization of chemical instabilities, very much as the theory of fluctuations from equilibrium has been basic to our understanding of phase transitions and critical phenomena.[4] One question very basic to a description of fluctuations in nonequilibrium steady state systems is the validity of the Einstein equation (Eq. IV.1). Following the development of the "local equilibrium theory" of nonequilibrium processes,[5] Prigogine and Mayer[6] postulated the extension of the Einstein formula to this class of phenomena. A general proof of this proposal has never been given, although the Einstein formula does seem to apply to linear (nonequilibrium) systems as well as to some nonlinear ones.[7,8] Quite recently, a significant controversy has developed over whether a model reacting system (first examined by Nicolis[9]) violates Eq. IV.1.[10] Even if this controversy is resolved in favor of the Einstein formula, there will still be a large number of models

containing unstable steady states or marginal steady states for which this formula simply cannot work.[8] With one exception, studies of the fluctuation behavior of nonequilibrium systems have been confined to models of chemically reacting systems where fluctuations in such continuum properties as temperature, energy, density or pressure have been ignored. The one exception is a study by Babloyantz and Nicolis[11] in which energy fluctuations in a Knudsen gas model (non-reacting) system were examined.

In this proposition we outline the application of theories of fluctuation behavior to both concentration and temperature fluctuations in a simple model (recently proposed by Nitzan and Ross[12]) of an illuminated chemically reacting system. We consider the isomerization reaction

$$A \underset{k_2}{\overset{k_1}{\rightleftharpoons}} B \qquad (IV.2)$$

taking place under constant illumination by monochromatic light which is absorbed by A alone. This system is assumed to be in thermal contact with a bath at a temperature T_e, but no mass transfer into or out of the system occurs (in contrast to other systems previously examined[7,8]). The radiationless relaxation of A is assumed to occur on a time scale short compared to all other processes, so that the illumination simply provides a mechanism for input of energy into the system, where the rate of input is proportional to the concentration of A. The feedback mechanism is provided by the chemical reaction (IV.2), since the heating of the system (which occurs because

of light absorption by A) causes the temperature dependent rate
constants to change, which in turn results in a change in the concen-
tration of the absorber A through this chemical reaction. The perti-
nent dynamical variables in this system are A (the concentration of
species A) and T (the temperature), and the time evolution of these
variables is governed by[12] (ignoring diffusion effects)

$$\frac{dA}{dt} = - (k_1 + k_2)A + k_2 a \qquad \text{(IV.3a)}$$

$$\frac{dT}{dt} = \alpha A - \beta(T - T_e) - \lambda \frac{dA}{dt} \qquad \text{(IV.3b)}$$

where A + B = a and the two rate constants k_1, k_2 are assumed to
have Arrhenius temperature dependence ($k_i = \kappa_i \exp(-R_i/kT)$). The
first term on the right hand side of Eq. IV.3b arises from light
absorption (hence α is proportional to light intensity and to the absorp-
tion coefficient), the second term refers to equilibration of the system
with the surrounding bath, and the third arises from the enthalpy change
which occurs as a result of chemical reaction ($\lambda = (R_2 - R_1)/\epsilon$ with ϵ
proportional to the heat capacity of the system). A steady state analy-
sis of Eqs. IV.3ab leads to

$$A_0 = k_2(T_0)a/(k_1(T_0) + k_2(T_0)) \qquad \text{(IV.4a)}$$

$$T_0 = T_e + \frac{\alpha a}{\beta} [(\kappa_1/\kappa_2)\exp[(R_1 - R_2)/kT_0] + 1]^{-1} \qquad \text{(IV.4b)}$$

The second of these two equations may be solved graphically for the
steady state temperature T_0. Nitzan and Ross[12] show that one or
three solutions for T_0 may be obtained, depending on the values of the

parameters describing the system. In the case of three steady states, a stability analysis indicates that one of these is unstable with respect to fluctuations around it while the other two are stable. When multiple steady states exist, continuous and smooth changes in external parameters (such as α and $R_2 - R_1$) can cause noncontinuous transitions between them as well as hysteresis effects. Near these points of transition between different steady states, fluctuations in both T and A become extremely important since they provide the primary mechanism responsible for the transition.[4] This places great emphasis on characterizing fluctuation behavior in this system and is a primary motivation for the proposition. A study of fluctuations is interesting also because the type of nonlinear behavior exhibited in Eqs. IV.3ab differs in its qualitative form from that in the constant temperature, open, chemically reacting systems previously studied,[7,8] and hence provides a significantly different example for testing the validity of the Einstein formula. Also, because temperature and concentration are strongly coupled in Eqs. IV.3ab, it will be interesting to analyze for correlations in fluctuations of these quantities. Such correlations might be important for the efficient transition between two steady states. An analysis of fluctuation behavior near the one unstable steady state exhibited by this system might give us a more quantitative feeling for the uninhibited growth in these fluctuations which is usually assumed[8] to exist at unstable states.

Let us now consider possible approaches for characterizing the temperature and concentration fluctuations in the illuminated systems. A very straightforward approach to studying concentration

fluctuations is based on a master equation formulation in which a Markovian stochastic approximation is used to solve for the probability function $P(x, t)$ (analogous to $P(x)$ in Eq. IV.1) which gives the probability of finding a concentration x at time t.[7-10] The general form of the master equation for $P(x, t)$ is

$$\frac{dP(x, t)}{dt} = F[P(x, t)] \qquad (IV. 5)$$

where F is a nonlinear difference operator which may be derived by analogy to the chemical rate laws. Eq. IV.5 may be solved by the method of moments[7] by which we obtain a set of partial differential equations for the moment generating function $f(s_x, t)$. These partial differential equations have been solved analytically for a number of systems,[13] including the constant temperature limit of Eq. IV.3a[14] (which is obtained when the illumination is turned off). To include the effect of temperature fluctuations or the related energy fluctuations (so that $P = P(A, T, t)$ or $P = P(A, E, t)$), we can use the energy transfer model of Babloyantz and Nicolis[11] which "discretizes" the relevant continuous variable (E in their case). A differential difference equation analogous to Eq. IV.5 is again obtained and this equation may also be solved by the moment method. In order to use this approach, we shall need to develop models of the energy transfer processes occurring in the illuminated systems. Specifically, the transfer of energy into (via light) and out of (via heat conduction) the chemically reacting system, as well as the production of energy (from the enthalpy of reaction) must be modelled in ways analogous to the Knudsen gas

model of Ref. 11. This should enable us to determine $P(A, E, t)$ and hence the energy-concentration (or temperature-concentration) fluctuation behavior. Finally, we should point out that it is certainly possible that we shall not be able to analytically solve the partial differential equation for the moment generating function $(f(s_A, s_T, t)$ in this case). If approximate techniques also cannot be used to solve it then a numerical solution will be necessary.

References

1. L. Onsager and S. Machlup, Phys. Rev. 91, 1505 (1953).

2. L. D. Landau and E. M. Lifshitz, Statistical Physics, trans. J. B. Sykes and M. J. Kearsley, Addison-Wesley, (Reading, Mass.), 1969, Chap. 12.

3. A. Einstein, Ann. Physik, 33, 1275 (1910).

4. A. Nitzan, P. Ortoleva, J. Deutsch and J. Ross, J. Chem. Phys. 61, 1056 (1974).

5. I. Prigogine, Introduction to Thermodynamics of Irreversible Processes, 3rd Edition, Interscience, New York (1967).

6. I. Prigogine and G. Mayer, Bull. Classe. Sci. Acad. Roy. Belg. 41, 22 (1955).

7. G. Nicolis and A. Babloyantz, J. Chem. Phys. 51, 2632 (1969).

8. G. Nicolis, Adv. Chem. Phys. 19, 209 (1971).

9. G. Nicolis, J. Stat. Phys. 6, 195 (1972).

10. N. Saito, J. Chem. Phys. 61, 3644 (1974); A. Nitzan and J. Ross, J. Stat. Phys. 10, 379 (1974); Y. Kuramoto, Prog. Theor. Phys. 49, 1782 (1973); R. M. Mazo, J. Chem. Phys. 62, 4244 (1975).

11. A. Babloyantz and G. Nicolis, J. Stat. Phys. 1, 563 (1969).

12. A. Nitzan and J. Ross, J. Chem. Phys. 59, 241 (1973); A. Nitzan, P. Ortoleva and J. Ross, J. Chem. Phys. 60, 3134 (1974).

13. I. G. Darvey, B. W. Ninham and P. J. Staff, J. Chem. Phys. 45, 2145 (1966); I. G. Darvey and P. J. Staff, J. Chem. Phys. 44, 990 (1966).

14. D. A. McQuarrie, J. Chem. Phys. 38, 433 (1963).

PROPOSITION V

Abstract

The calculation of the relative rates of intersystem crossing from the photoexcited S_1 state of benzoquinone (and related quinones) to the different spin polarization levels of the lowest excited triplet state T_1 (n, π^*) is proposed. A model of the reduction of these triplet quinones to semiquinone radicals by alcohols, phenols and amines is then used to relate the extent of triplet spin polarization to the experimentally observable chemically induced dynamic electron polarization (CIDEP) effect in the radicals. A comparison of observed and predicted polarization ratios should provide a valuable test for the validity of the triplet polarization mechanism (as opposed to the radical pair mechanism) in producing the observed CIDEP effect.

Chemically induced dynamic electron polarization (CIDEP) refers to the production of a non-Boltzmann distribution of electron spins in the paramagnetic products of a chemical reaction. In a typical experiment, the transitory ESR spectra of the radical products which result from UV or electron beam irradiation of aromatic or conjugated organic compounds are observed.[1] Since the ESR relaxation rates of the radicals (in solution) are in the 10^{-5} to 10^{-6} sec range, an initially polarized spin distribution will thermalize within that time period. The ratio of the initial electron spin polarization (measured from thermal equilibrium) to the equilibrium polarization is called the polarization ratio γ, and the deviation of γ from zero measures the non-Boltzmann character of the spin populations.[2] Since their discovery in the late 1960's, CIDEP and its close relative CIDNP (chemically induced dynamic nuclear polarization) have been the subject of numerous experimental and theoretical studies.[3] In spite of this, the primary mechanism responsible for CIDEP is still the subject of considerable controversy.[1,2,4-8] At present, two mechanisms for production of the nonthermal spin distributions seem to be compatible with most experiments. These are the radical pair mechanism and the triplet polarization mechanism. To demonstrate these two theories, we consider the UV irradiation of 1,4 benzoquinone in an alcohol solution (as was recently investigated by Adeleke et al.[9]). The benzoquinone is initially excited to the S_1 state which quickly relaxes by intersystem crossing to the $T_1(n,\pi^*)$ lowest excited triplet state. The triplet quinone is then reduced by the solvent via hydrogen atom abstraction to form a 1,4 benzosemiquinone radical and a phenoxy

solvent radical. CIDEP is observed in both radicals. The radical pair theory assumes that the observed spin polarization arises from interaction between the semiquinone and phenoxy radicals <u>after</u> they have been formed by chemical reaction.[4,5,10] Any polarization of the triplet state before reaction is ignored. Rather, it is postulated that the two product radicals form a solvent stabilized radical pair at a separation where the splitting of magnetic spin states arising from hyperfine effects and g tensor shifts is comparable to the exchange energy of the two unpaired electrons. In such a situation, considerable mixing of radical pair triplet and singlet states takes place, resulting in a net spin polarization on each radical. The triplet mechanism, on the other hand, assumes that the initial polarization of the three spin sublevels of the T_1 state of the quinone is preserved during the chemical reaction so that the observed spin polarization is a direct reflection of the triplet polarization produced by spin orbit effects during intersystem crossing.[6-9] It has also been suggested[2] that both mechanisms are operative, but that different ones are important in different circumstances. In an important recent experiment,[9] the dependence of semiquinone spin polarization on the orientation of polarized UV excitation light was measured and found to be in agreement with the predictions of the triplet mechanism and not with those of radical pair theory. At the same time, the radical pair mechanism has been quite successful in explaining a variety of other experiments,[6] and its accuracy in predicting CIDNP spectra is well known.[3]

One important unknown in the theory of the triplet mechanism in benzoquinone and related quinones is the relative rate of population

of the individual spin sublevels of the T_1 triplet state before chemical reaction. In this proposition, we consider the calculation of these rates of intersystem crossing so as to enable an estimation of the initial triplet polarization and hence of the polarization ratio in the semiquinone radical product. Such a calculation would enable an estimate of the relative importance of triplet versus radical pair mechanisms in producing the observed CIDEP effect. The application to benzophenone is suggested because (a) this and related quinones have been studied extensively from a number of different viewpoints by CIDEP techniques,[2,9-11] (b) ISC rates for it have been studied by picosecond spectroscopy[12] (which does not distinguish the spin polarizations) so some cross checking of the theory is possible, (c) the molecule is simple enough and has enough symmetry so that a reasonably accurate characterization of the electronic and vibrational states will be possible.

To calculate the rates of intersystem crossing, we suggest that the second order perturbation procedure of Henry and Siebrand[13] be followed. In this method, the rate constant for the transition between vibrational level n of the S_1 electronic state and level m of the T_1 state is given by

$$k_{n \to m} = \frac{2\pi}{\hbar} \rho_m \left| H_{nm} \right|^2 \tag{V.1}$$

ρ_m is the density of vibrational states in the T_1 manifold near level m, and H_{nm} is the vibronic matrix element of the interaction hamiltonian H_1 (expanded to second order). If we write H_1 as

$$H_1 = H_{SO} + T_N$$

where H_{SO} is the spin orbit interaction (which mixes states of different spin multiplicities) and T_N represents the nuclear kinetic energy operator (which mixes Born-Oppenheimer states of the same multiplicity), then the application of second order perturbation theory to the $S_1 \rightarrow T_1$ transition includes (a) a direct $S_1 \rightarrow T_1$ mechanism (in first order) and (b) indirect $S_1 \rightarrow T_n \rightarrow T_1$ mechanisms (in second order). According to the procedure of Henry and Siebrand, evaluation of H_{nm} requires the calculation of (a) spin orbit and nuclear kinetic energy electronic matrix elements, and (b) Franck-Condon vibrational overlap factors. Hameka[14] has considered the calculation of the electronic matrix elements in applications to benzene and acetone using an LCAO-MO procedure. Presumably, a similar method could be used for benzoquinone, although it might be desirable to use more accurate wavefunctions in computing the integrals required. Calculation of the vibrational normal mode spectrum, the Franck-Condon factors, and the densities of states has been considered by Burland and Robinson.[15]

Once the rates of population of the individual triplet state spin sublevels are determined, we must develop a model for the chemical reaction (benzoquinone + solvent $\rightarrow$ benzosemiquinone radical + solvent radical) so that the polarization ratios in the product radicals can be calculated. This has been considered by Wong et al.,[8] who developed a model based on the following assumptions: (a) that spin is conserved in the chemical reaction, and (b) that competition between reaction of triplet benzoquinone and thermalization of its polarized spin distribu-

tion provides the primary solvent effect on the polarization ratio.
In addition, any contributions from radical pairs to the spin polariza-
tion is ignored. The assumptions in this model enable a calculation
of the polarization ratio in the radical with a minimum of dynamical
information (only the overall reaction rate and the triplet state spin
lattice relaxation rate are needed[2]). We suggest using this model as
a zero order test of the triplet mechanism. After that, refinements
to the theory such as the approximate inclusion of surface crossing
in the reaction mechanism can be made to determine the sensitivity
of the polarization ratios to the assumptions in the model given above.
Other approximations which should be tested are (a) the neglect of
solvent interaction on the $S_1 \rightarrow T_1$ intersystem crossing rate, and
(b) the possibility of direct solvent reaction with other than the
lowest vibrational level of T_1, or with electronic states other than T_1.

References

1. For a summary of a variety of experiments and a discussion of some of the older theories, see C. Richard and P. Granger, in NMR: Basic Principles and Progress (Vol. 8), edited by P. Diehl, E. Fluck and R. Kosfeld, Springer Verlag, Berlin, 1974, p. 107.

2. P. W. Atkins, A. J. Dobbs, G. T. Evans, K. A. McLauchlan and P. W. Percival, Mol. Phys. 27, 769 (1974).

3. Pertinent reviews are: (a) J. Potenza, Adv. Mol. Relax. Processes 4, 229 (1972); (b) G. L. Closs, Adv. Mag. Res. 7, 157 (1974); (c) J. K. S. Wan, S. K. Wong and D. A. Hutchinson, Acc. Chem. Res. 7, 58 (1974).

4. R. Kaptein and J. L. Oosterhoff, Chem. Phys. Lett. 4, 195, 214 (1969).

5. F. J. Adrian, J. Chem. Phys. 54, 3918 (1971).

6. F. J. Adrian, J. Chem. Phys. 61, 4875 (1974).

7. J. B. Pedersen and J. H. Freed, J. Chem. Phys. 62, 1706 (1975); ibid., 61, 1517 (1974); and references therein.

8. S. K. Wong, D. A. Hutchinson and J. K. S. Wan, J. Chem. Phys. 58, 985 (1973) and references therein.

9. B. B. Adeleke, K. Y. Choo and J. K. S. Wan, J. Chem. Phys. 62, 3822 (1975).

10. P. W. Atkins, K. A. McLaughlin and P. W. Percival, Chem. Commun. 121 (1973).

11. S. K. Wong and J. K. S. Wan, J. Am. Chem. Soc. 94, 7197 (1972).

12. R. M. Hochstrasser, H. Lutz, G. W. Scott, Chem. Phys. Lett. $\underset{\sim}{24}$, 162 (1974).

13. B. R. Henry and W. Siebrand, J. Chem. Phys. $\underset{\sim}{54}$, 1072 (1971).

14. H. F. Hameka and J. L. Oosterhoff, Mol. Phys. $\underset{\sim}{1}$, 358 (1958).

15. D. M. Burland and G. W. Robinson, J. Chem. Phys. $\underset{\sim}{51}$, 4548 (1969).